Instituut voor
Kern- en Stralingsfysica
Departement natuurkunde en sterrenkunde
Faculteit Wetenschappen

KATHOLIEKE UNIVERSITEIT
LEUVEN

Probing the nuclear structure along the Z=82 closed shell: decay- and laser spectroscopic studies of exotic Pb, Bi and Po nuclei

Promotoren:
Prof. Dr. M. Huyse
Prof. Dr. P. Van Duppen

Proefschrift ingediend tot
het behalen van de graad van
doctor in de wetenschappen
door

Hilde De Witte

Leuven 2004

Dankjewel!

Bij het beëindigen van dit proefschrift wil ik eerst en vooral mijn promotoren, Prof. Dr. Mark Huyse en Prof. Dr. Piet Van Duppen, bedanken. Niet alleen gaven ze mij de mogelijkheid dit werk aan te vatten, maar ze zorgden er ook voor dat ik met plezier op deze vier jaar terugkijk. In het bijzonder hun hulp en enthousiasme tijdens de experimenten heb ik weten te appreciëren.

The members of the jury I would like to thank for the careful reading of this manuscript and for their many helpful comments.

Experimenten zijn nooit het werk van één persoon alleen...
Serge, die aan de basis lag van een deel van dit werk en die me wegwijs maakte in het CERN-gebeuren;
Karen, Sarah, Magda, Ivan, Astrid, voor de goede sfeer tijdens de vele shifts;
Andrei, for your invaluable help during the runs and the analyses;
Maxim, for demystifying many aspects of laser spectroscopy;
Ulli, Valentin, the ISOLDE-crew for excellent beams and collaboration;
Brigitte, Jan, Jocelyne, Leo, Nathalie, Peter,
many heartfelt thanks for your help during the ISOLDE experiments!

Een aantal andere IKS-leden verdienen nog een speciaal woordje van dank;
Luc & Joris, ofte "the IT-team" voor instant-oplossingen van onhandelbare computers en dito programma's; Josée, Katia en Sally voor hun hulp in de al even ondoorgrondelijke wereld van de administratie; Willy voor het oplossen van *last-minute* technische problemen. De mensen van de mechanische en elektronische ateliers ben ik dankbaar voor het zorgvuldige werk in de afgelopen jaren.
De collega's op het IKS en in het bijzonder de mensen van de kernspectroscopiegroep zorgden voor een aangename werksfeer: Astrid, Daniel, Dieter, Dima, Irina, Ivan, Jan, Jan, Jarno, Jean-Charles, Johnny, Karen, Kirill, Magda, Marius, Marisa, Marisia, Oleg, Paul, Riccardo, Rob, Sarah, Sarah, Shelly, Yuri, bedankt. Jarno wil ik in het bijzonder danken voor de ontspannende babbel af en toe, het antwoorden van mijn vele vragen en het nalezen van verschillende delen van deze tekst.

I would also like to thank members from various theoretical groups: Michael Bender, Ivan Borzov, Ruben Fossion, Kris Heyde, Paul-Henri Heenen and Nadya Smirnova for their help and patient explanations.

Tante *K*, bedankt voor het zorgvuldig nalezen van deze tekst, en nog zoveel meer. Honderdvijftig bladzijden kernfysica, ongetwijfeld een ware nachtmerrie voor je...

Paps, Mams, Paperina: het thuisfront. Omdat jullie er al die jaren voor mij waren, vol eeuwig geduld en oneindig vertrouwen!

Pas, voor jou wilde ik het laatste woordje bewaren, maar woorden schieten tekort... jij maakte deze tijd uniek.

Hilde
Leuven, November 2004

Contents

Introduction

The atomic nucleus is a many-body system, consisting of A particles (Z protons and N neutrons) bound by the nucleon-nucleon or *strong* interaction. The Coulomb repulsion between the charged protons and the weak interaction, governing the β decay process, also play a role in the nucleus. Theoretical models predict the existence of over 6000 different nuclei. While only 284 of them occur as stable or primordial nuclides on earth, the others are radioactive, decaying via α, β or particle emission, or fission. About 3600 nuclides have been experimentally observed to date.
Figure 1 shows the chart of nuclides in the N-Z plane: the black squares represent the stable nuclides; the color code for the various radioactive decay modes is given in the figure caption. The grey region shows the theoretically predicted nuclides, delimited by the so-called drip lines. Beyond the drip lines, the binding energy of an additional nucleon vanishes. The precise location of the drip line differs between various theoretical models. This chart also shows the *magic numbers*, specific proton or neutron numbers that give additional stability to the nucleus. They are in many aspects comparable to the noble gas configurations of the electrons in atoms.

A fully analytical description of the nuclear A-body system requires the solution of the Schrödinger equation, $\mathcal{H}\Psi(1,..,A) = E\Psi(1,..,A)$. The non-relativistic Hamiltonian, $\mathcal{H}$, is given by

$$\mathcal{H} = \sum_{i=1}^{A} \frac{\overrightarrow{p}_i^2}{2m_i} + \sum_{i<j=1}^{A} V(\overrightarrow{r}_i, \overrightarrow{r}_j), \tag{1}$$

where the first term represents the kinetic energy and $V(\overrightarrow{r}_i, \overrightarrow{r}_j)$ is the two-body potential. We restrict the nucleon-nucleon interaction to two-body terms only; however, it should be noted that in some cases, such as, for example, the *ab-initio* treatment of light nuclei, the addition of three-body forces is desirable [Nav03].
Except for the lightest nuclei, Eq. 1 cannot be solved exactly and reliable approximations turn out to be essential. The models based on the movement of the individual particles in a potential, are referred to as *microscopic models*. A different class of

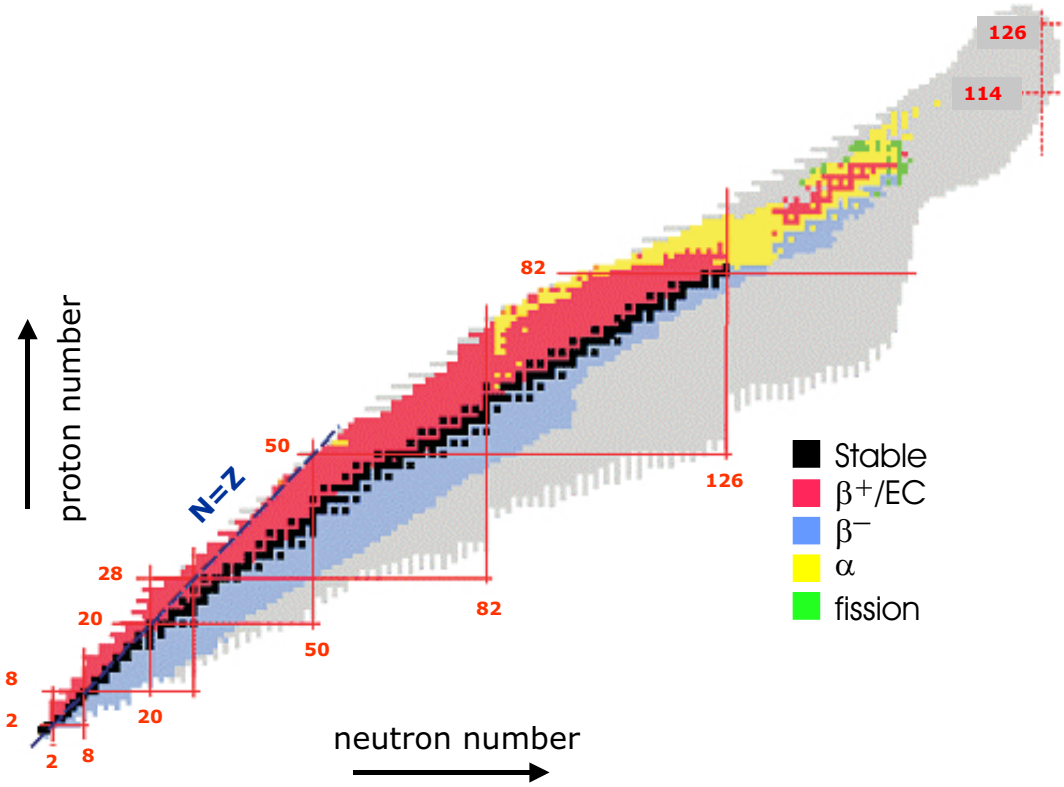

Figure 1: The chart of nuclides. The colors refer to the decay modes of the isotopes: yellow for α decay, pink for β^+, blue for β^- decay and green for spontaneous fission. The stable isotopes are colored in black. The grey area corresponds to the unknown, but predicted isotopes.

approximations satisfies our intuitive, but naive picture of the nucleus as a drop-like entity. These *macroscopic models* have proven to be particularly successful in the description of global nuclear properties. A short description of different theoretical approaches will be presented in Chapter 1.

The increasing amount of experimental data on nuclei far away from the valley of β-stability, forms an excellent testing ground for many theoretical models and their predictive power, towards the most distant regions of the nuclear chart. Technically, the production of these *exotic* nuclei is often a very demanding task: tiny cross section, short half-lives, etc., call for very efficient, selective and fast techniques.

In this work, various experimental nuclear structure aspects around the doubly-magic nucleus ^{208}Pb are being addressed. In particular, the single-particle structure of the neutron-rich lead (Z=82) and bismuth (Z=83) isotopes was investigated. The

trend towards collective behaviour in the even-even, neutron-rich polonium (Z=84) isotopes was followed. In the second part, the evolution of the nuclear shapes in the very neutron-deficient lead isotopes, around the neutron mid-shell at N=104, was studied.

Chapter 2 outlines the experimental set-up at the ISOLDE (CERN) mass separator, where the experiments were carried out, along with a brief reminder of some basic aspects of nuclear spectroscopy. Chapter 3 presents an overview of the current experimental and theoretical knowledge in this area; whereas the information on the neutron-rich isotopes is limited by severe problems in their production, a wealth of experimental data has been obtained below the N=126 shell gap, both in in-beam studies, decay and laser spectroscopy.
The fourth chapter presents the results of a β decay study of neutron-rich lead and bismuth isotopes, followed by a description in the shell model framework. Chapter 5 discusses a study of the half-lives in neutron-rich thallium isotopes. Half-life measurements constitute an important input and a testing ground for global model calculations, aiming at the prediction of nuclear properties far off stability, in the regions of astrophysical interest.
At the neutron-deficient side, with respect to ^{208}Pb, intruder configurations - intruding into the normal low energy configurations- have been a debated topic over the last 20 years [Hey83]. Both at, below and above the Z=82 proton shell closure, experimental evidence for this phenomenon has been found in the past. The intruder states in the neutron-deficient lead isotopes give rise to the occurrence of deformed states at low excitation energy, coexisting with the spherical configuration. The last chapter covers the results and discussion of an in-source laser spectroscopy measurement, focussing on the systematics of the charge radii for lead isotopes, extended beyond mid-shell and aiming to highlight possible shape effects in the ground states.

Chapter 1

Theoretical models

In this chapter some of the widespread theoretical descriptions of the atomic nucleus are reviewed, in order to elucidate the concepts used in the forthcoming discussion of the isotopes in the lead region. Consequently, it is in no sense meant to be exhaustive. A division is made into microscopic and macroscopic models. The microscopic description reflects the behaviour of the constituting particles in a potential , while the collective geometric approach describes the nucleus as an incompressible liquid drop. Both models are successful in reproducing specific structure properties. Single-particle properties will only be well described if a microscopic treatment is followed, while other properties, involving the coherent movement of a large number of particles, will be appropriately described in a collective approach. In a shell model approach, they will be incorporated using coherence. Nevertheless, both approaches are consistent: the residual interaction, applied in the shell model approach, can drive a nucleus to develop correlated motion of many nucleons, which is the starting point of the collective models.

1.1 Microscopic approach

1.1.1 Mean field approximation

The atomic nucleus consists of A interacting nucleons, neutrons and protons, confined in the nuclear volume by the attractive nucleon-nucleon interaction. The exact description involves a complex many-body problem (see Eq. 1) that cannot be solved exactly, but for the lightest nuclei. Successful *ab-initio* calculations have been performed to date, up to A=13 [Nav03].
A drastic simplification is offered by the basic properties of the nucleon-nucleon interaction:

- The attractive, strong interaction is a short-range force: on the 10^5 times larger scale of the atomic description, its effect is almost negligible.

- The saturation of the binding energy per nucleon around a value of 8 MeV, indicates that the nucleons can interact only with their nearest neighbours. This is also reflected in the nearly constant nuclear density.

Combined with the Pauli exclusion principle, these properties validate the concept of independent single-particle motion, in an average or *mean field U,* built by the nucleons themselves. The Hamiltonian can then be rewritten as:

$$\mathcal{H} = \sum_{i=1}^{A}(T_i + U_i) + \left[\sum_{i<j=1}^{A} V(\overrightarrow{r}_i, \overrightarrow{r}_j) - \sum_{i=1}^{A} U_i\right] = \mathcal{H}_0 + \mathcal{H}_{res}, \tag{1.1}$$

i.e. the sum of the one-body Hamiltonians plus the *residual interaction* between the nucleons.
An appropriate parametrization of this average potential, however, is not straightforward. The analytically solvable harmonic oscillator potential is often used as a starting point, but its radial shape is not realistic and a better approximation is given by the Woods-Saxon potential (see Fig 1.1):

$$U(r) = \frac{-U_0}{1 + \exp[(r - R)/a]}, \tag{1.2}$$

with U_0 the potential depth, R the nuclear radius, R=1.2×A$^{1/3}$ fm and a the surface diffuseness parameter. In order to reproduce the experimentally observed shell structure, an additional correction term is required. An appropriate description was found by Mayer [May49] and Haxel, Jensen and Suess [Hax49]: the addition of an attractive spin-orbit term $\propto \overrightarrow{l} \cdot \overrightarrow{s}$ revealed the experimental magic numbers.

The average potential $U(r)$ can also be derived, in a self-consistent way, from the effective nucleon-nucleon interaction (Skyrme and Gogny forces, *e.g.*, are the most widely used ones), using the Hartree-Fock variational method.
Various extensions to this model exist. The *relativistic mean field* represents the nucleons by Dirac spinors and includes explicitly the meson exchange in the nucleon-nucleon interaction. It incorporates the spin-orbit force in a natural way. A detailed account of this method can be found in [Rin96]. Moreover, the Hartree-Fock calculations are often complemented by a microscopic treatment of the like-nucleon pairing, *e.g.*, in the BCS formalism (see Sect. 1.1.2).

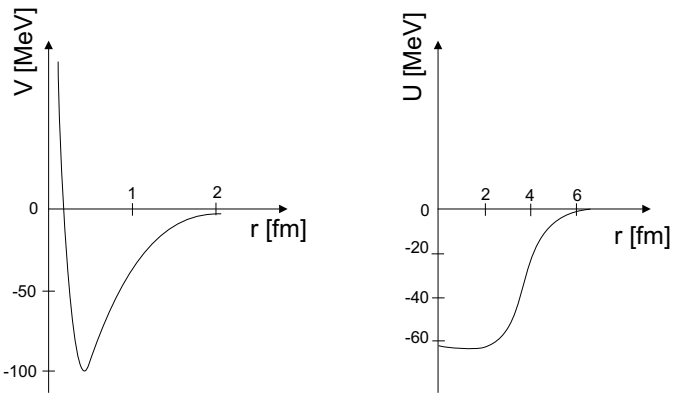

Figure 1.1: Schematic representation of the two-body potential. Left: free NN potential, with a repulsive hard core. Right: regularized, mean field potential of the Woods-Saxon type.

In nuclei with one nucleon (particle or hole) outside the doubly closed shells, the independent particle motion is a good approximation. If one considers the doubly closed core as an inert structure of $I^{\pi}=0^{+}$ spin and parity, then the excited states are the consecutive single-particle levels. This is shown in Fig. 1.2 for the levels around Z=82 and N=126. The energy values have been determined experimentally.

With the departure from closed shells, however, the necessity of the residual interaction between the valence particles appears. This includes the attractive p-n interaction and the pairing interaction between like nucleons, which will be discussed in Sect. 1.1.2.

1.1.2 Spherical shell model

In the nuclear shell model, in addition to the mean-field, the effects of the residual interaction in Eq. (1.1) are taken into account. In practice, one needs to diagonalize the full Hamiltonian matrix $\mathcal{H}$. The basic ingredients in a shell model calculation are an appropriate model space, an interaction and a computer code to solve the eigenproblem [Cau04].

As mentioned before, only the lightest nuclei can be calculated by ab-initio methods [Pie02]; for heavier nuclei, one needs to define a smaller model space, large enough to include the dominant components of the low-lying states and small enough to make the system technically solvable. The shell structure of the nucleus presents a natural truncation: the nucleus can be divided into an inert core and a few active valence particles outside the closed shells.

Secondly, the effective interaction is determined for a given model space. We distinguish between the schematic interactions (having a simple radial shape) and the

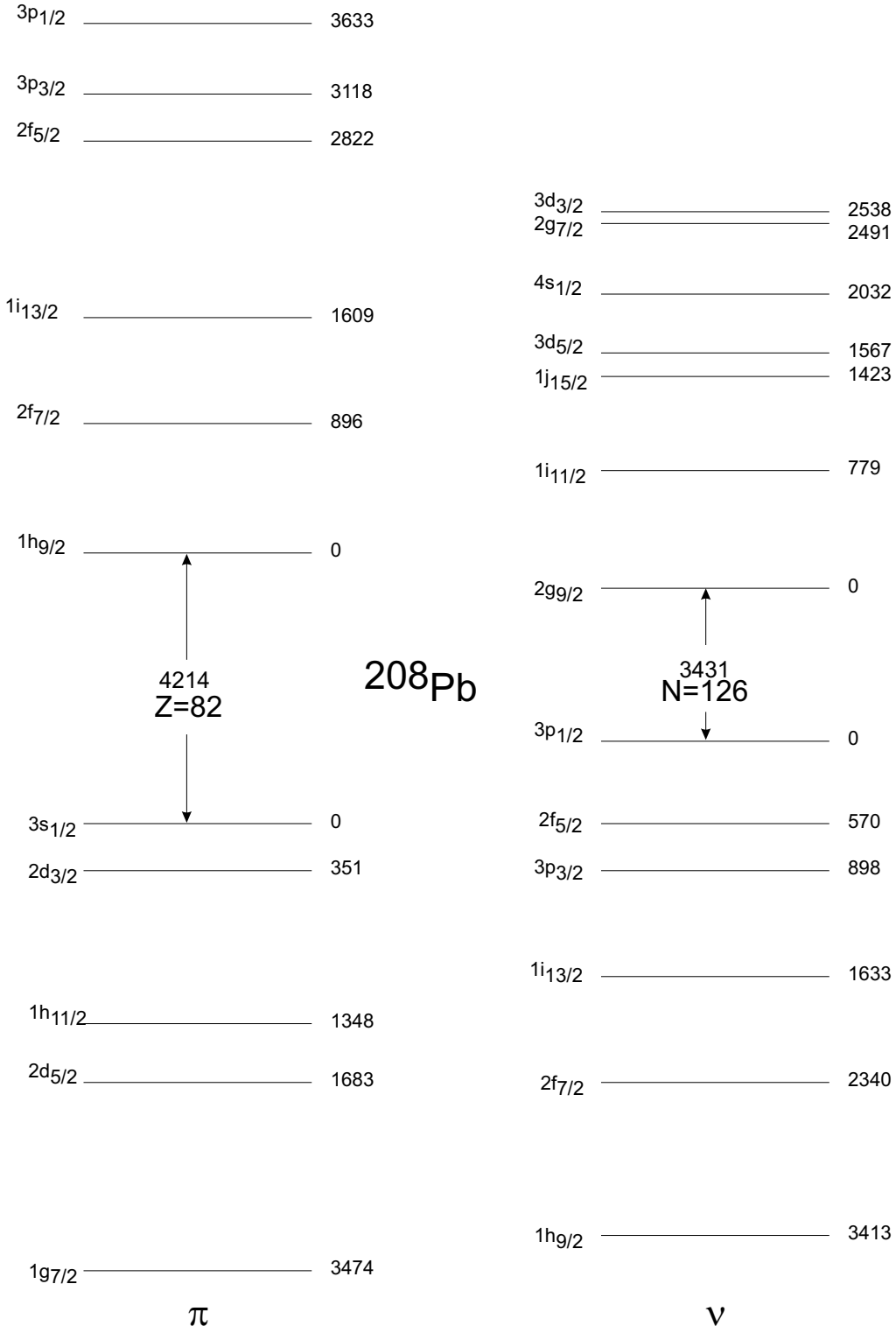

Figure 1.2: Experimental single-particle energies near the Z=82, N=126 shell closures. The data are obtained from ^{209}Pb, ^{207}Pb, ^{209}Bi and ^{207}Tl. Energies are in keV, relative to the closed shells.

realistic interactions derived from a free nucleon-nucleon interaction (see Fig 1.1), fitted to scattering data. Various modifications to the free interaction are needed: in-medium effects change the interaction considerably and regularization of the strongly repulsive core is necessary. This approach has been followed by Kuo and Herling, to derive an effective interaction around ^{208}Pb [Kuo71].
An alternative way consists in fitting the single-particle energies and the two-body matrix elements $\langle j_1 j_2 | V_{12} | j_3 j_4 \rangle$ to experimental data.

When nucleons of one type only are present outside the closed core (singly-closed shells), the residual interaction is dominated by the attractive pairing force between like nucleons. We will now pause here to summarize the basic properties of the pairing force, in a BCS-description. BCS stands for the Bardeen-Cooper-Schrieffer theory, borrowed from the theory of superconductivity [Bar57].
When treating identical particles in time reversed orbits the attractive pairing force can be used. Its matrix elements are given by:

$$\langle j_1 j_2 J | V_{pair} | j_3 j_4 J' \rangle = -G(-1)^{l_1+l_3} \sqrt{(j_1 + \frac{1}{2})(j_3 + \frac{1}{2})} \delta_{j_1 j_2} \delta_{j_3 j_4} \delta_{J0} \delta_{J'0}, \tag{1.3}$$

where G is the strength of the pairing force. The non-diagonal matrix elements correspond to the scattering of 0^+ coupled pairs of nucleons into different orbitals. A mixing of different 0^+ states results and the coherent state is pushed down in energy, forming the so-called pairing gap. Partial occupancies are created and a smearing of the Fermi surface results. Without the pairing interaction, all orbits are occupied in the ground state up to the Fermi energy and completely empty above; in the presence of pairing the situation of Fig. 1.3 occurs.
A convenient formalism for the treatment of pairing replaces the usual particles and holes by *quasi-particles* (qp), linear combinations of particle and hole wave functions, and particle-hole excitations by 2qp-excitations. In this formalism the single-particle energy ε_i becomes a quasi-particle energy E_i:

$$E_i = \sqrt{(\varepsilon_i - \lambda)^2 + \Delta^2}, \tag{1.4}$$

with λ the Fermi energy. The gap parameter Δ reflects the range over which the level occupancies are smoothened; it is proportional to the strength of the interaction G.
While the shell model relates the description of excited states to the closed shells, the BCS formalism defines a BCS vacuum state, including the partial occupancies. The excitation is now considered relative to the Fermi surface, rather than to the closed shell core. This produces an important truncation when many valence particles are present, as now the lowest excitations reduce to 2qp, 4qp,... configurations. The BCS

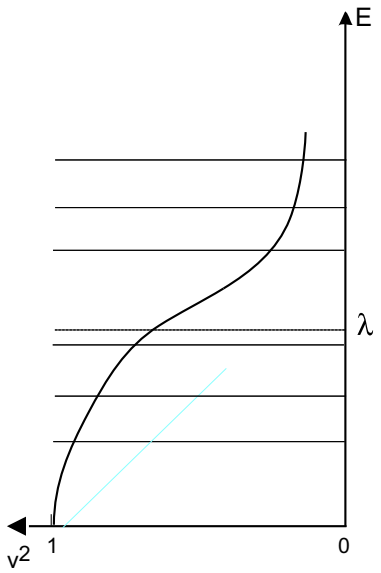

Figure 1.3: Schematic representation of the occupation probability, v^2, of the orbitals around the Fermi surface, λ, in the BCS ground state

ground state is given by:

$$|\widetilde{0}\rangle \equiv \prod_{\nu>0} \left(u_\nu + v_\nu a_\nu^+ a_{\overline{\nu}}^+\right) |0\rangle, \tag{1.5}$$

with v_ν^2 the occupation probability of the orbit ν and $u_\nu^2 = 1 - v_\nu^2$. A major drawback of the BCS-model is the non-conservation of the particle number, $n = \sum_i v_i^2$.

An alternative truncation scheme for the shell model space for semi-magic nuclei is offered by the broken-pair or generalized seniority model. The generalized seniority v_g corresponds to the number of particles not coupled to coherent S-pair states. Experimentally, the spectrum for semi-magic nuclei with many valence nucleon pairs is very similar to the one with one valence pair only. This would imply that at low excitation energy a single nucleon pair is broken. The empirical relation

$$E(v_g = 2) \geq E(v_g = 0) + v_g \cdot \overline{\Delta}, \tag{1.6}$$

with $\overline{\Delta}$ half the energy gap between the ground state and the non-collective excited states, suggests that seniority truncation corresponds indeed to a low energy truncation in shell model space. The approach can be generalized to valence particles of both types, provided only few (1 or 2) nucleons of the second type are present (see Sect. 4.9) [Hey94b].

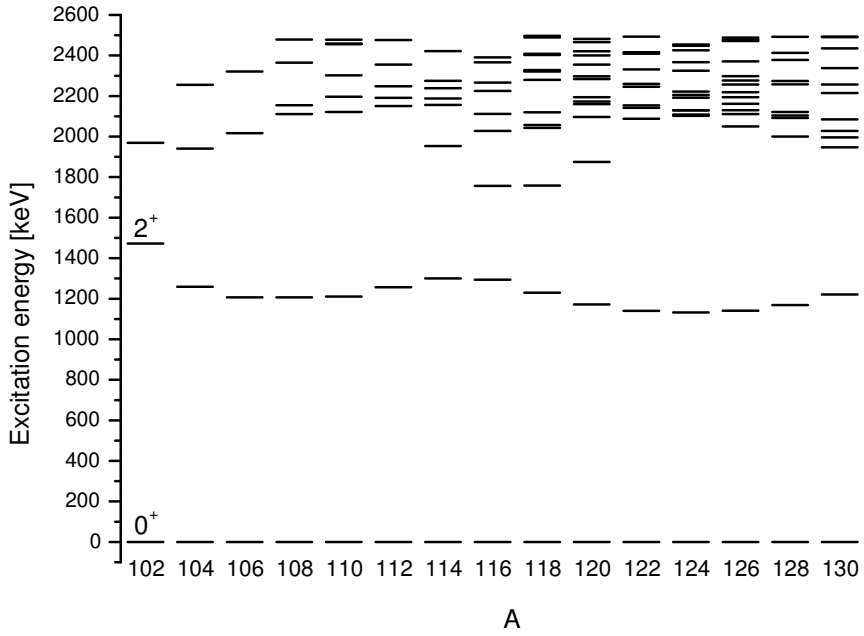

Figure 1.4: Excited states in the even-even Sn isotopes. Data are taken from the *National Nuclear Data Center* database [nnd].

The most obvious manifestation of the pairing interaction is the 0^+ ground state in all even-even nuclei and the large gap of ∼1-2 MeV between the ground state and the $J^\pi \neq 0^+$ non-collective states in singly-closed even-even nuclei. The experimentally observed gap corresponds to twice the pairing gap, as can be seen in Eq. (1.4). This is shown in Fig. 1.4 for the tin isotopes with A=102-130. The first excited 2^+ state is also lowered, although to a lesser extent, as predicted by a simple δ-interaction.

When both types of nucleons are present, the attractive proton-neutron interaction plays a crucial role. The Hamiltonian $\mathcal{H}$ can be split into two components, $\mathcal{H} = \mathcal{H}_m + \mathcal{H}_M$, where $\mathcal{H}_m$ and $\mathcal{H}_M$ represent the *monopole* and the *multipole* Hamiltonian, respectively [Pov01]. The effect of the monopole Hamiltonian is related to the evolution of the spherical mean field. Its behaviour is particularly clear when following a chain of isotopes with one nucleon outside the closed shell. This feature will be discussed in detail in Sect. 4.5. We limit the discussion of the multipole Hamiltonian $\mathcal{H}_M$ to the quadrupole (λ=2) component, neglecting all higher order multipoles. This long-range component of the residual interaction is responsible for the development of deformation with increasing number of valence particles. As such it complements the pairing force, which couples particles to $J, M = 0$, and favours sphericity.

The success of the nuclear shell model partially lies in the inclusion of the dynamical correlations in the model space. Its main shortcoming is the quickly growing dimension of the matrix to diagonalize, when adding valence particles or orbitals. Various alternative methods have been introduced, such as a stochastic treatment of the many-body problem. The *Quantum Monte Carlo diagonalization* is discussed, for example, in [Ots01a]. Instead of diagonalizing the Hamiltonian matrix in the entire valence space, only those basis states that are important for the eigenstate to be calculated are selected and the diagonalization is performed in the reduced model space.
The symmetry-based truncation of the Interacting Boson Model is treated in Sect. 1.2.3.

Figure 1.5 summarizes the above issues, applying them to the lead region. In the ^{208}Pb core, the first excited state is found at an energy of E=2.615 MeV. Its spin and parity are $I^{\pi}=3^{-}$, corresponding to a collective octupole vibration (see Sect. 1.2.2). The spectra of ^{209}Pb and ^{209}Bi give the neutron and proton single-particle energies, also given in Fig. 1.2. In ^{210}Pb and ^{210}Po only one type of valence particles is present and the low-energy excitations are obtained by breaking the valence nucleon pair. The pairing interaction lowers the 0^{+} ground state, with respect to the other members of the broken-pair multiplet, by an amount equal to twice the pairing gap. The spectrum resembles that of a pure δ-interaction. In ^{212}Po both a pair of valence neutrons and protons are present; under the influence of the proton-neutron interaction the spectrum evolves towards the vibrational picture. In ^{210}Bi, the proton-neutron interaction between the neutron in $\nu g_{9/2}$ and the proton in $\pi h_{9/2}$ splits the degeneracy of the members of the multiplet with $I^{\pi}=0^{-}\cdots 9^{-}$, lowering the parallel and antiparallel couplings, with respect to the intermediate ones.

1.1.3 Deformed mean field: the Nilsson model

In Sect. 1.1.1 and 1.1.2, the discussion was limited to spherically symmetric potentials. In the presence of many valence nucleons outside the closed shells, the residual proton-neutron interaction can drive the nucleus to an energetically favourable deformed state. In the alternative description of the Nilsson model the nucleons move independently in a non-spherical potential, generating a deformed macroscopic shape.
A common parametrization of the nuclear surface is defined via the expansion of the nuclear radius in spherical harmonics, $Y_{\lambda}^{\mu}(\theta,\phi)$:

$$R(\theta,\phi) = c(\alpha)R_0\left[1+\sum_{\lambda}\sum_{\mu=-\lambda}^{\lambda}\alpha_{\lambda\mu}Y_{\lambda}^{\mu^*}(\theta,\phi)\right], \tag{1.7}$$

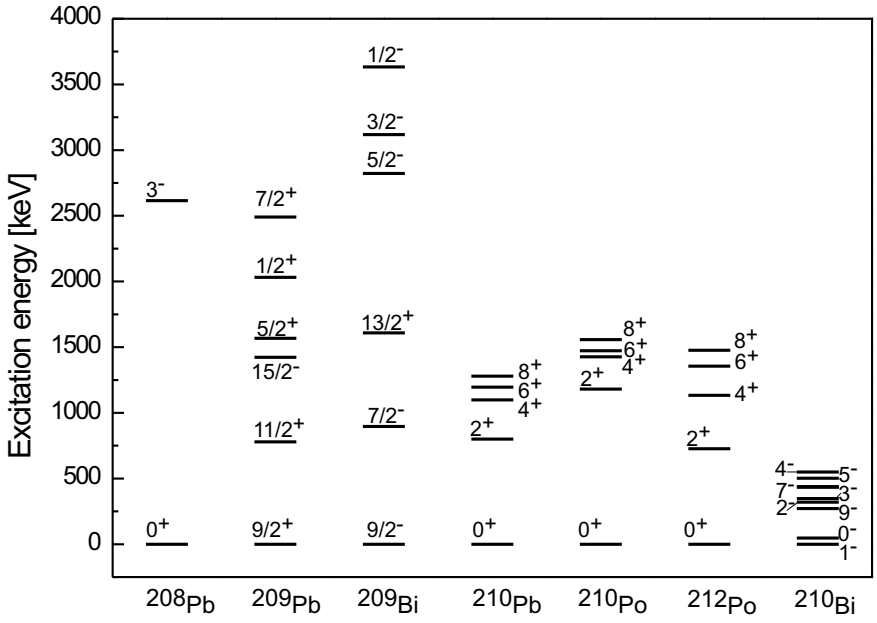

Figure 1.5: Illustration of the aforementioned structure properties, around the doubly magic nucleus ^{208}Pb: independent particle behaviour and the influence of the residual interaction.

where R_0 represents the radius of the spherical nucleus with the same volume and $\alpha_{\lambda\mu}$ are the expansion coefficients. The parameters $c(\alpha)$ are determined to fulfil the volume conservation condition. If we restrict the description to the most common quadrupole deformation, the above sum reduces to

$$R(\theta,\phi) = c(\alpha)R_0\left[1+\sum_{\mu=-2}^{2}\alpha_{2\mu}Y_2^{\mu^*}(\theta,\phi)\right]. \tag{1.8}$$

For axially symmetric shapes, all expansion coefficients $\alpha_{2\mu}$ with $\mu \neq 0$ vanish; the quadrupole deformation parameter is defined as β_2=α_{20}. If deviations from axial symmetry are included, a second deformation parameter γ is needed and defined as:

$$\alpha_{20} = \beta_2\cos\gamma \qquad \text{and} \qquad \alpha_{22} = \alpha_{2-2} = \frac{1}{\sqrt{2}}\beta_2\sin\gamma. \tag{1.9}$$

If γ is equal to 0° or -60°, the nucleus has a prolate or oblate deformation, respectively. Intermediate values of γ correspond to triaxially deformed nuclei.
The three remaining parameters, related to the Euler angles, define the orientation of the body-fixed frame in 3-dimensional space.

For a spherical nucleus, no preferential direction exists and all $(2j+1)$ substates for a given j are degenerate in energy. In an axially deformed nucleus, one can define the symmetry axis and the m-components will be split according to the projection on the symmetry axis, Ω. Hence the degeneracy of the $2j+1$ sublevels is lifted. Only the time-reversed orbits $+\Omega$ and $-\Omega$ are degenerate. Intuitively this can be understood as follows: if the core's matter distribution is not uniform, the energy of a nucleon orbiting the deformed core will depend on the overlap or on the orientation of the single-particle orbit with respect to the core. States with different Ω will thus have a different energy. The Nilsson diagram describes the evolution of the single-particle energies as a function of the deformation parameter. They are calculated using a deformation dependent Hamiltonian, *e.g.*, a deformed Woods-Saxon potential. Figures 1.6 and 1.7 show the example for Z$\geq$82 and 82$\leq$N$\leq$126.

The deformed mean field first solved the problem of reconciling the microscopic approach of the shell model with the observation of collective motion, like, *e.g.*, the nuclear rotation. The intuitive interpretation in the collective models is discussed in the next section.

1.2 Collective approaches

In the collective approaches we distinguish between the so-called geometric models and the algebraic models, like the Interacting Boson Model, discussed in Sect. 1.2.3. From the geometric side, we discuss the liquid drop mass formula, with the various refinements applied to it, as well as the geometric description of nuclear rotation and vibration.

1.2.1 Liquid Drop Model

In the early days of nuclear structure, the intuitive picture of the nucleus as an incompressible drop of fluid was commonly accepted. The shell structure, well describing the atomic observations, was even believed to be inappropriate for the atomic nucleus. In the semi-empirical liquid drop formula, the binding energy of the nucleus is parameterized as follows (in a slightly generalized form of the original von Weizsäcker formula [Wei35]):

$$B.E. = a_v A \left[1 - \kappa_v \left(\frac{N-Z}{A}\right)^2\right] - a_s A^{2/3} \left[1 - \kappa_s \left(\frac{N-Z}{A}\right)^2\right] - \frac{3}{5}\frac{Z(Z-1)e^2}{4\pi\epsilon_0 R_c} + E_{pair}. \tag{1.10}$$

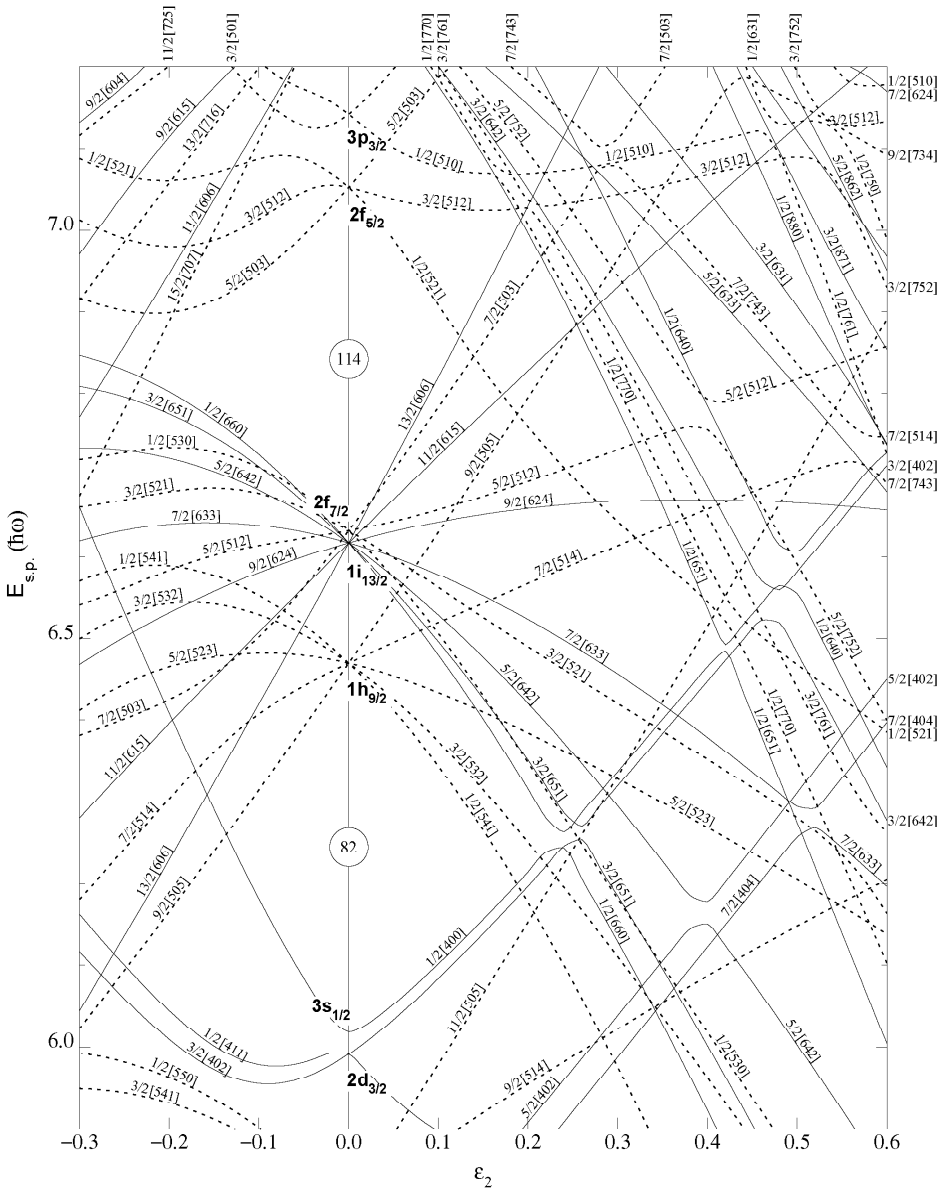

Figure 1.6: Nilsson diagram for Z≥82. The parameter ε_2 is related to the deformation parameter β_2 by the following relation: $\beta_2 = \sqrt{\frac{\pi}{5}}(\frac{4}{3}\varepsilon_2 + \frac{4}{9}\varepsilon_2^2 + \cdots)$. The figure is taken from [Fir96].

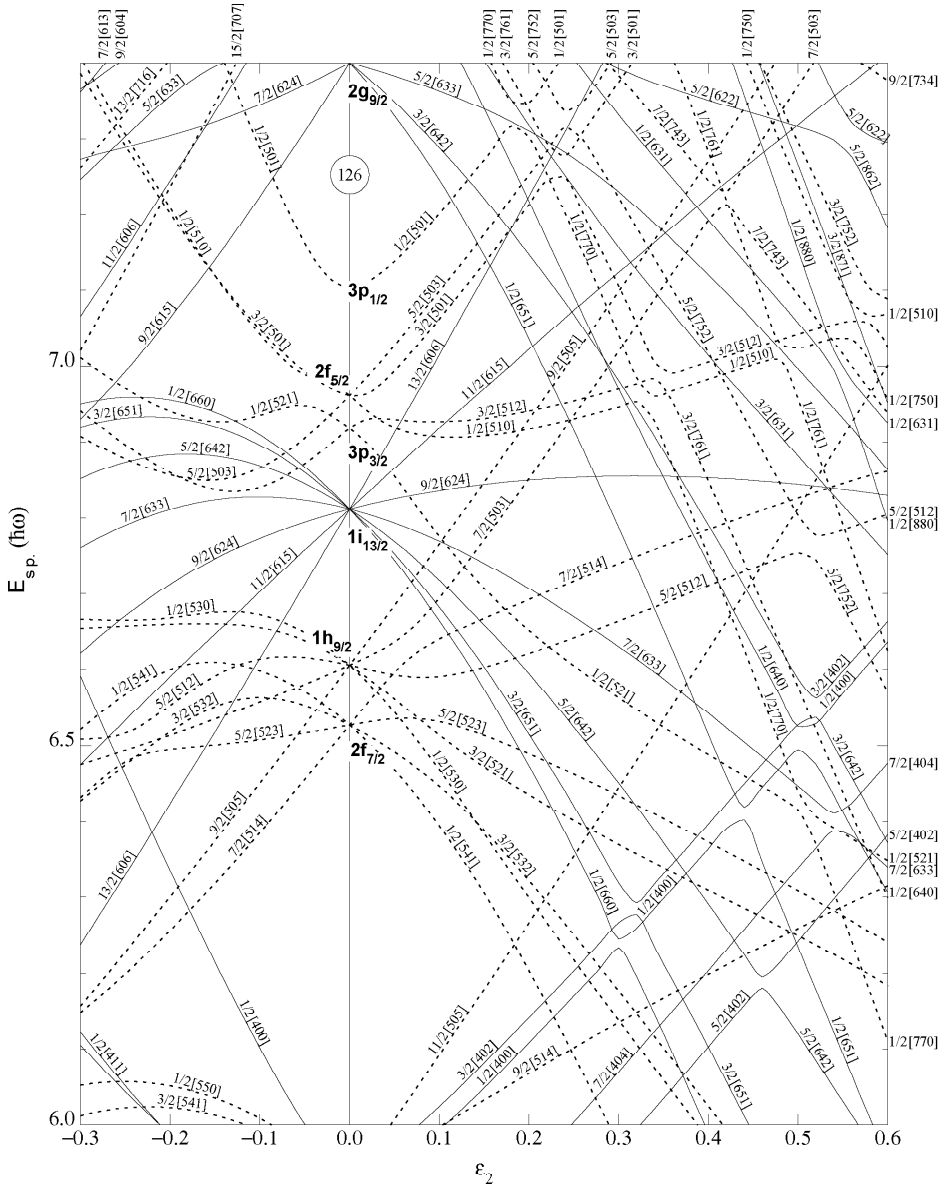

Figure 1.7: Idem as Fig. 1.6, but for neutrons (82≤N≤126). The figure is taken from [Fir96].

The first two terms are the volume and surface energy, respectively. The isospin dependence is discussed by Myers and Swiatecki [Mye66] and favours N=Z, limiting the effects of the Pauli principle. This effect is counterbalanced by the Coulomb repulsion between the protons, the third term of the expression (1.10), which favours a neutron excess. The observed odd-even effect in the nuclear masses leads to the addition of a pairing energy term E_{pair}=(-Δ,0,Δ) with $\Delta \approx 12/\sqrt{A}$ for odd-odd, odd-A and even-even nuclei, respectively [Seg82].

The comparison between semi-empirical and measured nuclear masses showed clear deviations around the closed proton and neutron shells, as well as at mid-shell and provided evidence for the need for shell corrections. Introduced by [Mye66] and further refined in the Strutinsky theorem [Str67], these corrections account for the non-uniform level density. This term is not only important for reproducing the nuclear masses of nuclei near closed shells, but it also generates non-spherical nuclear shapes.

Meanwhile, many refinements have been added to the liquid drop model, also with respect to the calculation of nuclear radii. In the droplet-model [Mye66], deviations from the spherical nuclear shape are included. The redistribution of the proton and neutron distribution increases all radial distributions and quadrupole moments. Finally, the sharp-surfaced distribution is corrected for the diffuseness and again results in an increase of the radial moments, constant for all nuclei. The mean square radius thus consists of three terms:

$$\langle r^2 \rangle = \langle r^2 \rangle_u + \langle r^2 \rangle_r + \langle r^2 \rangle_d, \tag{1.11}$$

a uniform (u), but shape dependent distribution, corrected for redistribution (r) and diffuseness (d).

The *Finite Range Droplet Model* (FRDM) [Moe95] is a macroscopic-microscopic model, with a slowly varying macroscopic part based on the droplet description, and quickly varying microscopic contributions. Besides the Strutinsky shell correction, a fully microscopic BCS-treatment of the pairing interaction is also incorporated. In the macroscopic part, finite-range aspects of the nucleon-nucleon interaction and the compressibility of the nucleus exponentially decreasing towards the center, are accounted for.

A recent review of the various mass formulae has been given in [Lun03]. However, not only masses but also radii, half-lives and various other global properties have been calculated with the microscopic-macroscopic models.

1.2.2 Nuclear vibration and rotation

Vibration

In this section, we consider the collective vibration of the nucleus around its equilibrium shape (see *e.g.* [Hey94a]). The time averaged shape is spherical, but the instantaneous shape is not. The lowest order vibration, in the expansion of Eq. (1.7), corresponds to λ=2, the quadrupole phonon (λ=1 corresponds to a displacement of the center of gravity); λ=3 is the octupole vibration. The vibration is included via a time dependence of the expansion coefficients, $\alpha_{\lambda\mu}(t)$. Formally, the Hamiltonian for a harmonic quadrupole vibration is written as:

$$\mathcal{H}_{vibr} = E_0 + \hbar\omega \sum_{\mu} \left(b^{+}_{2\mu} b_{2\mu} + \frac{1}{2} \right), \qquad \mu = 0, \pm 1, \pm 2 \tag{1.12}$$

where E_0 is the zero-point energy and $b^{+}_{2\mu}$ and $b_{2\mu}$ are the quadrupole phonon creation and destruction operators, respectively.
Adding one quadrupole phonon to the 0^+ ground state of an even-even nucleus gives rise to a 2^+ one-phonon state. The addition of a second phonon produces the 0^+, 2^+, 4^+ states of the two-phonon multiplet, at an energy of twice the one-phonon energy.

An alternative description of the nuclear vibration is the microscopic (Q)RPA approach (*Quasi-particle* random phase approximation), where the vibration is expanded in a single-particle or quasi-particle basis. A coherent mixture of particle-hole or two-quasi-particle excitations then replaces the phenomenological phonons. Details can be found, *e.g.*, in [Hey94b].
A good example of such a collective vibrational state is the octupole vibration in the doubly closed nucleus, ^{208}Pb, as shown in Fig. 1.5. This state is built by many particle-hole or two-quasi-particle excitations, none of which is dominant.

Rotation

In a laboratory fixed frame, the description of the quadrupole vibration of a nucleus requires 5 parameters, $\alpha_{\lambda,\mu}$. In the body fixed frame it reduces to 2 parameters, describing the elongation, β_2, and the departure from axial symmetry, γ. The three remaining parameters, expressed in terms of the Euler angles, describe the rotation of the nucleus. Quantal systems cannot rotate collectively around a symmetry axis, and for axially symmetric nuclei the rotation axis is always perpendicular to the symmetry axis.

The Hamiltonian describing the collective rotation of the nucleus is given by

$$\mathcal{H}_{rot} = \frac{\hbar^2}{2\Im}\overrightarrow{R}^2, \tag{1.13}$$

with $\Im$ the moment of inertia and $\overrightarrow{R}$ the rotational angular momentum. This leads to a sequence of states with energies

$$E_R = \frac{\hbar^2}{2\Im}R(R+1). \tag{1.14}$$

It has been observed experimentally that the moment of inertia is smaller than the rigid rotation value. Although the nucleus is seen to behave like a superfluid due to pairing interaction, the superfluid moment of inertia is also not the exact description. The nucleus presents an intermediate situation between rigid and superfluid rotation. Moreover, the moment of inertia changes with the spin in a rotational band.
For an extensive description of the rotational motion in nuclei, we refer to [Nil95].

1.2.3 The interacting boson model

The interacting boson model[1] describes the nucleus in terms pairs of protons and neutrons coupled to 0^+, called s-bosons, and to 2^+, d-bosons. In the sd-boson model, the higher angular momenta $g,\cdots$ are neglected, but they can in principle be incorporated. Together they span a six dimensional Hilbert space, with the column vector

$$b^+_\mu = \begin{pmatrix} s^+ \\ d^+_{+2} \\ d^+_{+1} \\ d^+_0 \\ d^+_{-1} \\ d^+_{-2} \end{pmatrix} \tag{1.15}$$

transforming according to the group U(6).
If the Hamiltonian can be written as a linear combination of the invariant operators of a complete chain of subgroups of U(6), then the eigenvalues can be calculated in closed form, in terms of the expectation values of the invariant operators. The problem is thus shifted to determining the group theoretical reductions of the U(6) group. If in addition the occurrence of the O(3) and O(2) subgroups (related to the angular momentum and its projection, respectively) is required, only few reductions remain, corresponding

[1] see for example [Hey94b] for a fuller discussion of this subject

to the anharmonic vibrator, rotor and γ-unstable rotor limits. This description of the physical system in terms of its symmetries gives an elegant approximation of the full shell model treatment. An example of this type of calculation in the neutron-deficient lead isotopes will be discussed in more detail in Chapter 6

Chapter 2

Experiments with the ISOLDE on-line mass separator

The study of rare, exotic nuclei is a major technical challenge as pure and intense beams are fundamental. All experiments described in this work have been performed at the ISOLDE on-line mass separator (CERN, Geneva) [Kug00]. In the first section, the isotope production will be discussed, followed by a description of the various selective steps towards pure beams. The second section is devoted to the specific needs of the decay experiments and subsequently the basic principles of the laser spectroscopy experiment are summarized. The last section shortly describes the data acquisition system.

2.1 Production of exotic beams at an on-line mass separator

2.1.1 Spallation

When a light, relativistic particle (*e.g.* a nucleon), with an energy of several hundreds of MeV or GeV, hits a heavy target, spallation of the target occurs. The reaction is considered as a two-step process: in a first step, after the impact of the projectile, the target nucleus is heated and individual nucleon-nucleon collisions take place. A few nucleons can be ejected and an excited pre-fragment is formed. In a second step, the residue further de-excites by evaporating more nucleons or light nuclei (α, ^{3}He,$\cdots$). The process is schematically drawn in Fig. 2.1.

Along with spallation, other reaction channels, namely fission and target fragmentation are also open. As a result, a large part of the chart of nuclides is populated and further selectivity is necessary.

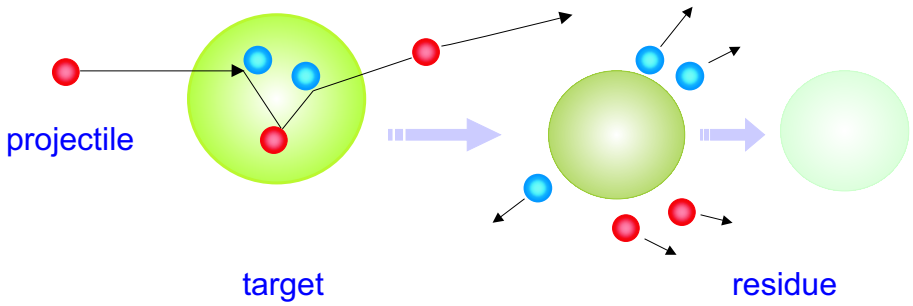

Figure 2.1: Schematic representation of the spallation reaction, induced by a relativistic light particle. The process is modelled as a two-step reaction.

2.1.2 Production technique

The four coupled synchrotrons of the PS(proton synchrotron)-booster produce a 2.4 μs long proton pulse of 3×10^{13} protons per pulse, with an energy of 1.0 GeV or 1.4 GeV. The pulses are separated by a multiple of 1.2 s. They are organized in the so-called *supercycle*, the 16.8 s long period of the CERN accelerator complex, shown in Fig. 2.2. The proton beam bombards a thick target (typically $\sim$50 g/cm^2), *e.g.* ^{238}UC$_x$/graphite or ^{232}ThC$_x$/graphite for the isotopes studied in this work. Subsequently, the reaction products, stopped in the target material, diffuse through the target and effuse via the transfer line towards the ion source. The various parts of the target-ion source unit are drawn in Fig. 2.3.

The production rate in the target is given by P=$\sigma N\phi$, with σ the production cross section for a particular isotope in the reaction, N the number of target particles exposed to the primary beam and ϕ the flux of bombarding particles. However, important losses occur between the production in the target and the arrival of the beam at the detection set-up. The release of the atoms from the target is a slow process (depending on the target material, geometry, temperature, ... and the extracted species) and decay losses can be large, especially for short lived isotopes. In order to reduce the diffusion time, the target is heated to about 2000°C. The release function $P(t)$ is defined as the probability density for an atom produced at $t = 0$ to be released at time t. The probability for a radioactive atom with decay constant λ_i to be released from the target and not decayed at time t is $P_i(t, \lambda_i) = P(t) \times e^{-\lambda_i t}$ [Let97].

Furthermore, the efficiency of the ionization process (see Sect.2.1.3) and of the beam transport must be taken into account.

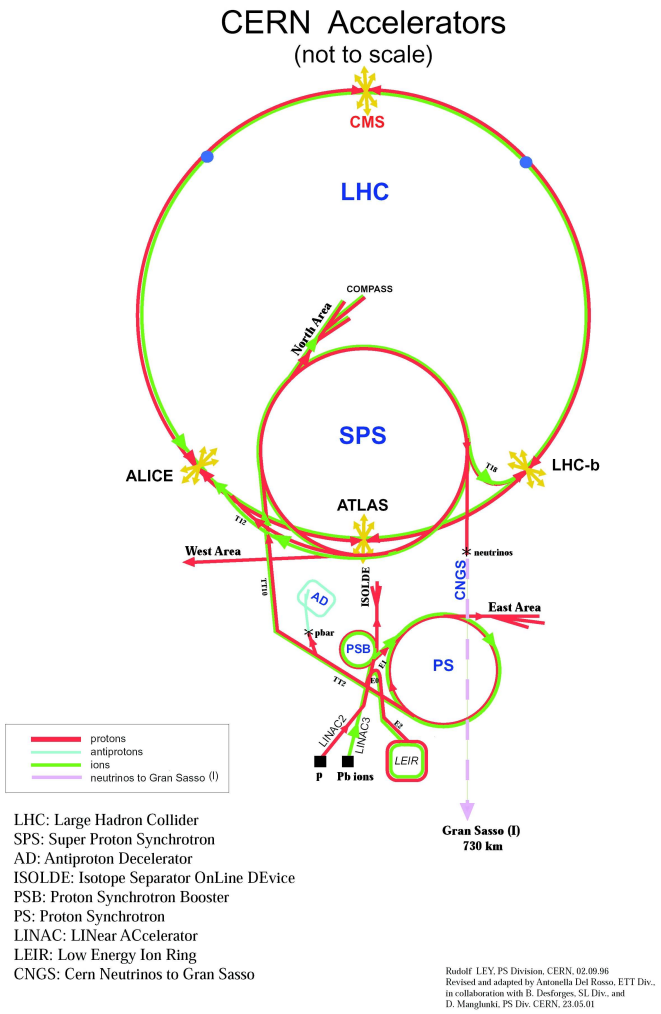

Figure 2.2: Lay-out of the CERN accelerator complex: the LHC ring should be completed in 2007. The proton beam for ISOLDE is provided by the PSB.

2.1.3 Ionization

Different types of ion sources are in use at ISOLDE. Besides the surface and plasma ionization sources, the element selective resonance ionization laser ion source (RILIS) is also available [Koe02]. The choice is mainly guided by the chemical properties of the element to be ionized. Important properties of an ion source are its selectivity and efficiency.

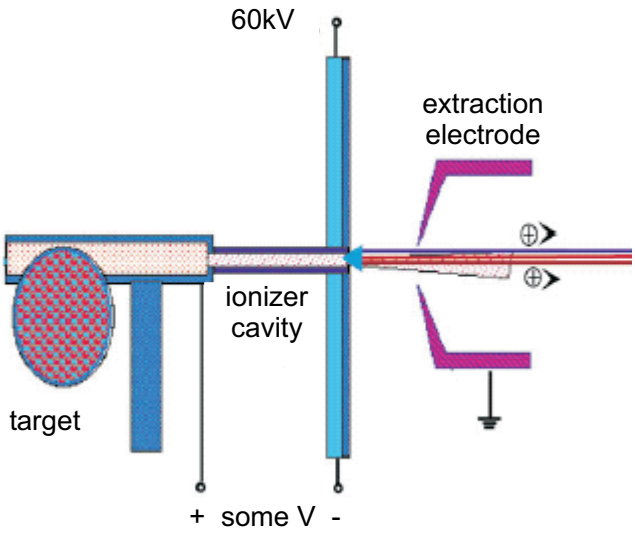

Figure 2.3: Schematic drawing of the ISOLDE target-ion source unit.

Surface ionization source

The underlying phenomenon is the thermal ionization of the atoms. An atom hits the hot surface of the ion source, loses an electron and is re-evaporated from the ion source walls as an ion. This process is very efficient whenever the element's ionization potential is lower than the work function, (*i.e.*, the energy needed to remove an electron from the Fermi level of a metal to the vacuum level) of the ionizer material, as is the case, for instance, with alkali. This is clearly illustrated by the omnipresence of francium (Z=87, electron configuration [Rn]$7s^1$) contaminants in the neutron-rich lead (Z=82) and bismuth (Z=83) beams at ISOLDE. Alkaline earth and rare earth elements, as well as the group 3A elements, characterized by a low ionization potential are surface ionized as well, albeit with a lower efficiency. The ionization potential for some of the elements around Z=82 is given in Table 2.1.

Plasma ion source

Ionization proceeds through electron impact in the plasma in the ionizer cavity. The efficiency of this method can reach 50% or even more. Nevertheless the method lacks selectivity, as almost all elements entering the ion source can become ionized.

Table 2.1: Ionization potentials for some of the elements around Z=82.

	W_i [eV]		W_i [eV]
Hg	10.44	Po	8.42
Tl	6.11	At	9.65
Pb	7.42	Rn	10.75
Bi	7.29	Fr	4.07

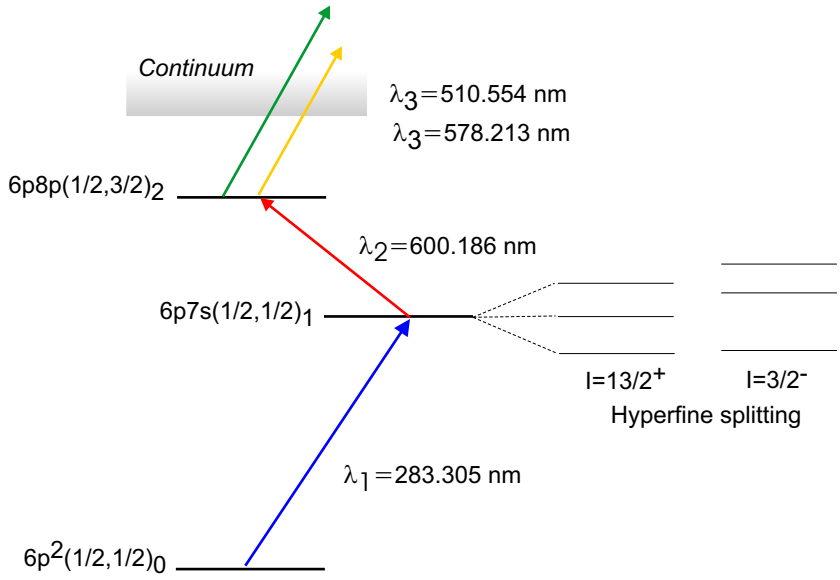

Figure 2.4: Three-step resonance ionization scheme applied for the ionization of lead in the RILIS.

Resonance ionization laser ion source

The atomic excitation scheme is a unique fingerprint of an element. This property forms the basis of the chemically selective RILIS technique: stepwise excitation of the atoms towards the continuum via photo-ionization. The ionization happens typically in a two- or three step excitation directly into the continuum or, more favourably, to an auto-ionizing state. Different tunable laser beams supply the required energy. Only when the laser frequencies match the transition frequencies will the atoms be ionized. The process is shown in Fig. 2.4 for the ionization of lead isotopes.

The ISOLDE-RILIS laser system [Fed03] consists of three tunable dye lasers with

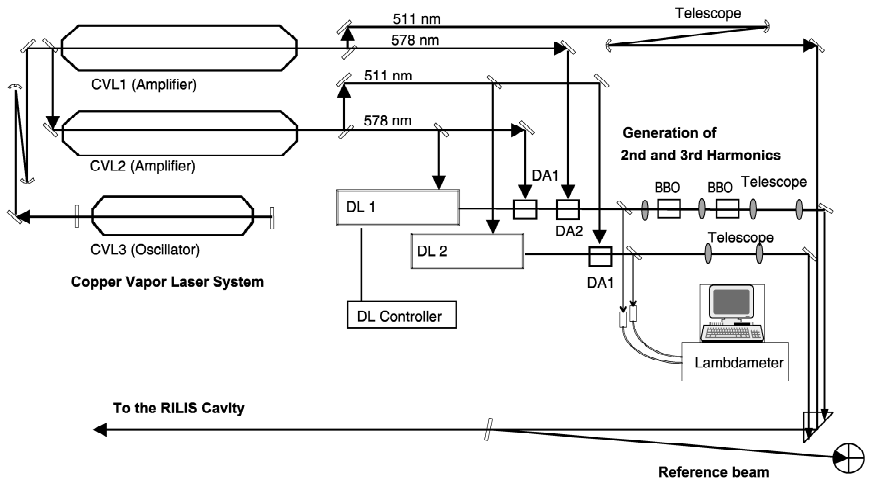

Figure 2.5: Schematic view of the ISOLDE-RILIS laser set-up. The picture is taken from [Fed03]. CVL: copper vapor laser, DL: dye laser, DA: dye amplifier.

wavelengths tunable in the range of 530-850 nm. Applying doubling or tripling of the fundamental frequency with non-linear β barium borate crystals gives access to the UV region, however with limited power. Wavelengths from 214 nm to 414 nm have been generated in this way. The dye lasers are pumped by two copper vapor lasers (CVL), with a repetition rate of 11 kHz and with a pulse duration of 18 ns. This high repetition rate is needed to increase the atom-photon interaction probability by matching the average residence time of the atoms in the ion source cavity ($\sim$100 μs). The CVL radiation contains two wavelengths of 511 nm and 578 nm, respectively. They can also be used to provide the necessary energy for the non-resonant transition to the continuum. Tuning of the laser wavelength is performed by rotation of a diffraction grating in the resonator of the dye laser. By using different gratings, the laser line widths can be varied in a range of 9 to 30 GHz. Inserting a Fabry-Perot etalon in the dye laser resonator produces a narrow-band generation with a line width of 1.2 GHz (see Sect. 2.3.3). Table 2.2 gives the ionization schemes used for the elements resonantly ionized in the present work: thallium, lead and bismuth.

The laser beams enter the ion source (typical size 3 mm diameter and length 30 mm) through the exit hole, after an optical path of 18 m from the laser hut to the target area. The ion source cavity is heated to about 2000°C or more, to limit the delay time and the losses due to absorption of the atoms on the tube material. Unfortunately, this makes the cavity act as a good surface ionizer for elements with a low ionization potential; consequently, the outstanding intrinsic selectivity is reduced.

Table 2.2: Excitation schemes for resonant laser ionization of thallium, lead and bismuth. The ionization efficiency ε_{ion} has been determined in off-line conditions [Fed03]. Resonant transitions in these schemes are:
for Tl $6p\ ^2P^0_{1/2} \rightarrow 6d\ ^2D_{3/2}$ λ_1=276.787 nm;
for Pb $6p^2\ ^3P_0 \rightarrow 6p7s\ ^3P_1$ λ_1=283.305 nm, $6p7s\ ^3P_1 \rightarrow 6p8p\ ^3D_2$ λ_2=600.186 nm;
for Bi $6p^3\ ^4S^0_{3/2} \rightarrow 6p^27s\ ^4P_{1/2}$ λ_1=306.770 nm, $6p^27s\ ^4P_{1/2} \rightarrow 6p^28p\ [1]_{3/2}$ λ_2=555.205 nm.

element	λ_1[nm]	λ_2[nm]	$\lambda_3[nm]$	P_1[mW]	P_2[mW]	P_3[mW]	ε_{ion}[%]
Tl	276.787	510.554 + 578.213		70	5000		27
Pb	283.305	600.186	510.554 + 578.213	70	500	5000	3
Bi	306.770	555.205	510.554 + 578.213	50	500	5000	6

2.1.4 Mass separation

Two target and mass separator systems are operational at ISOLDE: the general purpose separator (GPS) and the high resolution mass separator (HRS), differing mainly in their mass resolving power, $M/\Delta M$[1] equal to 2400 and 5000 (potentially up to 30000), respectively [iso]. A schematic drawing of the ISOLDE facility is shown in Fig. 2.6.

- GPS After extraction from the ion source cavity by a 60 kV extraction voltage, the ion beam passes a quadrupole triplet and doublet lens system, producing a parallel beam at the entrance of the analyzing magnet. The switchyard in the focal plane of the magnet allows the simultaneous extraction of three beams in a mass range of ±15% of the central mass. Additional ion optical equipment guides the beam to the user's set-up.

- HRS The high resolution separator performs the magnetic separation in two stages, using two bending magnets and associated lens systems. The HRS and GPS beam lines being merged, the same beam distribution can be used.

Various other production methods and separation techniques are applied at different facilities. While in the ISOL technique the reaction products are stopped in the

[1] ΔM is the full width at half maximum of a beam of ions with mass M in the focal plain of the separator

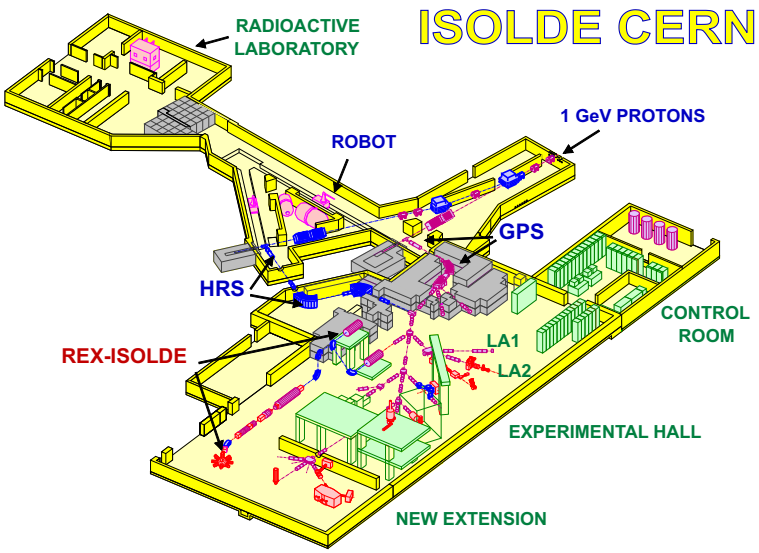

Figure 2.6: Schematic view of the ISOLDE facility. The picture is taken from [iso]. All experiments described in this work were situated at the LA1 or LA2 beam lines.

target, in-flight fragmentation uses a high-energy heavy ion beam on a thin target and exploits the kinematics of the reaction products, separating them in-flight. The use of thin targets limits the production in the target and the beam quality is poor, compared to the ISOL beams. However, the short separation times (in the μs region, compared to the seconds scale for ISOL) make it more suited for the study of short-lived nuclei or isomeric states. Fusion-evaporation reactions combined with fragment or recoil separators have shown to be particularly successful in the production of neutron-deficient nuclei. Contrary to the aforementioned techniques, it is a selective process.

2.1.5 Selectivity

Not only should an intense beam of the required isotope be delivered, but an efficient suppression of contaminants is also crucial. When using a spallation or a fragmentation reaction, induced by high energy projectiles, the resulting reaction product distribution is very wide. Hence powerful separation techniques are needed to filter the tiny amount of exotic ions out of the multitude of reaction products.
As mentioned above, the target-ion source system often allows for a first selection step. In particular the resonance ionization laser ion source has a high chemical selectivity. The selectivity is defined as the ratio of the photo-ion current to the surface-ionization current and intrinsically could reach 10^4 [Mis93]. The surface ionization of contaminants with a low ionization potential (especially alkali) in the hot cavity of the ion

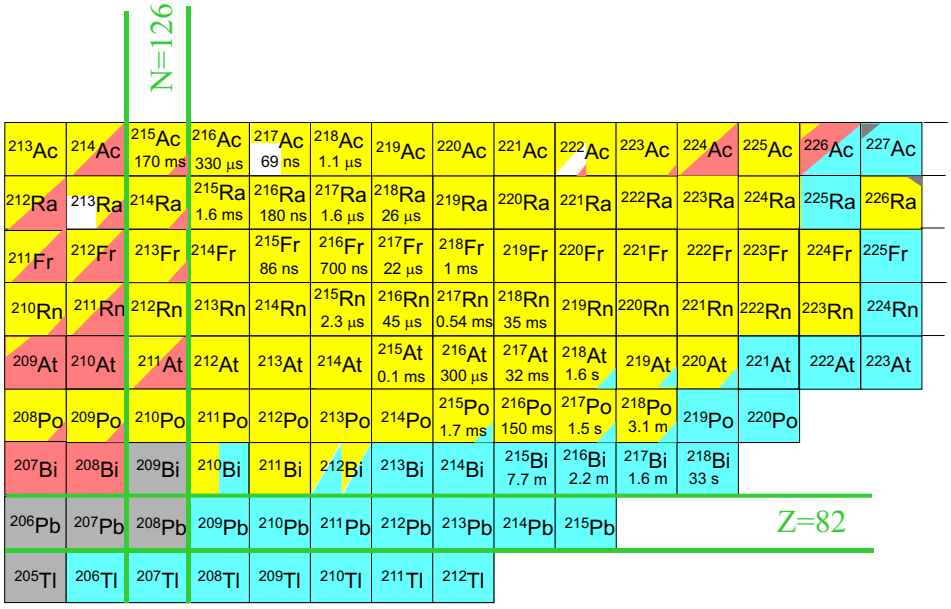

Figure 2.7: Chart of nuclides for the isotopes north-east of ^{208}Pb.

source can reduce this selectivity considerably. Combined with the much higher cross-section for the higher Z isobars, a study of the more exotic heavy bismuth or lead isotopes would be impossible, even using the element selective RILIS, because of an overwhelming francium background.

An additional selection technique makes use of the pulsed structure of the proton beam delivered to ISOLDE. While the lead and bismuth isotopes of interest have a half-life in the order of seconds or minutes, the contaminants are α-emitters with a short half life (ms-μs region). This is shown in Fig. 2.7 for the A=215-218 chains. The release of the ions is delayed, by closing the separator for some time after the beam impact, chosen such that the major part of the short-lived contaminants have decayed, while only a small fraction of the longer lived species has been lost. This technique is illustrated in Fig. 2.8 and more extensively discussed in [Van98]. We note that the α decay daughter activity will be efficiently suppressed through the mass selection of the separator.

2.1.6 Yield

The yield is defined as the ratio of the ion beam intensity and the primary beam current and is expressed in units of atoms/μC:

$$Y = \frac{N_{0i}}{N_p} 6.2 \times 10^{12} \int_{t=0}^{\infty} P_i(t, \lambda_i) dt, \tag{2.1}$$

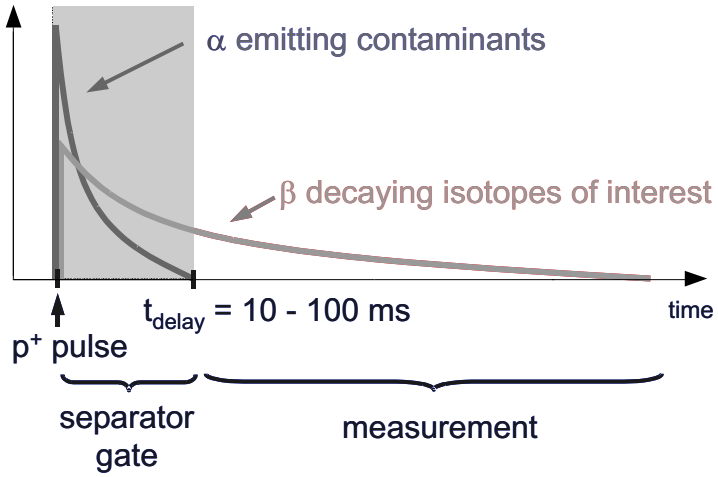

Figure 2.8: The pulsed release technique: the different time scales for the α decay of the contaminants and the β decay under investigation allow for a selective suppression.

where N_{0i} represents the number of ions created in one proton pulse of N_p protons and the integral of $P_i(t, \lambda_i)$ is the released fraction [Let97].
Fig. 2.9 shows the yields for the neutron-rich bismuth isotopes in the various experiments discussed in this work. As expected, the yield drops towards the more exotic, neutron-rich isotopes. The yields in the earlier experiments, using the plasma ion source and a proton energy of 1 GeV, are typically 2 orders of magnitude higher, compared to the last three runs (2001-2003), using the RILIS combined with a 1.4 GeV incident proton energy.
In these data, no clear influence of the target material is observed. Indeed, the yields deduced in the 2001 (uranium carbide) and 2002 (thorium carbide) runs are comparable. Calculations of Schmidt [Sch99] in the abration-ablation model show also very little dependence on the proton energy. A certain reduction of the yield could result from the difference in ionization efficiency between the hot plasma and the laser ion source. However, the observed difference of a factor 100 remains unexplained.

2.2 Decay spectroscopy

One of the best ways to explore the low-spin structure of nuclei far off stability is probably the study of radioactive decay. The alternative in-beam method feeds essentially states at high spin in a heavy-ion fusion evaporation reaction and the de-excitation proceeds mainly via the *yrast* (*i.e.* the states with lowest spin for a given excitation energy) sequence. Decay studies allow extraction of information concerning the exci-

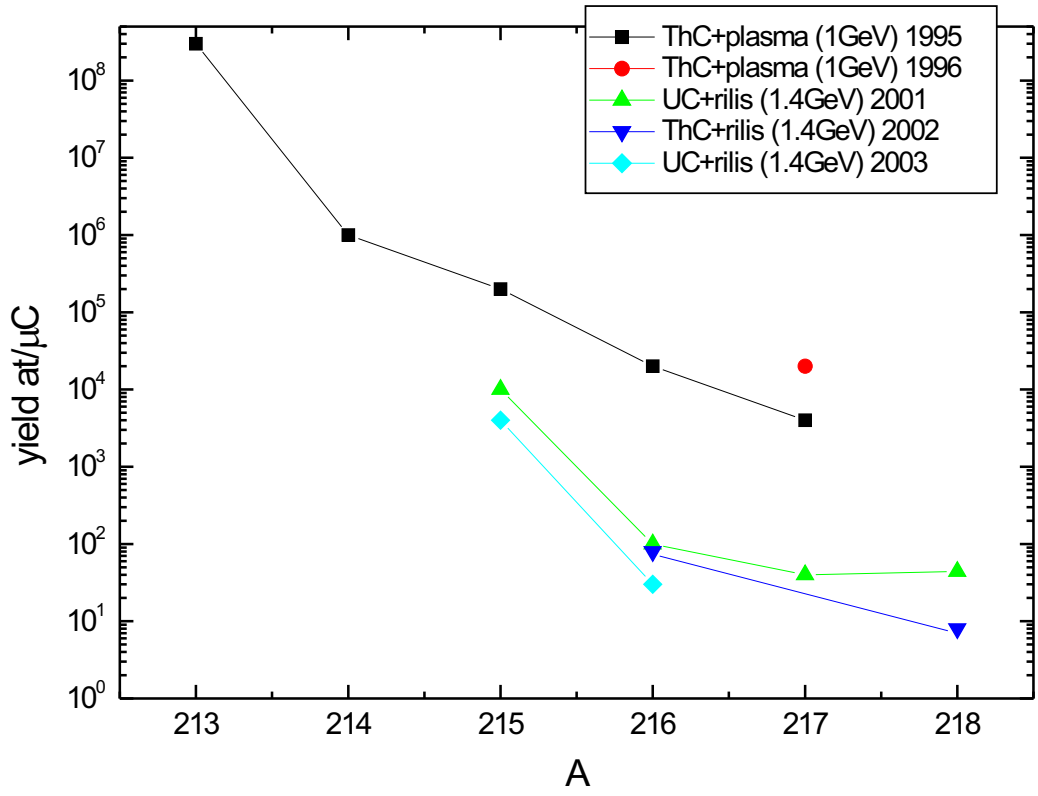

Figure 2.9: Experimental yields expressed in atoms per μC of incident proton beam for the neutron-rich bismuth isotopes at ISOLDE.

tation energy, spin and parity of low-lying states, half-lives and feeding patterns. With the second method applied in this work, atomic spectroscopy (see section 2.3), spins, magnetic moments and quadrupole moments of nuclear ground states and isomers are commonly determined.

2.2.1 α decay spectroscopy

In the α decay process an α-particle with an energy E_α is emitted from the mother nucleus (^{A}Z). The total released energy Q_α is equal to the sum of the kinetic energy of the α-particle plus the recoil energy of the daughter or in first order non-relativistic approximation:

$$Q_\alpha = E_\alpha \frac{A}{A-4} \quad \text{[MeV]}. \tag{2.2}$$

The experimental observables in α decay spectroscopy are the alpha energy E_α, intensity I_α, half-life $T_{1/2}$ and branching ratio b_α.

The α decay process is treated as a two-step process, namely preformation of an α-particle inside the nucleus followed by penetration through the Coulomb barrier. The probability for formation of the α-particle is related to the reduced width δ^2, containing most nuclear structure information:

$$\delta^2 = \frac{\lambda h}{P} \quad [\text{keV}] \tag{2.3}$$

with λ the partial decay constant and h the Planck constant. P is the barrier penetration probability which is calculated using the formalism of Rasmussen [Ras59].
The α decay can proceed to the ground state or to excited states in the daughter nucleus. The latter case is commonly referred to as *fine structure* α decay. The relative decay strengths towards the excited (exc) and the ground state ($g.s.$) in fine structure decay are expressed in terms of *hindrance factors* (H.F.):

$$\text{H.F.} = \frac{\delta^2_{g.s.}}{\delta^2_{exc.}} \tag{2.4}$$

for even-even nuclei. The hindrance factors for odd-A nuclei are defined in terms of the ground-state to ground-state transition in the even-even neighbours:

$$\text{H.F.}_o = \frac{\delta^2_{A+1} + \delta^2_{A-1}}{2\delta^2}. \tag{2.5}$$

For the detection of α-particles, passivated implanted planar silicon (PIPS) detectors were used, with a thickness of 300 μm and active area 150 mm^2 (except for the measurement of the ^{201}Fr α decay, presented in Appendix D). The efficiency of the detectors is given by the solid angle, the intrinsic efficiency being close to 1. Therefore the detector should be placed close to the implanted source, provided that the dead layer of the detector is thin enough.
Figure 2.10 shows the configuration used for the α decay measurements in this work. This so-called wind-mill chamber is extensively described in [Den92]. The beam from the ISOLDE separator was implanted in a 20 μg/cm^2 carbon foil (diameter 6 mm) mounted on a rotating wheel. The thickness of the foils is sufficient to stop the 60 keV separator beam, but still thin enough to maintain a good α-energy resolution. Indeed, a thicker catcher would degrade the energy resolution due to the spread of the energy loss of the α-particles. The wheel contains ten foils, out of which five are used during a cyclic measurement. This configuration allows to transport periodically the implanted activity to a decay station and remove longer-lived daughter activities. The movement of the wheel over an angle of 144° from implantation to decay, takes ∼1 s. Therefore the measurements of very short lived isotopes were performed at the implantation station.

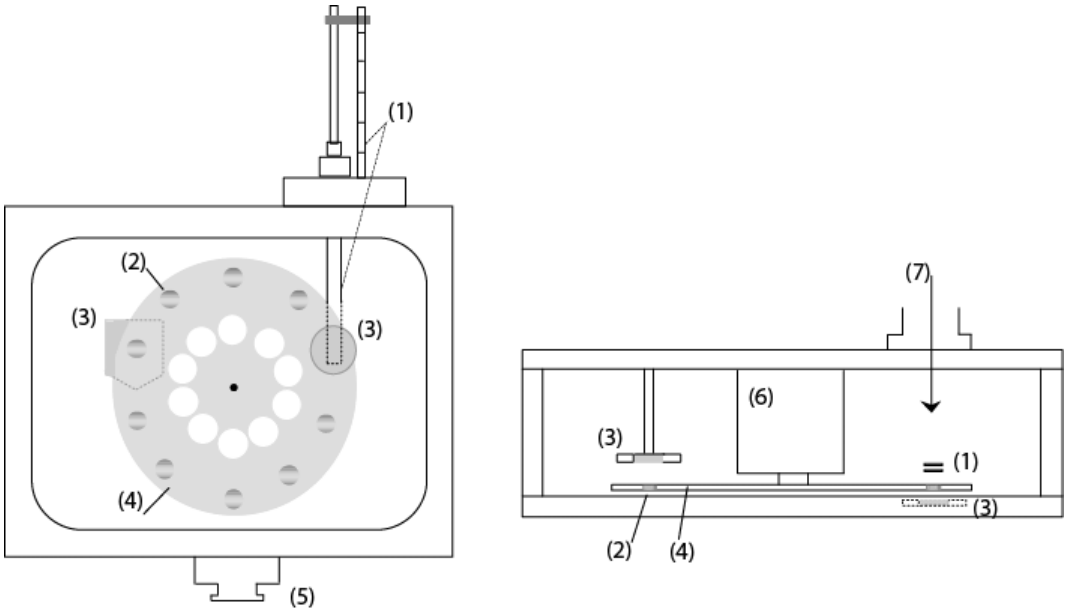

Figure 2.10: The wind-mill system. Left: front view, right: top view. (1) current measurement + collimator; (2) carbon foils; (3) α-particle detectors; (4) rotating wheel; (5) pumping hole; (6) step motor; (7) separator beam. Drawing based on [Den92].

Alpha particle detectors can be placed behind the carbon foil at the implantation position and at both sides of the foil at the decay station. Outside the vacuum chamber, γ-ray detectors can be added to perform α-γ or α-x coincidence measurements. In addition, the silicon detectors can also be used for electron detection.

2.2.2 β decay spectroscopy

The β decay can feed the ground state of the daughter nucleus or excited states that further de-excite via electromagnetic transitions to the ground state. Further off stability another de-excitation channel can occur: the β decay can, with a certain probability, feed levels above the particle emission threshold. Chapter 5 will treat this decay mode in more detail, for the case of the neutron-rich thallium isotopes.

For the detection of the charged β-particles, a plastic scintillator (NE102A) detector is used (surface: 31×25 mm^2, thickness: 1 mm). The intrinsic efficiency and thus the probability for interaction in the detector is high (typically 90 %), but due to the limited thickness of the detector, only a small part of the β-energy is deposited in the detector. Therefore this kind of detectors is commonly called ΔE detectors.
The light emitted from the scintillator is transmitted, via a plastic light guide, to

the cathodes of two small photomultiplier tubes, with a diameter of 6 mm each. The signal-to-noise ratio of the individual photomultiplier tubes is poor; if however, a simultaneous detection in both tubes is required, the noise level is significantly suppressed. The interaction probability of γ-rays with the scintillator is small (typically 1%). Hence the detector serves as a good indicator for β decay.

The γ-rays emitted after α- or β decay are detected in high-purity germanium detectors (HPGe). These semiconductor detectors are often used for γ-ray spectroscopy because of their excellent energy resolution. Energy calibrations were made, using on-line produced radioactivity, with well known decay energies. The detector efficiencies are calculated using the Monte-Carlo based simulation package GEANT (see Appendix B). This approach has been experimentally verified in [Wei99].
Figure 2.11 shows the coincidence set-up used in the experiment II (see Table 2.4). The separator beam is stopped in a 100 μm thick, 12.5 mm wide mylar tape. The detector set-up at the implantation position consists of a silicon PIPS detector for α-particle detection inside the implantation chamber and a 70% HPGe detector for γ-ray detection outside the vacuum, at the opposite side of the tape. This set-up was used for a decay and laser spectroscopy measurement of ^{185}Pb [And02a] and will not be discussed further in this work.
After the implantation time, the tape is moved towards a second, lead-shielded detector set-up where the decay is measured for the same period (*i.e.* equal to the implantation time). The cyclic measurements allow for a good half-life determination and a periodical removal of the long-lived activities. At the position of the scintillator detector, a small mylar window (diameter 6 mm, thickness 50μm) is present in the vacuum tube to reduce stopping of the β-particles. A LEGe (low-energy germanium) detector with an area of 38 cm^2 and a thickness of 25 mm is positioned behind the scintillator. This detector, with a 300 μm beryllium entrance window is particularly suited for the detection of X-rays and low-energy γ-rays. All detectors, including also 2 HPGe detectors are placed around the vacuum tube, as close as possible to the source in order to maximize the solid angle coverage.

A competing process to the γ-ray emission is internal conversion: the excitation energy of the nucleus is given to a bound electron which leaves the atom with an energy equal to the transition energy minus the electron binding energy. A vacancy in an inner atomic orbit results and is quickly filled by an electron from a higher orbit. The energy difference is released via emission of a characteristic X-ray. The ratio of the probability for internal conversion to the probability for γ-ray emission is called the

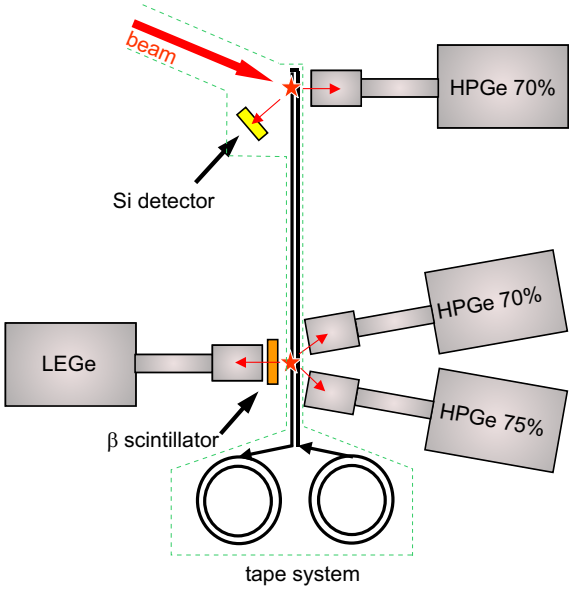

Figure 2.11: Schematic drawing of the tape system and detector set-up. After implantation (top), the tape is moved towards the decay set-up, consisting of 2 HPGe detectors, 1 LEGe and 1 scintillator (bottom). The picture is not to scale.

internal conversion coefficient, α:

$$\alpha = \frac{I(e^-)}{I(\gamma)}. \tag{2.6}$$

Depending on the atomic orbit involved, we distinguish between K,L,... conversion coefficients. The K-electrons have a non-vanishing probability to be found in the nucleus and a larger K-conversion probability results. The conversion coefficient depends on the electric or magnetic character of the transition and its multipolarity, the transition energy ($\propto E_\gamma^{-2.5}$) and the atomic number ($\propto Z^3$) [nnd]. This process plays a particularly important role in the 0^+-0^+ transitions which are forbidden for γ-ray emission, as the photon carries an intrinsic spin $1\hbar$.
One way of determining the conversion coefficient experimentally consists in comparing the observed γ-intensity with the associated X-ray intensity. This method requires, however, knowledge of the decay scheme.

2.3 Laser spectroscopy

The interaction between the nuclear charge distribution and the electromagnetic field of the atomic electrons affects the atomic spectrum, through the isotope shift and the hyperfine splitting (HFS). The interaction is purely electromagnetic and a common

approach is to expand the electromagnetic transition operator in a multipole series. The electric monopole corresponds to the nuclear charge and gives rise to an overall shift in the electronic fine-structure levels, the isotope shift. The magnetic monopole vanishes, as no analogue of the electrical charge is known to exist for the magnetic case. As the nuclear matrix elements are diagonal for states with a well defined I^{π}, only the even parity moments are contributing. The magnetic dipole and the electric quadrupole moment give rise to a splitting of the atomic levels, the HFS. A review of the measurement of nuclear radii and moments has been given by [Ott89] and more recently by [Bil95] and [Ney03].

2.3.1 Hyperfine structure

The coupling between the nuclear angular momentum $\overrightarrow{I}$ and the electronic angular momentum $\overrightarrow{J}$ defines the total angular momentum of the atom $\overrightarrow{F} = \overrightarrow{I} + \overrightarrow{J}$, where F ranges from $|I - J|$ to $(I + J)$. The hyperfine interaction removes the degeneracy, splitting the different F-levels. Their energy is given by:

$$W(F) = A\frac{K}{2} + B\frac{\frac{3}{4}K(K+1) - I(I+1)J(J+1)}{2(2I-1)(2J-1)I.J}, \tag{2.7}$$

with $K = F(F+1) - I(I+1) - J(J+1)$ and A the magnetic dipole coupling constant, related to the magnetic dipole moment by

$$A = \frac{\mu H_e(0)}{I \cdot J}, \tag{2.8}$$

with $H_e(0)$ the magnetic field created by the electrons at the nucleus.
The electric quadrupole coupling constant B relates to the spectroscopic quadrupole moment ${Q_s}^2$

$$B = eQ_s\frac{\partial^2 V}{\partial z^2}, \tag{2.9}$$

with $\partial^2 V/\partial z^2$ the electric field gradient produced by the electrons.
This splitting is schematically shown in Fig. 2.12.

The magnetic moment is calculated as the expectation value of the z component (μ_z) of the vector magnetic dipole operator $\overrightarrow{\mu} = g_l \overrightarrow{l} + g_s \overrightarrow{s}$, in the state M=I:

$$\mu(I) = \langle I, M = I|\mu_z|I, M = I\rangle. \tag{2.10}$$

[2]The spectroscopic quadrupole moment is different from the intrinsic quadrupole moment Q_0, which is induced by the non-spherical charge distribution of the nucleus and which is defined in the intrinsic frame of the nucleus.

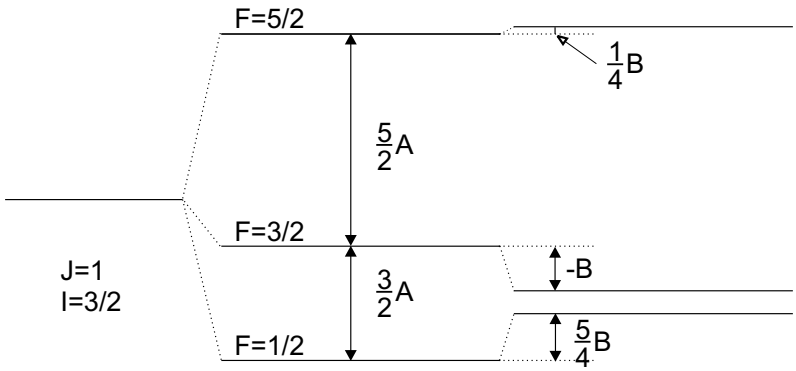

Figure 2.12: Schematic drawing of the hyperfine splitting for J=1 and I=3/2, including both magnetic dipole (A) and electric quadrupole splitting (B).

The gyromagnetic factors are given by g_s=5.58, g_l=1 for protons; g_s=-3.82, g_l=0 for neutrons.
In the shell model framework the single particle magnetic moments are given by the *Schmidt* moments:

$$\mu_{s.p.} = j\big(g_l \pm (g_s - g_l)\frac{1}{2l+1}\big) \tag{2.11}$$

for $j = l \pm \frac{1}{2}$.

In analogy to the magnetic dipole moment the electric quadrupole moment is defined as

$$Q_s(I) = \langle I, M = I|Q_z|I, M = I\rangle, \tag{2.12}$$

with Q_z the z-component of the quadrupole operator, defined in terms of spherical harmonics as

$$Q = \sqrt{\frac{16\pi}{5}} \sum_{k=1}^{A} e(k) r_k^2 Y_2^0(k). \tag{2.13}$$

2.3.2 Isotope shift

The isotope shift $\delta\nu_i^{AA'}$=$\nu_i^A - \nu_i^{A'}$ is defined as the shift of the resonance frequency of an optical transition i, measured in the isotopes A and A'. The isotope shift consists of two contributions: a *field* shift and a *mass* shift.
The mass shift is an effect of the finite mass of the nucleus. It is in turn a combination of two terms: the normal mass shift ($\delta\nu_{normal}$) is caused by the change in the reduced mass of the isotope, while the specific mass shift relates to the influence of the correlated electronic momenta on the nuclear motion. The normal mass shift is given by

$$\delta\nu_{i,normal}^{AA'} = \frac{m_e}{m_p} \cdot \frac{A - A'}{AA'} \cdot \nu_i^A, \tag{2.14}$$

where ν_i^A is the transition frequency, m_e and m_p are the electron and proton masses, respectively. As the specific mass shift has the same A-dependence, the total mass shift can be written as:

$$\delta\nu_{i,M}^{AA'} = M_i \cdot \frac{A - A'}{AA'}, \tag{2.15}$$

with M_i the mass shift constant, including both normal and specific mass shift. For light nuclei, the mass shift gives an appreciable contribution, but for heavier nuclei, the field shift is dominant.

The field shift follows from the effect of the finite charge distribution of the nucleus on the electron binding energies. It can be split into a nuclear factor $\lambda^{AA'}$ and an electronic factor F, which depends on the electron density at the nucleus. Finally, one can write:

$$\delta\nu_i^{AA'} = M_i \cdot \frac{A - A'}{AA'} + F_i\lambda^{AA'}. \tag{2.16}$$

The nuclear parameter $\lambda^{AA'}$ reflects the change of the nuclear charge distribution between the isotopes A and A' and can be written in terms of the nuclear radial moments:

$$\lambda^{AA'} = \delta\langle r^2\rangle + \frac{C_2}{C_1}\delta\langle r^4\rangle + \frac{C_3}{C_1}\delta\langle r^6\rangle + \ldots \tag{2.17}$$

The coefficients $C_1, C_2, \ldots$ have been tabulated by Seltzer [Sel69]. In good approximation, the mean square charge radius in the lead region is determined via the relation:

$$\lambda^{AA'} = 0.93 \cdot \delta\langle r^2\rangle, \tag{2.18}$$

which was estimated to be accurate to at least 2% [Tho83].

The determination of the electronic factors M and F often introduces large uncertainties in the determination of $\delta\langle r^2\rangle$. The mass shift can be calculated in a Hartree-Fock approach, but the results are not always satisfactory. For simple s→p transitions it has been shown experimentally that $|S| \lesssim N$, with N and S the normal and specific mass shift, respectively.

F is proportional to the change of the electron density at the nucleus in the transition, $\Delta|\psi(0)|^2$, and can in principle be calculated theoretically. However, electron screening effects can complicate this work considerably.

An alternative way of determining the electronic factors is possible if independent data are available, *e.g.*, from electronic or muonic X-ray experiments or electron scattering. The method known as the King plot analysis, expresses a linear behaviour between the modified[3] IS, measured in transitions where the electronic factors can be favourably

[3] multiplied by $\frac{AA'}{A - A'}$

calculated, and the optical isotope shifts. From the slope the ratio of field shifts is extracted; the intersection yields the difference of the mass-shift factors. An example of such a plot for lead is shown in [Tho83].

2.3.3 In-source laser spectroscopy at ISOLDE

As discussed in Sect. 2.1.3, the resonance ionization laser ion source offers a chemically selective ionization technique, via the stepwise excitation of the atoms of interest. In addition, the frequency of the first excitation step is sensitive to the isotope shift of the optical line, as well as to the hyperfine splitting. As a consequence not only isotopic, but also isomeric selectivity can been achieved.
The use of the RILIS for atomic spectroscopy was pioneered at the Leningrad Nuclear Physics Institute (Gatchina, Russia), where it was applied to short lived $^{154-156}$Yb isotopes [Alk92]. The technique was introduced at ISOLDE with the measurement of the $^{7,9,10-12,14}$Be isotopes shifts and the hyperfine structure in the silver isotopes, $^{107,122-129}$Ag [Seb98].

For atomic spectroscopy measurements, a narrow bandwidth laser (line width 1.2 GHz) is used for the first excitation step. Its frequency is scanned over the resonance. The frequency is tuned by the rotation of the diffraction grating and the etalon in the dye laser resonator. In contrast to other laser spectroscopic techniques, the scanning procedure is applied directly in the ion source. The main advantage of this technique is its sensitivity and hence its applicability to exotic nuclei with a low yield, at the expense of precision however. The high temperature (around 2000°C) in the cavity increases the line width because of Doppler broadening.
After extraction from the ion source, the ion beam follows its usual pathway towards the implantation point (tape or carbon foil, in these experiments). The radioactive decay is measured and the yield as a function of the laser frequency is obtained.

2.4 Data acquisition

Throughout this work, an MBS (MultiBranch System)-based data acquisition system was used, running on the real-time LynxOS platform. The MBS [mbs] software package has been developed at GSI (Darmstadt, Germany) in order to serve the increasing requirements of modern spectroscopy experiments, using *e.g.* segmented detectors. In the configuration employed in this work, the MBS-based acquisition was combined

with conventional NIM-based electronics and VME[4]-interfaces.
The details of the electronics set-up are described in Appendix A. We mention here only the type of information that can be obtained from each detector in this specific configuration.
From the α- and γ-detectors both energy and timing signals are extracted. The ΔE-scintillator detector only provides timing information as the β-particles only loose a small fraction of their energy in the detector. Data are taken in two different, but simultaneous, modes of operation: multiscaling and list-mode.

- In the **multiscaling** mode, all energy signals are read into a 1-dimensional histogram, without any conditions on the event (*singles* data). All correlations between the different detectors are lost.
  A time sequence is imposed on the measurement: the measurement cycle of implantation and decay is divided into 8 or 16 time bins. Each bin corresponds to a separate histogram. This multiscaling operation gives valuable information, *e.g.* for the determination of half-lives. The main advantage is that the method is fast and high count rates can be handled.

- The **list mode** records energy and timing information for all detectors, for those events satisfying a certain coincidence condition. In all experiments discussed in this work, the coincidence trigger selected the multiplicity $M \geq 2$ events. The event multiplicity M is defined as the number of detectors firing during the coincidence time window (1 μs). For the β decay set-up presented earlier (Sect.2.2.2) the selected events will be either of $\gamma - \gamma$ or $\beta - \gamma$ type.
  For each event, the energy information for all detectors and the time differences between them are stored. In addition, a TDC (time-to-digital convertor) determines the absolute time between the start of the measurement cycle and the event. This information is important for the determination of half-lives.
  This mode gives the most complete information, but for high counting rates the dead-time can be large and a coincidence condition is unavoidable.

Dictated by a trigger module, the MBS-DAQ system handles the read-out procedure and the periodic transfer of the data to the hard disk of a linux-server. Separate triggers for singles and coincidence read-out are issued. An additional external trigger was used in the laser spectroscopy measurements and added the laser frequency as an additional parameter to the list mode file.
All data were eventually converted to *hbook* format for analysis in the PAW environ-

[4]VME is another electronics standard, like NIM. It stands for VersaModule Europe. In this approach every module in a crate is specified by its hardware address.

ment (physics analysis workstation, developed at CERN) [paw], both for on-line and off-line analysis. The hardware, data structure and analysis software are discussed in more detail in [Van02].

Table 2.3: Overview of the experiments discussed in this work. All experiments used the 1.4 GeV proton beam from the ISOLDE facility (except for run I, where the proton beam energy was 1.0 GeV.) Details on measurement cycles and detectors are given in the corresponding chapters.

run	year	nuclides	target	ion source	data taking	Sect.
I	1996	^{213}Pb	$^{232}ThC_2$ (55 g/cm^2)	plasma	$\beta\gamma - \gamma\gamma + \gamma$ singles	4.1
II	2001	^{215}Pb	$^{238}UC_2$-C (50 g/cm^2)	RILIS	$\beta\gamma - \gamma\gamma + \gamma$ singles	4.1
		^{218}Bi		RILIS	$\beta - \gamma\gamma + \gamma$ singles	4.2
		^{211}Tl		surface	neutron counter	7.2
III	2002	^{200}Fr	$^{232}ThC_2$-C (51 g/cm^2)	surface	$\alpha\gamma+ \alpha$ singles	5.1
		^{201,203,205}Fr		surface	$\alpha\gamma + \alpha$ singles	App.D
		^{211}Tl		surface	neutron counter	7.3
IV	2003	$^{183-189}$Pb	$^{238}UC_2$-C	RILIS	α singles, laser spectroscopy	6.3
		^{215}Bi		RILIS	α, γ singles	4.1

Chapter 3

Present status of nuclear structure research around Z=82

Experimental limitations, mainly related to production of the lead, bismuth and polonium isotopes above the neutron shell closure at N=126 explain the poor knowledge of their nuclear structure. Having only a few nucleons outside the doubly magic nucleus ^{208}Pb, the nuclear shell model seems to be the most appropriate model for describing the precise nuclear structure features. Besides the progress in these calculations, the achievements of various experimental techniques will be the subject of the first section. At the neutron-deficient side, low-lying deformed states have been experimentally observed in the singly-magic lead isotopes and their neighbours when approaching the neutron mid-shell ($N \sim 104$). They are called intruder states, in reference to their intrusion into the normal low-energy spectrum. The consequent shape coexistence and the possible mixing between regular and intruder states of same spin and parity attracted the attention to this region. The second section will highlight some experimental accomplishments as well as the predictions of the most successful theoretical approaches.
The last section is devoted to the measurement of nuclear moments and charge radii. Results in the lead region are presented, along with selected experimental techniques.

3.1 Neutron-rich isotopes

3.1.1 Overview of the experimental achievements in the production and study of neutron-rich isotopes with Z≥82

The neutron-rich isotopes in the vicinity of ^{208}Pb have remained quite unexplored for a long time. Heavy-ion fusion-evaporation reactions, although very prolific at the

neutron-deficient side (see Sect. 3.2.1), are inapt for the production of the very neutron-rich isotopes, because the N/Z ratio of these isotopes is too high.

The nearest neighbours of ^{208}Pb, with one proton or neutron (particle or hole) outside the closed shell, have been studied in detail using transfer and stripping reactions on stable lead targets. They provided valuable information on the single particle excitations. Similar direct reactions allowed the investigation of the configurations when adding one or two more nucleons. As an example, we consider the study of the level scheme in ^{211}Bi. The near-yrast sequence was populated up to the $21/2^-$ isomeric state in the reaction ^{209}Bi(t,p)^{211}Bi [Mai89]. A level scheme was built, based on the results from γ-γ coincidences and conversion electron data, and the isomeric half-life was deduced. However, the technique is limited to nuclei close to stability, where suitable targets are available.

Alpha decay chains from heavy actinium and thorium isotopes, either naturally occurring or artificially produced, can also be used as an alternative production method. In this context we mention, for instance, the work of Liang *et al.* [Lia97, Lia99]. These studies concentrated mainly on the transition region between the shell model configurations near ^{208}Pb and the region of stable octupole deformation in the actinide region.

Deep inelastic heavy-ion reactions have been shown to populate high-spin yrast states in stable and moderately neutron-rich isotopes. The combination with high-resolution γ-spectroscopy considerably extended the knowledge of the high-spin excitations in ^{208}Pb and its neighbours: detailed information was obtained for $^{208-210}$Pb [Rej00, Rej98, Rej97], ^{211}Bi [Lan01] and ^{211}Po [For98]. The access to the very neutron-rich isotopes is hampered by the neutron-evaporation for thermal energy release [Rej98].

Two alternative methods, based on the fragmentation of actinide nuclei, permitted the further extension beyond N=126 in recent years: projectile fragmentation and proton induced spallation. Decay studies at the ISOLDE on-line mass separator yielded spectroscopic information, including half-lives and decay schemes, on the β decay of bismuth isotopes up to ^{217}Bi [Kur03a] (see Fig. 3.1). In the present work, this systematic study is extended to ^{218}Bi and ^{215}Pb. Crucial for this region is the use of the pulsed release (Sect. 2.1.5) which enhances the selectivity. A detailed account of these measurements will be presented in Chapter 4.
The complementarity of fragmentation and ISOL experiments lies in the different time scales involved. The ISOL technique suffers from relatively long release times of the

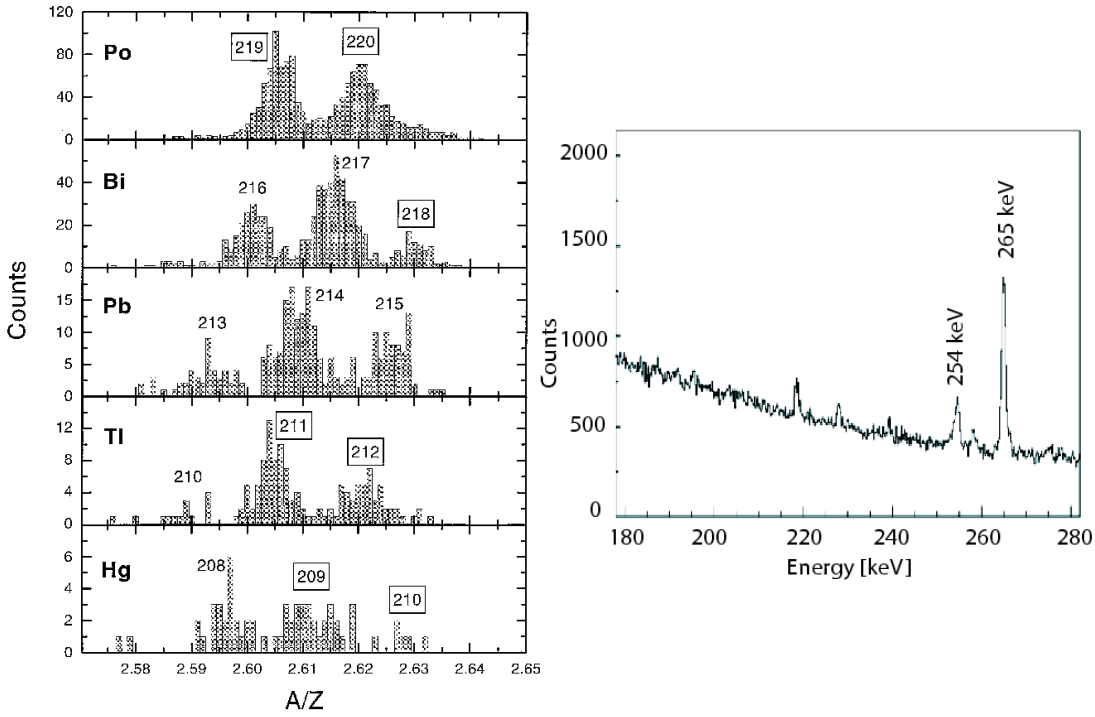

Figure 3.1: Left: Mass-to-charge spectra for the Hg-Po isotopes produced in the fragmentation of ^{238}U. The framed values present the isotopes identified for the first time in this experiment. The picture is taken from [Pfu98]. Right: Singles γ-spectrum from the β decay of ^{217}Bi obtained using resonance laser ionization at ISOLDE. The labelled γ-lines belong to the decay of ^{217}Bi. Picture taken from [Kur03a].

activity from the thick target, which excludes the observation of short lived isomeric states. The fast fragmentation method populates high-spin isomers, even if short lived (down to 10 ns) with a sizeable probability. The region of neutron-rich trans-lead isotopes is particularly suited in this respect. The presence of the high-j orbitals $\pi h_{9/2}$, $\pi i_{13/2}$, $\nu g_{9/2}$, $\nu h_{11/2}$ and $\nu j_{15/2}$ around the Fermi surface (see Fig. 1.2) presents a favourable situation for the formation of isomers. In the projectile fragmentation of a relativistic ^{238}U beam (at 1 GeV per nucleon) on a beryllium target (1 g/cm^2), Pfützner *et al.* [Pfu98] identified several neutron-rich isotopes in the Hg-Po region via time-of-flight, magnetic rigidity and energy loss measurements, shown in Fig. 3.1. Half-lives of μs isomeric states were determined in ^{211}Bi and ^{212}Pb. Up till now these measurements did not yield any further spectroscopic information than the mere existence of the isotopes, because of the low statistics.

3.1.2 Shell model treatment of the heavy lead isotopes

The basic input for a shell model calculation includes the single particle energies and the effective interaction, adapted to the specific model space. Nuclei with only a few particles or holes outside the closed core provide a direct test of the shell model residual interaction matrix elements. Particularly successful was the residual interaction derived by Kuo and Herling [Kuo71] from a free nucleon-nucleon potential and renormalized for truncations of the model space. The corresponding model space for nuclei above ^{208}Pb contains all orbitals for Z=82-126 (protons) and N=126-184 (neutrons). The presence of many orbitals with high spin renders the calculations computationally heavy. As a consequence, untruncated calculations for, *e.g.*, ^{211,212}Pb, with only 3 or 4 valence particles, were accomplished only in the 1990s [War91], with a slightly modified interaction.
More recently, progress has been made by deriving new realistic effective interactions, based on improved NN potentials [Cov99].

Single particle energies are usually taken from experiment, but the shift between the experimental yrast state and the centroid of a specific orbital, may influence the results. In particular the octupole degree of freedom is to be considered around ^{208}Pb, because of the presence of various orbitals with $\Delta\ell = \Delta j = 3$.

3.2 Neutron-deficient isotopes

3.2.1 Experimental achievements

In contrast to the isotopes above N=126, the neutron-deficient side of the nuclear chart around Z=82 is favourably produced in heavy-ion fusion reactions. A few isotopes close to the compound nucleus are formed. For stable beam and target combinations, they are situated at the neutron-deficient side, as the stability line bends, away from the N = Z line. Both in-beam and decay studies supplied a tremendous amount of experimental data; a brief discussion of the study of intruder states is given in Sect. 3.2.4.
Proton-induced spallation of a heavy target, *e.g.*, a uranium carbide target, in combination with the selectivity of the RILIS has been successfully applied for the production of neutron-deficient thallium, lead and bismuth at ISOLDE. Lead isotopes down to ^{183}Pb were produced and the measured yields are reported in [Koe03].

3.2.2 Intruder states and shape coexistence in a shell model approach

The intruder excitations observed in the neutron-deficient lead isotopes present another case where the representation of the nucleus as an inert core of closed shells surrounded by valence nucleons cannot satisfactorily describe the low-energy nuclear structure.
The following discussion is focussed on even-even nuclei in the lead region, although intruder states and shape coexistence have been observed as well in odd-mass and odd-odd nuclei [Hey88] and at closed (sub)shells, other than Z=82 (see, *e.g.*, [Woo92] for a review). In the even-even lead isotopes this phenomenon is manifested by the occurrence of low-lying, deformed 0^+ states involving multiparticle-multihole ($2p$-$2h$, $4p$-$4h$, ...) excitations across the closed proton core [Hey87]. A schematic drawing is presented on the left side of Fig. 3.2.
The intruder excitation energy is understood as a subtle interplay between the magic proton gap, the pairing interaction between like nucleons and the deformation driving proton-neutron interaction. The expression for the $2p$-$2h$ 0^+ energy reads:

$$E_{intr}(2p-2h) \simeq 2(\varepsilon_{j_\pi} - \varepsilon_{j'_\pi}) + \Delta E_M(2p-2h) - \Delta E_{pair} + \Delta E_Q(2p-2h). \quad (3.1)$$

The first term on the right represents twice the energy needed to overcome the energy gap (2×3.5 MeV) in the unperturbed system. The monopole correction term, ΔE_M, reflects the change of the proton single particle energies when varying the neutron number across a series of isotopes; hence it is not a constant. The precise radial dependence of j_π and $j_{\pi'}$ will decide whether or not the intruder state is favoured by the monopole interaction. The pairing correlation energy, ΔE_{pair}, of the additional particle pair and the hole pair gives extra binding to the system. The long-range quadrupole part of the proton-neutron interaction, ΔE_Q, is active between the valence protons and the open neutron shell. In the SU(3) formalism the latter contribution is written as

$$\Delta E_Q(2p-2h) \simeq 2\kappa \Delta N_\pi N_\nu, \quad (3.2)$$

with $\kappa = \kappa_0 \sqrt{(\Omega_\pi - N_\pi)(\Omega_\nu - N_\nu)}$ the quadrupole interaction strength, ΔN_π the number of extra proton pairs formed and N_ν the number of active neutron pairs. Ω_π and Ω_ν are the shell model degeneracies. This last contribution gives rise to the characteristic parabolic mass dependence of the excitation energy, reaching a minimum near the mid-shell (N$\sim$104), where the number of valence neutrons is maximal. Figure 3.2 (right) plots the different terms of Eq. 3.1 as a function of the neutron number.

A similar formula can be written for the $4p$-$4h$ case [De 00]: the ΔE_M and ΔE_Q energies are simply scaled to the number of particle-hole excitations. For the pairing

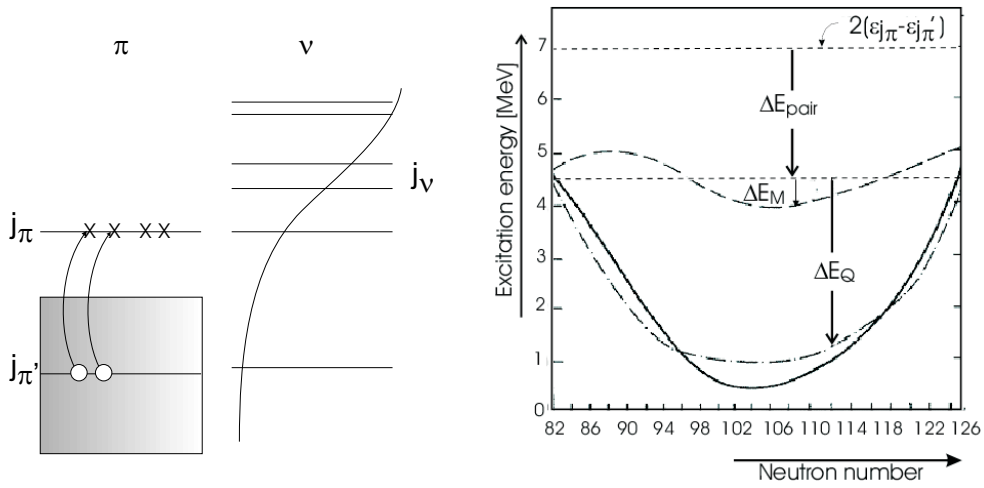

Figure 3.2: Left: $2p$-$2h$ proton excitation from the regular orbital $j_{\pi'}$ to the intruder orbital j_{π}. The neutron orbitals are filled in a BCS-type distribution. Right: Different contributions to the total energy of $2p$-$2h$ 0^+ intruder states. Figure based on a drawing of [Hey87].

contribution, scaling is not sufficient: the Pauli blocking reduces the gain per pair when increasing the number of pairs:

$$\frac{\Delta_{pair}(n/2)}{\Delta_{pair}(1)} = \frac{n}{2} \cdot (1 - \frac{n}{2\Omega} + \frac{1}{\Omega}) \tag{3.3}$$

where $n/2$ is the number of pairs and Ω is the shell model degeneracy of the state.

3.2.3 Further theoretical developments

The spherical shell model representation of the mp-nh states discussed above offers the advantage of an analytical expression of the excitation energy, but various alternative approaches have been developed. In a deformed mean field approach, for instance, the occurrence of deformed intruder states at low energy is understood in a different, but fully equivalent way [Hey89]. At prolate or oblate deformation, orbitals which lie above the Z=82 shell closure at sphericity can be occupied at low excitation energy cost. For instance, it can be seen from Fig. 1.6 that the $1/2^+[400]$ and $9/2^-[505]$ Nilsson orbitals cross for an oblate deformation of $\beta_2 \sim 0.1$.

The potential energy surface (PES) calculations in the Nilsson-Strutinsky approach by May *et al.* [May77] predicted the existence of three isomers at low excitation energy in ^{188}Pb, corresponding to a spherical shape in the ground state, and additional prolate

and oblate minima around 1-2 MeV, as shown in Fig. 3.3. In the same calculation, a prolate character for the rotational band at I≥2 in ^{184,186}Pb was suggested. These features were established experimentally later on in [All98] and [Hee93], respectively. We note that these calculations were limited to axially deformed shapes. Triaxiality is included in the work of R. Wyss *et al.*; a detailed account of these results for the lead and polonium isotopes is given in [Van03a]. The inclusion of axial asymmetry can affect, for instance, the height of the barrier between the coexisting minima and hence their mixing, as was shown by [Rod04] for ^{186}Pb.

Further refinements of the mean field approach include the restoration of the basic symmetries that are broken in the PES calculations discussed above. An example of the addition of correlations beyond the mean-field is found in the Generator Coordinate Method [Ben04, Dug03]. Following the Hartree-Fock mean-field calculation with a constraint on the quadrupole moment, the particle number is projected, as the common treatment of pairing in the BCS approach has the inherent drawback of particle number non-conservation. Subsequently, the rotational symmetry is restored, producing states with good angular momentum in the laboratory frame. Finally, configuration mixing with respect to the collective coordinate is included. The results of this approach are presented in Fig. 3.3. While the agreement with experiment is good for the prolate minimum and the associated band, the excitation energy of the oblate band is largely overestimated.

An alternative method, approximating the large scale shell model results, is the *Interacting Boson Model* (IBM). Configuration mixing IBM calculations have been performed [Fos03, Fos04] for the neutron-deficient lead isotopes near mid-shell; level schemes as well as charge radii have been extracted. These calculations will be discussed and compared to the experimental data obtained in this work in Sect. 6.4.

3.2.4 Spectroscopic studies of shape coexistence

A clear signature of intruder levels is their population in two- and four-nucleon transfer reactions, sensitive to the occupancy of specific shell-model orbitals. This approach has been successfully applied to a series of even-even isotopes in the tin region; for a review, see *e.g.* [Woo92]. For the lead isotopes approaching the proton dripline however, suitable targets are not available and other approaches are called for. The two methods described below, fine-structure α decay and in-beam spectroscopy, offer complementary results that contribute to the global picture of shape coexistence in

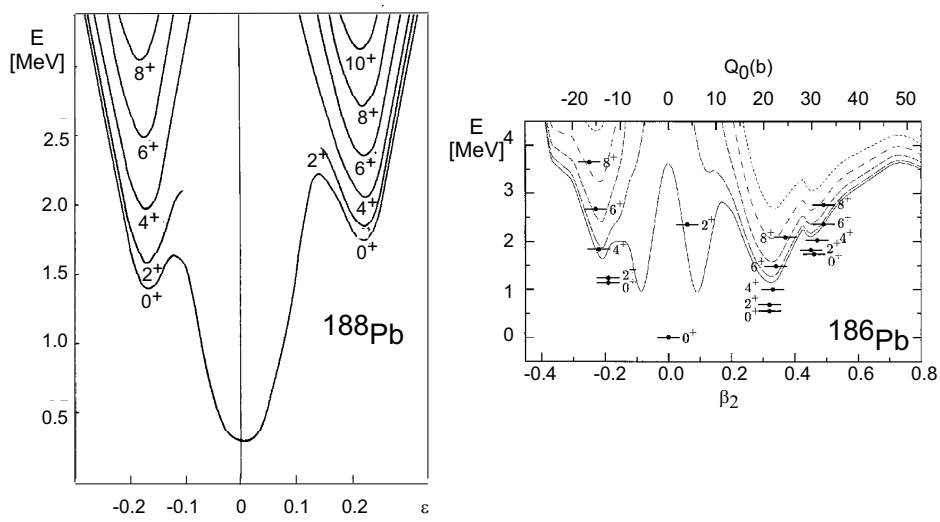

Figure 3.3: Left: Deformation energy for the lowest lying rotational states in ^{188}Pb in the Nilsson-Strutinsky model. Picture taken from [May77]; Right: Spectrum of the lowest positive parity bands with even angular momentum and K = 0, as a function of the deformation. The angular momentum projected energy curves are shown for comparison. The energy reference is that of the calculated 0^+ ground state. Picture taken from [Dug03].

the neutron-deficient lead region.

Fine-structure α decay

When approaching the neutron mid-shell, where theory predicts the lowest excitation energy for the intruder states, levels in Pb can be populated through fine structure α decay of Po isotopes. Therefore α decay, which feeds into the low-lying level structure, is an ideal tool for the exploration of shape coexistence in this region [Van00].

Alpha decay from the 0^+ ground state in the mother nucleus can only populate low-lying 0^+ and (with lower probability) 2^+ states. Excited states in the daughter nucleus subsequently decay via electromagnetic transitions to the 0^+ ground state. For an excited 0^+ state, direct γ-decay towards the 0^+ ground state is forbidden, as the photon carries an intrinsic spin of $1\hbar$. For the lead isotopes with N$\leq$112 the 0^+ state is the first excited state (see Fig. 3.4), leaving E0 transitions as the only available decay path. Hence observation of α-electron coincidences offers a reliable tool to identify the intruder states and determine their excitation energy.

In-beam spectroscopy

In the nuclear shell model, multiparticle-multihole excitations can give rise to collective rotational bands built on top of them. In contrast to the α decay described above, in-beam γ-ray spectroscopy studies following heavy-ion fusion-evaporation mainly probe the decay of high-lying high-spin states via γ-cascade emission along the yrast line. The 0^+ bandheads are often missed in in-beam spectroscopy measurements due to out-of-band decay, whence the need for complementary information from decay work.

Energy systematics in the lead isotopes

The systematics of the positive parity states up to $I^\pi=10^+$ are shown in Fig. 3.4 for the lead isotopes in the mass region from A=182 to A=206. They present the results both from in-beam studies, yielding mainly data on the yrast states and from α- and β decay spectroscopy providing information on the non-yrast states.

Owing to the presence of the Z=82 closed shell, the lead isotopes are expected to remain predominantly spherical in their ground state. When approaching the mid-shell, states of oblate and prolate character were predicted at low excitation energy [May77]. The first observation of low-lying 0^+ states in the neutron-deficient lead isotopes dates from 1984, when excited 0^+ states were observed in $^{192-198}$Pb, following β decay [Van84] and identified through the E0 character of their de-excitation. From ^{194}Pb on, the intruder states, associated with an oblate deformation on the basis of theoretical predictions, even descend below the 2_1^+ state. The 0_2^+ states have been further explored down to ^{184}Pb in consecutive fine structure α decay studies [Wau94, Bij96, And99a]. This configuration is seen to drop steeply in energy between N=126 and N=104, where the shell model predicts the minimum excitation energy. This is in agreement with the levelling-off of the curve at this neutron number. In ^{188,186}Pb, a third 0^+ state was identified and associated with a predominantly prolate configuration [And00, Le 99b]. There is, however, no experimental discrimination between the oblate and prolate deformations at present and moreover, the configurations will be mixed.
A similar lowering in excitation energy is also seen for the yrast $I\geq 2$ states from ^{196}Pb down to ^{186}Pb. In ^{196}Pb, besides the yrast band, a collective band of presumably oblate character is observed [Pen87], while for ^{192,194}Pb the information is mainly limited to the 2_2^+ states. Rotational bands have been identified in the more neutron-deficient isotopes, $^{190-182}$Pb [Dra98, Hee93, Coc98, Jen00]. They have been associated with prolate configurations on the basis of their similarity with the well-known prolate bands in the mercury isotones. They become yrast from ^{188}Pb downwards and their

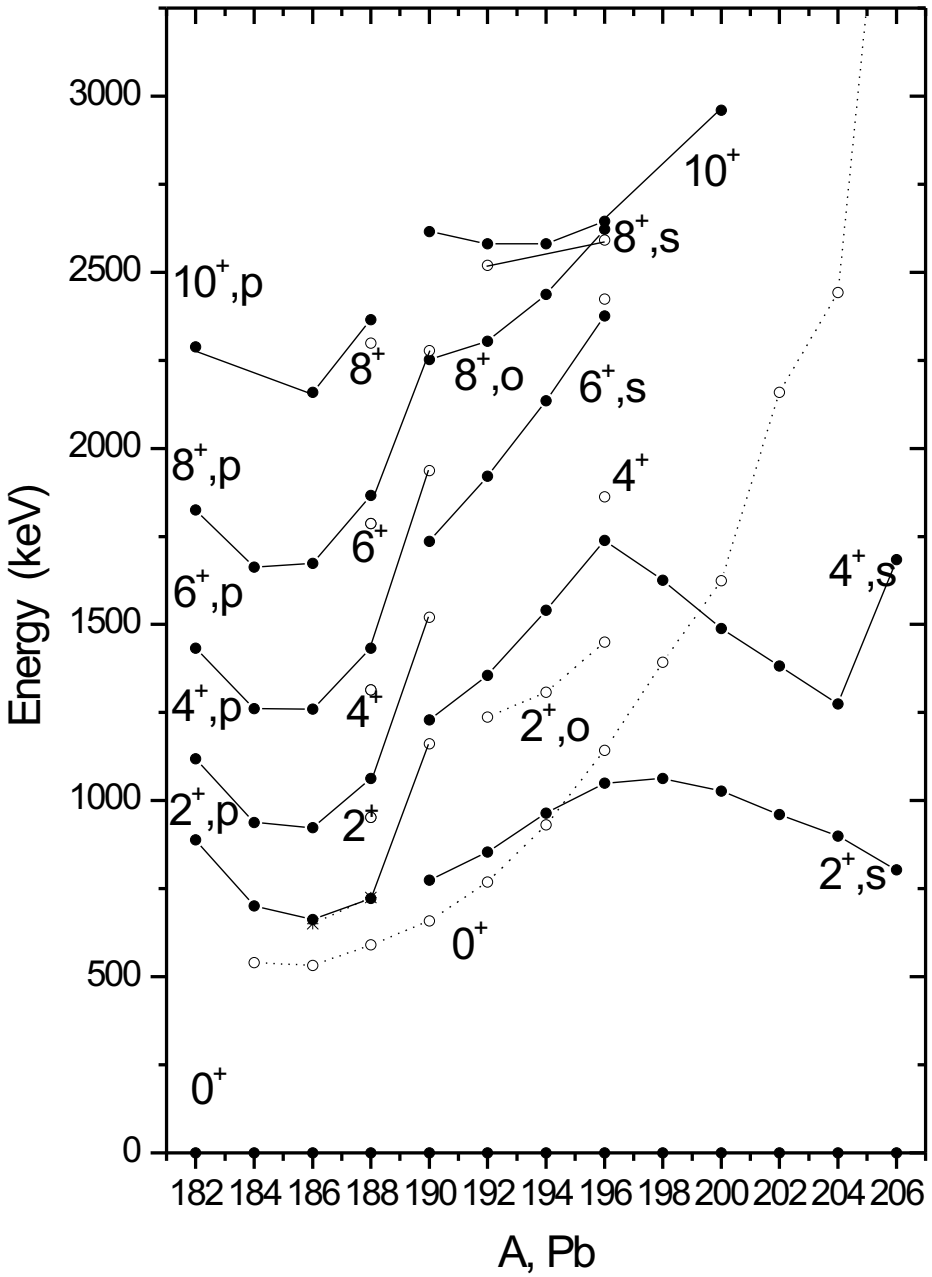

Figure 3.4: Energy systematics of the positive parity states in the neutron-deficient lead isotopes. Filled circles represent the yrast levels, open circles the non-yrast states. The indications s: spherical, o: oblate, p: prolate, and the connecting lines are based on the most probable interpretation of the character of the involved states. Picture taken from [Van03a].

excitation energy is seen to be minimized in ^{186}Pb. In ^{188}Pb a second, yrare band is observed [Dra03] and tentatively associated with an oblate shape.
In the heavier isotopes, the intruder states climb high up in excitation energy and the spherical neutron quasi-particle configurations dominate the low-energy excitation scheme.

In order to get a complete picture of the shape coexistence in a series of isotopes, not only the regular and intruder excitations and the associated collective bands are of importance, but the mixing between the different configurations also needs to be established. (A description of the basic two-level mixing model is presented in Appendix C.)
The α decay hindrance factor for the decay towards the excited 0^+ state versus the decay towards the ground state provides information on the particle-hole character of the states connected by the α decay and is a measure of the mixing between the normal and the intruder state in both the mother and the daughter nucleus. This concept is clarified in a two-level mixing model [Wau94], where only the protons determine the transition probability and the neutrons are treated as spectators.
An alternative direct measurement of the shape mixing is the monopole transition strength between the intruder state and the ground state. Related to this is the measurement of the charge radii reported in this work. They correspond to the diagonal matrix element of the monopole operator while the E0 transition probability probes the non-diagonal elements. This subject is treated in detail in the next section.

3.2.5 Monopole transition strength and shape mixing

In terms of the single-particle degrees of freedom, the monopole operator $\hat{T}$(E0) is given by

$$\hat{T}(E0) = \sum_k e_k r_k^2, \tag{3.4}$$

with e_k the effective charge of the k^{th} nucleon and r_k its position. The sum is over all nucleons in the nucleus.
The absolute monopole transition probability, W($E0$) is given by:

$$W(E0) = \frac{\ln 2}{(T_{1/2}(0^+))_{E0}} = \rho^2(E0) \sum_j \Omega_j(Z,E). \tag{3.5}$$

The monopole transition strength $\rho^2(E0)$ between the initial (i) and the final state (f) contains the relevant nuclear structure information and is given by

$$\rho^2 = \langle 0_f^+ | \sum_k \frac{\overrightarrow{r}_k^2}{R^2} |0_i^+\rangle^2, \tag{3.6}$$

with R the nuclear radius. Ω_j is an electronic factor, which depends on the Z of the nucleus and on the transition energy. Its values are tabulated for the different orbital decay channels j=K,L,... [Hag69].
Using Eq. 3.5, the transition probability W(E0) and hence also the strength $\rho^2(E0)$ is readily calculated when the half-life of the excited state can be determined.

In a two-level mixing model, the ground state and the excited state can be written as a linear combination of the unperturbed spherical and deformed states:

$$|0^+_{gs}\rangle = a\ |\text{sph}\rangle + b\ |\text{def}\rangle \tag{3.7}$$

$$|0^+_{exc}\rangle = b\ |\text{sph}\rangle - a\ |\text{def}\rangle, \tag{3.8}$$

with $a^2 + b^2$=1. Anticipating the two-parameter formula, Eq. 3.10, discussed in the next section, the monopole transition strength between the excited and the ground state is:

$$\rho^2_{exc\rightarrow gs} = a^2 b^2 \left(\frac{3Z}{4\pi}\right)^2 (\langle\beta^2\rangle_{def})^2. \tag{3.9}$$

The connection between the shell model monopole operator and the collective variables is elaborated in [Woo99]. From equation 3.9 it is understood that large E0 strength is an indication of strong mixing (large b^2) between nuclear states with largely different deformation. The mixing between the excited and the ground state can be extracted, provided the deformation $\langle\beta^2\rangle_{def}$ is known.
This method has been applied by Dendooven *et al.* [Den92] to determine the mixing in $^{190-194}$Pb. The half-life of the excited 0^+ states was measured via an α-e$^-$ coincidence measurement in a fine structure α decay study. A mixing of 0.3%, 0.5% and $\geq$ 2% was obtained for the admixture of the oblate intruder state in the spherical ground state in ^{194,192,190}Pb, respectively.

3.3 Nuclear moments and charge radii

3.3.1 Nuclear properties from isotope shifts

As mentioned in Sect. 2.3.2, the isotope shift consists of a mass shift and a field shift. The mass shift needs to be evaluated, but it does not contain the relevant nuclear structure information; only the field shift does.
The field shift arises from the change in the nuclear charge distribution when changing neutron number. Although the isotope shift is typically less than 10^{-5} of the transition

frequency, it can be determined to a precision of 0.1-1 % in laser spectroscopic measurements. This accuracy allows the observation of small changes in the nuclear charge distribution. Besides the volume change, when adding an extra neutron, deformation also can contribute to an increase of $\langle r^2 \rangle$. To lowest order, the mean square radius of an axially symmetric deformed nucleus is given by

$$\langle r^2 \rangle_{def} = \langle r^2 \rangle_{sph} (1 + \frac{5}{4\pi} \langle \beta_2^2 \rangle), \tag{3.10}$$

where $\langle r^2 \rangle_{sph}$ represents the mean square radius of the spherical nucleus, and the collective coordinate β_2 gives the quadrupole deformation. In addition, fluctuations around the minimum of the potential well also contribute to $\langle r^2 \rangle$: they can increase $\langle \beta_2^2 \rangle$ although $\langle \beta_2 \rangle$ may be equal to zero. This dynamical effect of the zero-point motion is not reflected in the quadrupole moment, which depends on $\langle \beta_2 \rangle$ rather than on $\langle \beta_2^2 \rangle$.

In the case of mixing between spherical and deformed states, as in the shape coexisting picture sketched in the previous section, the deviation of the ground state radius from the spherical mean square radius value is given by:

$$\langle 0_{gs}^+ | r^2 | 0_{gs}^+ \rangle - \langle \text{sph} | r^2 | \text{sph} \rangle = b^2 (\langle r^2 \rangle_{def} - \langle r^2 \rangle_{sph}), \tag{3.11}$$

using the notation of the two-level mixing model introduced before. Applying the two-parameter formula, Eq. 3.10, for the radius of an axially deformed shape, this relation can be rewritten as

$$\langle 0_{gs}^+ | r^2 | 0_{gs}^+ \rangle - \langle \text{sph} | r^2 | \text{sph} \rangle = b^2 \frac{5}{4\pi} \langle \beta_2^2 \rangle \langle r^2 \rangle_{sph}. \tag{3.12}$$

The deviation will be large when the unperturbed states have different radii, *i.e.*, different deformation, and when the mixing is important. Hence the mean square charge radii are sensitive to the mixing of the normal and intruder states when shape coexistence is present.

3.3.2 Nuclear properties from the hyperfine structure

An estimate of the single-particle magnetic moment is given by the Schmidt moments (Eq. 2.11). However, even for nuclei with one nucleon outside closed shells, significant deviations form this value have been found. In ^{209}Bi, for instance, the magnetic moment has been determined experimentally to be μ= 4.11 μ_N, while the Schmidt value for a proton in the $\pi h_{9/2}$ orbital is 2.62 μ_N. Two different effects have been used to

explain the deviation: meson exchange current effects, and first and second order core polarization.
Magnetic moments, or more precisely nuclear g-factors, are shown to be very sensitive to the orbital occupied by the valence nucleons and to the purity of the configuration. The coupling of the valence particles to spin-flip matrix elements between spin-orbit partners across closed shells (first order core polarization) also significantly affects the magnetic moment. On the contrary, they are rather unsensitive to the number of paired particles (or holes) or to quadrupole particle-core coupling. As a consequence, the magnetic moment can stay constant over a larger chain of isotopes. In addition, it is also not sensitive to whether a specific orbital is occupied in a normal or in an intruder configuration. The magnetic moment of the $9/2^-$ intruder state in the thallium isotopes, for instance, is in good agreement with that of the $9/2^-$ normal state in the bismuth isotopes.

Unlike the magnetic dipole moment, the electric quadrupole moment is sensitive to the quadrupole collectivity and the deformation of nuclei. Under the assumption of strong coupling, the spectroscopic quadrupole moment of a well-deformed axially symmetric nucleus is related to the intrinsic quadrupole moment by

$$Q_s = \frac{3\Omega^2 - I(I+1)}{(I+1)(2I+3)} Q_0, \tag{3.13}$$

with Ω the projection of the nuclear angular momentum I onto the symmetry axis. In good approximation the intrinsic quadrupole moment is related to the deformation parameter β_2 by the relation

$$Q_0 = \frac{3ZR_0^2}{\sqrt{5\pi}} \langle\beta_2\rangle (1 + 0.36\langle\beta_2\rangle), \tag{3.14}$$

where the nuclear radius R_0 is usually taken as $1,2 \cdot A^{1/3}$ fm. A review of the study of magnetic and quadrupole moments in exotic nuclei has been presented recently in [Ney03].

3.3.3 Various experimental methods in atomic spectroscopy

Measurements of nuclear moments and charge radii of exotic, short-lived radioactive nuclei require sensitive methods that can be used in on-line or in-beam conditions. The choice between the different techniques is dictated by the available production mechanisms, the production rate, life-time, decay mode ... A large variety of experimental techniques exists, comprising both optical and non-optical methods.
For detailed reviews of the various approaches, we refer to [Jac79, Ott89, Ney03].

As an example of the non-optical methods, we consider the nuclear magnetic resonance technique (NMR). A prerequisite for this method is a spin-polarized ensemble of atoms. The spin-polarization or its destruction by an applied rf-field is visualized, *e.g.*, by measuring the β-asymmetry in the radioactive decay, and allows a precise determination of the nuclear g-factor. Various similar methods, often requiring a spin-oriented ensemble, give access to a precise measurement of I and g, but not the isotope shift. The direct measurement of g-factors additionally provides an important input for the extraction of the magnetic moments from the measured HFS, using Eq. 2.8.

The optical methods, on the other hand, use transitions with frequencies in the UV, visible or IR range. Not only the HFS, but also the optical isotope shift can be extracted. These techniques use monochromatic light of a tunable frequency, nowadays easily supplied by tunable dye lasers.
One of the most powerful optical methods applicable to exotic nuclei is collinear laser spectroscopy [Ant78]. A fast ion beam, *e.g.*, an on-line mass separated beam interacts will a collinear laser beam, preferably after neutralization in a charge-exchange cell. The response of the atomic system to the laser photons can be monitored via the yield of fluorescence photons, down to an ion beam flux of 10^4/s. Alternative detection methods have been provided, often with increased sensitivity. Moreover, it has been shown that the collinear geometry inherently provides a resolution close to the natural line width. The result is a sensitive and precise measuring technique.

An alternative laser method is resonance ionization spectroscopy, exciting atoms to the continuum via a two- or three step path, using the first step for atomic spectroscopy. The response of the system is monitored by counting the ions, often after mass separation. The in-source resonance ionization spectroscopy (Sect. 2.3.3), applied in this work, is characterized by an outstanding sensitivity, giving access to very exotic isotopes with low production rates, as an additional sample preparation step is avoided. The resolution, however, is strongly reduced by the Doppler broadening in the ion source cavity. For the heavy elements the optical isotope shift is large, and a useful accuracy can be achieved. The performance of collinear laser spectroscopy and resonance ionization spectroscopy methods is compared in [Klu03].

Alternative methods exist for measuring the nuclear charge radii, like electron-scattering cross sections measurements and isotope shift measurements in muonic X-ray spectra. As large amounts of the isotope under study are needed (grams of material needed for targets), the techniques are essentially limited to stable isotopes. How-

ever, they often offer valuable complementary information for the reliable extraction of charge radii from optical isotope shift measurements (see Sect. 6.3.3).

3.3.4 Atomic spectroscopy in the lead region

Mercury: the textbook example of shape coexistence

In the early isotope shift measurements by Bonn *et al.* [Bon71, Bon72] a large and sudden increase in the nuclear charge radius was observed between ^{187}Hg and ^{185}Hg. This was tentatively explained as a transition from a weakly deformed ($\beta_2 \approx 0.15$) to a strongly deformed ($\beta_2 \approx 0.31$) shape. Similar effects were observed earlier around N=88 in the rare earths region. However, in the mercury case, the transition to deformed shapes occurs very closely to the magic proton gap and was hardly to be expected.
The measurement was extended to ^{183,181}Hg in [Bon76], but as the β-asymmetry measurements used in this experiment are not applicable to I=0 states, no data were obtained on the even-even isotopes.
The first information on the even isotopes came from complementary nuclear spectroscopy experiments. In in-beam and β decay experiments, the ground state of the mercury isotopes down to A=184 was shown to be near-spherical. At higher spin, a strongly deformed band crossed the ground state band.

Using laser spectroscopy, the $\delta\langle r^2\rangle$ of the even isotopes $^{188-184}$Hg was measured at ISOLDE [Kue77] and confirmed the near-spherical ground state shape. The resulting odd-even staggering is one order of magnitude higher than the normal odd-even staggering[1] and is inverted. This behaviour is explained as the coexistence of two different shapes at low excitation energy (see Sect. 3.2.2). Particularly clear in this respect is the case of ^{185}Hg, where the isomer shift between the well-deformed ground state and the weakly oblate isomer has also been measured [Dab79]. A summarizing picture is shown in Fig. 3.5 and presents a clear illustration of the sensitivity of the charge radii to deformation effects in the nucleus.

Other isotopes

A shape transition, similar to the one at ^{185}Hg, has been observed in the charge radii of the gold isotopes (Z=79), when the neutron mid-shell is approached [Wal87]. However, no extreme odd-even staggering is observed: it seems that the odd proton has a stabilizing influence on the nucleus with respect to deformation [Wal87]. A recent

[1]The normal OES is observed in almost all regions of the nuclear chart. The $\delta\langle r^2\rangle$ of the odd-neutron isotopes is smaller than the average of their even-N neighbours.

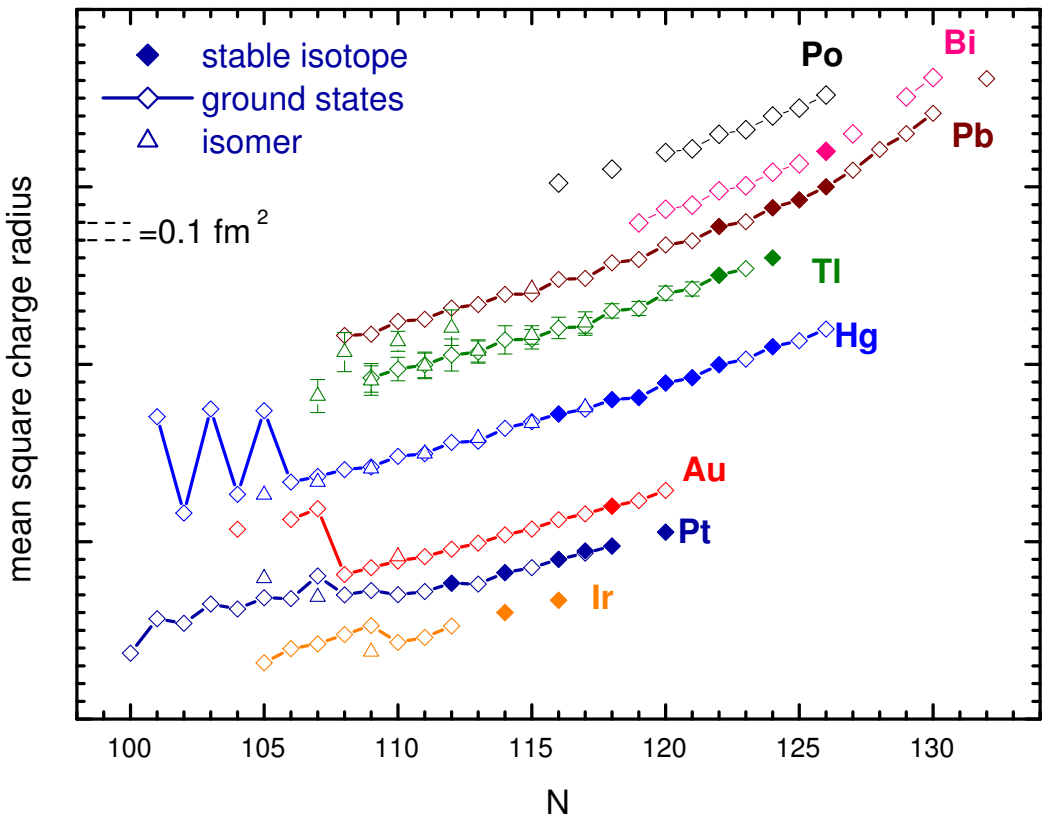

Figure 3.5: Mean square charge radii for various elements around lead. The $\delta\langle r^2\rangle$ scale should be taken for each element separately. Experimental data are taken from [Ott89, Kro88, Din90, Hil92, Le 99a, Kow91, Cam95, Pea00]

COMPLIS[2]-experiment revealed a similar effect in the iridium series (Z=77). For the iridium isotopes heavier than A=186, a modest prolate deformation is assumed in the ground state; at A=186, the systems jumps to a higher prolate deformation and the 1/2[541] state (from the spherical $\pi h_{9/2}$ orbital) becomes the ground state [Ver00]. The fact that the effect between A=187-186 is smaller in the iridium chain than it is in gold, might be related to the fact that Ir is going further away from the closed shell, towards the well deformed transition region.

In the platinum isotopes, with Z=78, both nuclear spectroscopy and isotope shift measurements showed a shape transition between A=186 and 185, from presumably triaxial (or oblate) to prolate deformed [Duo89]. However, it is not accompanied by an abrupt discontinuity in the $\delta\langle r^2\rangle$, like in the mercury series. Moreover, the odd-even

[2]COMPLIS is a dedicated laser spectroscopy set-up for the study of refractory elements at ISOLDE.

staggering close to the mid-shell is inverted, compared to the normal OES, as in the mercury case. It has been explained as an alternating shape transition between triaxial deformation for the even-even isotopes and a purely prolate shape of the odd-A ones [Le 99a].

In the lead isotopes, as well as in the bismuth (Z=83) and polonium (Z=84) series, the measurements of the charge radii have not yet reached the neutron mid-shell. Intruder orbitals are active in this region and could interfere in the ground state configuration. The extension of the Pb chain down to ^{183}Pb is presented in Chapter 6.

Chapter 4

Neutron-rich isotopes around Z=82

4.1 Experimental details

An overview of the target-ion source combinations and the detector configurations used in the different experiments was given in Table 2.4. Details of the detection set-up and the measurement cycle, specific for each experiment, are presented next.

run I

Out of the 12 proton pulses constituting a supercycle, 6 were sent to the ISOLDE target. The separator beam gate was closed for 200 ms after proton impact on the target. This pulsed release (Sect. 2.1.5) resulted in a considerable reduction of the isobaric contamination. Finally, the ions reached the detection setup, where the activity was implanted into a movable aluminized mylar tape.
A 450 mm^2, 500 μm thick Si-detector for α-particles, a LEGe (active surface 3850 mm^2, thickness 25 mm, 300 μm beryllium entrance window) and a HPGe (60 % relative efficiency) for X-ray and γ-ray detection surrounded the source in close geometry. Sandwiched between the tape tube and the LEGe detector, a 0.5 mm thick plastic ΔE-detector completed the setup.
Data were collected in cycles, consisting of a growing-in and a decay period, during which the beam gate was closed. A 144 s long collection was followed by a 216 s long beam off period, during which decay data were taken both in list mode and in multiscaling mode (dividing the decay time in 8 bins of 26 s each). After every cycle of implantation and decay, the tape was moved to evacuate any long lived activity.

run II

A major improvement of the experimental conditions is expected from the combination of the pulsed release with the laser ion source. The chemically selective ionization of the lead and bismuth isotopes in the hot, niobium ion source cavity (2100°C) was achieved in three steps, following the excitation schemes given in Table 2.2.
In this experiment separate implantation and decay positions were used. The activity was implanted into an aluminized mylar tape and then transported towards the lead shielded decay station, where the radioactive decay was measured for the same period. The detection set-up was depicted in Fig. 2.11. By comparing the peak areas of β-delayed γ-rays in γ-singles and β-gated γ spectra, the detection efficiency for β-particles in the scintillator was determined to be 8(1)%.

The supercycle was extended to 14 proton pulses or 16.8 s. Seven pulses per supercycle impinged on the ISOLDE target during the ^{215}Pb data collection, with an intensity of 3.1×10^{13} particles per pulse. A 100 ms beam gate closure was applied after every proton impact. Data were taken simultaneously in list mode and multiscaling mode (8×32.850 s), in cycles of 268.8 s or 16 supercyles.
The measurement of the ^{218}Bi β decay received 10 proton pulses per supercycle and the beam gate was reduced to 20 ms. The implantation period was 168 s or 10 supercyles, optimized for the shorter half-life.

run III

For details on run III we refer to App. D.

run IV

A concluding experiment focussed on the determination of the ground state feeding in the β^- decay of ^{215}Bi towards ^{215}Po. The laser ionized bismuth ions were implanted into a 20 μg/cm^2 carbon foil, placed on a rotating wheel (Fig. 2.10). After an implantation time of 33.6 s the wheel moved over an angle of 144° towards the detection set-up. A LEGe detector, placed behind the foil, measured the γ-radiation accompanying the ^{215}Bi decay for 235.2 s. During this measurement period, the separator gate was closed and no implantation took place. A Si-PIPS detector (surface 150 mm^2, thickness 300 μm) was placed in front of the foil at a distance of 10 mm. It recorded the α decay of the daughter, ^{215}Po. For calibration purposes, data were collected for ^{216}Bi with a different cycle: 67.2 s implantation, 532 s decay.

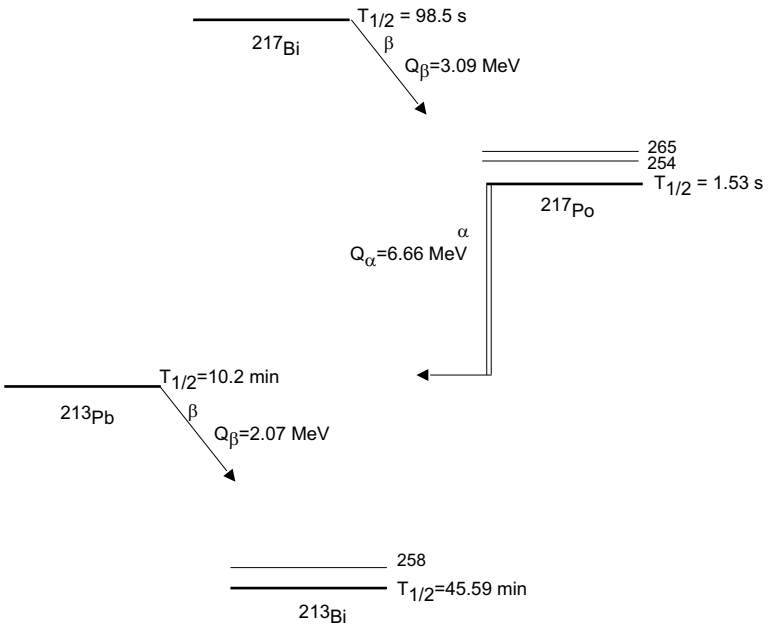

Figure 4.1: The decay scheme of ^{217}Bi-^{217}Po-^{213}Pb. Data taken from [Kur03a].

4.2 Beta decay of ^{213}Pb

The ^{213}Pb half-life had been determined earlier to be 10.2(3) min [Ako92]. The decay was not directly observed but via the growth of the 45.59 min ^{213}Bi activity. The ground state spin has not been measured, but on the basis of systematics a $9/2^+$ spin and parity can be tentatively assigned.
Four γ-transitions (257.88(4), 335.33(10), 593.10(10) and 758.9(1) keV) were assigned to the ^{213}Bi level scheme in the fine-structure α decay of ^{217}At [Chu97], defining three excited states, at 257.88(4), 593.10(10) and 758.9(1) keV, respectively.

^{213}Pb was produced as the α decay daughter of ^{217}Po, directly feeding the ground state [Lia97]. The subsequent β^- decay towards ^{213}Bi is discussed in this work (Fig. 4.1). ^{217}Po was produced in the β^- decay of ^{217}Bi, which was observed for the first time in this experiment and the results are described in [Kur03a].

Figure 4.2 shows the singles γ-spectrum obtained at mass 217 during run I. The level scheme of ^{213}Bi was considerably extended on the basis of the γ-γ-coincidence data. The level at 758.9 keV could not be confirmed in this work. Table 4.1 lists the assigned γ-rays, placed in the level scheme, along with their relative γ-intensities and the coincidence relations. The γ-detection efficiency has been determined using calibrated γ-ray sources.

The internal K-conversion coefficient for the 257.7 keV transition, deduced by the fluorescence method[1], is α_K=0.56(4). This is slightly at variance with the value of α_K=0.45(4) given in [Chu97], though both give rise to a predominant $M1$ character for this transition, when compared to the theoretical coefficient, α_K=0.60 for an $M1$ transition [nnd].

Figure 4.3 shows the LEGe spectrum obtained during run II with and without resonant tuning of the lasers in the ion source to bismuth. The assignment of the γ-rays at 254.1, 257.7 and 264.6 keV to the decay of bismuth or its daughters is confirmed by their exclusive presence in the on-resonance spectra. The intensity ratio of the 257.7 keV line and the γ-rays from the ^{217}Bi decay is different in Figs. 4.2b and 4.3. From the time behaviour of the 257.7 keV line in the subsequent time units of the multiscaling, it is inferred that a substantial part of the activity was implanted next to the tape in run I, preventing it from being carried away. This explains the relative enhancement of the 10.2 min activity from ^{213}Pb. In run II this problem was avoided by measuring at the decay station, after transport of the source. Therefore the latter data have been used to derive the direct feeding to the ^{213}Bi ground state in the ^{213}Pb decay. Moreover, the use of the RILIS for selective bismuth ionization allows to suppress the direct production of ^{217}Po.

Knowing the absolute β branching of the 264.6 keV line[2] originating from ^{217}Bi, β decay feeding to the ^{213}Bi ground state was calculated using the intensity ratio of the 257.7 keV to 264.6 keV transitions (Fig. 4.1). The observed intensities are corrected for internal conversion. For the 257.7 keV the total $M1$ conversion coefficient is used. The multipolarity of the 264.6 keV and 254.1 keV lines has not been firmly established. For the 264.6 keV line $E1$ or $E2$ character have been suggested in [Kur03a]; the 254.1 keV transition can be $E1$, $E2$ or $M1$ and all possibilities have been included in the calculation. Theoretical conversion coefficients [nnd] are used.
The cycle correction, a function of the half-lives involved and the measurement cycle, accounts for the fraction of nuclei implanted on the tape but not decayed in front of

[1]The number of 257.7 keV γ-rays is compared to the bismuth X-ray intensity, in the spectra gated on the 913.8, 1037.7, 1085.5, 1187.0, 1237.4 and 1285.5 keV lines, after correction for the relative detection efficiency.

[2]This value is obtained by comparison of the 264.6 keV γ intensity and the α intensity following the ^{217}Po decay. The value of the ground state feeding in the ^{217}Bi - ^{217}Po decay adopted in this work (16 - 50% depending on the multipolarity) is at variance with the upper limit of 5% quoted in [Kur03a]. The difference arises because a different γ-detector has been used for its evaluation and ambiguity on the efficiency determination occurred.

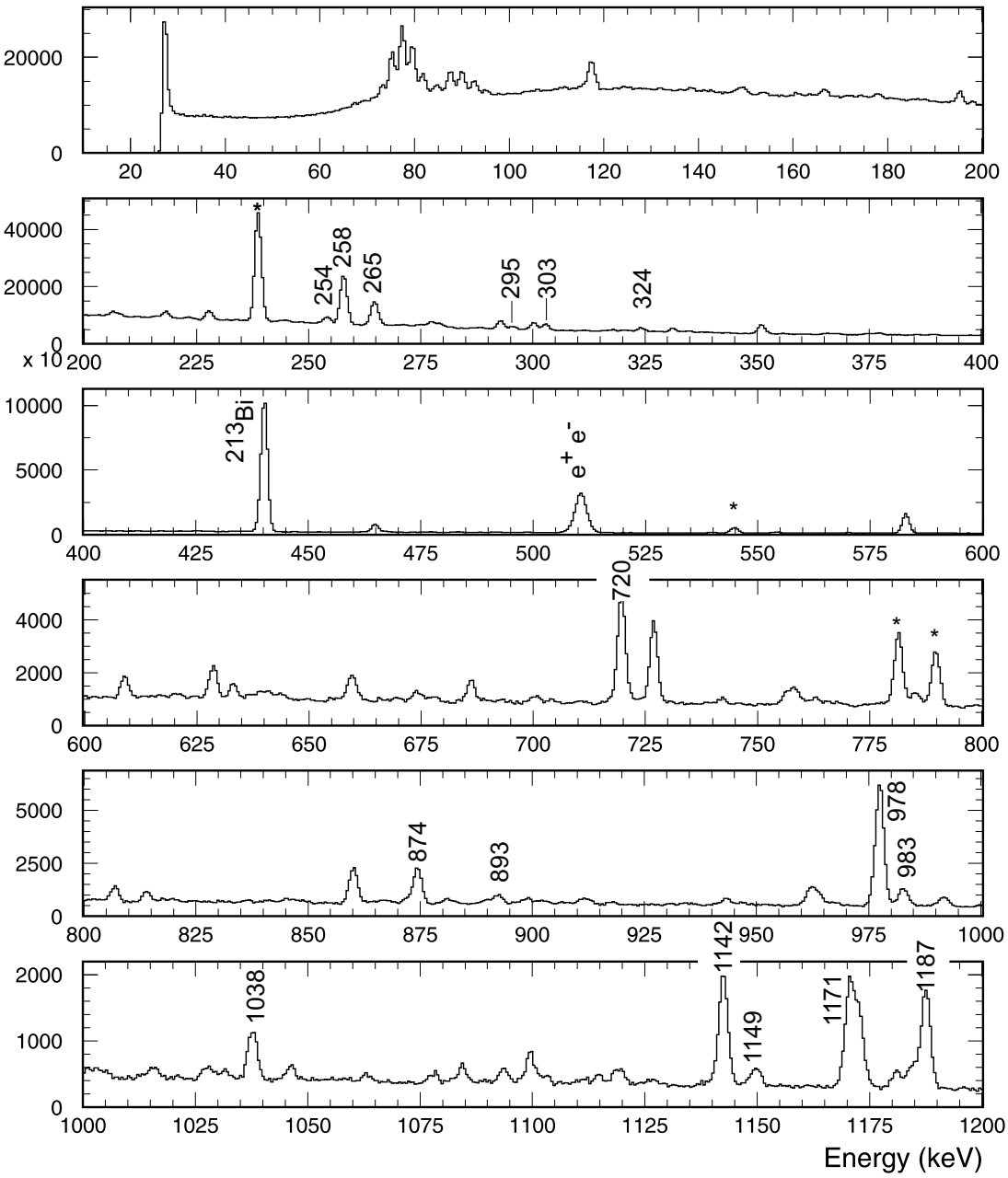

Figure 4.2a: γ-singles spectrum taken during the first 26 s in the decay of an A=217 source. Data are from run I. Energy labels in keV. Lines marked with $\star$ belong to ^{209}At.

Table 4.1: Energies, relative intensities, normalized to the 257.7 keV γ-ray, and coincidence relations for the γ-rays following the β decay of ^{213}Pb.

Energy [keV]	I_γ [%]	Coincident γ-lines
103.5(5)		874.3
248.0(5)		1037.7
257.7(1)	100.	223.4, 295.4, 334.9, 720.3, 874.3, 893.1, 913.8, 944.5, 964.7, 1029.6, 1037.7, 1085.5, 1187.0, 1237.4, 1285.5, 1335.5
274.3(5)	4.0±1.9	1171.0
295.4(5)		257.4, 893.1
302.7(1)	12.3±1.6	1142.4
324.2(1)	9.5±1.2	1171.0
334.9(1)	3.2±0.5	77.1, 87.3 ,257.7, 295.4, 389.8
389.8(5)		74.8.0, 77.1, 257.7, 334.9, 462.7, 592.9
462.7(5)		
467.8(5)		977.5
565.5(5)		720.3, 977.5
592.9(1)	4.0±0.7	74.8, 77.1, 87.3, 389.8, 462.7
720.3(1)	61.7±8.0	74.8, 77.1, 87.3, 89.8, 257.7, 467.8, 565.5
874.3(10)	26.7±3.5	74.8, 77.1, 103.5, 467.8
893.1(10)	6.8±1.0	257.7, 295.4, 302.7
913.8(10)	3.2±0.8	74.8, 77.1, 87.3, 257.7
944.5(1)	7.3±1.1	257.7
964.7(1)	26.4±3.5	74.8, 77.1, 87.3, 89.8, 223.4, 257.7
977.5(1)	111.4±14.6	74.8, 77.1, 467.8, 565.5
982.9(1)	17.0±2.3	74.8, 77.1, 87.3, 462.7
1029.6(1)	4.8±0.7	74.8, 77.1, 257.7
1037.7(1)	16.7±2.3	74.8, 77.1, 87.3, 89.8, 257.7
1085.5(3)	4.6±0.7	74.8, 77.1, 257.7
1142.4(1)	39.9±5.3	74.8, 77.1, 87.3, 89.8, 302.7
1149.3(1)	6.9±1.0	77.1, 87.3, 295.4
1171.0(1)	60.6±8.0	74.8, 77.1, 274.3, 324.2
1187.0(1)	41.2±5.5	74.8, 77.1, 87.3, 257.7
1237.4(1)	8.2±1.2	74.8, 77.1, 87.3, 89.8, 257.7
1285.5(1)	6.8±1.0	74.8, 77.1, 87.3, 257.7
1335.5(1)	4.2±1.2	
1445.4(1)	7.5±1.1	
1592.1(1)	8.6±1.2	

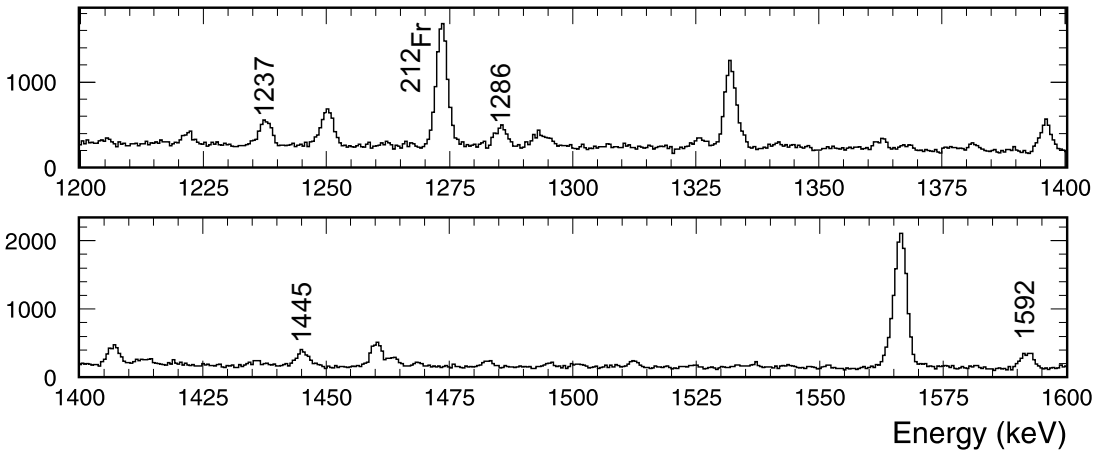

Figure 4.2b: *Continued* γ-singles spectrum taken during the first 26 s in the decay of a A=217 source. Data are from run I. Energy labels in keV. Lines marked with $\star$ belong to ^{209}At.

the detector during the measurement time. In this correction the 1.53 s half-life of ^{217}Po has been neglected owing to the much longer half-lives of 98.5 s and 10.2 min for ^{217}Bi and ^{213}Pb, respectively.
Moreover, the recoil of the ions following α decay needs to be considered. For an implantation energy of 60 keV the recoil energy of the α decay can be sufficient for the ion to escape from the tape. Lead ions recoiling out of the tape at the implantation point are lost for detection at the decay station. The recoil fraction determined to be 0.31(4) in [Wau91] has been adopted.
Including, in addition, corrections for the detection efficiency and the γ-intensity, a ground state feeding of $\leq 34\%$ results for the ^{213}Pb -^{213}Bi decay, assuming $M1$ multipolarity for the 257.7 keV line.

The level scheme finally adopted is presented in Figure 4.4. The feedings should be regarded as upper limits (or lower limits for the $\log ft$ values), as weaker γ-rays can remain unobserved, in particular when the β decay strength is strongly fragmented.
The applied time cycle of implantation and decay did not allow to obtain new information concerning the ^{213}Bi β^- decay towards ^{213}Po ($T_{1/2}$=45.59(6) min [Ako92]).

4.3 Beta decay of ^{215}Pb

This section reports on the first measurement of the ^{215}Pb β decay. In the daughter nucleus ^{215}Bi, a γ-ray cascade had been observed, populated via a high-spin isomer in ^{215}Bi, shown in Fig. 4.7. An extensive discussion of this isomeric decay can be found

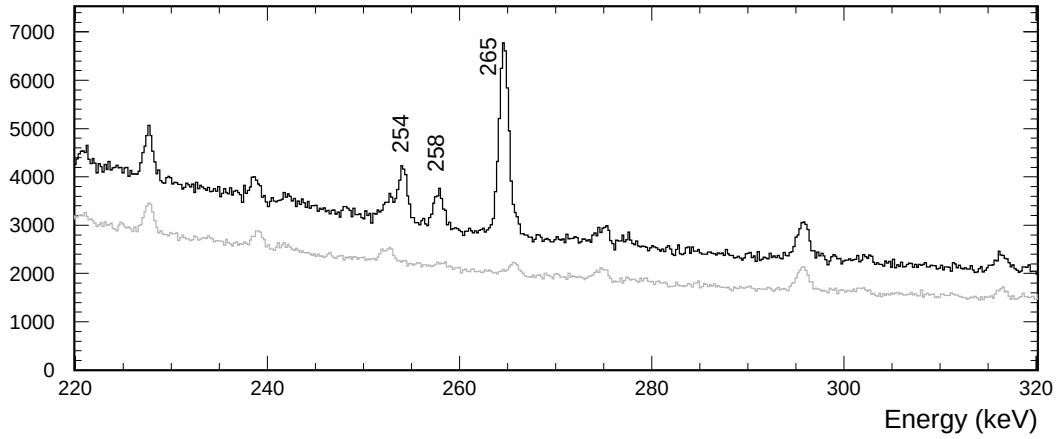

Figure 4.3: Singles LEGe spectrum taken at mass 217, recorded in cycles of 8×32.5 s. Lasers resonant on bismuth (black); lasers off (grey). Data from run II.

in [Kur03b]. No further experimental information was available.

The element selectivity of the resonance ionization laser ion source provides a powerful identification technique for the first study of the ^{215}Pb β decay. Indeed, the comparison of the spectra taken with and without laser irradiation in the ion source, reveals the lead related γ-rays and the daughter activities. During this experiment, data were collected for 12 hours with the lasers resonantly tuned to lead and for 2 hours without laser irradiation. Figure 4.5b shows the β-gated γ spectra with and without resonant laser ionization. The γ-ray at 183.5(3) keV, present only in the on-resonance spectrum, was assigned to the β^- decay of ^{215}Pb. The resonant line at 293.7 keV was known to belong to the β decay of ^{215}Bi [Map77].

The main contaminants in the spectra are associated with the β decay of ^{84m}Br. Being close to the maximum of the fission peak in the applied reaction, this isotope is produced abundantly. It most likely passes through the mass separator in molecular bounds with stable barium isotopes. Figure 4.6 presents an off-line mass scan performed on the target, before the start of the experiment, and shows the presence of stable barium impurities in the target container.
Moreover, γ-lines from ^{212}Fr and ^{209}At, as daughter of ^{213}Fr, are observed. The cross section of the francium and actinium isotopes in this mass region is typically three to four orders of magnitude larger and in addition they are characterized by a low ionization potential (4.07 eV and 5.17 eV, respectively), hence a high ionization efficiency. Therefore, even if only the tails of their mass distribution survive the mass separation

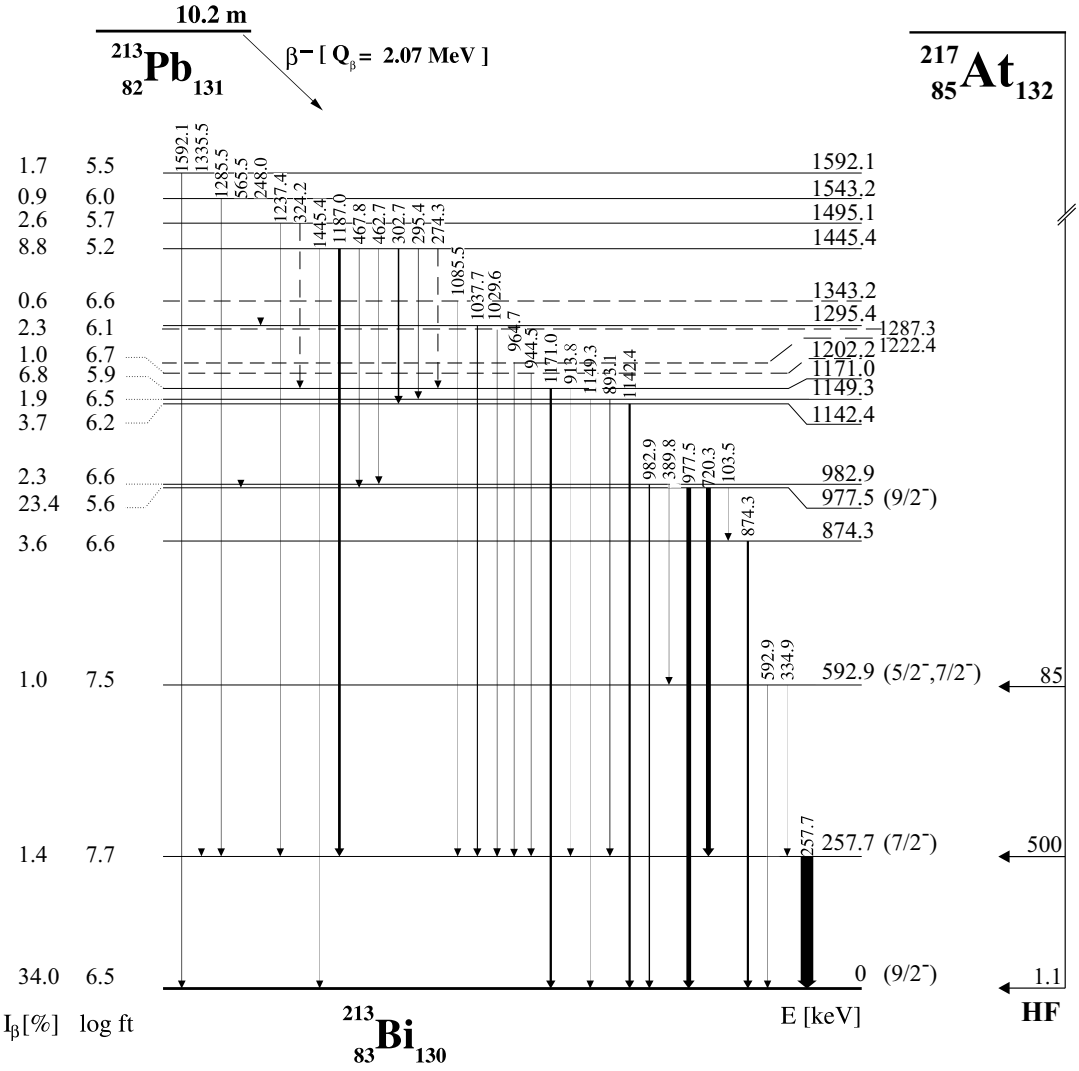

Figure 4.4: Deduced decay scheme of ^{213}Pb. The half-life and Q_β value are taken from literature [Ako92]. The α decay data are taken from [Chu97].

stage, these products are expected to appear in considerable amounts in all spectra. Finally, noble gases like, for instance, radon migrate through the mass separator, finally reaching the implantation station.

Weaker transitions, not observed in the total β-gated γ spectra, within the available statistics, were found in coincidence with the 183.5 keV line and were ascribed to ^{215}Pb on the basis of this coincidence relation and the coincidence with bismuth KX-rays. Figure 4.8 shows the γ-spectrum gated on the 183.5 keV line. The gated spectra are produced with a background correction, accounting for the large Compton

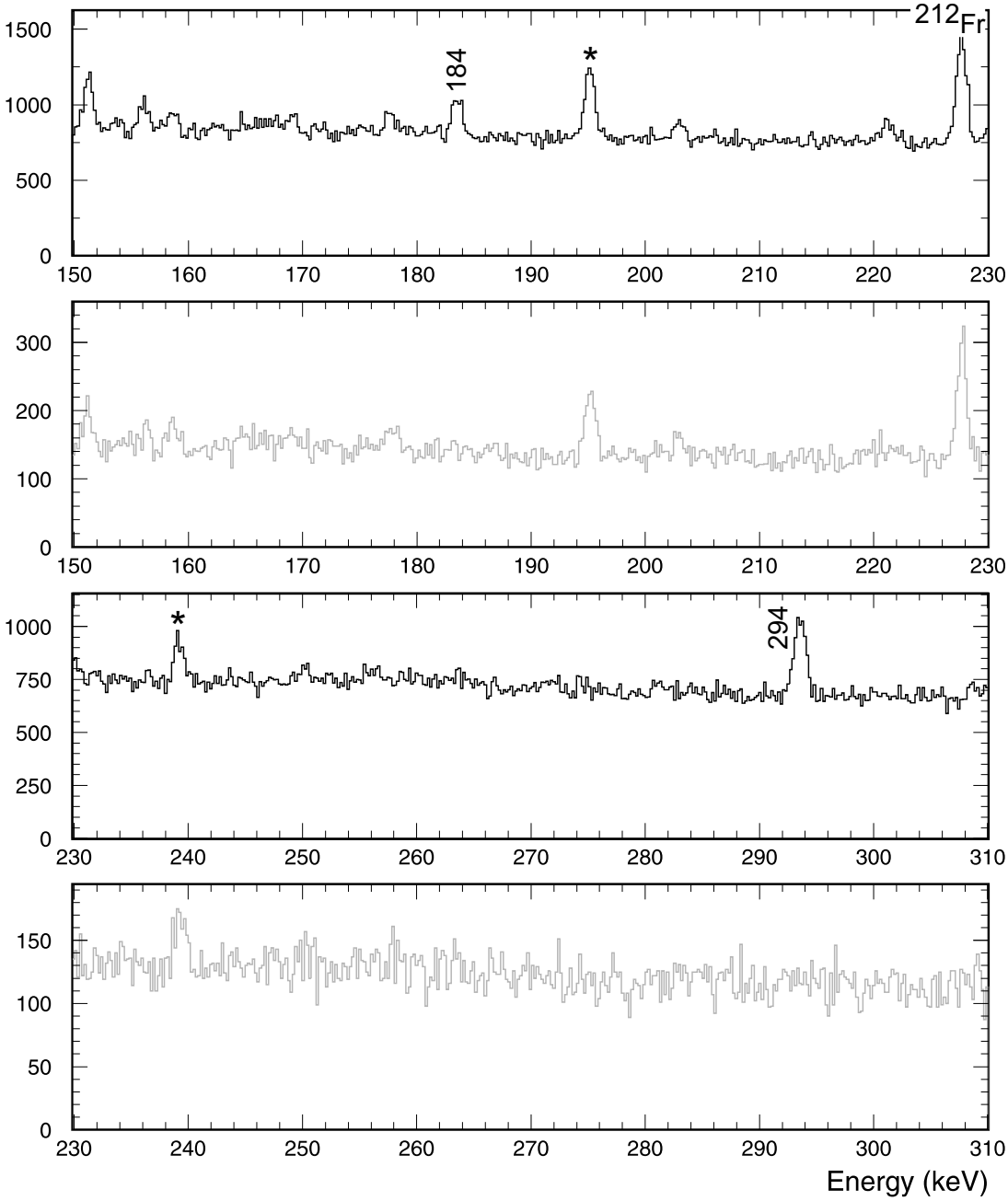

Figure 4.5a: β-gated LEGe spectrum obtained at mass 215. On-resonance, with laser tuned to Pb (black) versus lasers off (gray). Data from run II. Lines marked with $\star$ belong to ^{209}At, present as the daughter of the contaminant ^{213}Fr.

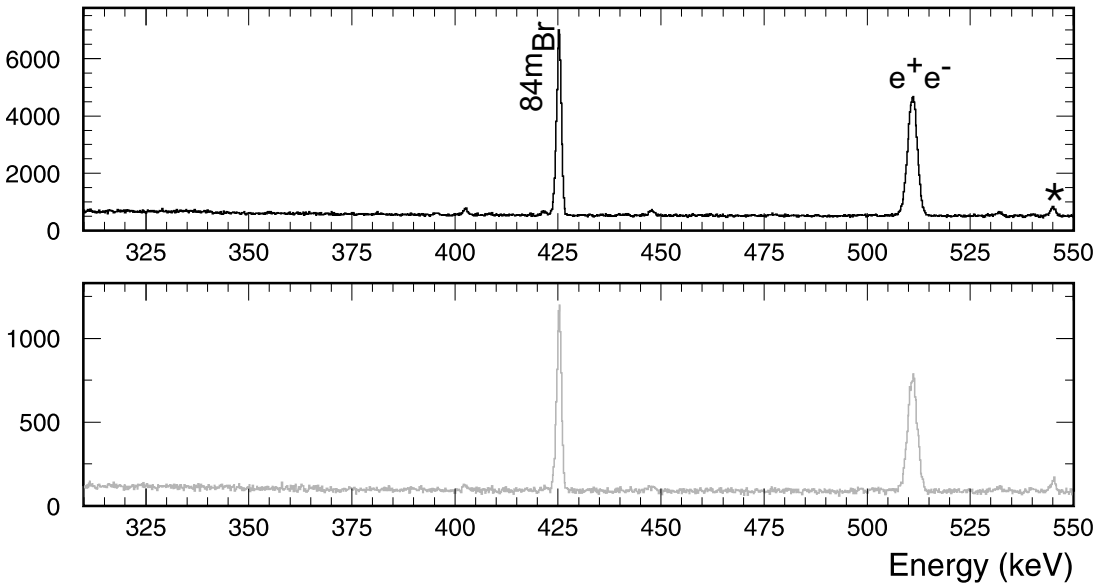

Figure 4.5b: *Continued* β-gated LEGe spectrum obtained at mass 215. On-resonance, with laser tuned to Pb (black) versus lasers off (gray). Data from run II. Lines marked with $\star$ belong to ^{209}At, present as the daughter of the contaminant ^{213}Fr.

background underneath the γ-line. The Compton background of the 511 keV annihilation radiation is particularly prominent and the background subtraction gives rise to an artificial peak at an energy of 511 keV-E_γ, with E_γ the energy used for the gate setting. Energies and relative γ-intensities, not corrected for true summing effects, are listed in Table 4.2. The intensities are corrected for the detection efficiency, using a GEANT simulation [gea], and normalized to the 183.5 keV line. The proposed level scheme is presented in Figure 4.9.

Using the same method as in the ^{213}Bi case, the K-conversion coefficient for the 183.5 keV transition in ^{215}Bi has been deduced. All X-rays (22(9) counts for Kα_2) observed in the spectrum gated on *e.g.* the 985 keV γ-ray have been associated with the 183.5 keV transition (54(10) counts), as the other known γ-transitions have a much lower conversion coefficient. From the comparison of both intensities α_K is determined, after correction for detection efficiency and relative X-ray intensities. From the spectra gated on the 985 keV and 839 keV γ-rays, an average K-conversion coefficient for the 183.5 keV transition of $\alpha_K = 1.4(4)$ was deduced. This value agrees with a predominant M1 character for this transition ($\alpha_{K,theoretical} = 1.88$ for a pure M1 transition).

Figure 4.10 shows the time behaviour of the 183.5 keV γ-ray intensity. The data

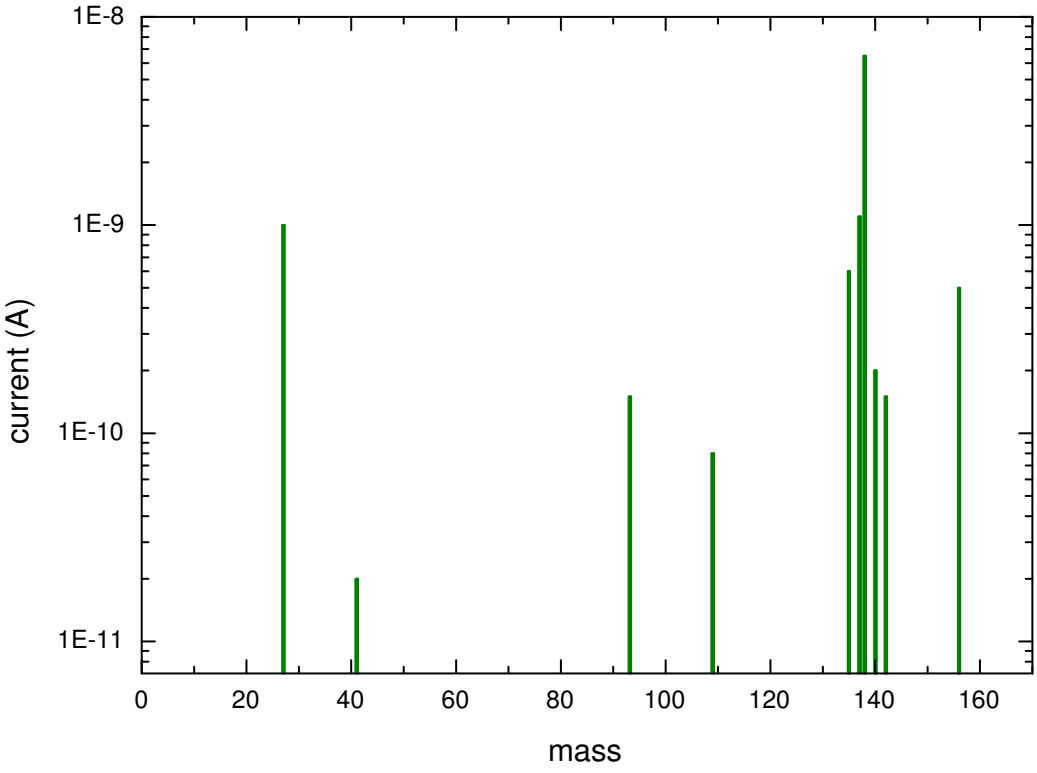

Figure 4.6: Off-line mass scan for the target unit used in run II: the peaks around mass 140 reflect the presence of barium contaminations in the target container.

Table 4.2: Energies, relative intensities, normalized to the strongest γ-ray, and coincidence relations for the γ-transitions following the ^{215}Pb β decay.

Energy [keV]	I_γ [%]	Coincident γ-lines
183.5(3)	100(19)	671, 760, 839, 985, 1016, 1327
671(1)	14(5)	Bi Kα_2, 184
760(1)	12(5)	Bi Kα_2, 184, 1016, 1200
839(1)	21(7)	Bi Kα_2, 184
985(1)	24(8)	Bi Kα_2, 184
1016(1)	14(5)	184, 760
1200(1)	17(11)	760
1327(1)	17(6)	184

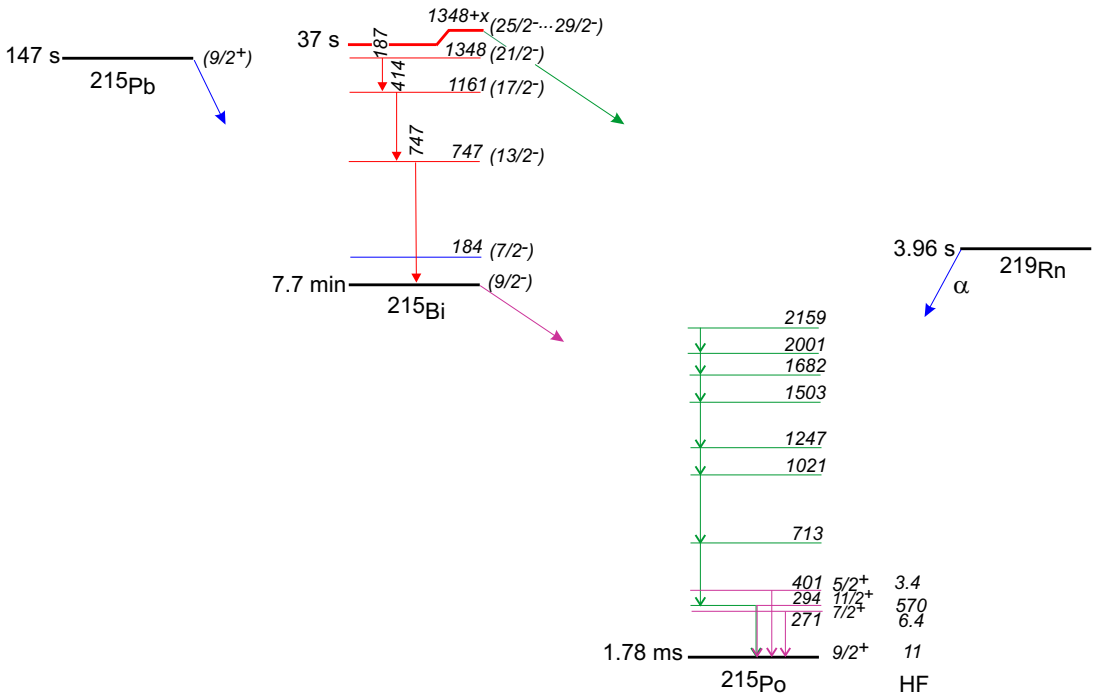

Figure 4.7: Decay scheme for ^{215}Pb, ^{215}Bi, ^{215}Po. Data on ^{215m}Bi and ^{215}Po are from [Kur03b].

were fitted using a single component exponential function, both in multiscaling mode and in list-mode. A weighted average for the half-life was determined to be 147(12) s.

Under the assumption of $I^{\pi} = 9/2^{+}$ for the ground state of the mother, determined by the odd neutron in the $\nu g_{9/2}$-orbit, and $I^{\pi} = 9/2^{-}$ for the ground state of the daughter, with the additional proton occupying the $\pi h_{9/2}$-orbit, considerable β-feeding to the ground state is expected. The details of the calculation of the ground state feeding are outlined below.

First the absolute branching ratio of the 293.5 keV line in the ^{215g}Bi decay is determined by comparing its γ-intensity to the 7386.1(8) keV α-intensity of the ^{215}Po α decay. These data were obtained in run IV. Figure 4.11 shows the corresponding α- and γ-spectra obtained with the resonant tuning of the RILIS to bismuth. The 293.5 keV intensity was corrected for the contribution of the ^{215m}Bi β decay, calculated through the observed intensity of the 187-414-747 keV cascade.

This procedure, however, requires a reliable efficiency calibration of the γ-detector relative to the α-detector. This relative efficiency calibration was performed by comparing the 100% 2^{+}-0^{+} γ-transition in the ^{216}Bi β decay [Kur00] to the ^{216}Po α-intensity

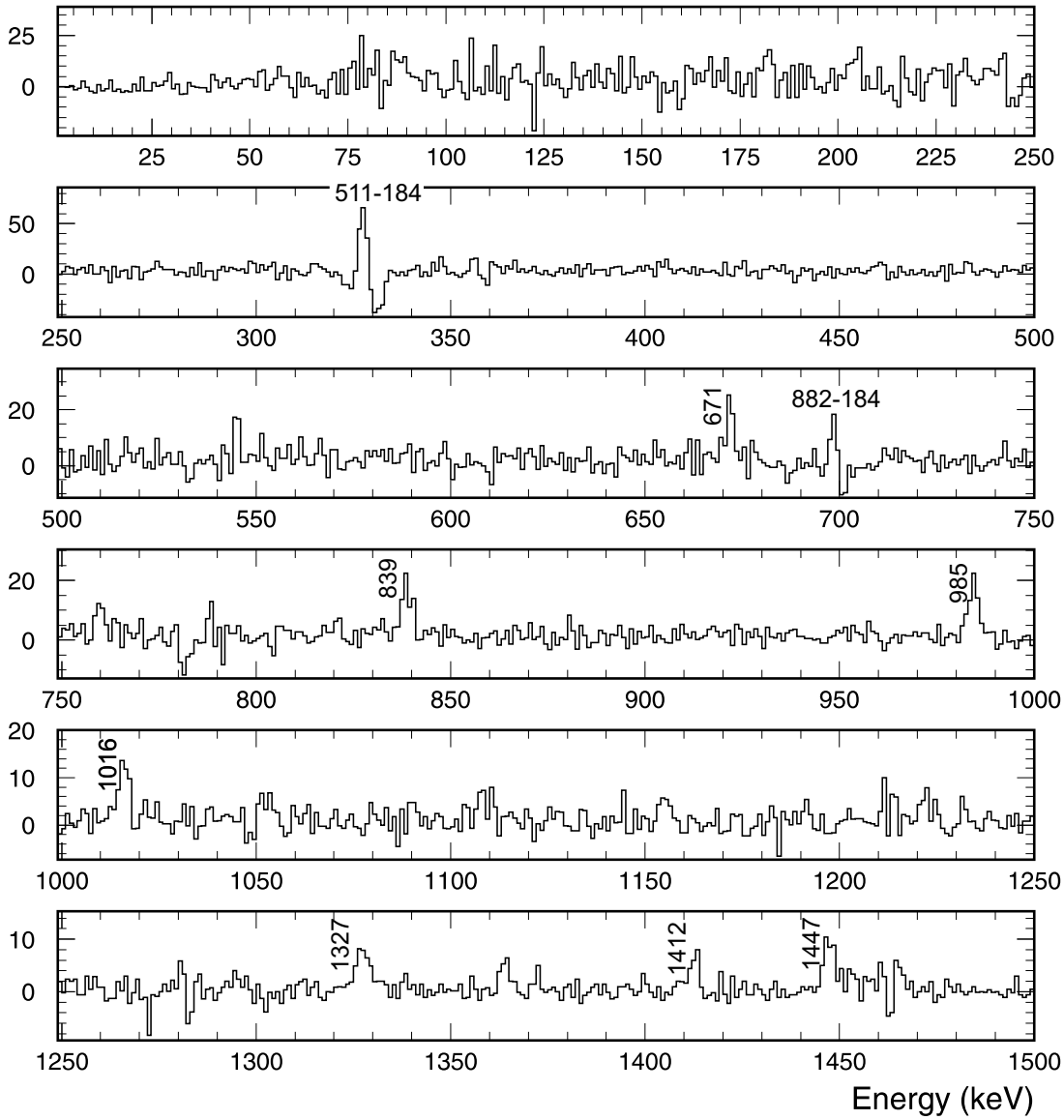

Figure 4.8: Background subtracted coincidence spectrum: 70%+75% HPGe spectra, gated on the 183.5 keV transition of the ^{215}Pb β decay in the LEGe spectrum. Energy labels are in keV.

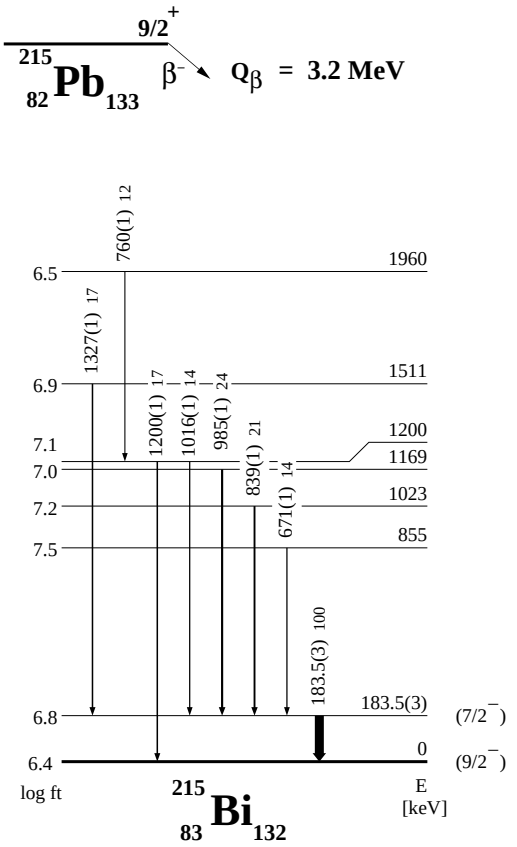

Figure 4.9: Decay scheme of the β decay of ^{215}Pb. Q_β value taken from [Moe97].

(E_α=6778.3(5) keV, I_α= 99.9981(3) %), after correction for the ^{213}Fr contamination overlapping the ^{216}Po α-line ($E_\alpha(^{213}Fr)$=6775.0(17) keV). The energy dependence of the γ-detector efficiency resulted from a GEANT simulation.

Finally, the intensity of the γ-ray at 183.5 keV, originating from the ^{215}Pb β decay, is compared to the 293.5 keV line. Corrections were made for the difference in half-life and γ detection efficiency. These data were obtained with the RILIS tuned to resonantly ionize lead (run II). Assuming pure M1 character for both the 183.5 keV and 293.5 keV lines [Kur03b], we obtain feedings of $\leq$ 67(5) % and $\leq$ 12(8) % to the ^{215}Bi and ^{215}Po ground states, respectively. These values represent only upper limits for the ground state feeding, because of possibly unobserved γ-rays feeding the ground state.

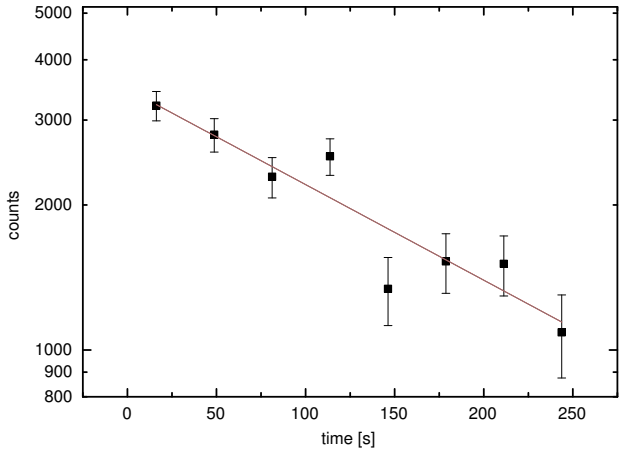

Figure 4.10: Time behaviour of the intensity of the 183.5 keV line in the eight consecutive bins of the multiscaling mode. Data from LEGe detector in run II.

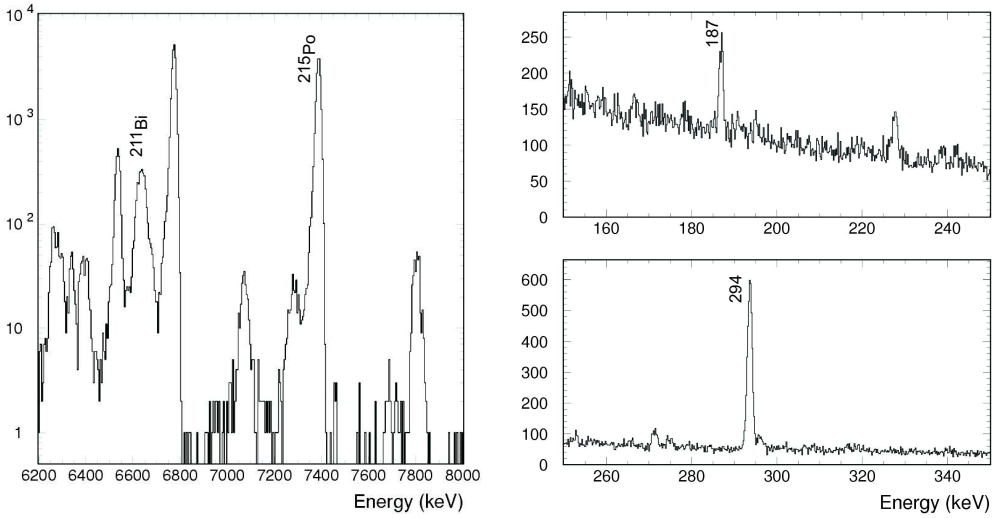

Figure 4.11: Left: Alpha spectrum obtained at mass 215 during 235.2 s at the decay position with resonant laser ionization of bismuth. Right: LEGe spectrum under the same conditions. Data from run IV.

4.4 Systematics of the odd-A Pb-Bi-Po isotopes

We start this discussion with the mass A=209 chain closest to the ^{208}Pb doubly magic nucleus. In an extreme single-particle approach, the proton in the $1h_{9/2}$ orbital is expected to determine the ground state of the closed shell nucleus ^{209}Bi, while the

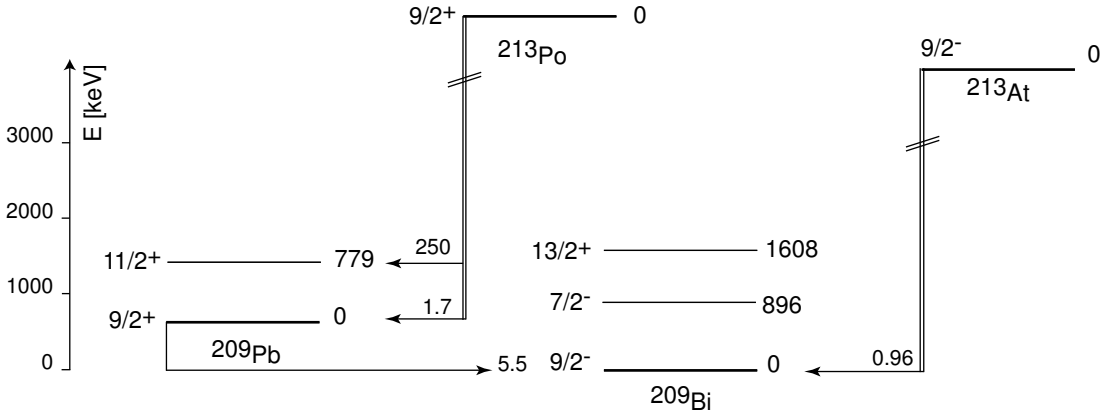

Figure 4.12a: Systematics of the odd-A lead-bismuth-polonium isotopes: mass 209. For the β decay the logft values are given; for α decay the hindrance factor. Data from [Fir96]. The energy scale to the left is relative to the ground state of ^{209}Bi.

ground state in ^{209}Pb is a $\nu 2g_{9/2}$ state. 100% β-feeding to the ground state of ^{209}Bi, corresponding to the $\nu 2g_{9/2}$ - $\pi 1h_{9/2}$ first forbidden transition is observed with a logft of 5.5. The α decay hindrance factor for the $^{213}_{85}$At ground state to ground state decay is 0.96, consistent with a $\pi(1h_{9/2})^3\nu(2g_{9/2})^2 \; - \; \pi(h_{9/2})^1\nu(g_{9/2})^0$ transition.

The same spin and parity assignments are kept for the heavier odd-A lead and bismuth isotopes. The direct β feeding of the Bi ground state decreases to 91.3% [Mai89], $\leq$ 34% and $\leq$ 67% in ^{211}Bi, ^{213}Bi and ^{215}Bi, respectively, or in terms of logft values an increase to 6.0, $\geq$ 6.5 and $\geq$ 6.4 is observed. A summarizing picture is shown in Fig 4.12*a-d*.

The first excited state in ^{209}Bi is associated with a proton excitation to the $2f_{7/2}$ orbital. The low Q_β value does not allow to populate this level. In the β decay of ^{211}Pb, the $7/2^-$ level is fed with a logft of 7.2 and with a hindrance factor of 440 in the α decay of ^{215}At, confirming the configuration change. Feeding with low logft value instead, occurs to $9/2^-$ levels at 832.0 keV (logft = 5.7) and 1109.5 keV (logft = 5.6).

The picture in ^{213}Bi is highly similar. The α decay from the $9/2^-$ ground state of ^{217}At feeds the ground state with HF = 1.1, while a hindrance factor of 500 to the level at 258 keV is deduced. On the basis of systematics, we tentatively assign the 258 keV level a $7/2^-$ spin and parity, corresponding to a $\pi(f_{7/2})^1\nu(g_{9/2})^4$ configuration. This assignment is also consistent with the predominantly M1 character of the 257.7 keV deexciting γ-ray. Close to the energy of the first excited state of the

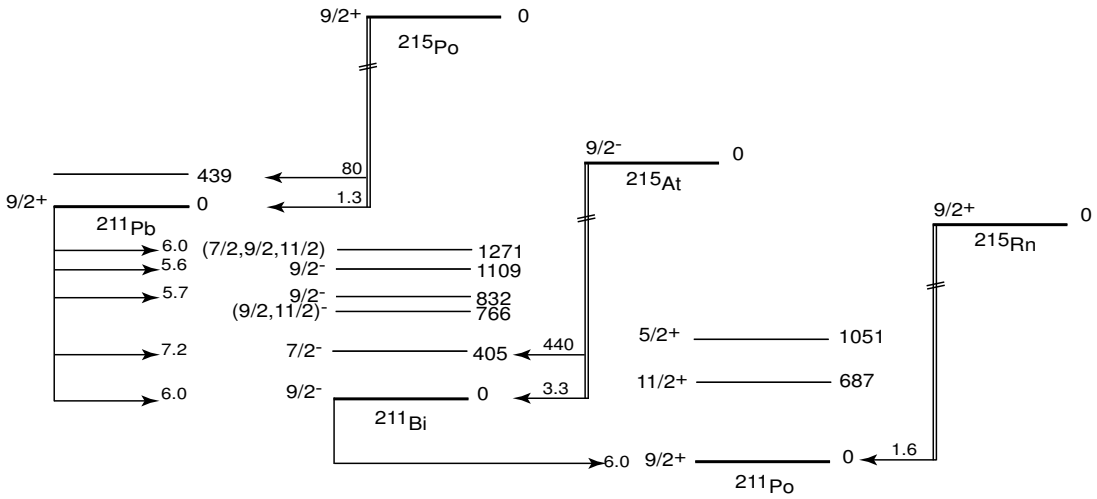

Figure 4.12b: Systematics of the odd-A lead-bismuth-polonium isotopes: mass 211. Data from [Fir96].

even-even neighbour ^{212}Pb, E(2^+ = 804 keV), we expect a multiplet corresponding to the $\pi h_{9/2} \otimes {}^{212}$Pb configuration, with spins $5/2^- \cdots 13/2^-$. The logft value of only 5.6 towards the 978 keV level, suggests a tentative $9/2^-$ assignment for this state. The logft = 7.5 towards the 593 keV line, along with the tentative M1 assignment for the 335 keV γ-line [Chu97] favours a $(5/2,7/2)^-$ assignment. For the other states no spin or parity assignments are given.
The decay scheme of ^{215}Pb is considered too incomplete to draw firm conclusions. However, it seems that the ground state and the first excited state (at 184 keV) are similar to those of the lighter bismuth isotopes.

The observed redistribution of the β strength in the odd-A lead isotopes could possibly be attributed to an admixture of $\nu 1i_{11/2}$ neutron pairs in the lead ground state when filling the $\nu g_{9/2}$ orbital. These admixtures imply the opening of different β decay channels. Such an effect is expected from pair scattering and is also present in shell model calculations for the N=126 isotones [Cau03], where a retarded filling of the $\pi h_{9/2}$ orbital is predicted, due to pair scattering in the $f_{7/2}$ and $i_{13/2}$ orbitals .

A similar evolution of the β feeding pattern is observed for the doubly closed shell at ^{132}Sn. Although more neutrons that can undergo β decay become available, the logft value for the $\nu 2f_{7/2}$ - $\pi 1g_{7/2}$ ground state to ground state transition increases between ^{133}Sn and ^{135}Sn [She02]. Not only neutron pair scattering is suggested but also an increased admixture of the proton $1g_{7/2}$ in the excited states of ^{135}Sb is evoked.

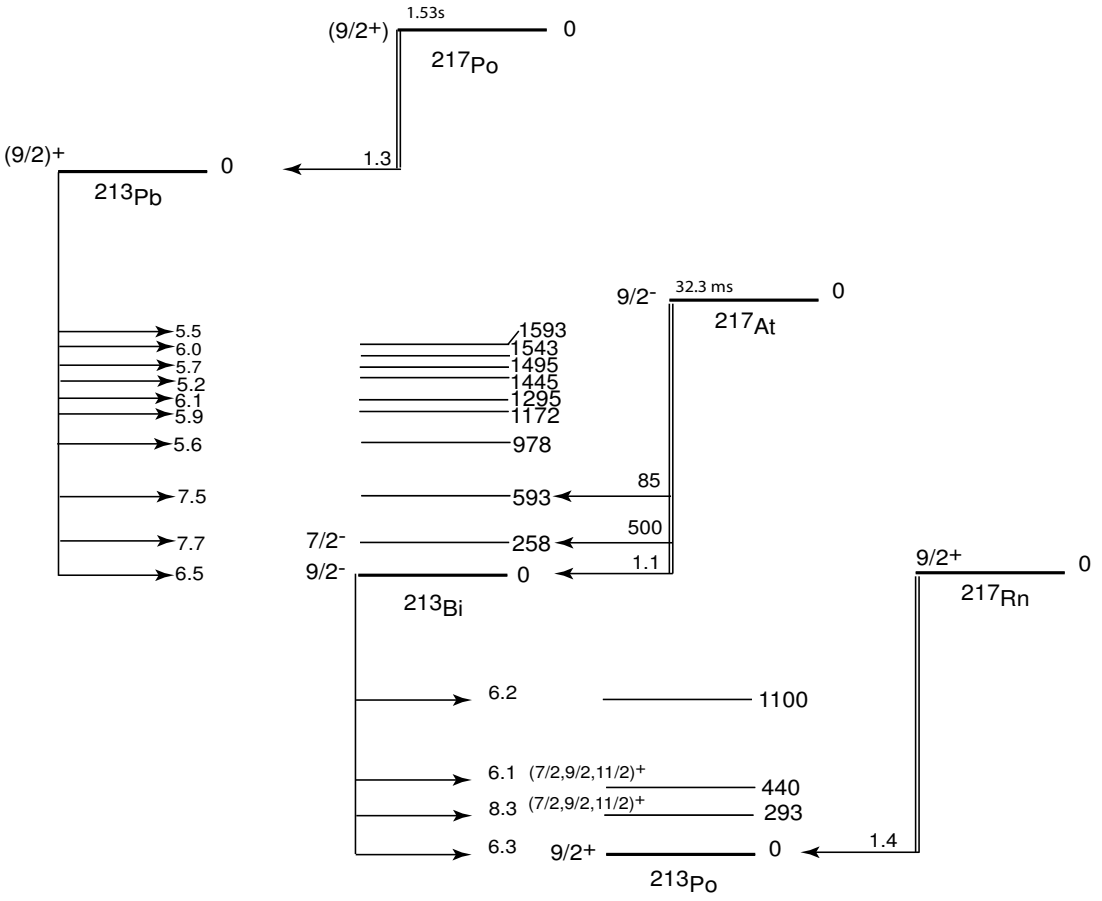

Figure 4.12c: Systematics of the odd-A lead-bismuth-polonium isotopes: mass 213. Data from [Fir96, Chu97] and from this work.

.

As in the β decay of the lead isotopes, the $\log ft$ for direct feeding to the ground state of the odd-A polonium isotopes is increasing from 6.0 in the ^{211}Bi decay to 6.3 and 7.0 for ^{213}Bi and ^{215}Bi, respectively. A $11/2^+$ level at 687 keV in ^{211}Po, associated with the $(\pi 1h_{9/2})^2$ $(\nu 1i_{11/2})$ configuration, is identified in the ^{210}Po(d,p) reaction [Bha79], but is has not been observed in ^{211}Bi decay. While in ^{213}Po spin assignments are lacking, in ^{215}Po a candidate for the $(\pi 1h_{9/2})^2$ $(\nu 2g_{9/2})^4$ $(\nu 1i_{11/2})$ configuration is found at 294 keV. The assignment is based on the high α decay hindrance factor [Lia99], compared to the hindrance factor of the $(\pi 1h_{9/2})^2(\nu 2g_{9/2})^5$ multiplet. The $\log ft$ value of 6.0 can again be understood as an increased contribution of $\nu 1i_{11/2}$ pairs in the ^{215}Bi ground state.

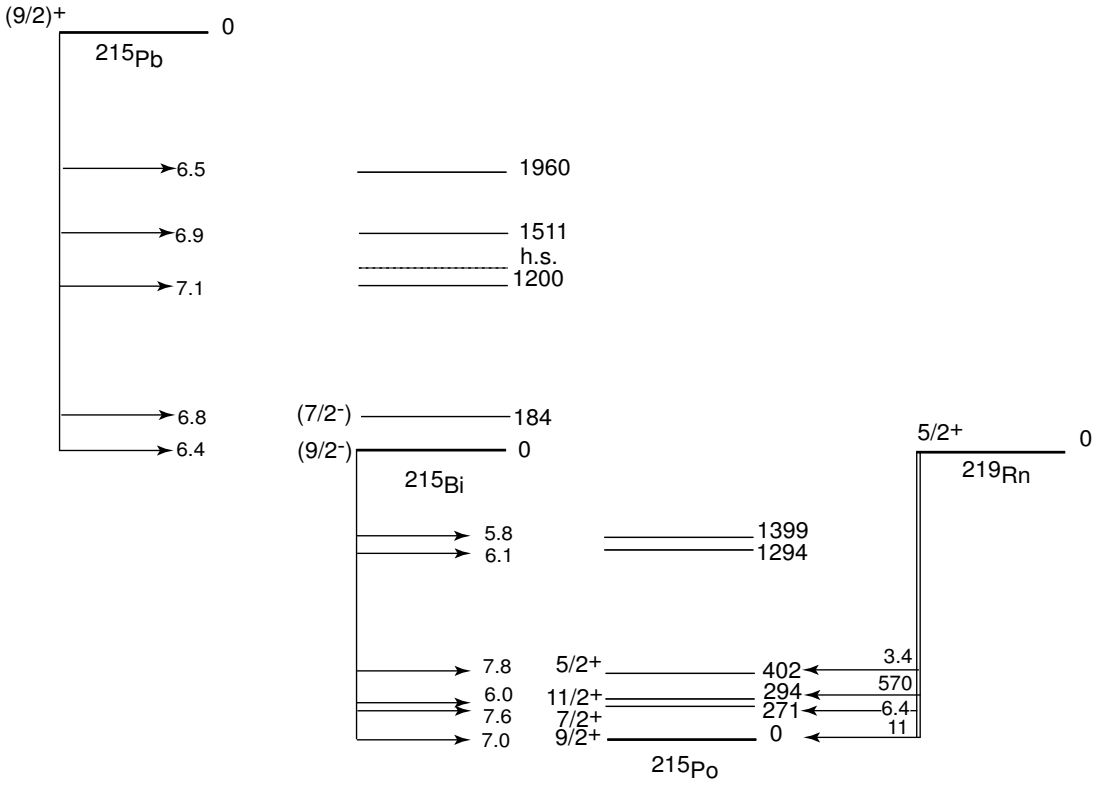

Figure 4.12d: Systematics of the odd-A lead-bismuth-polonium isotopes: mass 215. *h.s.* refers to the β decaying high-spin state in ^{215}Bi [Kur03b]. Data from [Lia99, Kur03b] and from this work.

.

4.5 Monopole migration in the nuclear shell model

For the semi-magic nucleus ^{209}Bi, the level scheme reflects the single particle levels, occupied by the 83$^{\text{rd}}$ proton, coupled to the ^{208}Pb core. The corresponding single-particle energies were given in Fig. 1.2. The most remarkable feature of the results on the odd-A bismuth isotopes is the steady decrease of the first excited state. Figure 4.13 presents the energy of the first excited state, relative to the $9/2^-$ ground state.

While the first excited state in the odd-mass Bi isotopes stays relatively constant at the neutron deficient side, its energy drops steeply when neutrons are being added beyond N = 126. A similar feature has been observed at different magic shell closures. In the odd-A copper isotopes (Z=29), the proton single-particle orbitals filled above Z = 28 are $2p_{3/2}$, $1f_{5/2}$, $2p_{1/2}$ and $1g_{9/2}$. The corresponding $5/2^-$ state, for instance, approaches the $3/2^-$ ground state at A > 69 [Fra01], when the $\nu 1g_{9/2}$ orbital is being

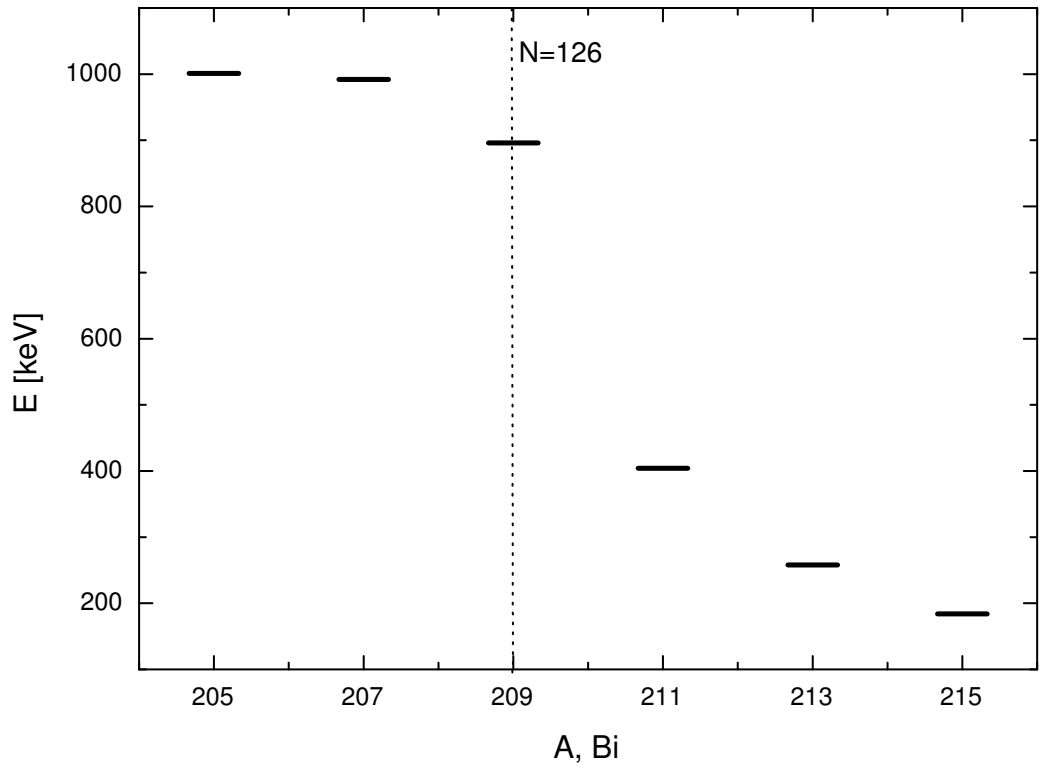

Figure 4.13: Energy systematics for the first excited state in the odd-A bismuth isotopes.

filled. This behaviour is shown on the left side of Fig. 4.14 and is discussed extensively in [Smi04], in a nuclear shell model context.
In the antimony isotopes (Z=51), shown on the right side of Fig. 4.14, the $d_{5/2}$ single particle level is found at 963 keV in ^{133}Sb, while in ^{135}Sb the $5/2^+$ state is observed at only 282 keV above the $7/2^+$ ground state. This state could be reproduced theoretically, only after the $d_{5/2}$ single particle energy was lowered by 300 keV [She02].

In the shell model this behaviour is explained as an effect of the proton-neutron interaction, and more precisely of its monopole component, whence the designation of *monopole migration*. According to [Gra04, Ots01b], the interaction is particularly strong for proton-neutron spin-orbit partners ($\Delta\ell$=0, S=0) and for (Δj=2, $\Delta\ell$=1, S=0) proton-neutron pairs. In addition, an identical number of nodes in the radial wave functions is required for large radial overlap. The orbitals that occur at low energy in the present odd-A bismuth isotopic series, namely $1\pi h_{9/2}$, $2\pi f_{7/2}$, $2\nu g_{9/2}$ and $1\nu i_{11/2}$, do not satisfy these conditions, except for the radial quantum number of

$2\pi f_{7/2}$-$2\nu g_{9/2}$ and $1\pi h_{9/2}$-$1\nu i_{11/2}$. Below, we present the basic formalism accounting quantitatively for the energy shift, as elaborated in [Smi04].

In the presence of the proton-neutron interaction, the effective single particle energy $\widetilde{\epsilon}_j$ is written as:

$$\widetilde{\epsilon}_j = \epsilon_j + \sum_{j_\nu} E_{j_\pi j_\nu}(2j_\nu + 1)v^2_{j_\nu}, \tag{4.1}$$

i.e., the sum of the bare single particle energy and the average proton-neutron interaction energy. $v^2_{j_\nu}$ is the occupation probability in the BCS model for the available neutron orbitals and $E_{j_\pi j_\nu}$ is the average matrix element, given by:

$$E_{j_\pi j_\nu} = \frac{\sum_J (2J+1)\langle j_\pi j_\nu; J|V|j_\pi j_\nu; J\rangle}{\sum_J 2J+1}, \tag{4.2}$$

where V is the two-body potential and J are the possible total angular momentum values.

We remark, however, that Eq. 4.1 represents the centroid of a specific orbital, rather than the energy of the yrast state. Only if this state exhausts the full single particle strength, both quantities are equal. The first excited $7/2^-$ takes part of the $\pi f_{7/2}$ strength, but admixtures of a $\pi h_{9/2}\ \nu g^2_{9/2}$ three-quasi particle state are expected. The experimental centroids are given by:

$$E(nlj) = \frac{\sum_k S^k_{nlj} E^k_{nlj}}{\sum_k S^k_{nlj}}, \tag{4.3}$$

with S^k_{nlj} the spectroscopic factor. Unfortunately, knowledge of the spectroscopic factor is often missing.
In order to reproduce the energy of the lowest-lying states in the shell model, a full diagonalization is required. Calculations will be performed by A. De Maesschalck and N.A. Smirnova (Universiteit Gent).

4.6 Beta decay of ^{218}Bi

4.6.1 Level scheme and half-life

The β decay of ^{218}Bi was observed for the first time during run II, where the use of the RILIS facilitated the identification. The ^{218}Bi isotope was produced earlier at

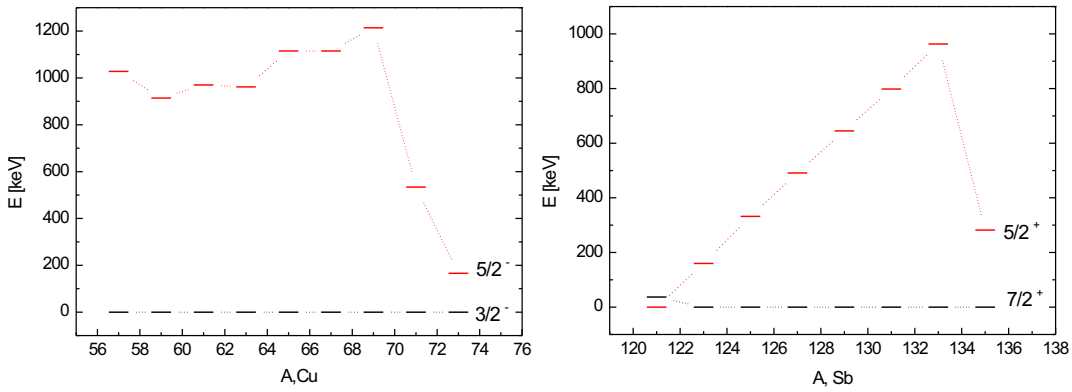

Figure 4.14: Monopole migration in the Cu (Z=29) isotopes (data taken from [Fra01]) and Sb (Z=51) isotopes (data taken from [She02]).

GSI in a projectile fragmentation reaction, but no spectroscopic information was obtained [Pfu98].
A 510(2) keV γ-ray was observed in the α decay of ^{222}Rn and associated with the 2^+-0^+ transition in the daughter ^{218}Po [Mad56].

The assignment of γ-rays to the decay of ^{218}Bi is very similar to the procedure used for the analysis of ^{215}Pb. Comparison of the β-gated γ spectra collected with and without laser irradiation of the ion source allowed to identify unambiguously the γ deexcitation pattern. As a general rule, a line was considered to be resonant whenever the difference of the peak integrals in lasers on and off spectra was larger than 3σ, σ being the standard deviation. The spectra are shown in Fig. 4.15. The measurement times with and without laser irradiation were 325 and 9 min, respectively.
The four strong γ-ray transitions at 263.0 keV, 385.7 keV, 425.5 keV and 509.7 keV are produced resonantly and their mutual coincidence relations allow to place them in a cascade. From the spectra gated on these transitions, weaker γ-lines populating the two upper levels of the cascade are identified, similar to the observations in ^{216}Bi [Kur00]. Figure 4.17 presents the gated spectrum, including background subtraction. In as far as the statistics allowed, it was cross-checked that the newly found lines were coincident with atomic polonium X-rays. A γ-γ coincidence matrix was constructed, the relations of which are printed in Table 4.3, along with the energies and the relative intensities of the γ rays. These intensities were divided by the efficiency of the detector set-up, determined by means of GEANT simulations (see App. B). Since the 509.8 keV line overlapped with the annihilation peak and the 425.5 keV line was corrupted by the ^{84m}Br contamination (see Sect. 4.3), normalization was performed

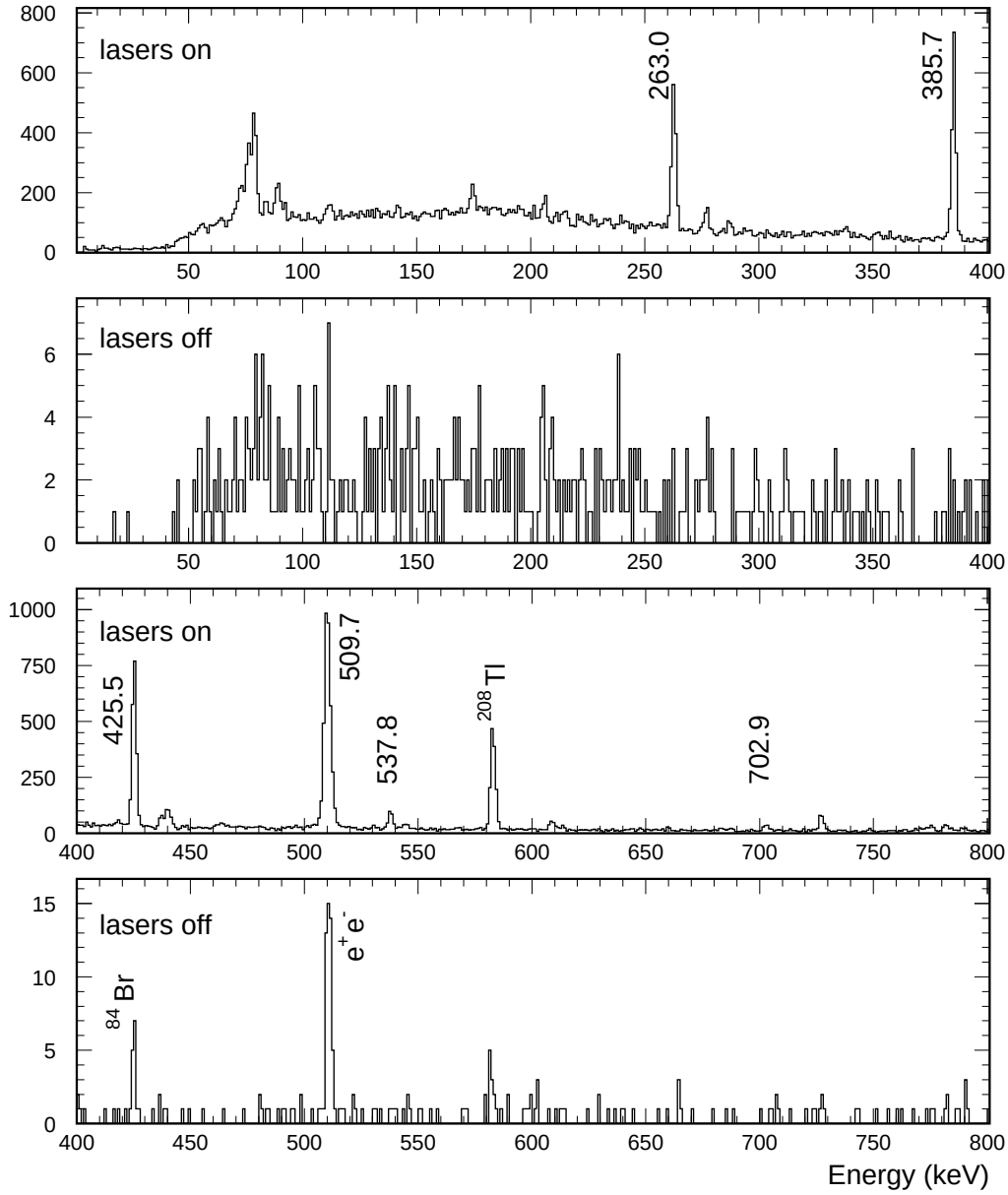

Figure 4.15: β-gated γ spectra (70%+75% HPGe) obtained at mass 218, on-resonance (lasers tuned to bismuth, upper spectrum) versus lasers off (lower spectrum). Energies are given in keV.

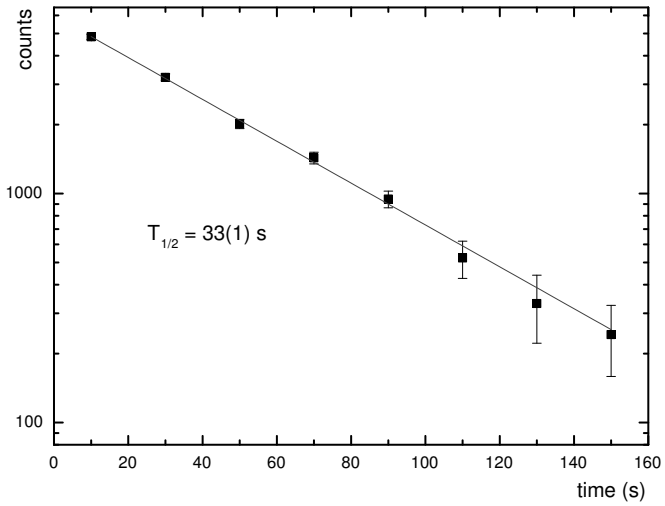

Figure 4.16: Half-life determination of ^{218}Bi. Intensity of the 263.0 keV and 385.7 keV γ-lines in the 75% and 70% HPGe detectors. The solid line shows the result of a single exponential fit.

with respect to the 385.7 keV γ-ray.

An exponential fit of the time behaviour of the 385.7 and 263.0 keV γ lines yielded a half-life of 33(1) s. The transitions at 425.5 and 509.8 keV could not be used, as they were contaminated by ^{84m}Br activity and annihilation radiation, respectively. For these transitions a two-component fit was performed, accounting for the known half-life of the contaminant. The resulting half-lives were consistent with the adopted $T_{1/2}$ value: 36(4) s and 41(7) s for the 425.5 keV and 509.7 keV lines, respectively. This corroborates the assignment of these contaminated lines to the ^{218}Bi decay scheme.

For the remaining γ-rays the half-life was also determined, if statistics allowed. They were shown to be consistent, albeit systematically somewhat longer, due to underlying Compton events from the contaminations, which were never completely removed in the background subtraction. For the 176.6 keV, 287.1 keV and 418.3 keV lines no half-lives could be extracted and their assignment is based completely on the coincidence relations, including coincidences with polonium X-rays for the 418.3 keV line.

The ordering of the transition in the cascade was based on their relative intensities and the known 2^+-0^+ transition energy (see above). On the basis of systematics and generalized seniority arguments, the three remaining lines are placed on top of each other in decreasing energy order.

Table 4.3: Gamma-ray energies E, coincidence relations, and relative intensities I_γ of γ rays assigned to the decay of ^{218}Bi

Energy [keV]	I_γ [%]	Coincident γ-lines
174.5(9)	<2.2	263.0, 385.7, 425.5, 509.7
176.6(9)	<1.3	263.0, 385.7, 425.5, 509.7
263.0(1)	59(16)	174.5, 176.6, 287.1, 385.7, 418.3, 425.5, 463.5, 509.7, 702.9
287.1(2)	<2.7	176.6, 263.0, 385.7, 425.5, 509.7
385.7(1)	100.0	174.5, 263.0, 287.1, 418.3, 425.5, 437.0, 463.5, 509.7, 537.8, 702.9
418.3(5)	6(2)	263.0, 425.5, 509.7
425.5(1)	95(27)	174.5, 176.6, 263.0, 287.1, 385.7, 437.0, 463.5, 509.7, 537.8
437.0(2)	4(2)	385.7, 425.5, 509.7
463.5(6)	6(2)	385.7, 425.5, 509.7
509.7(1)	134(42)	174.5, 176.6, 263.0, 287.1, 385.7, 425.5, 437.0, 463.5, 537.8
537.8(1)	12(3)	385.7, 425.5, 509.7
702.9(3)	7(3)	263.0, 385.7, 509.7

We remark that the cross-over transitions at 437.0 keV (263.0+174.5 keV) and 463.5 keV (287.1+176.6 keV) do not result from true summing, as their intensities are much higher than the 174.5 keV and 176.6 keV intensities.

The level scheme is depicted in Fig. 4.18. Within the error bars, the intensity of the 425.5 keV line is equal to that of the 385.7 keV transition. Hence, there is no direct β feeding to the level at 935.2 keV. The observed feeding pattern to the higher-lying 6^+ and 8^+ states, together with the absence of β decay to the 935.2 keV 4^+ level, renders feeding to the 2^+ level at 509.7 keV unlikely. The large uncertainty in the intensity de-exciting this state, due to the contamination of the peak, is consistent with this assessment. Theoretical E2 conversion coefficients were used for the four γ transitions in the $8^+ \rightarrow 0^+$ cascade to determine the β feeding to the remaining levels and calculate the $\log ft$ values.

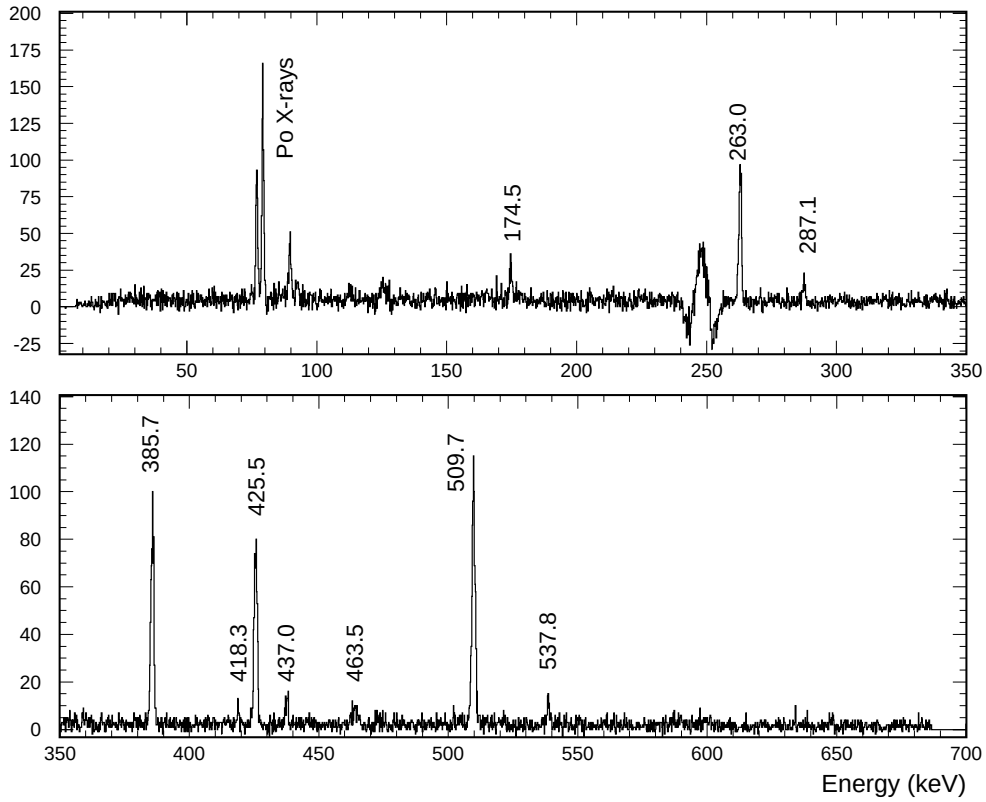

Figure 4.17: Background subtracted coincidence γ spectra of LEGe detector with gate on the 263.0 keV, 385.7 keV and 425.5 keV γ-lines (in 70%+75% HPGe). Energies are given in keV.

Taking into account a transmission ratio from the focal plane of the separator to the detector set-up of 85(2)%, the simulated efficiency of the set-up, and adopting a branching ratio of 100 % for the 425.5 keV ray, the production rate of ^{218}Bi was determined at 44(8) at/μC. This number includes a correction for γ summing, conversion, the fraction of the activity removed by the tape before having decayed, and the fraction not released from the ion source due to the period of 20 ms the separator is closed after impact of the proton beam, as explained above.

4.6.2 Half-life calculation of ^{218}Bi and neighbouring nuclei.

The measurement of β decay half-lives in the $N = 126$ region is an important test for global nuclear structure calculations used for nucleosynthesis modelling. For most

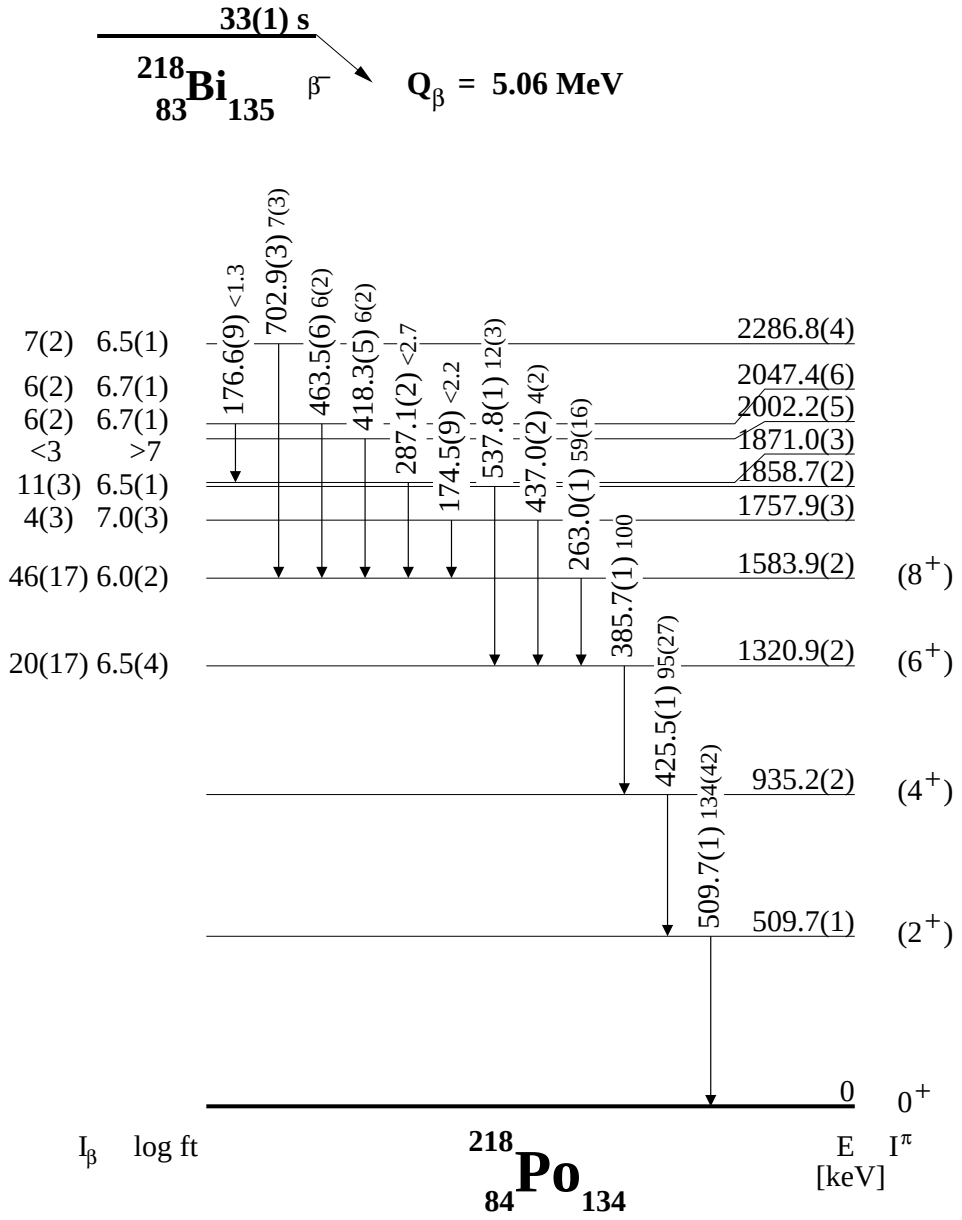

Figure 4.18: Proposed level scheme of ^{218}Po. The log ft values are lower limits as γ rays from higher levels can have escaped detection. The Q-value is taken from [Moe95].

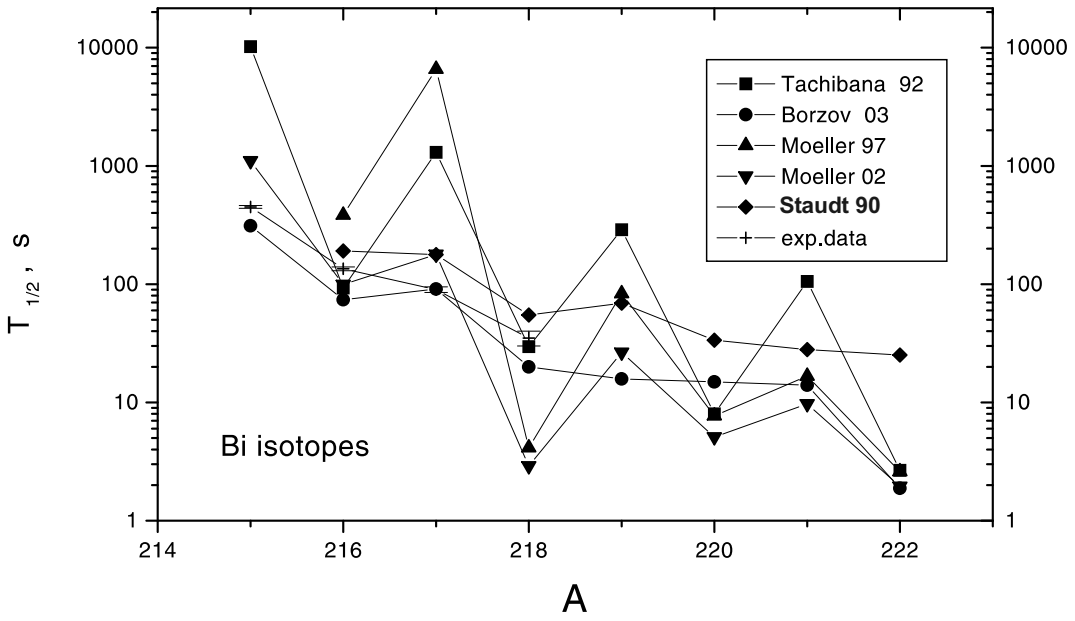

Figure 4.19: Beta-decay half-lives of bismuth isotopes predicted by different models [Moe97, Bor03, Sta90, Tac90] and compared with experimental data taken from [Ruc90, Kur00, Kur03a] and the present measurements.

of the nuclei involved in the r-process, any experimental information is missing and the astrophysical calculations have to rely on extrapolated ground state and decay properties. Beta decay half-lives define the time scale of the r-process and the relative r-process abundances [Lan03]. However, near the r-process paths from $Z \approx 60$ to $Z \approx 90$ and $N = 126$, the various global models encounter difficulties as not only the Gamow-Teller (GT), but also the first-forbidden (FF) decays are expected to play a role [Bor03]. The self-consistent treatments of β decay half-lives are of special interest, as they are more reliably extrapolated to regions far from stability and carry the advantage that the predictions of β decay rates are based on the same ground-state description as that to calculate the nuclear masses.

Our results are compared to the theoretical values calculated by I. Borzov, taking into account both allowed and first-forbidden decays [Bor03]. This model is based on the self-consistent description of ground states in the framework of the energy-density functional theory. The β decay strength functions are calculated in the continuum QRPA-like framework of the finite Fermi-system theory (FFS).

In Fig. 4.19 we compare the experimental half-lives of $^{215-217}$Bi [Ruc90, Kur00, Kur03a], together with the value for ^{218}Bi, with the predictions from the global approaches for $^{215-222}$Bi [Moe97, Bor03, Sta90, Tac90]. The total half-lives of the GT decay calculated within the FRDM + RPA model [Moe97] over- or underestimate the experimental half-lives sometimes by an order of magnitude; the scale of the predicted odd-even effects is generally too large. In the recent micro-statistical version of the FRDM model [Moe02], the gross-theory calculation of the FF decay is combined with the FRDM + RPA description of the GT decay. This model provides shorter total half-lives than the ones calculated for the GT decay in [Moe97]. However, the deviation for ^{218}Bi remains large.
Staudt *et al.* calculate the half-lives in the microscopic QRPA approach, using a Nilsson potential and including a residual Gamow-Teller interaction [Sta90]. Its strength is directly fitted to the experimentally known half-lives for every isotopic chain, which is a purely empirical procedure. On the other hand, as the odd-even behaviour of the calculated half-lives is reasonable, having included the $T = 0$ pairing, such a procedure may in some cases give a sound extrapolation to the closest experimentally unknown nuclei. However, as the FF transitions are not included, it is clear that the experimental half-lives of the bismuth isotopes will be overestimated.
The Gross Theory statistical calculations [Tac90] average over the β-strength distribution in the daughter nucleus. Forbidden transitions are included in a parametric description. The results display a large odd-even effect not observed experimentally.
The calculated half-lives from [Bor03] show a fairly regular A behaviour for $^{218-221}$Bi, whereas a shorter half-life of 1.8 s is predicted for ^{222}Bi. The good agreement with the experimental data, along with the microscopic basis of this calculation, gives confidence in its predictive power further away from stability.

4.7 The ground state spin of the odd-odd bismuth isotopes

In the simplest shell-model configuration for ^{218}Bi the last proton resides in the $1h_{9/2}$ orbital and the last neutron in $2g_{9/2}$, giving spin and parity 0^- to 9^-. In a simplified approach, the relative energy splitting of this multiplet follows a parabolic rule in I(I+1), as discussed by Paar [Paa79]. The results are illustrated in Fig. 4.20 for $^{212-218}$Bi. The shape varies from upward bend when the $\nu g_{9/2}$ orbital is less than half-filled, to downward bend in the second half of the shell, assuming a gradual filling of the $\nu g_{9/2}$ orbital. This gives rise to isomerism in the first case (low-spin and high-spin isomer) and to a 6^-, 7^- ground state for ^{216,218}Bi. In the intermediate case of the

half-filled shell in ^{214}Bi, a low-spin ground state results. When the shell is half-filled, a linear trend in I(I+1) is observed. This results from the inclusion of a dipole term, in addition to the quadrupole term in [Paa79].

For ^{216}Bi it has been argued that both a longer living state of unknown but low spin and a shorter living 6^-, 7^- or 9^- high-spin state decay via β disintegration [Kur00]. The high-spin state predominantly feeds the 8^+ level in ^{216}Po. In the case of ^{218}Bi, the distribution of the β strength towards or above the 6^+ and 8^+ levels in ^{218}Po would point to a spin of 6^- to 9^- for the mother nucleus, in agreement with the prediction of the parabolic rule. No experimental evidence has been found for the existence of a β decaying low-spin isomeric state in ^{218}Bi that would decay to a 2^+ daughter level, as observed in ^{216}Bi [Ruc90].

Although the analytical rule discussed above reflects the correct trends, a more reliable calculation should take into account the different orbitals present at low energy. Results of a full shell model diagonalization are presented below for ^{210}Bi and ^{218}Bi. The details of the calculation are presented in Sect. 4.9.

Figure 4.21 presents the shell model results for the $1\pi h_{9/2}$-$2\nu g_{9/2}$ odd-parity multiplet for ^{218}Bi, in comparison to the pure two-particle case of ^{210}Bi. We note that the proposed configurations have a quasi-particle character, due to pair scattering, especially to the $\nu i_{11/2}$ state. For details on the calculation, see Sect. 4.9.
Similar to the observations made with the parabolic rule, the convex, respectively concave, behaviour of the curves connecting the $1\pi h_{9/2}$-$\nu g_{9/2}$ multiplet energies, reflects the change from particle-particle to particle-hole nature in ^{210}Bi and ^{218}Bi, respectively. Nevertheless, a pure particle-hole configuration is not reached, as the odd-even spin staggering is smooth in ^{218}Bi as compared to ^{210}Bi. From the calculated trend, we conclude that the shell model prefers a 8^- ground state for ^{218}Bi, with the 5^- to 7^- levels only about 40 keV above. The calculated multiplet structure does not support the existence of a low-spin isomer, which, indeed, we did not observe. The 10^- level belongs to the $\pi h_{9/2}$-$\nu i_{11/2}$ configuration. Interestingly, this level has come down in energy in ^{218}Bi.

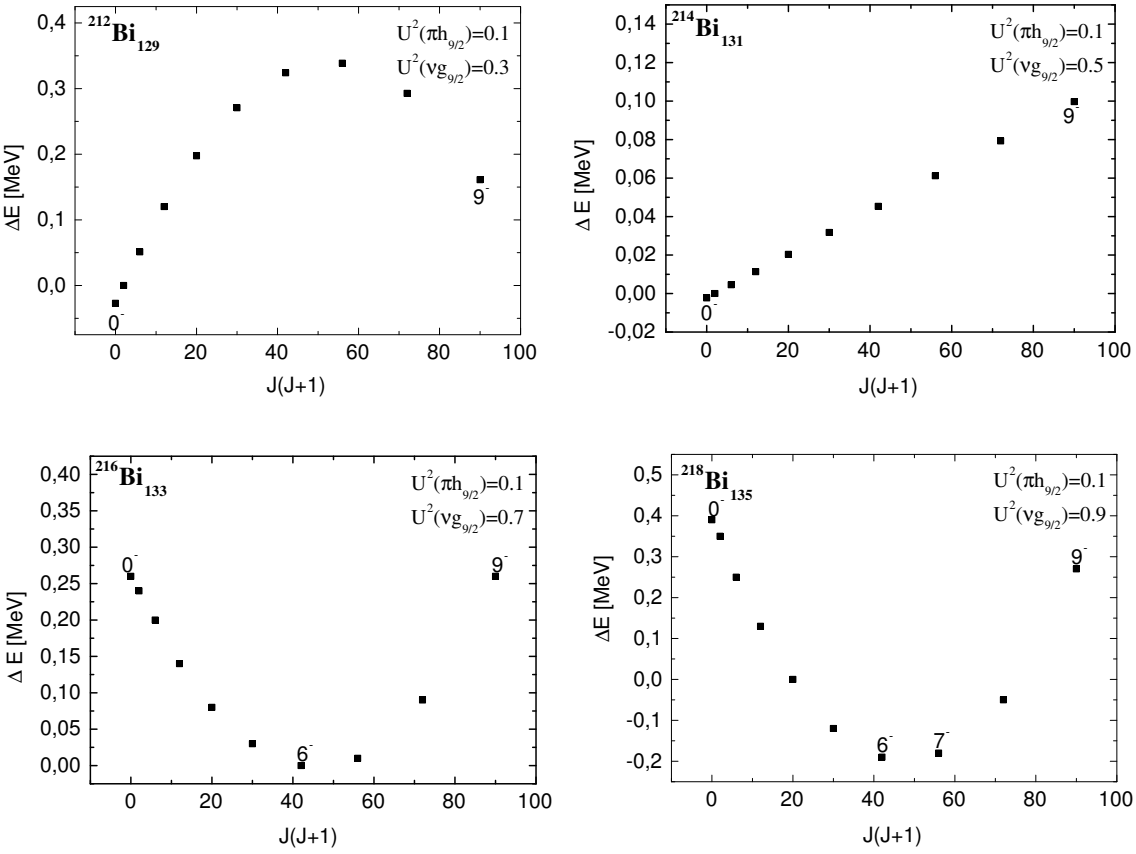

Figure 4.20: Relative energy splitting for the members of the $1\pi h_{9/2}$-$2\nu g_{9/2}$ proton-neutron multiplet in the odd-odd bismuth isotopes with A=212-218, calculated with the Paar parabolic rule [Paa79]. U^2 is the relative orbital occupancy, *i.e.*, the number of particles in the orbital divided by $2j+1$, the maximal occupancy of the orbital j.

4.8 Systematics of the even-even polonium isotopes

The ground state of ^{218}Po can be conveniently described as a closed core with one additional pair of protons in the $1h_{9/2}$ or $2f_{7/2}$ orbital and four pairs of neutrons in $2g_{9/2}$ or $1i_{11/2}$. The easiest way to create excitations consists in aligning the spins of the valence pairs. The observed sequence of the 509.8, 425.5, 385.7, and 263.0 keV transitions could therefore be interpreted as an E2 cascade linking 8^+, 6^+, 4^+, and 2^+ levels to the 0^+ ground state of ^{218}Po. This would justify the assumptions in the earlier discussion of the γ intensities and β feeding.

The evolution of the energies of the 8^+, 6^+, 4^+, and 2^+ levels in the even-even polonium isotopes is shown in Fig. 4.22. The lower part of the ^{210}Po level scheme is

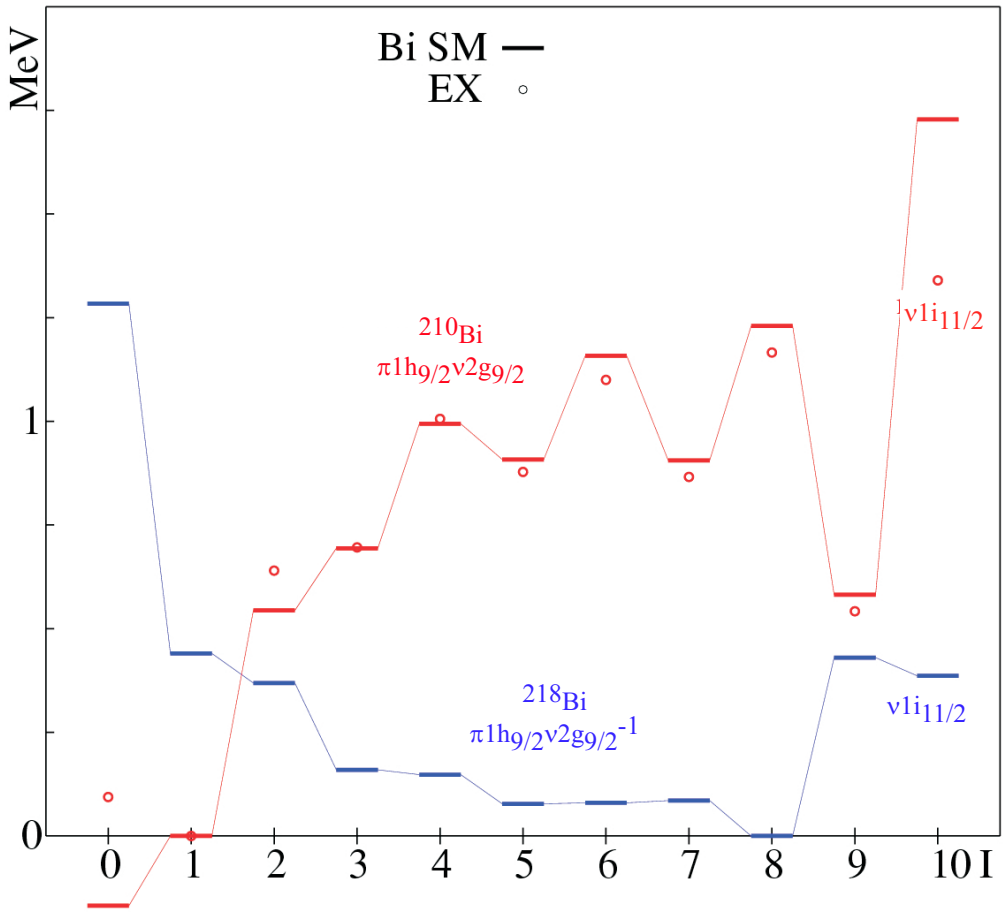

Figure 4.21: Calculated and experimental excitation energies of the $\pi h_{9/2}$-$\nu g_{9/2}$ and $\pi h_{9/2}$-$\nu i_{11/2}$ multiplets in ^{210}Bi and ^{218}Bi. The circles are experimental data for ^{210}Bi from [Fir96].

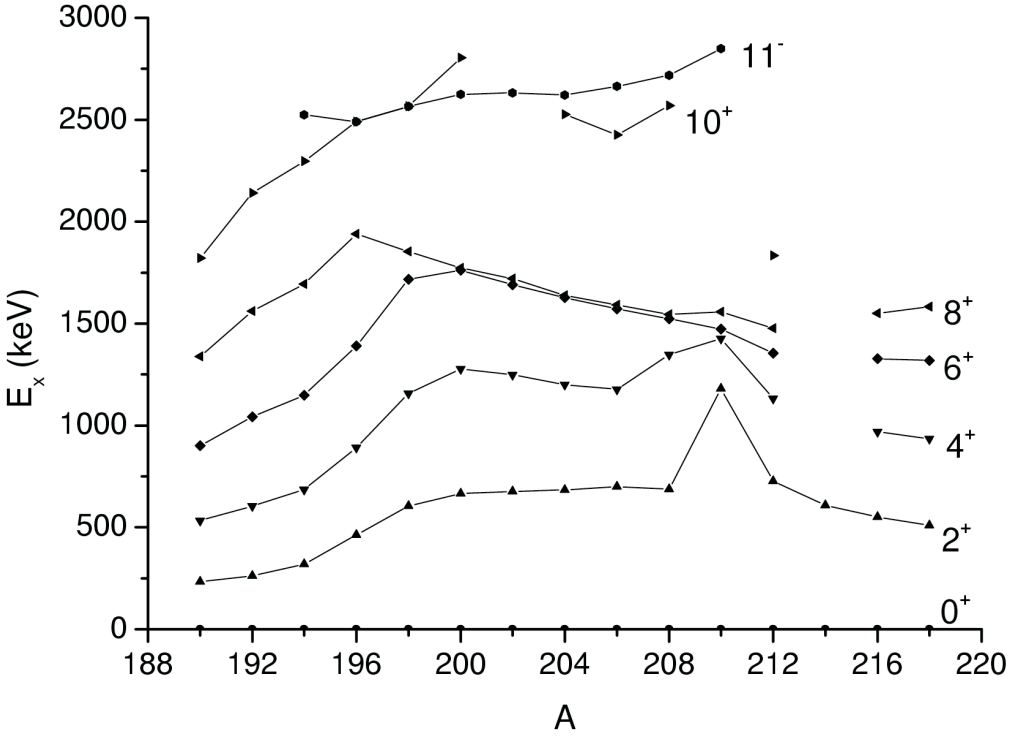

Figure 4.22: Evolution of the level structure in polonium isotopes. Data are taken from [Bij98, Jul01a, Van03b, Kur00, Fir96]

dominated by the $\pi 1h_{9/2}^2$ configuration. As neutrons are being added to the nucleus, this structure mostly survives, although mixing with other broken valence pairs becomes apparent. The distances among the excited states gradually increase, while the 2^+ and 4^+ levels descend. This feature is more pronounced beyond ^{210}Po than below. Just below the N=126 neutron shell closure, the neutrons are placed in low-j orbitals ($3p_{1/2}$, $2f_{5/2}$ and $3p_{3/2}$) that have only a small overlap with the high-j proton orbitals above Z=82 ($1h_{9/2}$, $2f_{7/2}$ and $1i_{13/2}$). The result is a typical seniority scheme between A=200 and A=206. Moreover, the neutrons can only create low-spin states and consequently they have no influence on the high spin levels. The $\nu 1i_{13/2}$ orbital starts to contribute only around N=114, and the appearance of intruder excitations at low excitation energy changes the picture drastically.

The valence neutron pairs beyond ^{210}Po occupy the $2g_{9/2}$ (I = 0..8), $1i_{11/2}$ (I = 0..10) and $1j_{15/2}$ (I = 0..14) orbitals, having a large π-ν interaction with the $1h_{9/2}$ protons.

4.9 Shell model description

Shell model calculations for ^{218}Po were carried out by E. Caurier. The Kuo-Herling interaction as revised by Warburton and Brown [War91] was used in a model space that includes the $1h_{9/2}$, $2f_{7/2}$, and $1i_{13/2}$ protons orbitals and the $2g_{9/2}$, $1i_{11/2}$, and $1j_{15/2}$ neutrons orbitals. No low-j orbitals were included. Single-particle energies were taken from ^{209}Bi and ^{209}Pb (Fig. 1.2) and calculations were performed with the NATHAN code [Cau99]. Seniority truncation was used, *i.e.*, successively more pairs were allowed to be broken. The number of broken pairs C ranged from 1 to 4. For instance, in the case of $C = 4$ eight particles of the two protons and eight neutrons in ^{218}Po could spread freely over the available orbits.

In Fig. 4.23 the calculated ^{218}Po level scheme is compared to the experimental data. Only yrast states are shown, while there may be more states between 1.5 and 2 MeV of either parity. The energy of the 2^+ state is reproduced nearly correctly. From the trend of convergence for increasing C agreement will likely be reached for $C = 5$, which, unfortunately, cannot be calculated within the present model. The calculated position of the 4^+ level lies too high and may require renormalization of the interaction. The deviation cannot be ascribed to a lack of convergence. The 6^+ and 8^+ levels are too low in energy and, in contrast to the data, closely resemble the results of a simple δ-interaction. The experimental data suggest the development of collectivity in this neutron-rich polonium nucleus, which is not at all reproduced by the calculation.
Finally we mention that the downsloping energy of the $2\pi f_{7/2}$ strength observed in the odd-A isotopes (Sect. 4.5) is not taken into account; the single particle energies are taken from the "closed shell +1" isotopes. For a more realistic result, the influence on the even-A bismuth and polonium isotopes should be evaluated.

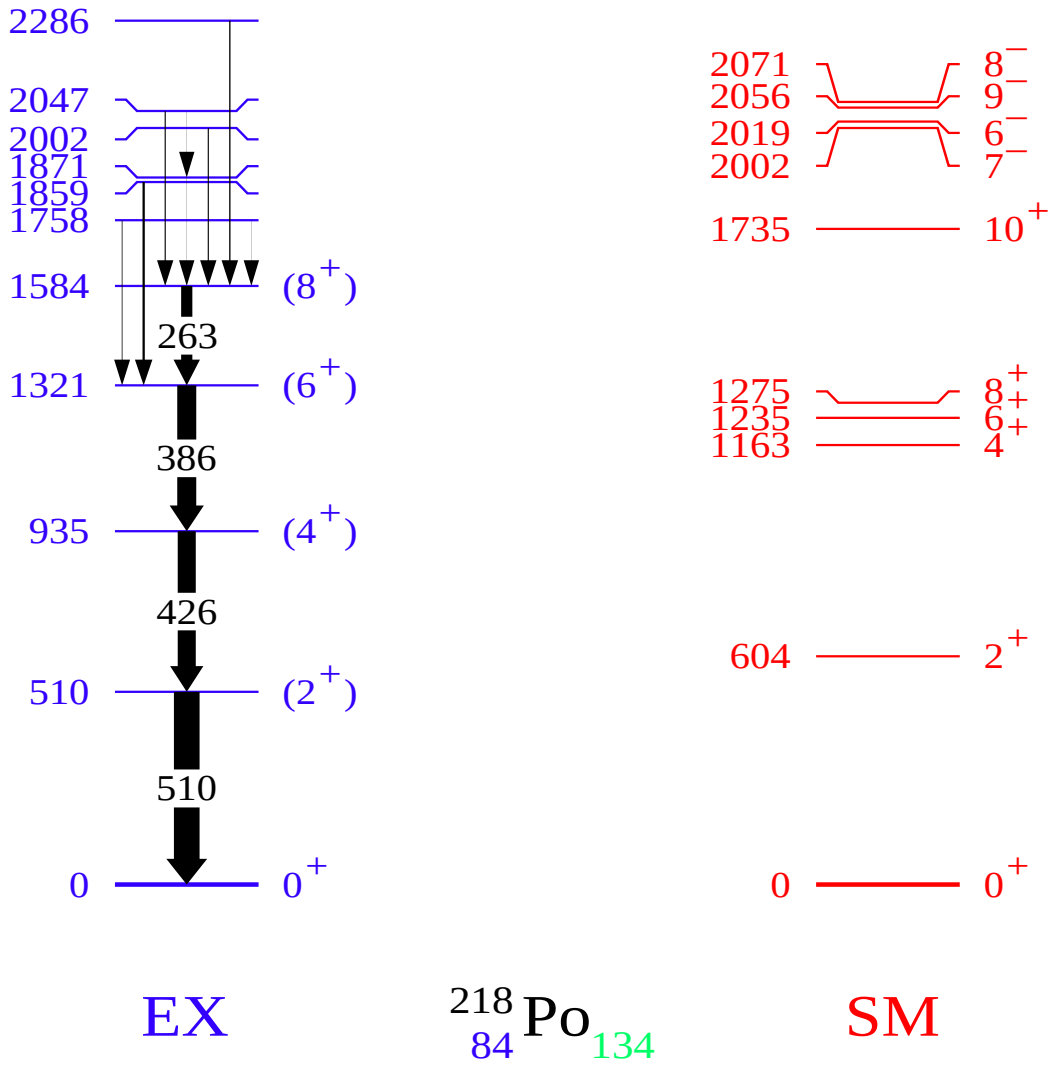

Figure 4.23: Experimental (left) and calculated (right) level scheme for ^{218}Po.

Chapter 5

Beta-delayed neutron emission from the heavy Tl isotopes

Modelling of the astrophysical r-process often relies on the predictions of global or microscopic models, in particular with respect to ground state- and decay properties of exotic nuclei. Indeed, in the regions of astrophysical interest, experimental data are often unavailable. One of the key observables is the β-decay rate. In this chapter a dedicated measurement of the half-lives of neutron-deficient thallium isotopes is discussed. Two attempts were made to deduce the half-lives through the expected β-delayed neutron emission branch.

5.1 Beta-delayed neutron emission

When a nucleus becomes more and more neutron rich, the neutron separation energy decreases. Combined with an increasing Q_β window when leaving the stability line, it is possible that the β decay feeds states lying above the neutron separation threshold in the daughter nucleus. This situation is schematically sketched in Fig. 5.1.

In terms of the β decay probability w_{if}, between an initial state i and a final state f, the β-delayed neutron emission probability can be written as:

$$P_{1n} = \frac{\sum_{S_{1n}<E_f<Q_\beta} w_{fi}}{\sum_{0<E_f<Q_\beta} w_{fi}}, \tag{5.1}$$

with S_{1n} the one-neutron separation energy, equal to BE(Z+1,N) - BE(Z+1,N-1). This probability has been calculated by Möller *et al.* [Moe97] in the QRPA framework, using a Yukawa potential plus pairing and a residual Gamow-Teller interaction for calculation of the β decay properties.

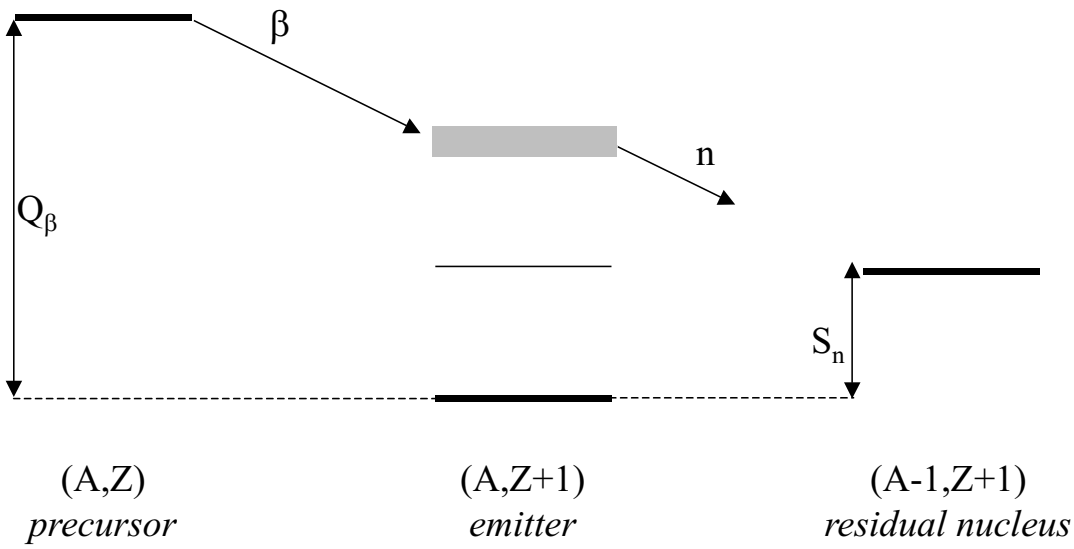

Figure 5.1: Schematic drawing of the β-delayed neutron emission process.

Table 5.1: Half-lives and β-delayed neutron emission probabilities for the neutron-rich thallium isotopes, calculated in the QRPA framework. Results are from [Moe97]. The more recent calculations, which also include FF decays [Moe02], give β-delayed neutron emission probabilities which are 2-7 times lower than the values quoted in this table.

A	$T_{1/2}$	P_{1n} [%]
211	$>$ 100 s	$\sim$ 0
212	$>$ 100 s	0.01
213	$>$ 100 s	95
214	$>$ 100 s	49
215	20.38 s	99

For the neutron-rich thallium isotopes a considerable β-delayed neutron branching is calculated. The results are presented in Table 5.1.

The β-delayed neutron expectation incited the measurement of the thallium half-lives via their neutron emission branch. Moreover, no neutron emission is predicted in the daughter nuclei or surface ionized contaminations, like for instance francium. As such, this method suppresses the isobaric contamination, which hampered the study of these thallium isotopes via β-delayed γ-spectroscopy. In runs II and III (Table 2.4) data were taken on $^{210,211,213-215}$Tl; experimental details are discussed in the next section.

5.2 Experimental details

Two sets of data, taken during run II and III, respectively, were collected for the neutron-rich thallium isotopes. Both experiments made use of the resonance ionization laser ion source to selectively ionize the thallium isotopes. The beam gate was closed for 100 ms after each proton pulse.
Data were taken in single mode, with a 20 ms, resp. 2 ms veto gate after each proton pulse in run II and III. This veto is applied to avoid background from promptly emitted spallation neutrons.

The beam was implanted in a catcher in the vacuum tube, positioned in the center of a cylindrical neutron long-counter, shown in Fig. 5.2. The emitted neutrons are slowed down in a paraffin moderator before entering the ^{3}He proportional counters. They are shielded from external radiation by a cadmium layer and borated paraffin. Through the reaction ^{3}He(n,p)^{3}H a charge signal proportional to the neutron kinetic energy is build up.
The detection efficiency for mono-energetic neutrons in the range of 45 keV to 2 MeV was determined to be 19(1) % [Ber00].

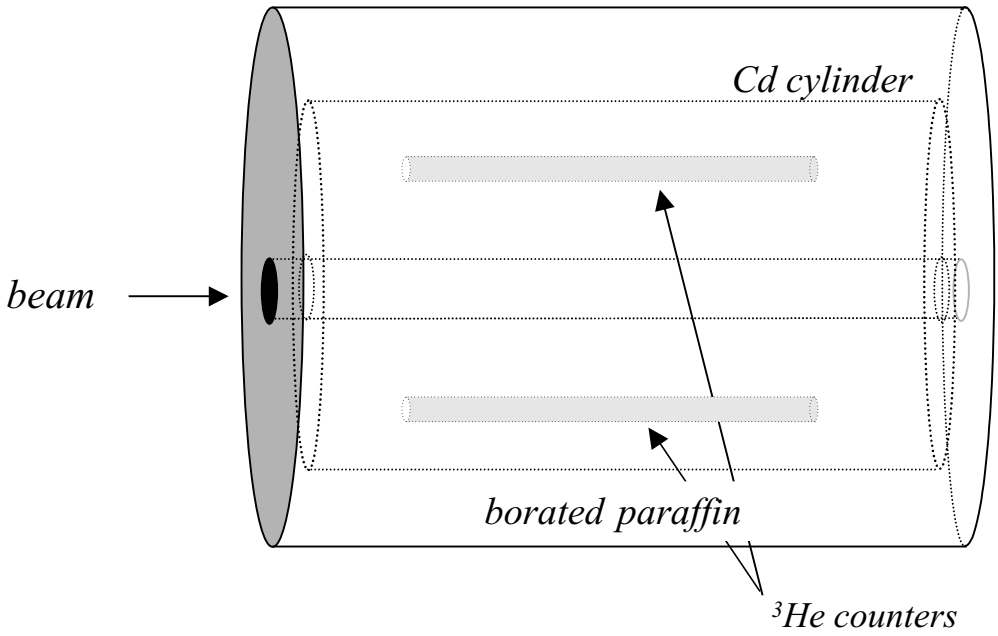

Figure 5.2: Schematic drawing of the neutron-counter.

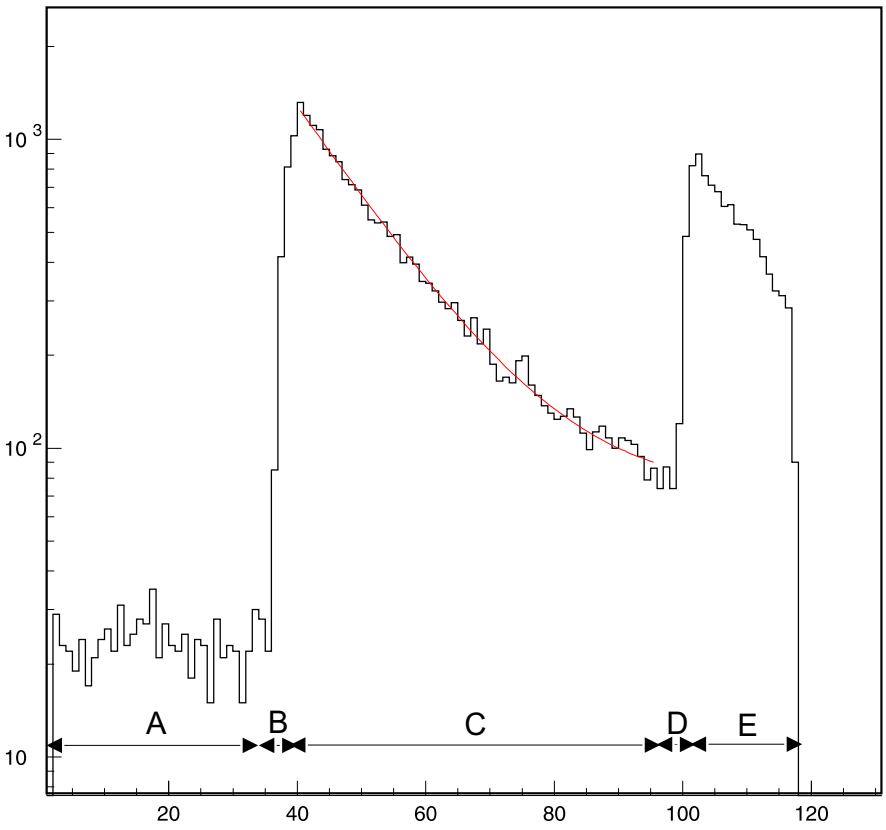

Figure 5.3: Data obtained at mass 211 during run II. The regions defined by the arrows correspond to the following time structure: A, background; B, implantation, on-resonance for 120 s; C, decay - beam gate closed; D, implantation, lasers off for 60 s; E, decay - beam gate closed.

5.3 Experimental results

Figure 5.3 presents the data obtained at mass 211 in run II. From a two-component fit plus constant background to the decay following the implantation with the lasers on resonance (region C in Fig. 5.3), a half-life of 173(14) s is deduced for the first component. As a matter of fact, this half-life is equal the known half-life of ^{211}Fr, $T_{1/2}$ = 186(1) s [Fir96]. A longer lived component could correspond to the 9.3 min activity from ^{207}Rn, the α decay daughter of ^{211}Ra. A single-component fit to the lasers off part (region E) gives a comparable half-life: 175(8) s.

A similar effect was seen at mass 214, where a half-life consistent with the ^{214}Ra half-life was observed. As a possible explanation (α,n) reactions on the aluminum walls of the implantation chamber were suggested. They could be induced by α parti-

Table 5.2: Stopping power for α particles in aluminum and count rate for the ^{27}Al(α,n) reaction

α energy [MeV]	dE/dx [MeV/(mg/cm^2)]	count rate [/μA·s]	rate [/s]
5.0	6.090×10^{-1}	$4{,}09\times10^{6}$	13
6.0	5.398×10^{-1}	$1{,}22\times10^{7}$	39
7.0	4.864×10^{-1}	$3{,}59\times10^{7}$	115
8.0	4.437×10^{-1}	1.47×10^{8}	471
9.0	4.087×10^{-1}	4.13×10^{8}	1320
10.0	3.795×10^{-1}	1.08×10^{9}	3445

cles produced in the decay of the higher-Z isobars, like francium or radium, which are abundantly produced.

As a test of this hypothesis, the ^{27}Al(α,n) reaction rate is calculated. The count rate, expressed in counts per second and per particle μA is given by

$$C = 3,8 \times 10^6 \frac{\sigma \cdot dx}{A}, \tag{5.2}$$

with σ the cross section in millibarn, dx the target thickness in mg/cm^2 and A the mass number of the target.
Integrated over the target thickness, the count rate reads:

$$C = \frac{3.8 \times 10^6}{A \cdot \frac{dE}{dx}} \int \sigma(E) dE. \tag{5.3}$$

Experimental data for the cross section as a function of the energy, are taken from [Ste64]. The α energies in this mass region vary between roughly 5 MeV and 10 MeV and the corresponding electronic stopping powers are calculated using SRIM [sri]. Table 5.2 gives the numerical results for this calculation for α energies between 5 and 10 MeV. Including a francium yield of $\sim10^8/\mu$C, the count rate is given in events per second. One way of circumventing this problem is to use a material with a much lower (α,n) cross section. We carried out the same calculation for the induced reaction rate on gold. Experimental data for the cross section as a function of the energy are only available down to 10 MeV [Cap85] and a linear extrapolation from 10 MeV downwards was used. Table 5.3 presents the numerical results and the obtained reduction.

From these results, it is concluded that a reduction of the induced reaction rate by a factor $10^3 - 10^4$ could be obtained, bringing the count rate at the neutron detector

Table 5.3: Stopping power for α particles in gold and count rate for the ^{197}Au(α,n) reaction

α energy [MeV]	dE/dx [MeV/(mg/cm^2)]	count rate [/s]	ratio (Au/Al)
5.0	2.328×10^{-1}	0,01	$1{,}1\times10^{-3}$
6.0	2.150×10^{-1}	0,03	$6{,}3\times10^{-4}$
7.0	1.999×10^{-1}	0,04	$3{,}7\times10^{-4}$
8.0	1.870×10^{-1}	0.07	1.5×10^{-4}
9.0	1.760×10^{-1}	0.12	9.2×10^{-5}
10.0	1.664×10^{-1}	0.20	5.9×10^{-5}

down to 0,01-0,1 counts per second. This would reduce the background to the detector noise level and allow to detect the resonant β-delayed neutron signal from the thallium isotopes.

The thickness of the gold layer needed to fully stop the α particles is calculated in SRIM and gives a range of 15.82 μm for an α energy of 8 MeV. A gold layer of approximately 15 μm was deposited on the inside walls of the implantation chamber by electroplating and the experiment was repeated in run III.
Figure 5.4 shows the results obtained at mass 213 from run III. Surprisingly, again no difference is observed between the laser on- and off-spectra and the half-lives do again correspond to the known half-lives of the contaminant, that is ^{213}Fr ($T_{1/2}$ = 34.6(3) s [Fir96]). It is not fully understood why this second attempt equally failed. Explanations can possibly be found in an incomplete or insufficient coating of the walls.
To conclude, we mention that in run II, data were also collected with the $\beta\gamma\gamma$ set-up for ^{215}Tl. However, no resonant γ-rays were observed in about 4 hours of data taking. Hence, the thallium production was probably very low during this experiment.

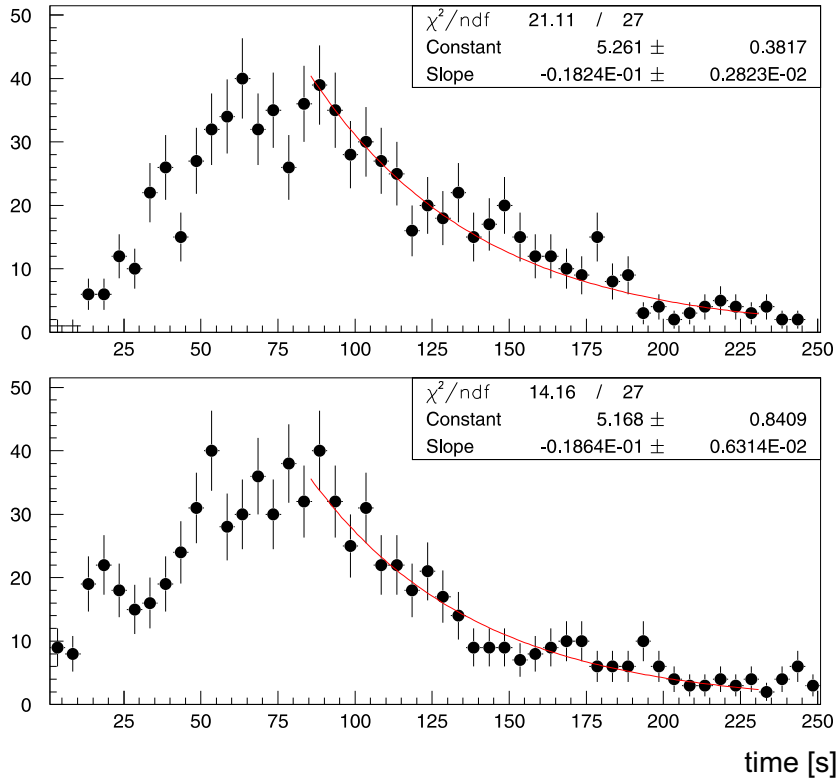

Figure 5.4: Data obtained at mass 213 during run III. Top: on-resonance; Bottom: lasers off.

Chapter 6

In-source laser spectroscopy of the neutron-deficient lead isotopes

The region of neutron deficient lead isotopes displays a rich nuclear structure, in particular near the neutron mid-shell where shape coexistence develops. The discussion in chapter 3 emphasized the complementarity of both nuclear and atomic spectroscopy. The low production rates obtained near and beyond N=104 limited the laser spectroscopic studies of the lead isotopes to $A \geq 190$ [Dut91]. The increased sensitivity brought about by the in-source laser spectroscopy was exploited by Andreyev *et al.* [And02a] and resulted in the identification of two α decaying isomers in ^{185}Pb. In this work, the experiment was repeated in a systematic way, following the isotopic chain from ^{188}Pb down to ^{183}Pb under improved experimental conditions.
The results presented in this section were obtained in a collaboration between the IKS-K.U.Leuven, the University of Mainz (Germany), IPN-Orsay (France) and the ISOLDE collaboration. The automated scanning procedure for the ISOLDE-RILIS was implemented by the Mainz group. Detection set-ups were provided by the Leuven group (α decay station) and IPNO ($\beta\gamma\gamma$ set-up).

6.1 Experimental details

The isotope shifts or charge radii in the lead region are commonly related to ^{208}Pb. As a matter of calibration of the wavemeter, laser scans were also performed on this stable isotope by measuring the ion current at A=208 in a Faraday cup.
For the radioactive ions, the count rate for each laser frequency was monitored by

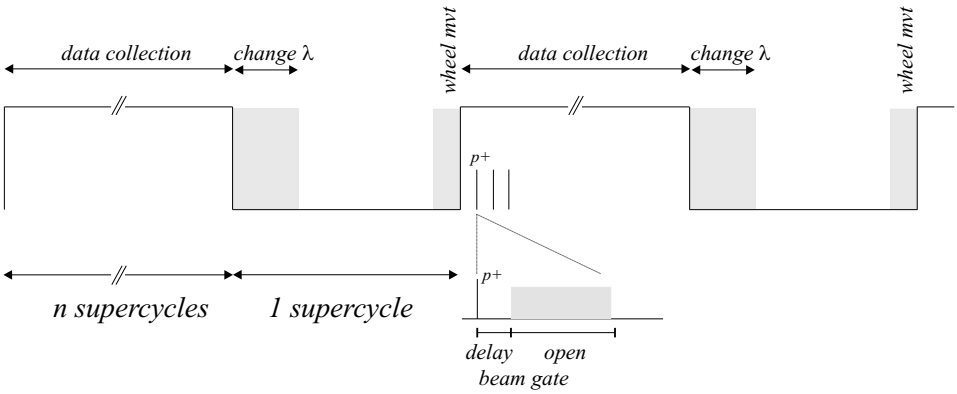

Figure 6.1: Typical measurement sequence for the laser scans.

measuring their characteristic α particles or γ-rays. In the following discussion, we will concentrate exclusively on the α-emitting isotopes and only quote the results from the γ-decay of the β-emitters for completeness.

The principle of the in-source laser spectroscopy measurements and the detector set-up for α decay were discussed in Sect. 2.2.1 and 2.3.3. Data were taken during the implantation period with the PIPS detector placed behind the carbon foil. All data were collected in list mode (Sect. 2.4), triggered by the α-detector. Besides the energy information obtained from the PIPS detector, the time between the start of the measurement cycle (for a specific frequency) and the event, measured by a TDC, was also written to the file. The energy calibration of the PIPS detector was performed using well known on-line produced Pb, Tl or Hg activities.

The complete measurement cycle was synchronized with the 16.8 s long supercycle of the ISOLDE beam. This means that data were always collected for an integer number of supercycles. In between the different measurements, when the laser frequency was being changed and stabilized, the α-trigger for the data acquisition was blocked for one supercycle. Meanwhile the laser control PC sent the averaged frequency of the previous setting to the data acquisition, using the serial RS232 communication protocol. This frequency was added as a separate parameter to the data file. The periodic movement of the wheel containing the carbon foils was also related to the supercycle signal.

In the analysis, the α-energy data are sorted on the basis of the frequency read-out and written to a separate spectrum for each laser frequency.

All measurement cycles are given in table 6.1 and a complete electronics scheme is sketched in Appendix A.

Table 6.1: Summary of the applied measurement cycles. The columns present in this order: the mass number; the step between two subsequent laser frequencies, measured in the visible region (*i.e.* before the frequency doubling). ± means that scans were performed in both directions: increasing or decreasing frequency; the beam gate delay/open sequence, triggered by the proton pulse signal, unless written explicitly. The beam gate was adjusted to keep the count rate in the α-detector at a level manageable for the list mode α-singles read-out; the number of proton pulses per supercycle; the time of the measurement at each frequency; the time of the wheel movement with respect to the start of the cycle; the number of complete scans recorded with these settings.
a: started with supercycle *b*: consecutive pulses

A	step [cm^{-1}]	beam gate [ms]	pulses/scy	cycle[s]	wheel[ms]	nbr scans
183	0.02	10/1180	6	168	15000[a]	1
	±0.02	1/1180	6	168	1[a]	4
184	0.01	10/1180	6	16.8	31800	3
	-0.01	10/1180	6	16.8	1[a]	2
185	0.01	10/300	6	16.8	31800	2
	-0.01	10/300	7	16.8	31800	1
186	0.01	10/100	6	33.6	48600	3
	0.01	10/50	6	33.6	48600	1
187	0.01	4305/6000[a]	3[b]	16.8	31800	3
188	±0.01	1200/100	3	16.8	31800	1
	-0.01	1000/100	3	16.8	31800	1
	-0.01	8000/4000[a]	3	16.8	31800	1

An automated laser frequency scanning was implemented for this experiment [Sel03]. It included an automatic change of the etalon and diffraction grating position, frequency read-out with feed-back control, as well as the communication to the user's data acquisition system using the RS232 or TCP/IP protocols. It was PC based and provided an interface for easy selection of scanning range, frequency step between subsequent settings and, if required, a reference frequency (within the same isotope), to which to laser will be tuned at regular intervals.

When using the RILIS for atomic spectroscopy, the power of the laser in the first excitation step was reduced, at the expense of photo-ionization efficiency, to avoid power broadening of the absorption line. Figure 6.2 shows this effect for a laser scan

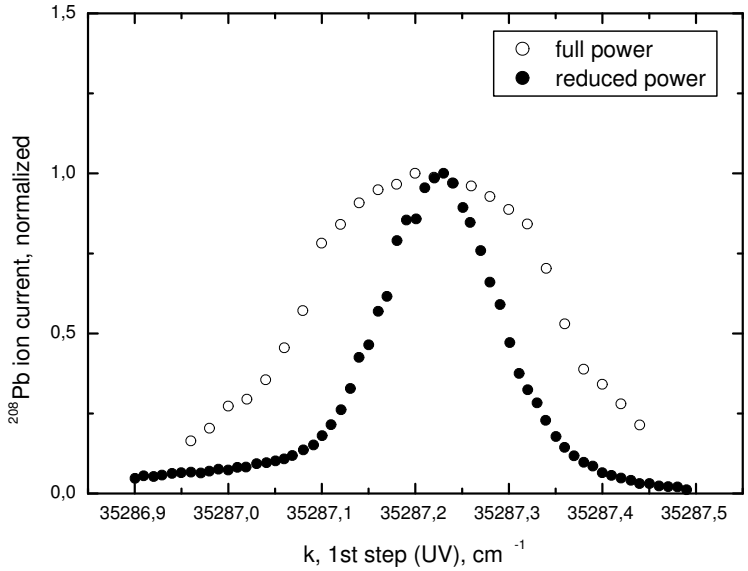

Figure 6.2: Laser scan for ^{208}Pb with full power and reduced power (5% transmission filter). High power induces a considerable broadening of the line shape.

on ^{208}Pb, comparing the full and reduced power measurements. The line widths are 10 GHz and 4.5 GHz respectively. As only the first excitation step is used for scanning, the other steps are preferably saturated to ensure maximal ionization efficiency. In the third step, however, saturation was not reached, because of lack of laser power.

6.2 Stable isotopes[1]

The wavemeter may exhibit a slow drift during the time of the run, for instance because of temperature instabilities in the laser hut, making absolute wavelength measurements less reliable. The accuracy for relative measurements, however, has been estimated to 0.0014 cm^{-1} or 42 MHz for ^{208}Pb. Therefore measurements of the ^{208}Pb resonance frequency at regular times increase the precision of the isotope shift determination. Figure 6.3 shows the measured resonance frequency for ^{208}Pb as a function of time, on the timescale of the total run. In order to determine the wavenumber $k(^{208}\mathrm{Pb})$ at the time of a particular radioactive measurement, a linear fit is made:

$$k(^{208}\mathrm{Pb}) = 35287.21240(74) - 2.56(22) \times 10^{-6} t, \tag{6.1}$$

[1]The analysis of the stable lead isotopes was entirely carried out at Mainz University [Sel03], but is discussed here for completeness, as all isotope shifts are related to it and as the analysis procedure for the radioactive isotopes is similar.

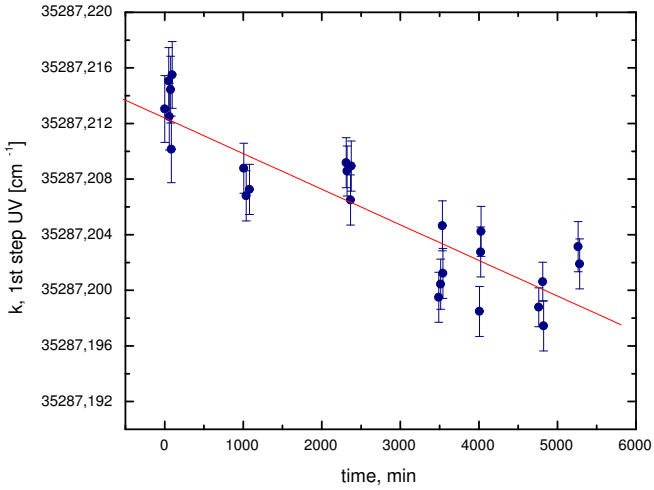

Figure 6.3: Variation of the resonance wavenumber for ^{208}Pb as a function of time, in minutes, as a result of the drift of the wavemeter. The errorbars are statistical and depend on the step size in the frequency scan (0.02,0.01 or 0.005 cm^{-1}, before frequency doubling)

where t is the time in minutes elapsed since the first scan of ^{208}Pb and k is given in units of cm^{-1}. An alternative determination was based on the stepwise interpolation between every two stable lead scans. Both approaches yield similar results and average values will be quoted in the next sections.

Besides the discussed measurements on ^{208}Pb, a few laser scans have also been made for the stable isotopes ^{206,207}Pb. They will not be discussed further.

Fitting procedure

The natural line shape of a spectral line corresponds to a Lorentzian function. The width of the 283 nm transition used in this work is 28 MHz [Tho83]. Various mechanisms, however increase this linewidth. We distinguish between the homogeneous and inhomogeneous broadening. When all atoms of the sample have the same absorption probability for a certain radiation frequency, the line will be homogeneously broadened and the Lorentzian line shape is conserved.
In the case of Doppler broadening, the absorption probability depends on the velocity of the atom in the ion source and results in a Gaussian profile. The width is given by

$$\Delta\nu_D = \frac{2\nu_0}{c}\sqrt{\frac{2k_BT}{M}\ln 2}, \tag{6.2}$$

with ν_0 the transition frequency, k_B the Boltzmann constant, T the ion source cavity temperature in Kelvin and M the atomic mass number. It typically contributes for 2.6 GHz to the linewidth.
Including both the Gaussian contribution and the (approximately Lorentzian) laser profile, a Voigt function[2] seems to be well adapted:

$$I_{voigt}(k) = I_0 \int G(k')L(k-k')dk', \tag{6.3}$$

where $G(k)$ is a Gaussian profile and $L(k)$ is the Lorentzian contribution.

In practice, the laser line shape is not symmetrical. It is influenced by, *e.g.*, the mutual orientation of the diffraction grating and the etalon, the frequency doubling, *etc.* Therefore, a free parameter for the laser line asymmetry has to be included. A product of two Lorentzians, shifted with respect to each other by an amount Δk, was used:

$$L(k) = L_0 \cdot g(k) \cdot f_{mod}(k, \Delta k), \tag{6.4}$$

with

$$g(k) = \frac{\gamma}{2\pi}\frac{1}{k^2 + (\gamma/2)^2} \quad \text{and} \quad f_{mod}(k, \Delta k) = \frac{a\gamma}{2\pi}\frac{1}{(k-\Delta k)^2 + (a\gamma/2)^2}. \tag{6.5}$$

with γ and $a\gamma$ the widths of the respective components. The expression for the laser line shape replaces the pure Lorentzian in Eq. 6.3.

We note also that the ATOS wavemeter does not determine the maximum of the peaks in the interference pattern (k_{max}), although this option is provided. Rather it is used in the 'crude' mode, where the center of gravity of the peak is measured (k_{CoG}). For an asymmetric line shape there is a difference between both modes ($k_{CoG} \neq k_{max} = k_0$) which can amount to 100 MHz. This effect has been taken into account in the fitting procedure.
The position of the maximum of the scanning curve, as well as the difference between the maximum and the center of gravity of the laser profile, have been deduced from the fitting. The extracted resonance frequency needs to be corrected accordingly: in order to extract from the wavenumber k_{CoG}, measured by the wavemeter, the actual wavenumber k_0 a correction is applied, $k_0 = k_{CoG} + \Delta k_{\text{corr}}$.
The free parameters in the fit are, for a single line, the constant background, the peak amplitude and position, and the laser profile width and the shift, Δk between both Lorentz profiles. The Doppler width is kept constant.

[2]The Voigt function corresponds to the convolution of a Lorentzian and a Gaussian distribution.

Table 6.2: Properties of the α-emitting lead isotopes used for atomic spectroscopy measurements: half-life, α-branching ratio and yield. The yields are taken from [Koe03] and represent the yields with full power in the first excitation step. Reducing the first step power for line broadening reasons, compromises the yield. When two isomers are present, the given yield corresponds to the sum.
h.s.: high spin ($13/2^+$) and l.s.: low spin ($3/2^-$)

A	$T_{1/2}$ [s]	b_α [%]	yield [at/μC]	Ref.
188	25.1(1)	9.3(8)	1.10^6	[Fir96, And99b]
187 (h.s.)	18.3(5)	12(2)	5.10^5	[Fir96, And02b]
187 (l.s.)	15.2(3)	9.5(2.0)		[Fir96, And02b]
186	4.82(3)	38(9)	4.10^4	[Fir96, And99b]
185 (h.s.)	4.3(2)	50(25)	1.10^3	[And02a]
185 (l.s.)	6.3(4)	50(25)		[And02a]
184	0.60(9)	80(15)	2.10^2	[Coc98], [Van03c], [And04]
183 (h.s.)	0.415(20)	100	1.10^1	[Jen02]
183 (l.s.)	0.535(30)	100		[Jen02]

6.3 Analysis of the radioactive lead isotopes

6.3.1 Alpha decay

Table 6.2 presents the list of α-emitters used in the present atomic spectroscopy study. The nucleus ^{189}Pb has also a small α-branch, but its longer half-life ($T_{1/2}$=51(3) s) makes it unsuitable for use with the present wind-mill configuration. Moreover, the poor knowledge of its β-decay scheme and technical problems with the tape transport system did not allow for a reliable scan of its hyperfine structure.

For every laser frequency setting an α spectrum is recorded and the characteristic α lines are integrated. Figure 6.4 shows subsequent histograms of a laser scan of ^{185}Pb. The step size was 0.02 cm^{-1} before frequency doubling. The α-lines at 6288 keV and 6486 keV have been assigned to a low spin isomer, the line at 6408 keV to a high spin isomer [And02a]. These two isomers, with tentative spin and parity $I^\pi=13/2^+$ and $I^\pi=3/2^-$, display an obviously different behaviour as a function of the laser frequency.

This is a consequence of their different hyperfine splitting, as sketched schematically in Fig. 2.4. The extraction of the isotope shift and the hyperfine structure constants will be discussed in Sect. 6.3.4.
For the low intensity peaks, for instance for those further away from the resonance frequency, the counts of the α peak have been summed, after correction for background α activity. For the stronger lines, a Gaussian fitting with a low-energy exponential tail and a constant background are used.

6.3.2 Isotope shift measurement

The variation of the frequency of an optical transition from one isotope to another is known as the isotope shift. As discussed in Sect. 2.3.2 this quantity is related to the charge radius of the nucleus.

^{190}Pb: a test case

As a test of the reliability of the method, the previously known isotope shift of ^{190}Pb was remeasured. The scanning over the absorption resonance was monitored through the 942 keV γ-ray following β decay. A typical $\beta\gamma\gamma$ detection setup in combination with a tape transport system was used for this purpose and is not described in further detail. Figure 6.5 shows the experimental curve obtained [Rou03].
The isotope shift for ^{190}Pb had been measured earlier at GSI using collinear laser spectroscopy [Dut91]. However, in that experiment a different atomic transition was used, namely the 723 nm $6p^2(^1D_2) \rightarrow 6p7s(^3P_1)$ transition. Therefore the isotope shift values cannot be directly compared. We anticipate the results of Sect. 6.3.3 and compare the deduced values for the mean squared charge radii $\delta\langle r^2\rangle^{208,190}$. They are equal to 0.839(10) fm^2 and 0.840(10) fm^2 in our data and the GSI results, respectively. We note, however, that although the final accuracy on the charge radii is similar, the accuracy on the isotope shift is not: it is 100 MHz in our experiment, compared to 5 MHz in the collinear laser spectroscopy data. The uncertainty on the charge radius is dominated by the uncertainty on the electronic factors used in its calculation (see Sect. 6.3.3).

Corrections for laser power

The stability of the system, including production in the target and ionization efficiency, is monitored by measuring the α or γ yield for a particular reference frequency (k_{ref}) at regular time intervals during a scan. The typical structure of the scans was: $k_1, k_2, k_3, k_{\mathrm{ref}}, k_4 \ldots$ The stability of the laser set-up is additionally controlled by mea-

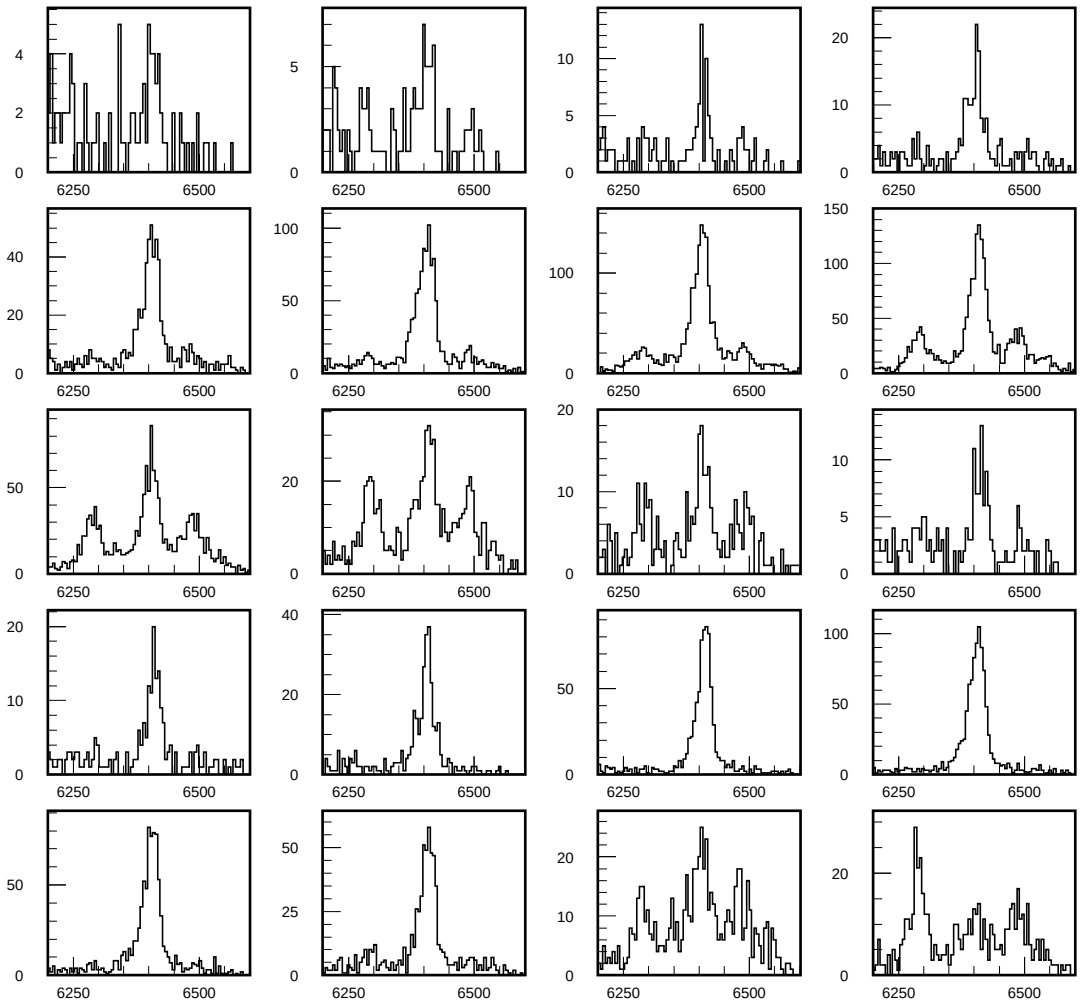

Figure 6.4: Alpha spectra (counts vs. α-energy in keV) for the subsequent settings of the first laser frequency for ^{185}Pb. The laser frequency step size was 0.02 cm^{-1} in the visible range. The α-lines at 6288 keV and 6486 keV have been assigned to the low spin isomer, the line at 6408 keV to the high spin isomer [And02a]. Sequence is from left to right, top to bottom.

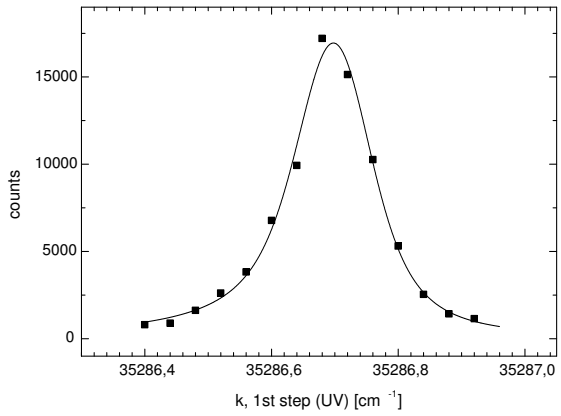

Figure 6.5: Number of counts in the 942 keV γ-line in the β-decay of ^{190}Pb versus laser frequency, corrected for fluctuations in the first step laser power. (Data for 1 detector and 1 scan, step size: 0.04 cm^{-1}, measurement time $\sim 1^h40$)

suring the laser power in the first and third steps.
Figure 6.6 shows the laser power readout and the number of counts in the α-line when the laser is tuned to the reference frequency, during one file. A periodic behaviour of the laser power is observed. This variation is most likely due to the desynchronization between the laser oscillator and the amplifiers. As it influences the ionization efficiency, the same trend is observed in the α count rate, superimposed on a continuous sloping down. In addition, photo-ionization does not only depend directly on the applied laser power, but in the multi-step excitation process, the timing of the laser pulses also has an influence. The raw spectra will be corrected for the variation of the laser power, using the linear dependence of the α count rate on the first step laser power.

Corrections for variation in isotope production

After correcting the reference data for the variation of the laser power, the α count rate versus the measurement number (physically, the time) still presents a downsloping trend, which is associated with the variation of the isotope production in the target. An additional polynomial correction is applied.

Influence of the second step

During the scan of the first laser excitation step, the frequency of the second step is kept constant. The width of the second laser line is approximately 60 GHz (including power broadening) while the scanning range for the even-A isotopes is typically of the order of 20 GHz. The same value of the second step frequency is also kept for all

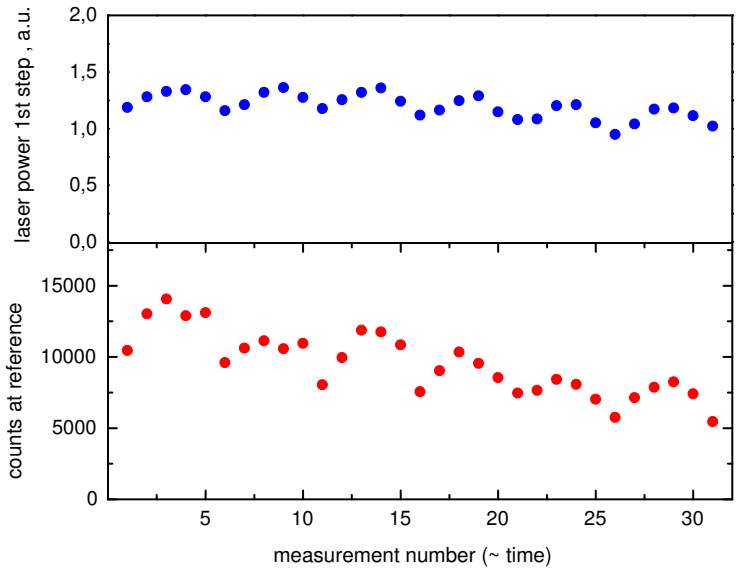

Figure 6.6: (Upper plot) Read-out of the laser power in the first excitation step, measured at regular time intervals during a scan. (Lower plot) α-intensity at the reference frequency, for the consecutive reference measurements.

isotopes, $^{183-188}$Pb, as the isotope shift is small compared to the line width of the second step.
Figure 6.7 presents the results of a scanning of the second laser frequency[3] in ^{184}Pb, in steps of 0.6 cm^{-1}, while keeping the first laser tuned to the resonance frequency. Besides a change in the ionization efficiency, the detuning of the second step also introduces an asymmetry of the response curve in the first step. This will be accounted for by the asymmetry parameter in the fitting procedure.

Figure 6.8 shows the scans of the first step in the odd-A isotope ^{185}Pb for two different settings of the second step. In this case the relative intensity of the three hyperfine components is affected. In the fitting of the spectra the peak amplitude is left as a free parameter and only the positions are used to deduce the isotope shift and the hyperfine constants, under the assumption of a particular nuclear spin value.
According to Fig. 6.7[4], care should be taken in the choice of the second laser frequency: depending on the slope of the curve, the asymmetry of the first step line could be

[3]No automatic scanning of the second step was implemented and the manual scanning was only performed for ^{184}Pb.

[4]Only one single scan has been made for the second step frequency. Hence, statistical fluctuations cannot be excluded.

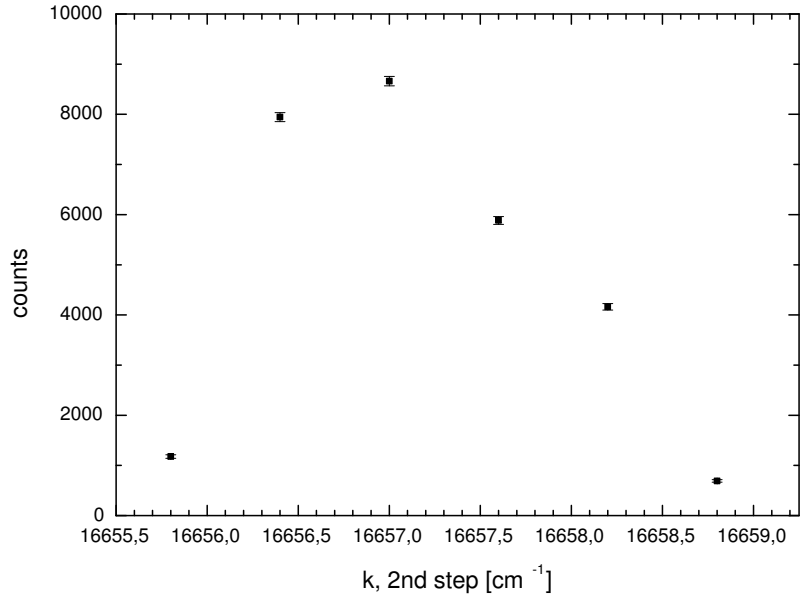

Figure 6.7: Scan of the second step frequency, while the first step is tuned to the resonance frequency. Data for ^{184}Pb.

different for the different hyperfine components. However, the example of Fig. 6.8 (k_2=16656.4 cm^{-1}) presents an unrealistically large detuning of the second step laser and under the actual experimental conditions the isotope shift is small compared to the width of the second step laser line. All scans (for A=183-190) have been performed with k_2=16657.6 cm^{-1}.

6.3.3 Isotope shift and charge radii

Figure 6.9 presents the scans for the even-even isotopes after correction for the fluctuations of the laser power or the production. From the centroid of the curve, the isotope shift relative to ^{208}Pb is deduced. The adopted isotope shift values correspond to the average of the isotope shifts determined via a *linear* and a *stepwise* interpolation of the ^{208}Pb measurements (see Sect. 6.2). The results are summarized numerically in Table 6.3. The errors include both the statistical standard errors and a 42 MHz uncertainty from the ^{208}Pb resonance frequency measurement.
Figure 6.10 presents a scan for the high- and low-spin isomers of the odd-A isotope ^{185}Pb. Again the isotope shift is determined from the position of the centroid of the curve.

The relation between the isotope shift and the mean squared charge radius was

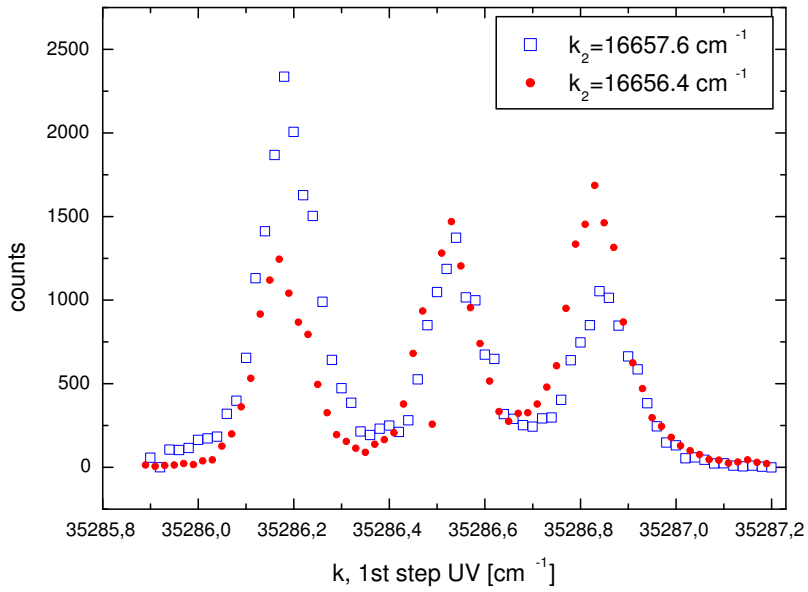

Figure 6.8: Influence of the detuning of the second step on the relative intensities of the 3 hyperfine components in ^{185}Pb. Data for high-spin isomer.

discussed in Sect. 2.3.2 (Eq. 2.16) and reads:

$$\delta\nu^{AA'} = M\frac{A - A'}{AA'} + F\lambda^{AA'}. \tag{6.6}$$

The specific mass shift was theoretically calculated: M = 0.19(25)×NMS [Kin85]. A King plot analysis, with a constraint on the above mass shift value, yielded $F_{\mathrm{Pb}}^{283.3\mathrm{nm}} = 20.36(18)$ GHz/fm^2 [Ans86]. We have adopted these values in the analysis. In the uncertainty on the mean squared charge radius, given in Table 6.3 also the uncertainty on the electronic factors M and F is incorporated.

6.3.4 Odd mass isotopes and the hyperfine splitting

As shown in Sect. 2.3 the hyperfine parameters A and B can be deduced from the position of the different hyperfine components, using Eq. (2.7). From the relative intensities a value of the nuclear spin can, in principle, be inferred in the most favourable cases. In these data, such a procedure is not feasible, as the second excitation step troubles to picture (see above). The occurrence of three hyperfine components however, excludes a I=1/2 assignment. Moreover, fitting the low-spin spectra with the assumption I=5/2, gives rise to a quadrupole moment which is on average an order of magnitude larger. Therefore, I=3/2 seems the most probable assignment. For the

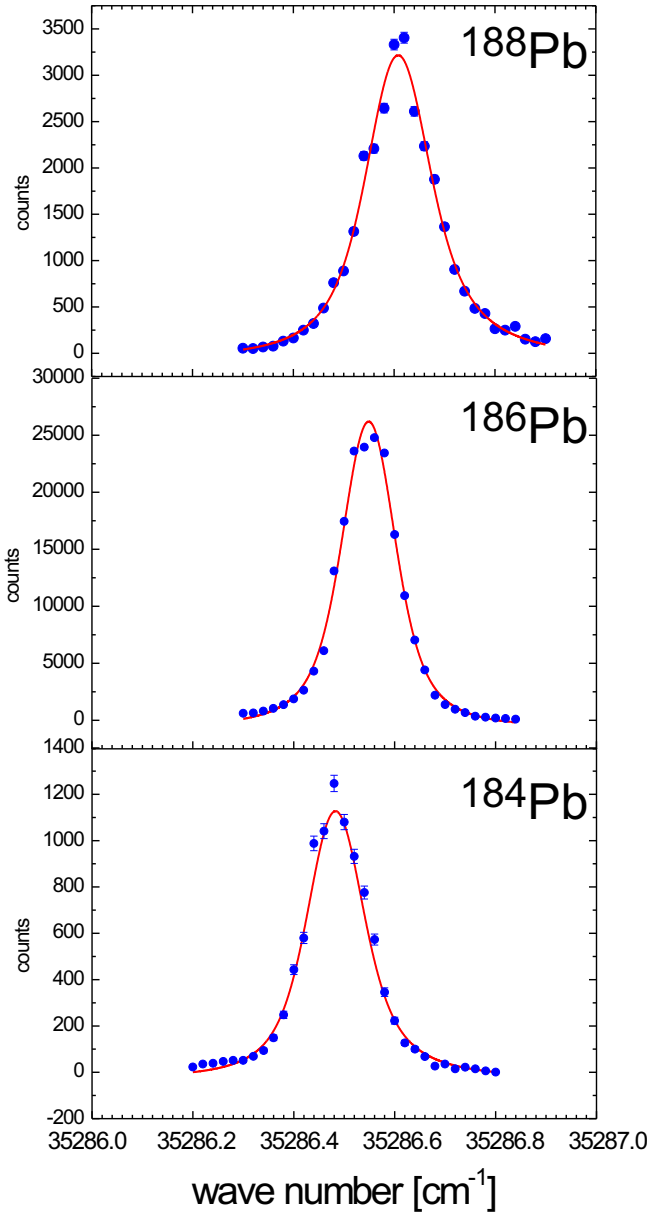

Figure 6.9: Laser frequency scan for the even-even lead isotopes ^{188,186,184}Pb: α-counts versus laser frequency. The dots represent the experimental data, the curve presents the fit in the above described model.

Table 6.3: Isotope shifts $\delta\nu^{A,208}$ and mean squared charge radii in fm^2, deduced from experiment. 'h.s.' and 'l.s.' stand for high and low spin, respectively.

Isotope	I^π	$\delta\nu^{A,208}$ (GHz)	$\delta\langle r^2\rangle$ (fm^2)
^{190}Pb	0^+	-15.86(10)	-0.8390(100)
^{188}Pb	0^+	-17.57(12)	-0.9297(100)
^{187}Pb	h.s.	-19.37(12)	-1.0250(110)
	l.s.	-18.78(12)	-0.9934(110)
^{186}Pb	0^+	-19.81(10)	-1.0480(110)
^{185}Pb	h.s.	-21.26(15)	-1.1246(130)
	l.s.	-20.66(15)	-1.0930(120)
^{184}Pb	0^+	-21.74(10)	-1.1502(120)
^{183}Pb	h.s.	-23.54(15)	-1.2453(140)
	l.s.	-22.95(15)	-1.2144(130)

high spin isomer, no conclusions can be drawn on the spin assignment.
When extracting the nuclear parameters μ and Q_s from the measured hyperfine constants A and B, precise atomic physics information is needed for determining B(0) and $\partial^2 V/\partial z^2$ (Eq. 2.8 and 2.9). A common way to determine the magnetic moment, circumventing this problem, uses scaling relations:

$$\frac{A_1}{A_2} = \frac{I_2\mu_1}{I_1\mu_2}, \tag{6.7}$$

where the indices refer to isotopes 1 and 2, respectively. In this relation the possible volume difference between the nuclei with masses A_1 and A_2 is not included. The volume correction to the ratio A_1/A_2, known as the *hyperfine anomaly*, was shown to be smaller than $\simeq 10^{-3}$ [Dut91].
In the lead isotopic chain, ^{207}Pb can be used as a reliable calibration point (I=1/2, A=8.8072(30) GHz, μ=0.59258(1)) [Ans86].

Figure 6.11 presents the results obtained for the $3/2^-$ and $13/2^+$ isomers obtained in this work, along with the values of the $13/2^+$ isomers for the heavier isotopes [Dut91] and the earlier values of [And02a], obtained with the same technique but under less controlled experimental conditions. The Schmidt line presents the single-particle moment for an $i_{13/2}$ or $p_{3/2}$ neutron. The calculation of Bauer *et al.* [Bau73]

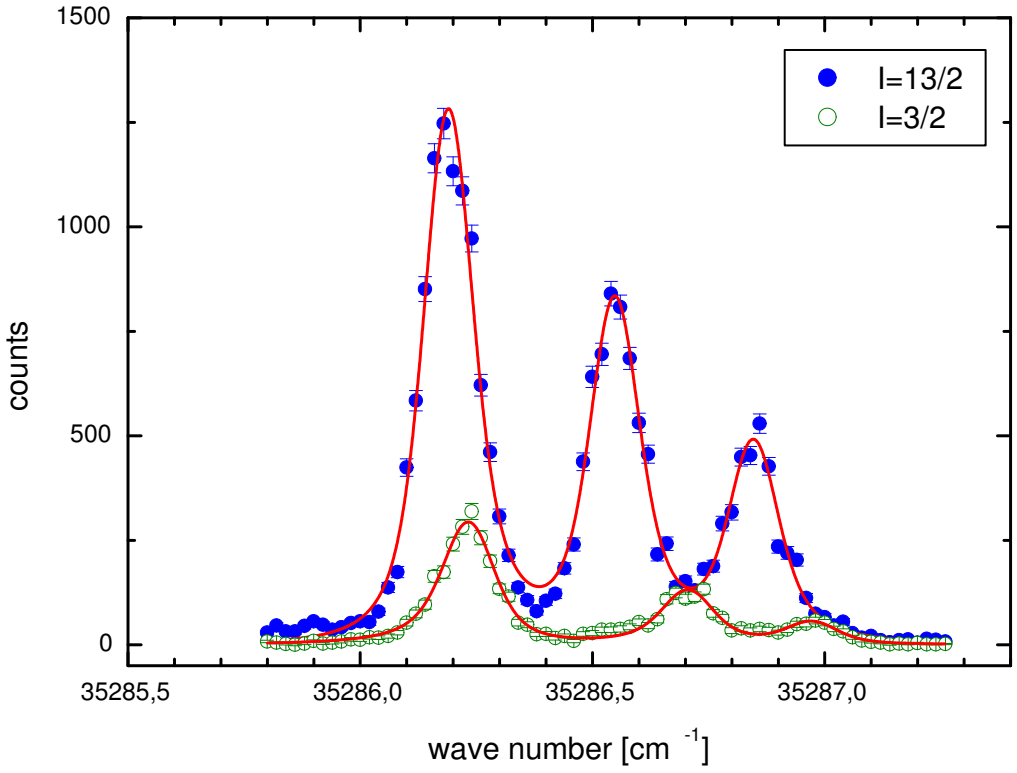

Figure 6.10: Laser frequency scan for ^{185}Pb: α-counts versus laser frequency. The dots represent the experimental data, the curve presents the fit in the above described model.

Table 6.4: Hyperfine constant A and the magnetic moment for $^{183-187}$Pb deduced from experiment. The magnetic moments have been deduced assuming a spin I=13/2 and I=3/2 for the high spin (h.s.) and the low spin (l.s.) isomer, respectively.

Isotope	I^π	A (GHz)	μ (μ_N)
^{187}Pb	h.s.	-1.383(6)	-1.210(5)
	l.s.	-5.584(25)	-1.127(5)
^{185}Pb	h.s.	-1.405(12)	-1.229(10)
	l.s.	-5.652(25)	-1.141(5)
^{183}Pb	h.s.	-1.423(6)	-1.245(5)
	l.s.	-5.742(25)	-1.158(5)

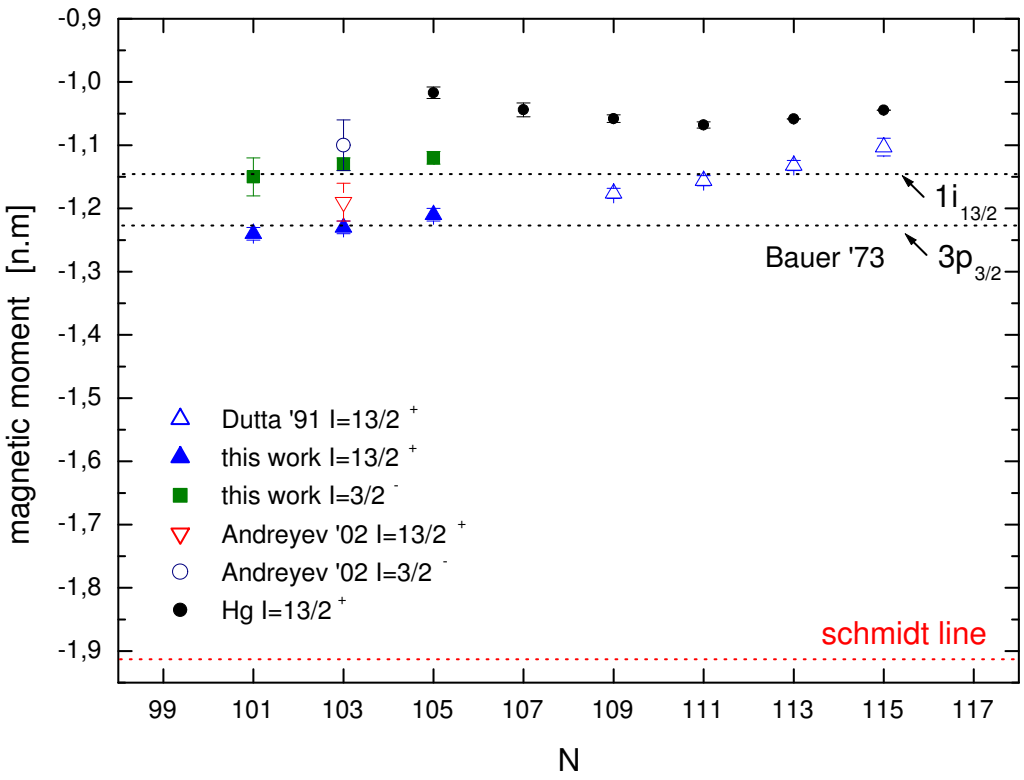

Figure 6.11: Magnetic moments for the neutron deficient odd-A lead isotopes. The theoretical curve, labelled "Bauer '73", is taken from [Bau73]. The single-particle Schmidt estimate is also drawn. Data for the lead isotopes are taken from [Dut91], [And02a] and this work. The values for the mercury isotopes were taken from [Sto].

uses effective g-factors, taking into account configuration mixing, core polarization and mesonic effects. The $13/2^+$ isomers follow a smooth trend from A=197 to A=183, with a slightly downsloping evolution towards the Schmidt line. This has been explained as a reduction of the first order core polarization effect, as less neutrons occupy the $\nu i_{13/2}$ orbital. For the mercury isotopes, however, this trend is different. The variation of the magnetic moment seems to be symmetric with respect to the half-filled $\nu i_{13/2}$ orbital ($101 \leq N \leq 114$) [Ney03].

6.4 Discussion of the experimental results

Figure 6.12 shows the charge radii for the lead isotopes down to A=183, including the results discussed above, along with the even-Z neighbours mercury (Z=80) and platinum (Z=78). The lead radii follow rather closely the trend predicted by the spherical droplet model (see Sect. 6.4.1), except for the deviation beyond the N=126 shell clo-

sure and a smaller deviation near the neutron mid-shell at N=104. This behaviour is in contrast with the mercury isotopes, where a large odd-even staggering sets in at N=105.
In the platinum series an overall deviation from the linear trend of the heavier isotopes (N≥113), indicates the influence of deformation near mid-shell. Such an effect is absent, or at least considerably smaller in the lead isotopes, confirming their spherical nature.
In the following discussion, we will present all results in reference to the spherical droplet model or alternatively, with respect to the parametrization of I. Talmi (Sect. 6.4.1). In addition, theoretical calculations have been performed in the interacting boson model and the generator coordinate model. We will discuss both methods and their results for the charge radii in Sections 6.4.2 and 6.4.3.

6.4.1 Parametrizations of the charge radii

In the liquid drop model the mass and charge distributions are identical and the radius varies with $A^{1/3}$. Although this offers a rather good first order approximation close to the valley of stability, the details of the isotopic variation are not reproduced. The more refined droplet model of Myers and Schmidt [Mye83] gives a more suitable framework for evaluating the charge radii along a chain of isotopes (see Sect. 1.2.1). Using theoretically determined deformation parameters, *e.g.* those of Möller *et al.* in the FRDM [Moe95], the radii can be evaluated in the droplet model. In the comparison with the experimental data, we will use the spherical droplet model, with zero deformation, in order to highlight possible shape effects.

Albeit small, a distinct deviation from the droplet model is observed for the lead isotopes between ^{194}Pb and ^{183}Pb in Fig. 6.12. If this deviation would be entirely associated with an axial quadrupole deformation using Eq. 3.10, an almost constant deformation $\langle\beta_2^2\rangle^{1/2} \sim 0.11$ would result for $^{190-184}$Pb. The B(E2) value of the 0^+-2^+ transition in ^{204}Pb is used as a reference to extract the β_2 value, following the method of [Le 99a]. The results are summarized in Table 6.5.

Another empirical approach has been applied to the calcium and lead isotopes by Talmi [Tal84], in order to reproduce the observed normal[5] odd-even staggering in the charge radii. In this case, however, we will only consider the predicted trend for the even-even isotopes.
The polarization effect of the valence neutrons on the closed proton core is considered.

[5] not to be confused with the deformation related odd-even staggering Hg

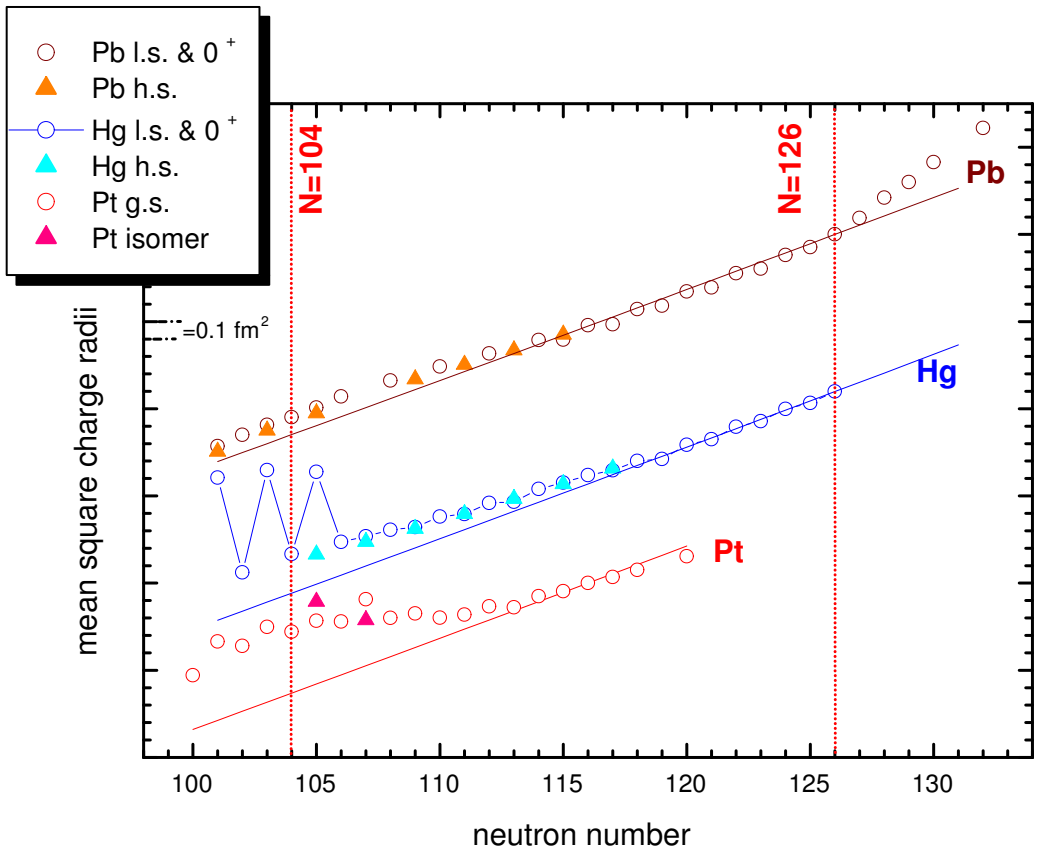

Figure 6.12: Mean squared charge radii for the lead, mercury and platinum isotopes, compared to the predictions of the spherical droplet model. The experimental error bar is smaller than the symbol size. The distance between the different chains is chosen arbitrarily for better display. One minor division on the vertical scale corresponds to 0.1 fm^2.

Including the monopole and quadrupole terms of the proton-neutron interaction, the square of the charge radius as a function of n, the number of valence neutrons, follows a parabolic behaviour:

$$\langle 0|\Sigma r_i^2|0\rangle = \langle \Sigma r_i^2\rangle + nC + \frac{1}{2}n(n-1)A + \left[\frac{1}{2}n\right]B, \tag{6.8}$$

with $\left[\frac{1}{2}n\right]$ the largest integer not exceeding $\frac{1}{2}n$. Knowing the effective interaction, this quantity could be calculated exactly for a single j^n shell. Alternatively, the coefficients A, B and C are fitted to the experimental data. For the neutron deficient lead isotopes, where several orbitals are active, the rule is only approximately valid. The variation of the squared charge radii as a function of the number of neutron holes n' counted

Table 6.5: Mean squared charge radii in fm^2 and extracted $\langle\beta_2^2\rangle^{1/2}$, using the B(E2) value for ^{204}Pb [Ram89] as a reference.

Isotope	$\delta\langle r^2\rangle^{A,204}$ (fm^2)	$\langle r^2\rangle_{sph}$ (fm^2)	$\delta\langle r^2\rangle_{sph}$ (fm^2)	$\delta\langle\beta_2^2\rangle$	$\langle\beta_2^2\rangle^{1/2}$
^{184}Pb	-0.927	29.415	-1.040	0.0097	0.11
^{186}Pb	-0.825	29.518	-0.937	0.0096	0.11
^{188}Pb	-0.707	29.621	-0.834	0.0108	0.11
^{190}Pb	-0.616	29.724	-0.731	0.0097	0.11
^{192}Pb	-0.535	29.828	-0.627	0.0078	0.10
^{194}Pb	-0.460	29.932	-0.523	0.0053	0.08
^{196}Pb	-0.383	30.036	-0.419	0.0031	0.07
^{198}Pb	-0.298	30.140	-0.315	0.0014	0.06
^{200}Pb	-0.206	30.245	-0.210	0.0004	0.05
^{202}Pb	-0.105	30.350	-0.105	0.0000	0.04
^{204}Pb	-0.000	30.455	-0.000	0.0000	0.04

from the closed shell at N=126 is

$$\delta\langle r^2\rangle = -n'C' - \frac{1}{2}n'(n'-1)A - \frac{B}{2}\left(\frac{1-(-1)^n}{2}\right), \tag{6.9}$$

with n'=2Ω - n and 2Ω=44. With the values of A, B and C' fitted to the experimental charge radii of $^{207-198}$Pb [Tho83, Tal84], we extrapolated Eq. 6.9 to A=184. In the case of even-even nuclei the pairing term (with coefficient B) vanishes. The results are shown in Fig. 6.13. Another parameter set, deduced from a fit to all data down to A=190, has also been used. In this case, however, a larger deviation occurs for the lighter isotopes.

Two more sophisticated approaches have been tested for their reproduction of the observed deviation from the spherical droplet model prediction. The influence on the charge radii of intruder configurations at low excitation energy is discussed in the algebraic IBM model and the mean-field based GCM model. These models are briefly explained in the next sections.

6.4.2 IBM calculation of the lead charge radii

Configuration mixing in the IBM was introduced in a general way by Duval and Barrett [Duv81], describing the different configurations in terms of different IBM calculations

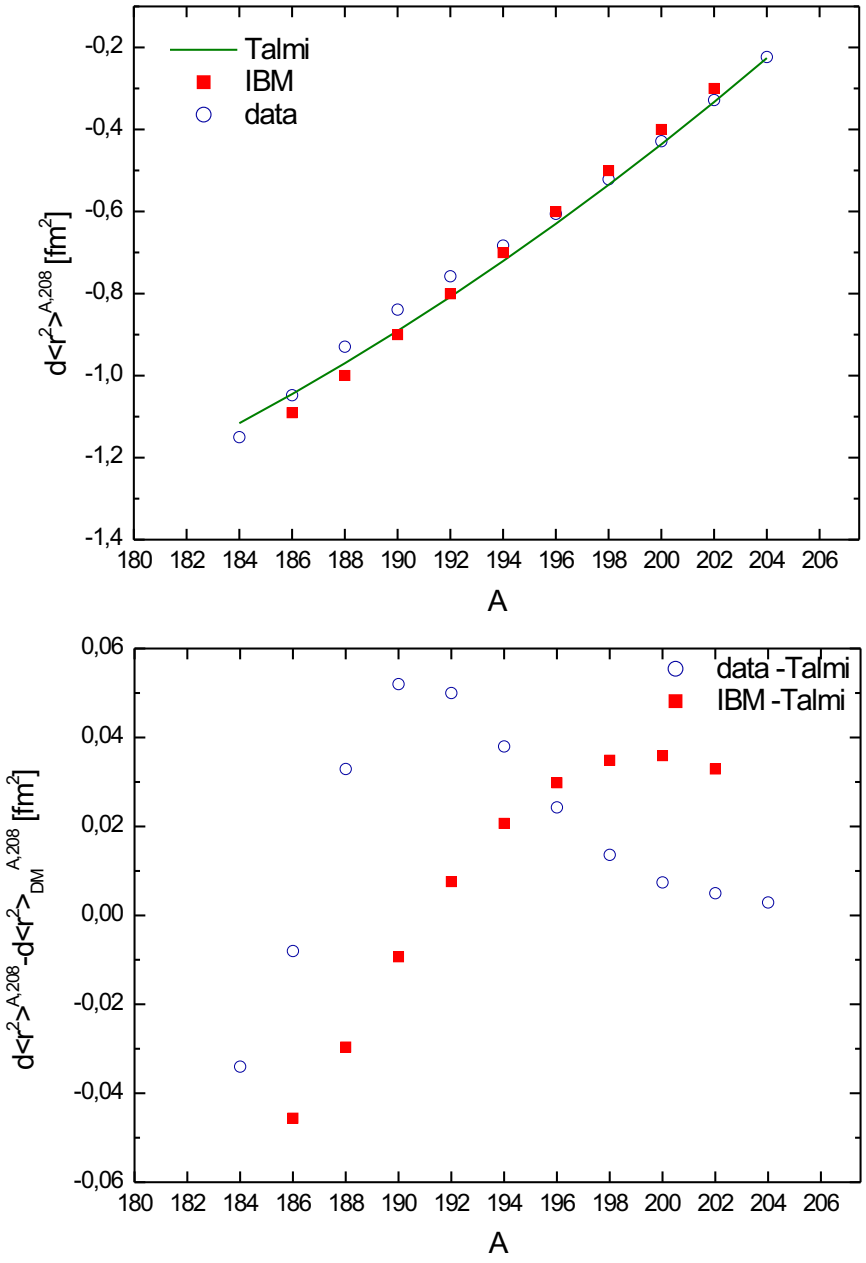

Figure 6.13: Top: Mean squared charge radii for the even-even lead isotopes. The experimental error bar is smaller than the symbol size. Data are compared to the empirical rule developed in [Tal84]. Parameters used in Eq. 6.9 are A=-0.001 fm^2, B=0.050 fm^2 and C'=0.058 fm^2 and were obtained by a least-squares fit to the data from $^{198-207}$Pb. Bottom: Experimental and calculated (IBM) deviation from the same empirical rule.

and subsequent mixing of the results. The $2p$-$2h$ excitations are formally included by the addition of two extra bosons. A simultaneous description of the coexisting configurations, $0p$-$0h$ (regular), $2p$-$2h$ and $4p$-$4h$ requires the inclusion of three different subspaces in the calculation: $[\mathrm{N}]\oplus[N+2]\oplus[N+4]$. The total Hamiltonian can be written as

$$\mathcal{H} = \mathcal{H}_{reg} + \mathcal{H}_{2p-2h} + \mathcal{H}_{4p-4h} + \mathcal{H}_{mix}, \tag{6.10}$$

where each separate contribution is written as

$$\mathcal{H}_{mp-mh} = \varepsilon \hat{n}_d + \kappa \hat{Q}_\pi \cdot \hat{Q}_\nu + \Delta_{mp-mh}, \tag{6.11}$$

where $\hat{n}_d$ is the d-boson number and ε is the energy difference between s and d bosons. The second term is the quadrupole-quadrupole interaction, with $\hat{Q}_{\pi,\nu}$ the quadrupole operator for protons and neutrons, respectively:

$$\hat{Q}_\rho = (s^\dagger_\rho \tilde{d}_\rho + d^\dagger_\rho \tilde{s}_\rho)^{(2)} + \chi_\rho (d^\dagger_\rho \tilde{d}_\rho)^{(2)}, \tag{6.12}$$

with $\rho = \pi, \nu$ and χ_ρ the ratio of the seniority conserving versus the seniority non-conserving part. The parameter Δ_{mp-mh} represents the energy needed to create the mp-mh excitation, corrected for the gain in pairing energy [Hey87].
The mixing Hamiltonian is given by

$$\mathcal{H}_{mix} = \mathcal{H}_{0p-0h/2p-2h} + \mathcal{H}_{2p-2h/4p-4h}. \tag{6.13}$$

Direct mixing between the regular and the $4p-4h$ configurations is absent and

$$\mathcal{H}_i = \alpha_i (s^\dagger_\pi s^\dagger_\pi + \tilde{s}_\pi \tilde{s}_\pi)^{(0)} + \beta_i (d^\dagger_\pi d^\dagger_\pi + \tilde{d}_\pi \tilde{d}_\pi)^{(0)}, \tag{6.14}$$

with $i = 0p-0h/2p-2h, 2p-2h/4p-4h$ mixes states with the same angular momentum. The mixing parameters are different for the two terms of Eq. 6.13, but are kept constant in the chain of lead isotopes down to the mid-shell. As a consequence, the results are symmetric with respect to the N=104.

This method has been applied to the neutron deficient lead isotopes [Fos03] and allowed to deduce an estimate of the mixing of the deformed configurations in the spherical ground states. The results of this mixing calculation are presented in Table 6.6. The resulting small mixing in the ground states of the heavier isotopes $^{190-194}$Pb agrees well with the experimental observation of [Den92], but for the lighter isotopes no such experimental data are available. For the mid-shell isotope, ^{186}Pb, a mixing of 25 % of the (oblate + prolate) deformed configurations in the 0^+ ground state is predicted and is expected to yield a sizeable effect on the charge radii. It should be noted, however,

Table 6.6: Constitution of the 0^+ ground state in the lead isotopes with A=186-196 calculated in the IBM framework. Magnitudes of the regular, $2p-2h$ and $4p-4h$ contributions are given in percent. Results are taken from [Fos03].

configuration	^{186}Pb	^{188}Pb	^{190}Pb	^{192}Pb	^{194}Pb	^{196}Pb
reg	75	93	96	98	99	99
2p-2h	18	7	4	2	1	1
4p-4h	7	1	0	0	0	0

that this strong mixing does not allow to reproduce the three minima that have been experimentally observed [And00]. The deduced potential energy surface in the geometric interpretation of the IBM solution [Fra04] only shows a spherical and a prolate minimum. A reduced mixing can solve this problem and restore the oblate minimum. Therefore, the mixing parameters α_i and β_i have been reduced in the present calculation of the monopole moments.

The nuclear radii in the IBM are usually parameterized as [Har97]

$$r^2 = r_c^2 + \gamma\langle\hat{n}_s\rangle + \beta\langle\hat{n}_d\rangle, \tag{6.15}$$

where r_c^2 is the core radius and $\hat{n}_{s,d}$ are the number operators of s and d bosons, respectively. This formula includes both the linear variation of the radius with the increasing number of bosons, as well as the deformation dependence through $\hat{n}_d$.

This approach has been used to calculate the charge radii of the even-even lead isotopes with A=186-202 (R. Fossion and K. Heyde [Fos04]). The results of this calculation are shown in Fig. 6.14, in comparison with the experimental data, and plotted as a deviation from the droplet prediction. The parameter γ is adjusted to reproduce the trend of the heavier isotopes, where deformation does not play a role. The parameter β has a major influence only on the radius of ^{186}Pb, where the only sizeable mixing is expected in the ground state. The values for β and γ were 0.4 and -0.1, respectively. The IBM results display an increasing deviation from the droplet model, but the slope is not as steep as the one of the experimental data (Fig. 6.14, bottom).

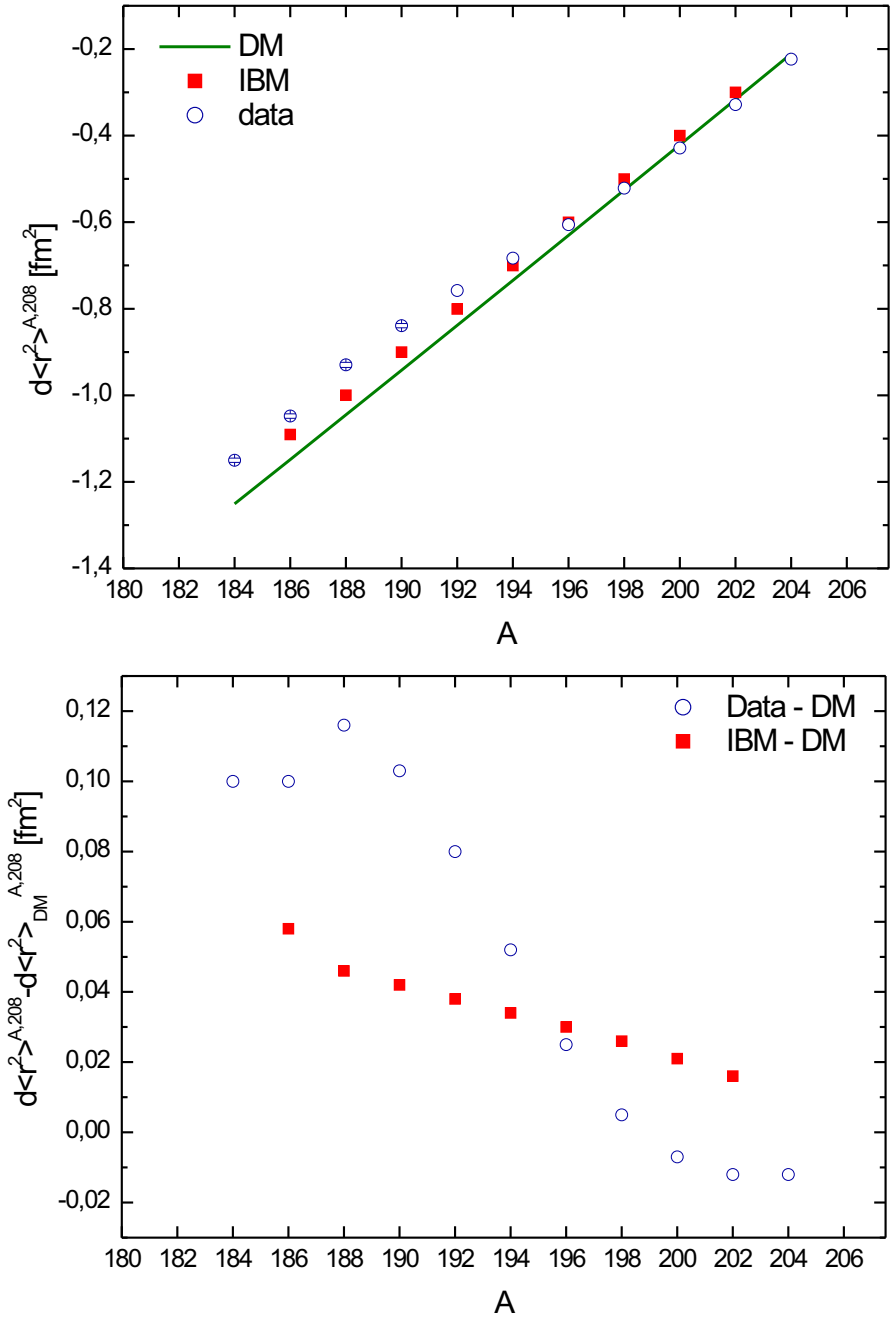

Figure 6.14: Top: Mean squared charge radii for the even-even lead isotopes. The experimental error bar is smaller than the symbol size. Data are compared to the spherical droplet model prediction and the IBM model (Sect. 6.4.2). Bottom: Experimental and calculated (IBM) deviation from the droplet model.

6.4.3 Generator Coordinate Model

The starting point of the generator coordinate model is a self-consistent mean-field calculation. The state vectors $|q\rangle$ are generated in the Hartree-Fock+BCS framework with a constraint on a collective coordinate, the quadrupole deformation in the present case. The wave functions of a deformed nucleus in the intrinsic frame break the rotational symmetry. Projection on angular momentum and on particle number, a symmetry broken by the BCS approach, results in a set of GCM states:

$$|JMq\rangle = \frac{1}{\mathcal{N}} \sum_K g_K^J \hat{P}_{MK}^J \hat{P}_Z \hat{P}_N |q\rangle, \tag{6.16}$$

where $\mathcal{N}$ is a normalization factor and $\hat{P}_{MK}^J, \hat{P}_Z$ and $\hat{P}_N$ are the projection operators onto angular momentum J, proton and neutron number, respectively. M and K are the angular momentum projections on the laboratory and the intrinsic z-axis, respectively. In the limit of axial and time-reversal symmetry, K is zero and the sum over K in Eq. 6.16 disappears. Subsequently, configuration mixing with respect to the collective coordinate, produces the final wave functions

$$|JMk\rangle = \sum_q f_{J,k}(q) |JMq\rangle \tag{6.17}$$

in a variational calculation. As these states have good angular momentum, the deduced moments and transition probabilities can be compared to the spectroscopic data in the laboratory frame.

This approach has been applied to the excitation spectra of the neutron deficient even-even lead isotopes in [Dug03, Ben04]. Agreement is obtained for the prolate 0^+ states, but the oblate bandhead energies are largely overestimated. The monopole transition strength $\rho^2(E0)$ has been calculated [Ben04] and compared to the experimental results of Dendooven *et al.* [Den89] for $^{190-194}$Pb. If the 0_2^+-0_1^+ transition observed in [Den89] is associated with the calculated oblate-spherical transition, then the calculation overestimates the experimental value by an order of magnitude. Therefore it is suggested that the model predicts a too large mixing of the oblate and the spherical configurations (see Eq. 3.9).

Proton radii[6] have also been calculated by M. Bender and P.-H. Heenen [Hee04]. The results are presented on the left side of Fig. 6.15. The deviation between the mean

[6] Proton radii, rather than charge radii, are calculated. No influence of the finite size of the proton is included. The substructure of the neutron is included in first approximation through a term N/Z r_n^2, with r_n^2 = -0.117 fm^2 the mean squared radius of the free neutron.

field and the GCM results is related to the spreading of the 0^+ ground state wave function in deformation space after the configuration mixing. This wave function is plotted on the right side of Fig. 6.15. Including the correlations beyond the mean-field, the agreement is satisfactory for the heavier isotopes ^{194,192}Pb. Approaching the neutron mid-shell, where the prolate configuration is also present at low energy, the calculation fails to reproduce the observed trend. In order to draw further conclusions, however, the influence of triaxiality should be taken into account. The treatment of pairing in these calculations could also be improved.

As the calculated energy of the oblate band is found to be too high in energy, the oblate-spherical mixing is expected to be too weak in the calculation. Increasing the mixing would bring the calculated $\langle r^2 \rangle$ closer to the experimental observations. However, a larger mixing would make the disagreement with the $\rho^2(E0)$ data even stronger.

Mixing of the prolate configuration into the ground state is small in these calculations, because of the higher barrier separating prolate and spherical states. Experimentally, however, it has been shown that in the lighter isotopes the prolate mixing dominates over the oblate mixing in the ground state [Dra03].

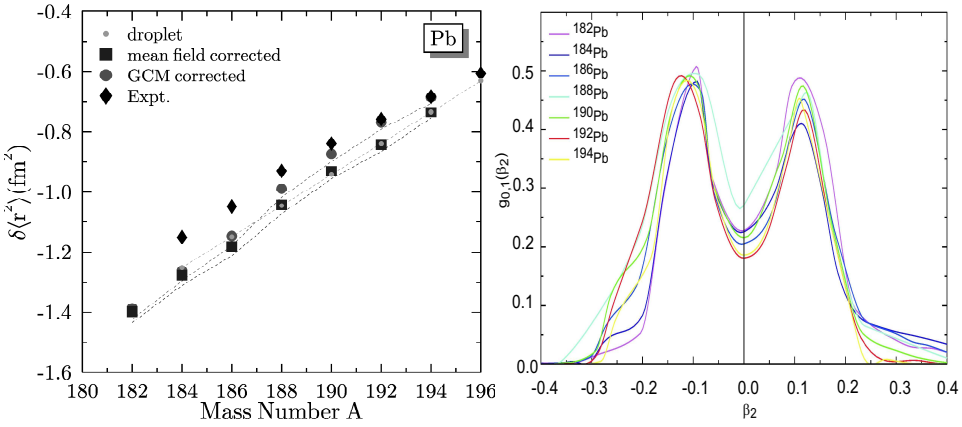

Figure 6.15: Left: Mean squared charge radii compared to the results from the spherical mean field and GCM calculations. The droplet curve is shown for reference. Right: GCM collective wave function of the 0^+ ground state in the intrinsic frame.

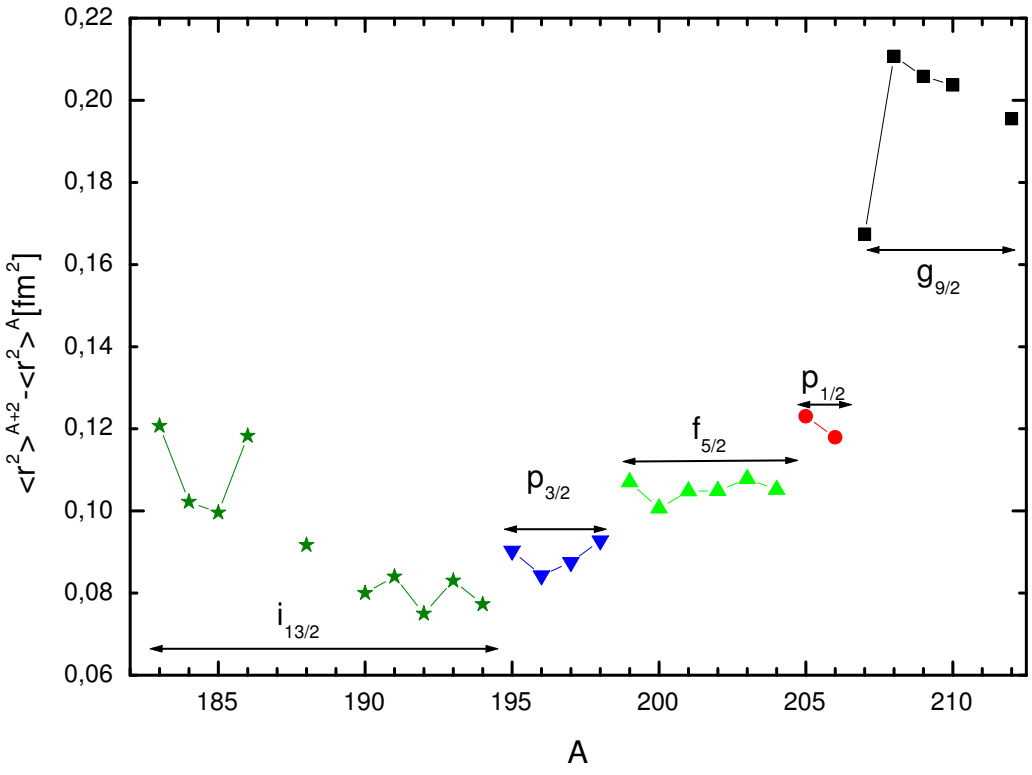

Figure 6.16: Brix-Kopfermann plot: differential isotope shift for the lead nuclei. The neutron orbital being filled in an extreme single-particle model is also given. Data for $^{183-188}$Pb taken from this work. The results for the heavier isotopes are from [Tho83, Ans86, Dut91]. In this plot, the droplet prediction would give an almost constant value of 0.10.

6.4.4 Sub-shell effects

An alternative representation of the charge radii is the Brix-Kopfermann plot: rather than the deviation from ^{208}Pb, the isotope shift between A,A+2 pairs of isotopes is displayed. This approach magnifies the subshell effects and simultaneously shows how the droplet model fails to account for any fine structure in the variation. The discontinuities at A=199 and 195 can be associated with a change in the orbital occupied by the odd neutron, resulting from the filling of the subsequent orbitals. Below A=195, the odd neutron resides in the $\nu i_{13/2}$ orbital, assuming a simple gradual filling of the shells. Surprisingly, the more neutron deficient isotopes with A$\leq$190 deviate from these clear trends.

6.4.5 Conclusion

As a conclusion, we can state that the lead ground states preserve their predominantly spherical character, with only limited mixing of the deformed intruder states. No odd-even staggering like the one observed in the mercury isotopes is observed. However, a better theoretical understanding of the observed deviation of the radii from the spherical droplet model is required, before any quantitative information on the admixture of the deformed configurations in the ground state can be extracted from the data presented in this work. If this deviation would be entirely associated with an axial quadrupole deformation using Eq. 3.10, an almost constant deformation $\langle\beta_2^2\rangle^{1/2} \sim 0.11$ would result for $^{190-184}$Pb.
Qualitatively, the preserved sphericity confirms the conclusions drawn from α decay studies. The ground state and intruder configurations in the mercury isotopes were shown to be almost pure, with an admixture of < 3 %. Combined with the hindrance factor deduced from the α decay from the lead ground state to the intruder state (HF = 21), Wauters *et al.* concluded that the mixing in the ground state of ^{188}Pb and ^{186}Pb should be small [Wau94]. Similar results were obtained from two- and three-level mixing calculations. From the charge radii, however, these conclusions are reached through direct observation, without any further assumptions.
In the lighter isotopes, the spherical-prolate mixing seems to dominate. In ^{188}Pb a 4% mixing of the prolate configuration in the 0^+ ground state was derived from a three-band mixing calculation [Dra03], compared to 1% of oblate admixture. In-band B(E2) values, deduced from lifetime measurements [Dew03], also suggest a predominantly prolate character for the 2_1^+ state in ^{188}Pb. High quality data for ^{186}Pb have recently been obtained at Jyväskylä.

The above discussion exclusively concentrated on the even-even isotopes. However, the charge radii of the odd-A isotopes follow similar trends, preserving their predominantly spherical character. Deformed states have been identified in ^{185}Pb, less than 300 keV above the spherical $3/2^-$ α-decaying state [And99a]. They have been associated with prolate minima, but in contrast to the odd-A mercury isotopes they do not become the ground state.

Chapter 7

Summary and future perspectives

In this work, a detailed β decay study has been performed of a selection of neutron-rich isotopes in the vicinity of ^{208}Pb. Results are presented on the decay of ^{213,215}Pb and ^{218}Bi. In a second part, a laser spectroscopic measurement of the neutron-deficient lead isotopes with A=183-188,190 is discussed. Charge radii and magnetic moments have been deduced.

Proton induced spallation of a heavy target nucleus has been used to produce nuclei in the scarcely explored region of neutron-rich isotopes near the Z=82 closed shell. The experiments were carried out at the ISOLDE on-line mass separator. The pulsed release of the activity was crucial in these studies: it allowed to suppress efficiently the higher-Z, surface ionized contaminations, which are abundantly produced in this mass region. This technique was used to extend the spectroscopic knowledge of the heavy bismuth isotopes and their β decay up to ^{217}Bi [Kur00, Kur03a, Kur03b]. In this work, the β decay of ^{213}Pb, produced in the ^{217}Bi decay chain is discussed.

Another major improvement of the set-up arises from the use of the elemental, or even isomeric, selectivity of the resonance ionization laser ion source (RILIS). The combination with the pulsed release provided the necessary selectivity to extend the systematics to ^{215}Pb. This isotope was identified unambiguously and β decay information was obtained. The RILIS discriminated clearly between the ^{215}Pb decay and the previously observed isomeric decay from ^{215m}Bi [Kur03b].
The evolution of the proton mean-field is followed in the odd-A bismuth daughter nuclei. A strongly downsloping trend was observed in the excitation energy of the first

excited state, presumably associated with a $\pi f_{7/2}$ configuration, relative to the $\pi h_{9/2}$ ground state (see Fig. 4.13). Observed in different closed shell regions, this behaviour was explained as an effect of the proton-neutron monopole interaction. A more concise understanding of this phenomenon in the bismuth isotopic series, however, needs further calculation.

Using the same experimental methods, the β decay of ^{218}Bi towards ^{218}Po was studied for the first time. The half-life has been deduced and a level scheme was built, on the basis of γ-γ coincidence relations. In the closed shell nucleus ^{210}Po, the spectrum corresponds to a pure broken-pair configuration. When, in addition, neutron pairs occupy the high-j orbitals beyond N=126, the nucleus will evolve towards a more collective behaviour, due to the interaction of the neutron pairs with the $(\pi h_{9/2})^2$ proton pair. The results for ^{218}Po have been compared to theoretical calculations in the shell model framework. The theoretical spectrum recalls the typical δ-interaction pattern, where the 4^+-6^+-8^+ states remain very close in energy, in contrast to the experimental observations (see Fig. 4.23).

The experiments with laser ionized thallium isotopes failed, both in the β-γ spectroscopy and the β-delayed neutron emission measurements. The latter experiment was meant to measure the half-lives of the neutron-rich thallium isotopes with A=211-215. From cross section calculations, as well as from off-line ionization efficiency measurements, the production was estimated to be sufficiently high. The non-observation of any resonantly ionized thallium still lacks a satisfactory explanation.

For the extension of these spectroscopic studies to even more neutron-rich nuclei, improved production, selection and detection methods are awaited. In particular for the heavier bismuth isotopes, where the pulsed release technique cannot be applied anymore, the isobaric contamination impedes a further study.

At the neutron deficient side, shape coexistence phenomena have received ample attention over the last decades, with the aim of characterizing the intruder states in a large series of isotopes. In the lead isotopes, the coexistence of deformed states at low excitation energy has been observed when approaching the neutron mid-shell between N=82 and N=126. The excitation energy is expected to reach a minimum at N$\sim$104, that is, when the neutron shell is half-filled. In ^{186}Pb, the occurrence of three 0^+ states at low excitation energy reflects the presence of three configurations with different deformations, spherical, oblate and prolate deformed, respectively [And00]. The mixing

of the coexisting configurations is an important input parameter for the full understanding of the low-energy structure in these nuclei. Alpha decay and bandmixing models only partially provide this information. The E0 transition probabilities and the charge radii, corresponding to the diagonal E0 matrix elements, are particularly sensitive to the mixing of configurations with different deformations.

The RILIS has been used for in-source atomic spectroscopy of the neutron deficient lead isotopes, $^{188-183}$Pb. The laser frequency is scanned across the first excitation step of a multi-step excitation scheme (Fig. 2.4) and the characteristic (α or γ) decay radiation of the produced lead ions is simultaneously detected. The resulting scanning curve contains the necessary information to deduce the isotope shift and the hyperfine constants, physically related to the nuclear charge radius and the nuclear magnetic moment. The extreme sensitivity of this method allowed the extension of the charge radii systematics to the most interesting region near the neutron mid-shell. A nearly spherical shape is deduced and odd-even staggering near the neutron mid-shell, like the one observed in the mercury neighbours, is absent (see Fig. 6.12). From the comparison with the spherical droplet model, however, a smaller deviation is observed between A=194 and A=183. Different theoretical approaches, namely the algebraic IBM and the Generator Coordinate Model, have been considered, but no satisfactory explanation has been found.
In addition, the magnetic moment has been deduced for the I=13/2$^+$ and I=3/2$^-$ states in the odd-A isotopes. They are consistent with those measured in the heavier lead isotopes [Dut91] and suggest a rather pure single-particle configuration for these states, corresponding to an odd neutron in the $i_{13/2}$ and $p_{3/2}$ orbitals.

In the near future these measurements will be extended to ^{182}Pb. Because of its short half-life ($T_{1/2}$=55^{+40}_{-35} ms), combined with the lower cross-section, the limits of the present technique will be reached with this experiment.
An alternative determination of the mixing strength is based on life time measurements of the excited 0$^+$ states in the even-even isotopes. These measurements were performed only for the heavier isotopes $^{194-190}$Pb [Den89]. An extension of this approach to the mid-shell isotopes would give direct access to the mixing parameters, even in the case of small admixtures.
Another interesting case for atomic spectroscopy studies is the region of neutron-deficient polonium isotopes near mid-shell. In contrast to the lead isotopes, where the ground state remains spherical, α decay studies showed that the deformed configurations dominate in the ^{190,188}Po ground states. A mainly oblate, resp. prolate

character was suggested for ^{190}Po and ^{188}Po [Van03b]. Moreover, in the odd-A isotope ^{191}Po shape staggering, comparable to the mercury case, has been inferred from α-decay studies [And99c]. The difference of the coupling of the odd neutron between the positive and negative parity states gives rise to a different shape for the ground state and the isomeric state. However, the ionization scheme for resonance ionization has not been tested at ISOLDE so far.

To conclude, we should mention that the recent and future radioactive ion beam facilities open up a wide range of experimental possibilities, offering new target and beam combinations. In particular for the intruder states in the neutron deficient lead isotopes, transfer reactions could offer complementary information on the underlying microscopic structure of the intruder states, as was shown for the tin isotopes in Sect. 3.2.4. Experiments using radioactive mercury beams are being considered at the REX-ISOLDE facility.

Appendix A

Electronics and data acquisition

Figure A.1 sketches the electronics set-up used in run IV. We briefly describe the main items below.
After amplification and shaping (*Amp*), the preamplifier signal of the silicon detector is sent to an ADC, where the pulse height is converted for digital treatment by the data acquisition. Its timing signal is processed by a timing filter amplifier (*TFA*) and a constant fraction discriminator (*CFD*), which produces a fast negative signal.
The *laser veto* serves as a suppression of the electromagnetic noise with a frequency of 11 kHz, corresponding to the repetition rate of the CVL lasers and picked-up by the detector's preamplifier.

For synchronization purposes, both the laser control and the data acquisition give a *ready* signal, whenever they can be (re)started. Combined in a logical AND-gate with the supercycle signal, these logical signals start a clock (called *MC, master clock* in the drawing) which determines the duration of a measurement on a specific laser frequency setting. This cycle is also imposed on the laser control, dictating the frequency changes.
The logical AND of the $\overline{\text{laser veto}}$, the fast α timing and the MC level, are used as a gate on the ADC and as a DAQ trigger signal (*Coincidence Trigger*). The Coincidence trigger unit produces a trigger pulse whenever two signals arrive within a preset coincidence window, 1 μs in this case. Presenting the α signal twice at its input, with a 40 ns time difference, reads the α singles data in list mode.
In addition, a time-to-digital convertor (*TDC*) measures the time difference between the start of the measurement cycle and the triggered event.
A separate clock triggers the read-out of the serial buffer of the DAQ power-PC for the wavelength read-out (λ *read-out*).
Finally, the wheel of the wind-mill system was moved after a preset time (see Ta-

ble. 6.1), synchronized either by the start of the MC or by the supercycle.

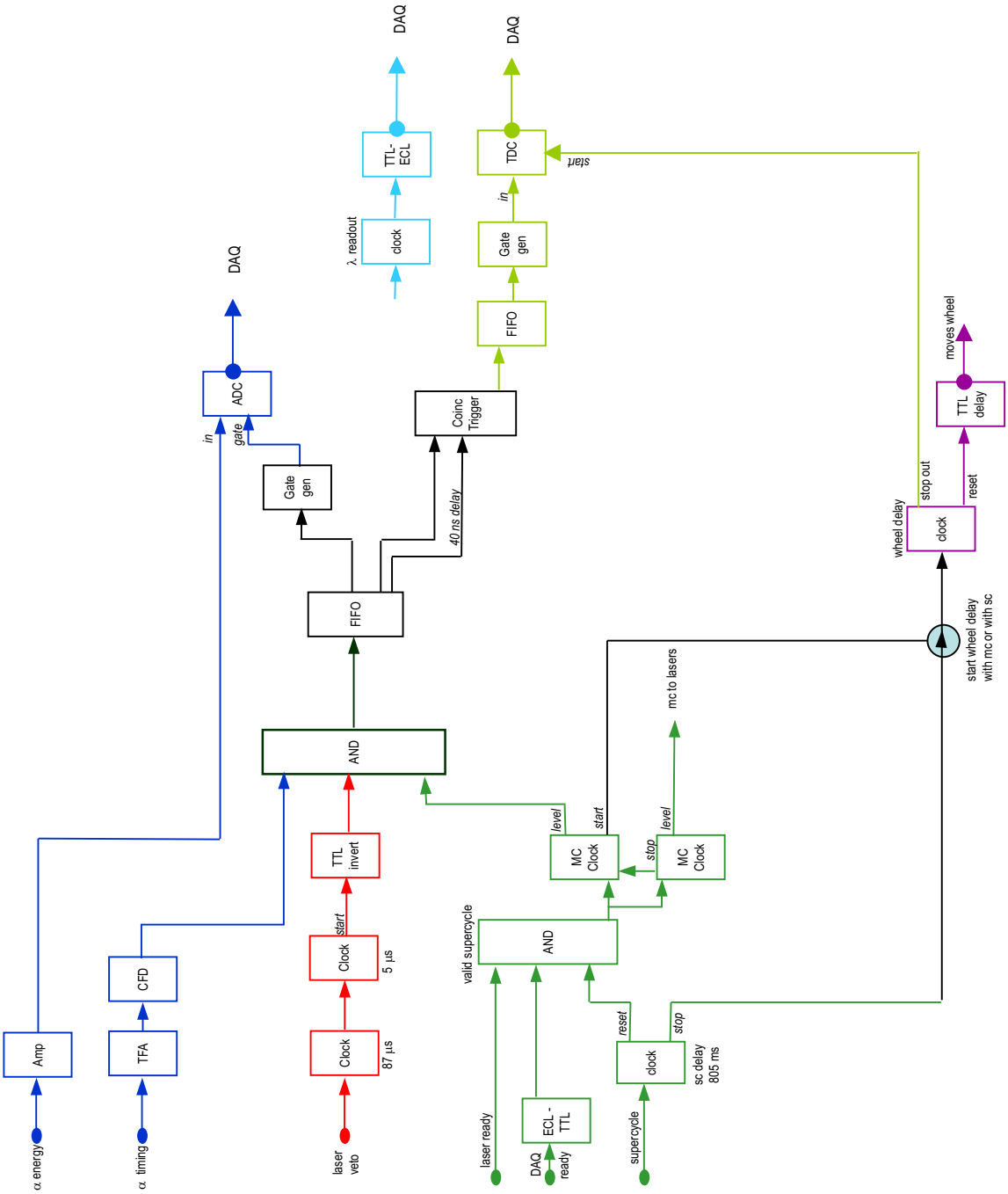

Figure A.1: Electronics scheme of the set-up used for the laser spectroscopic measurements in run IV.

Appendix B

Geant package for efficiency calculations

Rather than calibrated γ-sources, the GEANT simulation package has been used for the γ efficiency determination in run II. This CERN-developed tool simulates and visualizes the trajectory of particles through matter using the Monte Carlo method, as well as the detector response. The validity of this method for efficiency determination has been proven for a similar detection set-up in [Wei99].

As an input the program requires the precise description of the geometry and materials of the set-up. Typically 10^5 mono-energetic γ-rays are emitted in random directions. The energy deposited in the detector is calculated for every single event. This results in an energy spectrum, from which the photopeak efficiency and the total efficiency, needed to correct summing effects, are determined. This procedure is repeated for different energies in the detector range. As the results strongly depend on the detector-source distance, the relative efficiency is more reliable than the absolute one. The resulting efficiency curve ε-E is fitted with the following function (for 190 keV<E_γ <1400 keV for 75% and 70%; for 170 keV<E_γ <800 keV for LEGe):

$$log(\varepsilon) = A + B \times log(E). \tag{B.1}$$

The numerical results for the $\beta\gamma$ detector set-up used in run II are summarized in Table B.1.

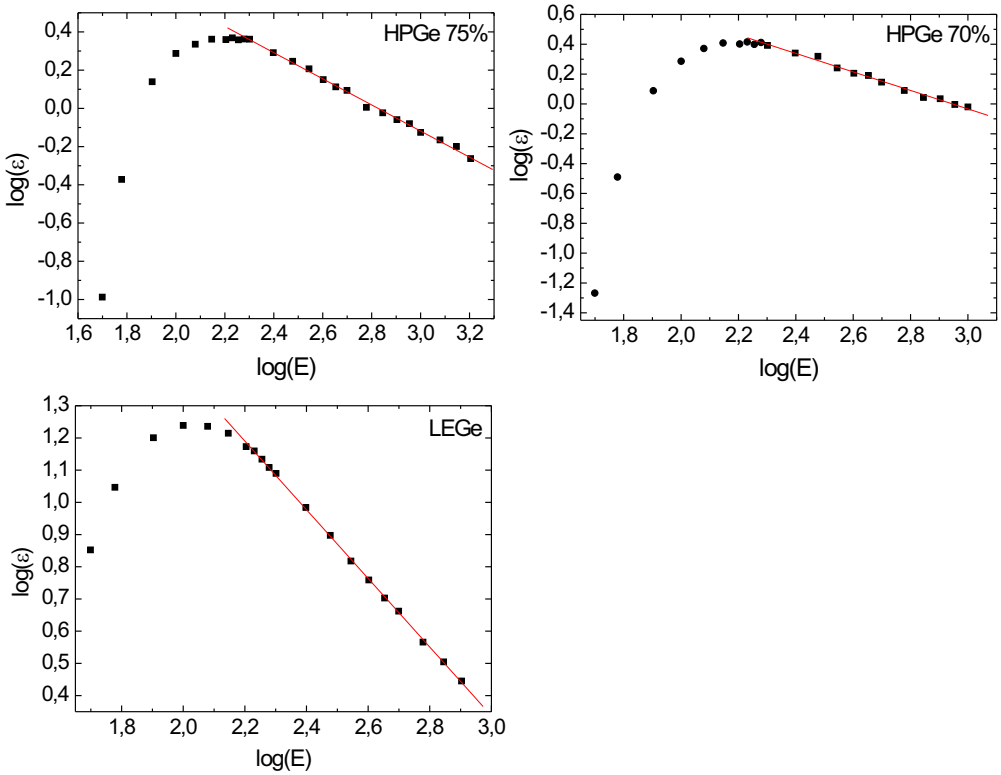

Figure B.1: GEANT results for the photopeak efficiencies of the germanium detectors used in run II.

Table B.1: Photopeak (Top) and total (Bottom) efficiencies simulated for the detectors used in run II, calculated using GEANT.

detector	A	B
75%	2.15 ± 0.03	-0.70 ± 0.01
70%	1.75 ± 0.02	-0.60 ± 0.01
LEGe	3.52 ± 0.02	-1.09 ± 0.01
75%	1.13 ± 0.02	-0.16 ± 0.01
70%	0.91 ± 0.02	-0.12 ± 0.01
LEGe	1.84 ± 0.01	-0.24 ± 0.01

Appendix C

Two-level mixing calculation

Consider two states denoted by ϕ_1 and ϕ_2 with energies E_1 and E_2, respectively, as shown in Fig. C.1. The residual interaction mixes these states and the resulting mixed wave functions can be written as linear combinations of the basis states ϕ_1 and ϕ_2:

$$\Phi_I = \alpha\phi_1 + \beta\phi_2 \tag{C.1}$$

$$\Phi_{II} = -\beta\phi_1 + \alpha\phi_2 \tag{C.2}$$

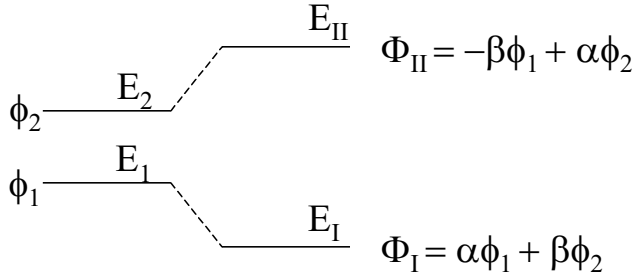

Figure C.1: Schematic illustration of two-state mixing. For definitions and notations, see text.

Their energy results from the diagonalization of the 2×2 matrix

$$H = \begin{pmatrix} E_1 & V \\ V & E_2 \end{pmatrix} \tag{C.3}$$

The eigenvalues depend on the unperturbed energies and the magnitude of the mixing matrix element, V, and are given by:

$$E_{I,II} = \frac{E_1 + E_2}{2} \pm \sqrt{\left(\frac{E_1 - E_2}{2}\right)^2 + V^2} \tag{C.4}$$

The mixing amplitudes α and β are calculated by combining the expression

$$\alpha(E_1 - E_I) + V\beta = 0 \tag{C.5}$$

with the normalization condition $\alpha^2 + \beta^2 = 1$.
In terms of the dimensionless ratio R=(E_2-E_1)/V, the amplitude β can be written as

$$\beta = \frac{1}{\sqrt{1 + \left(\frac{R}{2} + \sqrt{1 + \frac{R^2}{4}}\right)^2}} \tag{C.6}$$

The mixing amplitudes α and β are functions only of R, the ratio of the unperturbed energy difference to the mixing matrix element. Using this formalism it is possible to determine the unperturbed energies starting from the experimentally observed (perturbed) energies ($E_{I,II}$) of two levels, and vice versa, if the interaction matrix element V is known.

Appendix D

Alpha decay of neutron-deficient ^{200}Fr and heavier neighbours

In the neutron-deficient nuclei around Z=82, shape coexistence phenomena induced by proton excitations across the shell gap have been observed [Woo92, Jul01b]. A large amount of experimental data has been obtained through α and β decay studies as well as in-beam studies, focussing mainly on even-even nuclei. In the odd and odd-odd mass nuclei, proton excitations across the Z=82 shell gap give rise to isomerism, which can be investigated via α decay in *e.g.* the francium isotopes which disintegrate through the corresponding astatine and bismuth to thallium nuclei (see *e.g.* [Huy92]). A renewed interest in the study of very neutron-deficient francium isotopes resulted in conflicting results with respect to reported half-lives and to the observation of isomeric α decay. In particular, the α decay of ^{200}Fr was investigated in fusion-evaporation reactions at the recoil separators GARIS (RIKEN) [Mor95] and RITU (JYFL) [Enq96]. Both experiments report the observation of ^{200}Fr α decay, but with very different half-life values: $E_\alpha = 7500(30)$ keV and $T_{1/2} = 570^{+270}_{-140}$ ms in [Mor95] and $E_\alpha = 7468(9)$ keV and $T_{1/2} = 19^{+13}_{-6}$ ms in [Enq96]. These results were obtained by requiring spatial and temporal correlations of the implantation of the mother nucleus, its α decay and that of the daughter nucleus. Only six correlated chains were observed in each experiment. In this paper we report on a new study of the very neutron-deficient francium and astatine isotopes using intense high-quality sources produced with an on-line mass separator.

D.1 Experimental details

The experiment carried out at the ISOLDE on-line mass separator, used a 1.4 GeV pulsed proton beam (2.9×10^{13} protons/pulse) impinging on a 51 g/cm^2 ThC$_x$/graphite target. After diffusion out of the 2150°C hot target, the reaction products were guided to a 2050°C hot niobium cavity. Due to their low ionization potential (4.07 eV), the francium atoms were efficiently ionized by surface ionization in the hot cavity. After mass separation by means of the General Purpose Separator, the 60 keV A=200 beam was implanted into a 20 μg/cm^2 carbon foil. After proton impact on the target, ions were implanted for 80 ms and the subsequent decay was recorded for 1120 ms, which was the time left before the next proton pulse.
Data were also collected at masses 201, 203 and 205. For these measurements the time sequence was altered: the implantation/decay cycles were 100 ms/1100 ms, 1000 ms/ 15800 ms and 40 ms/16760 ms for A=201, 203 and 205 respectively.
Behind the carbon foil, a Si-detector (area 150 mm^2, thickness 300 μm for A=200,203,205; area 450 mm^2, thickness 1000 μm for A=201) was placed at a distance of 7 mm. For calibration of the Si detector the following isotopes were used: ^{196}At (E$_\alpha$ = 7055(7) keV [nnd]), ^{200}Po (E$_\alpha$ = 5863(2) keV [Fir96]), ^{203}Fr (E$_\alpha$ = 7133(4) keV [nnd]), ^{197g}At (E$_\alpha$ = 6960(5) keV [Smi99]), ^{197m}At (E$_\alpha$ = 6707(5) keV [Smi99]) and ^{199}At (E$_\alpha$ = 6643(3) keV [nnd]). These isotopes were produced in irradiations or as daughter activities at different masses. The α energy resolution was 30 keV FWHM for the data collected at mass 200, 203, 205 and 55 keV in the case of A=201.

D.2 Experimental results and discussion

D.2.1 ^{200}Fr decay chain

Figure 3.2 shows the α energy spectrum obtained at mass 200 in $\sim$ 3 hours of data collection. The α-lines at 5863 keV and 6468 keV are attributed to ^{200}Po and ^{200}At, respectively. Despite a larger N/Z ratio, leading to a three to four orders of magnitude higher production rate in the target, as compared to ^{200}Fr, the ionization efficiency for these isobars is substantially lower due to their much higher ionization potential (8.42 and 9.65 eV respectively). The measured α decay energy of ^{200}Fr is 7473(12) keV, in agreement with the literature values (see table D.1). The yield for ^{200}Fr was 2×10^{-1} ions/s in our experiment, compared to 3×10^{-4} ions/s in [Enq96].

The inset in fig. 3.2 shows the time behaviour of the α intensities for the ^{200}Fr and ^{196}At lines. The data for ^{200}Fr were fitted using a single exponential function

Table D.1: Energies and half-lives for α lines accompanying the Fr and At decays. (a) This α line has been used for energy calibration

Isotope	Energy[keV]	$T_{1/2}$	reference
^{200}Fr	7473(12)	49(4) ms	this work
	7500(30)	570^{+270}_{-140} ms	[Mor95]
	7468(9)	19^{+13}_{-6} ms	[Enq96]
^{196}At	7055(12)$^{(a)}$	389(54) ms	this work
	7053(30)	320^{+220}_{-90} ms	[Mor95]
	7044(7)	390^{+270}_{-120} ms	[Enq96]
	7048(5)	388(7) ms	[Smi00]
	7065(30)	253(9) ms	[Pu 97]
	7055(7)	300(100) ms	[Tre67]
^{201g}Fr	7379(7)	67(3) ms	this work
	7361(7)	69^{+16}_{-11} ms	[Enq96]
	7369(8)	53(4) ms	[Uus03]
	7388(15)	48(15) ms	[Ewa80]
^{201m}Fr	7454(8)	19^{+19}_{-6} ms	[Uus03]
^{197g}At	6963(4)$^{(a)}$	390(16) ms	this work
	6956(5)	370^{+90}_{-60} ms	[Enq96]
	6960(5)	388(6) ms	[Smi99]
	6959(6)	340(20) ms	[Uus03]
	6957	350(40) ms	[Coe86]
^{197m}At	6707(5)	2.0(2) s	[Smi99]
^{203}Fr	7132(5)$^{(a)}$	0.560(15) s	this work
	7133(4)	0.55(2) s	[nnd]
^{199}At	6643(4)$^{(a)}$	6.92(13) s	this work
	6643(3)	7.2(5) s	[nnd]
^{205}Fr	6916(5)	3.80(3) s	this work
	6915(4)	3.85(10) s	[nnd]
^{201}At	6343(4)		this work
	6344(2)	89(3) s	[nnd]

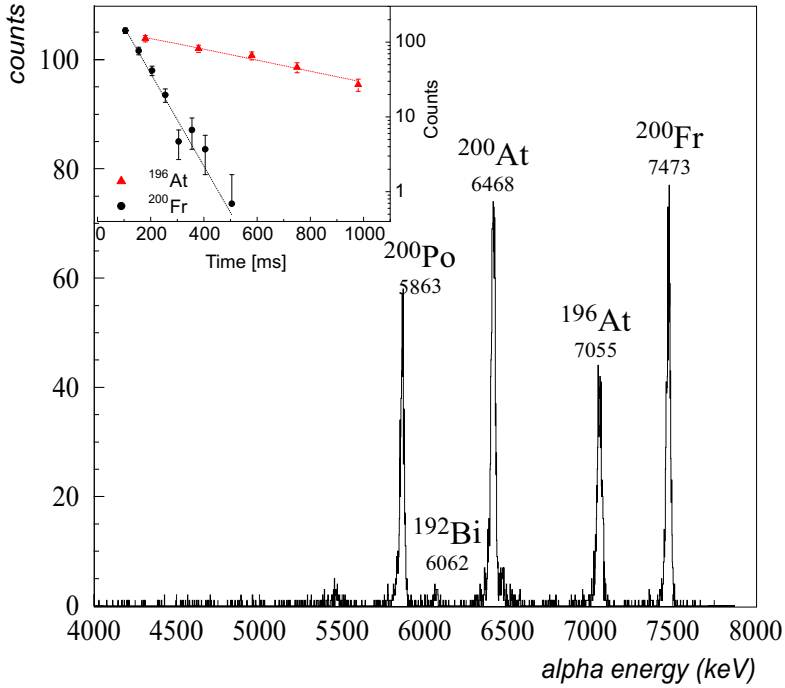

Figure D.1: The α spectrum recorded at A=200. The energy labels are in keV. The inset shows the time behaviour for the ^{200}Fr and ^{196}At activities.

combined with a constant background. The background, deduced from the part of the spectrum between 430 ms and 1200 ms after proton impact, represents 2.5% of the total intensity of the 7473 keV line. A half-life value of 49(4) ms is obtained, at variance with both the value obtained by Enqvist *et al.* [Enq96] and the earlier value by Morita *et al.* [Mor95]. The time behaviour of the ^{196}At α line intensity was fitted with a mother-daughter decay function; a half-life of 389(54) ms was deduced, which agrees with the earlier measurements, [Mor95], [Enq96] and [Smi00], but differs significantly from the value of Pu *et al.* [Pu 97], which used a fusion-evaporation reaction combined with the genetic correlation technique, similar to [Mor95] and [Enq96]. All data are summarized in table D.1.

The α-branching ratio for ^{196}At (only present as the daughter of ^{200}Fr) is obtained by comparing mother and daughter α intensities. After α decay, the daughter nuclei might recoil out of the catcher foil, decreasing the observed daughter activity. It should be noted that the recoil of daughter activity into the detector, enhancing the α detection efficiency for daughter activity, does not have to be considered as the thickness of the catcher foils is 20 μg/cm^2, compared to an average implantation depth of 8 μg/cm^2. A 25% recoil loss correction [Wau91], calculated with the SRIM simulation code [sri], was made. The final calculation yields an α-branching ratio of 94(5)% for

the decay of ^{196}At.
The α decay of ^{196}At proceeds to ^{192}Bi. The α lines from the decay of the 10^- (E_α = 6052 keV) and $(2,3)^+$ (E_α = 6060 keV) isomers of ^{192}Bi [Van91] could not be resolved within the experimental energy resolution. A spin assignment based on the α branching ratios of 12(5)% for the low spin and 10(3)% for the high spin isomer of ^{192}Bi [Van91] was also not feasible.

In the heavier odd-odd francium isotopes (A = 202, 204, 206), two or three isomeric, α decaying states were identified [Huy92]. In ^{200}Fr only one α branch could be identified in this study. The α-energy is the same in all measurements ([Mor95], [Enq96] and this work), within the experimental accuracy. However, one cannot exclude a doublet structure of this α-line, like *e.g.* in ^{202}Fr [Huy92]. In ^{202}Fr, both known α decays have similar decay properties (E_α = 7237 keV and $T_{1/2}$ = 0.34 s) and feed two α decaying isomers in ^{198}At, with different half-lives and tentative spin assignments of 3^+ and 10^-. A similar structure in ^{200}Fr cannot be excluded, but the observation of only one α branch in the daughter makes this assumption unlikely.
Three different half-life values have been measured for the ^{200}Fr decay. However, the result obtained at RITU [Enq96] and our data follow the systematics of the heavier isotopes, shown in a Geiger-Nuttall plot in fig. D.2. The value of [Enq96] has been determined on the basis of 6 events and meets the problem of estimating the accidental correlations which could affect the half-life determination. In our experiment, the good quality of mass-separated ISOL beams was exploited and the statistics were about 50 times higher.
The production mechanism used in the present work, high-energy proton induced spallation of ^{232}Th, is different from the heavy ion fusion evaporation reactions used in [Mor95], ^{169}Tm(^{36}Ar,5n) and [Enq96], ^{170}Yb(^{35}Cl,5n), which might lead to the population of different isomers in this study compared to [Mor95] and [Enq96]. However, a very different isomer population in the similar production mechanisms of [Mor95] and [Enq96] is not expected. In conclusion, our data do not show any evidence for α decay from an isomeric state in ^{200}Fr.

D.2.2 Odd-A francium isotopes: ^{201,203,205}Fr

Additionally, data were taken on the odd-A francium isotopes ^{201,203,205}Fr.

The obtained energies and half-lives are given in table D.1. In these nuclei, as in *e.g.* odd-A neutron-deficient bismuth and astatine isotopes, a $1/2^+$ shell model intruder state, resulting from a proton excitation from the $\pi s_{1/2}$ orbital, is expected and was

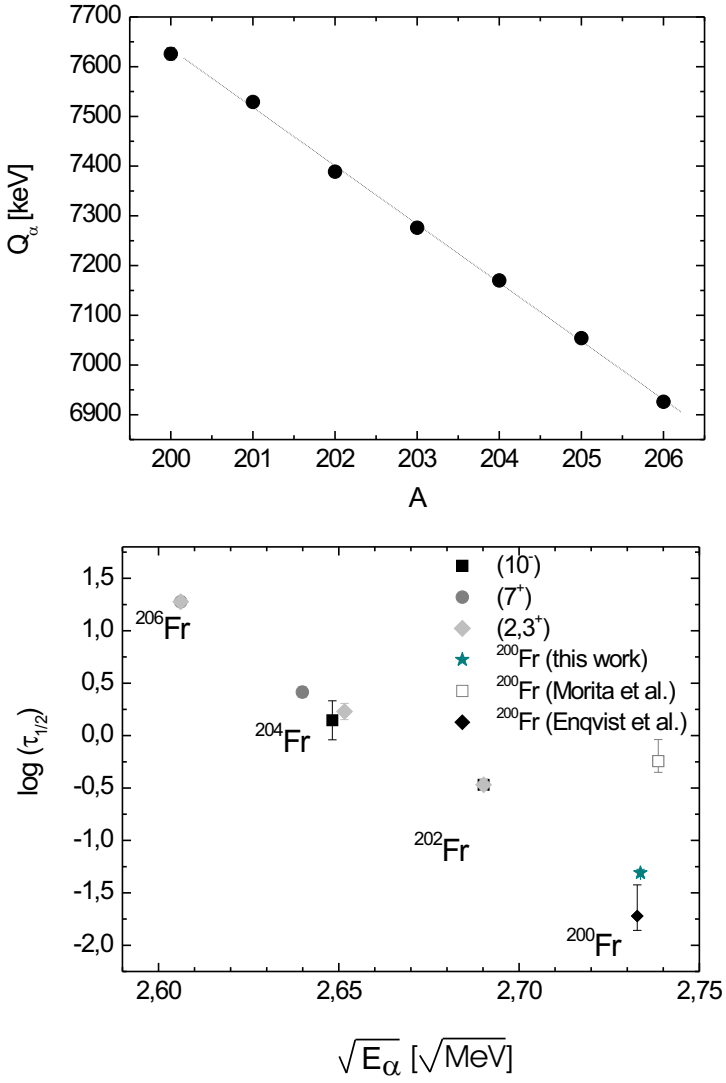

Figure D.2: Top: Q_α-systematics for the francium isotopes $^{200-206}$Fr. The straight line is shown to guide the eye; Bottom: Geiger-Nuttall plot for the even-A isotopes,$^{200-206}$Fr

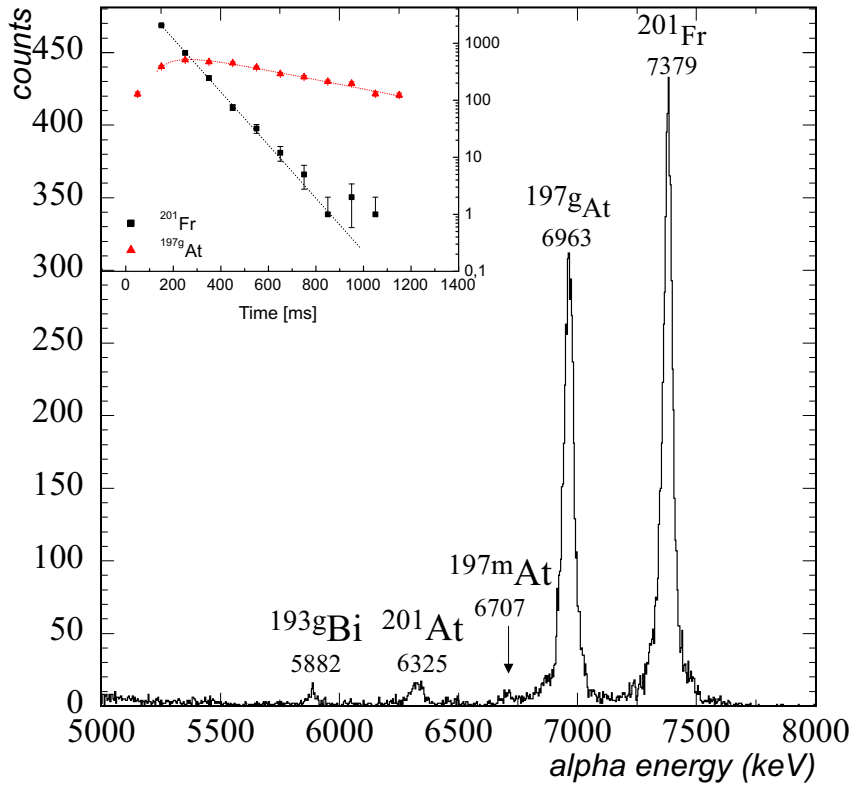

Figure D.3: Energy spectrum taken at A=201. The energy labels are in keV. The inset shows the time behaviour for the ^{201g}Fr and ^{197g}At activities.

observed for the first time at the RITU separator [Uus03] in ^{201}Fr. A compilation of the presently available experimental data is shown in fig. D.4, presenting the decay scheme for ^{201}Fr.

The energy spectrum obtained at mass 201 is shown in fig. D.3. Apart from the known α lines at 6325 keV from ^{201}At, 7379 keV from ^{201g}Fr and 6963 keV from ^{197g}At, the α transition of 6707 keV from the $1/2^+$ intruder state from ^{197m}At [Coe86] was observed. The presence of the latter α line at mass 201 can be explained by feeding from the α decay of the ^{201}Fr isomer as observed in [Uus03]. Indeed, the small shoulder at the high energy side of the 7379 keV α-line is probably caused by the presence of the 7454 keV α line of ^{201m}Fr. The extra α counts observed around 6475 keV could stem from the known α line of the decay of ^{193m}Bi and are consistent with the decay from the $1/2^+$ intruder states. Feeding from the ^{201}Fr ground state to the $1/2^+$ state in ^{197}At cannot be excluded but does not account for the observed intensity (see below).

The isomer ratio obtained for the production of the low spin state relative to the high spin state in ^{197}At was 3% (assuming b_α=100% for ^{197m}At). This value is comparable to

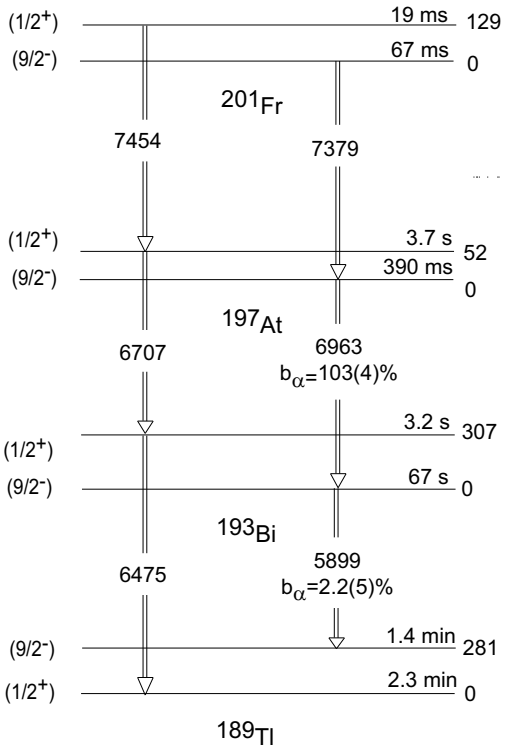

Figure D.4: Decay scheme of ^{201}Fr and ^{197}At. The α decay energy as well as the half-life for ^{201m}Fr are taken from [Uus03]. E_α and $T_{1/2}$ for ^{201g}Fr and ^{197g}At are taken from this work. The excitation energy of the $(1/2^+)$ state in ^{197}At has been taken from [Coe86], its half-life from [Smi99]. The ^{197g}At and ^{193g}Bi α branching ratios have been determined in this work. Other data are from [Fir96]

the ratios obtained in heavy ion reactions: $< 1\%$ in [Coe86] and 3.9 ± 1.2 % in [Smi99]. A careful investigation of the time behaviour of the ^{201g}Fr and ^{197g}At α lines gave half-life values of 67(3) ms and 390(16) ms, respectively. The data are summarized in table D.1. The α transition at 5882 keV was attributed to the decay of the ^{193g}Bi $(9/2^-)$ ground state [nnd]. From the intensity ratio of the ^{201g}Fr, ^{197g}At and ^{193g}Bi α lines, and taking into account the recoil loss correction [Wau91], an α branching ratio of 103(4)% for ^{197g}At and 2.2(5) % for ^{193g}Bi was obtained, consistent with the limits given in [Coe86]. The corresponding reduced widths (assuming ΔL=0 transitions) are 64(4) keV, 51(3) keV and 18(4) keV and the deduced hindrance factors, comparing with the even-even neighbours, are 1.3(2), 2.1(3) and 2.7(6) for ^{201g}Fr, ^{197g}At and ^{193g}Bi, respectively, indicating that these α transitions are unhindered and link states with the same configuration, spin and parity. For ^{201g}Fr, the hindrance factor is determined relative to ^{200}Rn only, as the reduced width for its second even-even neighbour, ^{202}Ra is only poorly known. In addition, upper limits for the branching ratios of the $9/2^-$-$1/2^+$

fine structure transitions have been calculated to be 2% for the ^{201g}Fr decay and 0.5% for the ^{197g}At decay. The corresponding lower limits of the hindrance factors (assuming ΔL=0 transitions) are 30 and 13, respectively, relative to the $9/2^-$-$9/2^-$ transitions. These numbers are consistent with experimental data on similar transitions in the α-decay of bismuth isotopes [Coe85], where hindrance factors an order of magnitude larger than the lower limits are reported.

Samenvatting

Inleiding en motivatie

De kern is een veeldeeltjessysteem dat bestaat uit Z protonen en N neutronen (beide ook nucleonen genoemd) die worden bijeengehouden door de sterke wisselwerking. Voor bepaalde proton- en/of neutronaantallen vertoont de kern een verhoogde stabiliteit. Ze worden magische getallen genoemd en kunnen vergeleken worden met de edelgasconfiguraties in atomen. Eén van deze magische getallen is Z=82, wat meteen de interesse voor dit gebied van de kernkaart verklaart, zowel op theoretisch als experimenteel vlak. Wanneer zowel het proton- als het neutronaantal magisch is, zoals voor $^{208}Pb_{126}$, noemen we de kern dubbelmagisch.

Een exacte analytische beschrijving van de kern als een A-deeltjessysteem is slechts mogelijk voor de lichtste kernen, met A$\lesssim$10. Voor een statistische behandeling is het aantal deeltjes ook in zwaardere kernen dan weer te klein. Daarom is de ontwikkeling van betrouwbare, benaderende modellen en het testen van deze modellen aan experimentele gegevens essentieel. De studie van exotische kernen, nl. de kernen ver van de stabiliteitslijn, is een uitdaging voor zowel theorie als experiment. Een bruikbaar theoretisch model moet de structurele veranderingen bij extreme N/Z verhoudingen kunnen reproduceren. Op het experimentele vlak vormt de productie van de meest zeldzame exotische kernen een uitdaging op zich, die telkens nieuwe technologische ontwikkelingen vereist.

Aan de neutronrijke zijde t.o.v. ^{208}Pb is de experimentele informatie heel beperkt, aangezien deze kernen moeilijk aan te maken zijn. Hun hoge N/Z verhouding laat niet toe ze te produceren in een fusie-evaporatiereactie. Ook diep-inelastische reacties met zware ionen slagen er niet in de meest neutronrijke isotopen de produceren. De reactieproducten verliezen namelijk hun excitatieënergie deels via de emissie van neutronen. Recent werd echter vooruitgang geboekt met projectiel-fragmentatie en spallatie van actinides. Deze laatste techniek werd met succes toegepast aan de ISOLDE on-line

massaseparator [iso] en zal in detail beschreven worden in de volgende paragraaf. Bismuthisotopen werden er systematisch geproduceerd tot ^{217}Bi [Kur00, Kur03a, Kur03b]. In dit werk werd het β-verval van ^{218}Bi en ^{215}Pb bestudeerd.

In de buurt van dubbelmagische kernen is het schillenmodel het meest succesvolle theoretische model. De kern wordt er verdeeld in een inerte romp en een aantal valentienucleonen. Deze laatste bepalen samen de laagenergetische geëxciteerde toestanden van de kern. Voor kernen waarvan één van de twee soorten kerndeeltjes zich in een gesloten schil bevindt, bepalen excitaties van individuele valentiedeeltjes van de andere soort het energiespectrum. Deze kernen zijn in hun laagste aangeslagen toestand sferisch door de extra stabiliteit van de gesloten configuratie. Wanneer zowel valentieprotonen als -neutronen aanwezig zijn, kunnen correlaties tussen deze deeltjes aanleiding geven tot collectieve excitaties. Hierbij beweegt een groot aantal nucleonen op een gelijkaardige manier; voorbeelden hiervan zijn collectieve vibraties en rotaties. De neutronrijke isotopen die in dit werk worden beschreven, hebben slechts enkele nucleonen buiten de dubbelmagische romp en kunnen bijgevolg met het schillenmodel beschreven worden.

In het neutronarme loodgebied spelen *indringtoestanden* een cruciale rol. Deze excitaties worden geassocieerd met deeltje-gat (paar)excitaties doorheen de magische schil (Z=82). Nabij de neutronschillensluiting worden ze verwacht bij hoge energie. Een combinatie van versterkte paringsinteractie en een toenemende $p-n$ interactie brengt deze toestanden lager in energie wanneer we het midden van de neutronschil (tussen N=82 en N=126) bereiken. De correlaties tussen de extra protonen, gecreëerd door de deeltje-gat excitaties, en de open neutronschil maken deze toestanden vervormd. Afhankelijk van het aantal deeltje-gat excitaties en de interactie met de valentienucleonen van de andere soort, zijn de indringtoestanden oblaat of prolaat vervormd. Wanneer configuraties met verschillende vervorming samen voorkomen bij lage excitatieënergie, spreken we van vormcoëxistentie. Dit fenomeen werd uitvoerig bestudeerd in zowel α-vervalstudies als in-bundelmetingen. In de even-even loodisotopen werden deze verschillende toestanden geobserveerd via de aanwezigheid van geëxciteerde 0^+-toestanden in het lage-energiespectrum. De observatie van rotationele banden gebouwd op deze toestanden geeft aan dat ze gedeformeerd zijn. In dit werk onderzoeken we in het bijzonder het effect van een mogelijke menging van de gedeformeerde configuraties in de overwegend sferische grondtoestand van de loodisotopen. Een direct meetgegeven in dit verband is de gemiddelde kwadratische straal van de grondtoestand.

Systematische metingen van de kernstralen werden uitgevoerd voor verschillende

elementen in het loodgebied (zie Fig. 3.5). De gevoeligheid van de gemiddelde kwadratische straal aan de vervorming van de grondtoestand wordt duidelijk waargenomen in de kwik isotopenreeks. Een ongewoon even-oneven effect werd geobserveerd in de stralen en werd geassocieerd met een zwak gedeformeerde grondtoestand in de even-even isotopen en een sterk gedeformeerde voor de oneven-A isotopen.
Voor de loodisotopen werd een systematische meting slechts uitgevoerd tot ^{190}Pb [Tho83, Ans86, Dut91]; de dalende productie liet niet toe het midden van de neutronschil, waar vormcoëxistentie werd geobserveerd, te bereiken met de gebruikelijke atomaire spectroscopische methodes. Dankzij de hogere gevoeligheid van de in-bron laserspectroscopie, die we in dit werk hebben gebruikt, konden we deze systematiek uitbreiden tot ^{183}Pb.

Experimentele Methode

Het aanmaken van exotische lood- en bismuthkernen

Alle experimenten beschreven in dit werk werden uitgevoerd aan de ISOLDE on-line massaseparator (CERN, Genève). De lood- en bismuthisotopen worden er aangemaakt in een proton-geïnduceerde spallatiereactie. Protonen met een energie van 1.0 of 1.4 GeV bombarderen een uranium- of thoriumcarbide/grafiet trefschijf. Door de dikte van deze trefschijf zullen vrijwel alle reactieproducten gestopt worden. Het hieropvolgende diffusieproces is eerder traag en sterk elementafhankelijk. Daardoor zullen een aantal elementen moeilijk of helemaal niet met deze techniek kunnen geproduceerd worden en zullen de kortstlevende isotopen ($T_{1/2} \lesssim 10$ ms) vervallen vooraleer ze uit de trefschijf treden. Om de diffusiesnelheid te verhogen, wordt de trefschijf verhit tot ongeveer 2000°C. Het belangrijkste voordeel van deze methode is echter dat de dikke trefschijf een hoge opbrengst garandeert.
De reactieproducten verlaten de trefschijf als neutrale atomen en worden vervolgens geïoniseerd. Verschillende ionisatiemechanismen kunnen worden aangewend:

- In een *plasma ionenbron* worden de atomen geïoniseerd door botsing met de elektronen in het plasma. Zowat alle elementen kunnen op deze manier worden geïoniseerd.

- Bij *oppervlakte-ionisatie* kunnen ionen gevormd worden door contact met de hete wanden van de trefschijfcontainer of de ionenbron. Dit proces is vooral belangrijk bij elementen met een lage ionisatiepotentiaal, bijvoorbeeld francium.

- In de *resonante ionisatie laserionenbron* (RILIS) wordt een specifiek element selectief geïoniseerd door een stapsgewijze excitatie met behulp van laserlicht. De

frequentie van het laserlicht is zodanig gekozen dat het overeenstemt met de verschillende atomaire overgangen van het element in kwestie. Hierdoor kunnen zuivere bundels van een specifiek element worden geproduceerd.

Hoewel de intrinsieke selectiviteit van de laserionenbron bijzonder hoog is, zal de uiteindelijke bundel vaak contaminaties vertonen t.g.v. oppervlakte-ionisatie in de bron. Zo vinden we bijvoorbeeld in alle neutronrijke lood- en bismuthbundels steeds franciumcontaminatie terug. Daarom wordt een extra selectieprocedure toegepast. De *gepulste uitstroom* methode werd uitvoerig beschreven in [Van98] en is schematisch voorgesteld in Fig. 2.8. Door gebruik te maken van de gepulste structuur van de protonenbundel kan de bundel periodiek onderdrukt worden, waardoor kortlevende isotopen zullen vervallen vooraleer de bundel naar het detectiestation wordt doorgelaten. In het neutronrijke gebied is deze techniek bijzonder efficiënt, daar de lood- en bismuthisotopen die we willen aanmaken een relatief lange levensduur hebben en de contaminerende isotopen kortlevende α-emitters zijn. Op die manier werd de zuiverheid van de lood-en bismuthbundels bekomen die cruciaal is in deze studie.
Uiteindelijk wordt de ionenbundel naar massa gescheiden in de massaseparator, alvorens te worden geïmplanteerd in een koolstoffolie of een bandtransportsysteem.

Vervalstudies

Eén van de beste manieren om de lage-spinstructuur van exotische kernen te onderzoeken is via hun radioactief verval. De alternatieve in-bundel methode, bijvoorbeeld, voedt hoofdzakelijk hoge-spintoestanden in een zware ionen geïnduceerde fusie-evaporatiereactie en de hieropvolgende de-excitatie gaat voornamelijk via de zogenaamde *yrast*-toestanden (*i.e.* de toestanden met de laagste excitatieënergie voor een bepaalde spin). Vervalstudies laten toe informatie te verkrijgen i.v.m. de excitatieënergie, spin en pariteit van de laaggelegen toestanden,evenals levensduren.

Verschillende detectieopstellingen werden gebruikt in dit werk. In een eerste experiment werd het gecorreleerde β- en γ-verval van de lood- en bismuthisotopen opgemeten. Hiervoor werden plastic scintillatiedetectoren (β-straling) en HPGe-detectoren (γ-straling) in een coïncidentie-opstelling gebruikt. Een schematische voorstelling van deze opstelling wordt getoond in Fig. 2.11.

In de α-vervalstudies in dit werk, werd de ionenbundel geïmplanteerd in een 20 μg/cm^2 dikke koolstoffolie. Aan de achterzijde van deze folie werden silicium PIPS detectoren geplaatst voor de detectie van de α-deeltjes. Figuur 2.10 toont deze configuratie.

Laser spectroscopische metingen

De tweede methode die in dit werk werd toegepast, nl. atomaire spectroscopie, wordt voornamelijk gebruikt om spins, magnetische momenten en kwadrupoolmomenten van de grondtoestand of van isomere toestanden te bepalen.
De interactie tussen de ladingsverdeling van de kern en het elektromagnetische veld van de atomaire elektronen beïnvloedt het atomaire spectrum, via de isotoopverschuiving en de hyperfijnsplitsing (HFS). Deze interactie is zuiver elektromagnetisch van aard en het is gebruikelijk de elektromagnetische transitie-operator te ontwikkelen in een multipoolreeks. De elektrische monopool komt overeen met de lading van de kern en veroorzaakt een globale verschuiving van de elektronische fijnstructuurtoestanden, die de isotoopverschuiving wordt genoemd. Het magnetische dipoolmoment en het elektrische kwadrupoolmoment geven aanleiding tot een splitsing van de atomaire toestanden, de HFS.

In dit werk gebruikten we de *in-bron* laserspectroscopie techniek. Hierbij wordt het principe van resonante laserionisatie in de RILIS-bron gebruikt. Bovendien wordt de frequentie van de laser in de eerste excitatiestap gevarieerd, doorheen het gebied van resonante excitatie. De intensiteit van de α-lijnen in het loodverval wordt opgemeten in functie van de laserfrequentie. Uit deze laserscans kunnen we dan de isotoopverschuiving en, voor de isotopen met een oneven massagetal, ook de hyperfijnsplitsing bepalen. Deze levert ons de waarde van het magnetisch dipoolmoment van de kern. In principe kunnen hieruit eveneens de elektrische kwadrupoolmomenten worden bepaald, maar deze worden in dit werk niet verder besproken.

Beta verval van neutronrijke lood- en bismuthisotopen

Beta-verval van ^{213,215}Pb

In een eerste experiment (zie Tabel 2.4) werd het β-verval van ^{213}Pb naar ^{213}Bi bestudeerd. In het β^--verval van ^{217}Bi werden ^{217}Po kernen geproduceerd, die op hun beurt via α-desintegratie vervielen naar ^{213}Pb (Fig. 4.1). Het niveauschema van ^{213}Bi werd aanzienlijk uitgebreid, op basis van γ-γ coïncidentiegegevens. Het uiteindelijke niveauschema is getoond in Fig. 4.4.

Een tweede experiment maakte gebruik van de selectiviteit van de RILIS om voor de eerste maal het β-verval van ^{215}Pb te observeren. In de dochterkern ^{215}Bi was enkel

een cascade van γ-transities gekend, die gevoed wordt via een hoge-spin isomeer in ^{215}Bi [Kur03b]. Geen verdere experimentele informatie was gekend.
De resonante laserionisatie speelde een cruciale rol in de identificatie van het ^{215}Pb β-verval. De vergelijking van de spectra met en zonder laserionisatie duidde onmiddellijk aan welke γ-lijnen verwant zijn aan het lood- of dochterverval. Op deze manier werd een transitie bij 183.5(3) keV toegekend aan het verval van ^{215}Pb. Op basis van coïncidenties met deze lijn of met de geassocieerde X-stralen, werd het niveauschema verder uitgebreid. De halfwaardetijd werd eveneens bepaald: 147(12) s.

In deze kernen ging onze aandacht naar de evolutie van de eerste geëxciteerde toestand in de oneven-A bismuthisotopen. Met slechts één proton buiten de gesloten protonschil, zijn deze isotopen bijzonder geschikt om de evolutie van het gemiddelde veld van de protonen te observeren. Een sterk dalende trend werd waargenomen (Fig. 4.13). Ook bij andere gesloten schillen werden dergelijke effecten geobserveerd. In het schillenmodel wordt dit gedrag verklaard als een effect van de proton-neutron interactie, en in het bijzonder van de monopool component. Daarom wordt het ook de *monopoolmigratie* genoemd. Om het geobserveerde effect in de bismuthisotopen echter met zekerheid hieraan toe te schrijven zijn verdere berekeningen nodig. Deze zullen worden uitgevoerd door A. De Maesschalck en N.A. Smirnova (Universiteit Gent).

Beta-verval van ^{218}Bi

Voor de eerste observatie van het β-verval van ^{218}Bi werd eveneens gebruik gemaakt van de RILIS en de identificatiemethode die hierboven reeds werd besproken. Het ^{218}Bi isotoop werd reeds eerder geproduceerd via een projectiel-fragmentatiereactie, maar er werd geen spectroscopische informatie omtrent het verval bekomen [Pfu98].
Een energieniveau bij 510(2) keV in de dochterkern ^{218}Po was gekend uit het α-verval van ^{222}Rn en werd geassocieerd met de 2^+-0^+ overgang in ^{218}Po [Mad56].
Vier sterke γ-transities bij 263.0 keV, 385.7 keV, 425.5 keV en 509.7 keV werden enkel in de spectra met resonante ionisatie geobserveerd en werden op basis hiervan toegekend aan het verval van ^{218}Bi. Hun onderlinge coïncidentierelaties laten toe ze in een cascade te plaatsen. De preciese ordening in de cascade is gebaseerd op de gekende 2^+-0^+ overgang, systematische beschouwingen en veralgemeende senioriteitsargumenten. Het niveauschema wordt getoond in Fig. 4.18.
Uit een exponentiële fit van het tijdsgedrag van de γ-lijnen bij 385.7 and 263.0 keV werd een halfwaardetijd van 33(1) s afgeleid. Dit resultaat werd vergeleken met theoretische berekeningen van de levensduur van de bismuthisotopen door I. Borzov. In

deze berekeningen werden zowel toegelaten als éénmaal-verboden overgangen in rekening gebracht [Bor03].

Uit de intensiteiten van de γ-lijnen leiden we af dat het β-verval voornamelijk de 6^+ en 8^+ toestanden in de dochterkern voedt (zie Fig 4.18). Dit betekent dat de grondtoestand van de moederkern een hoge-spin toestand is. De meest waarschijnlijke configuratie voor deze toestand is de koppeling van een proton in het $1h_{9/2}$ orbitaal aan een neutron in het $2g_{9/2}$ orbitaal. Deze koppeling geeft aanleiding tot een multiplet van toestanden met spin en pariteit $0^-..9^-$. Een hoge spin voor de grondtoestand is in overeenstemming met de eenvoudige parabolische regel, besproken door Paar [Paa79] (zie Fig. 4.20).

De grondtoestand van ^{218}Po kan in het schillenmodel worden beschreven als een gesloten romp met een extra protonpaar in de $1h_{9/2}$ of $2f_{7/2}$ orbitalen en vier neutronparen in $2g_{9/2}$ of $1i_{11/2}$. De eenvoudigste manier om geëxciteerde toestanden te vormen is door spins in de valentieparen te aligneren. De geobserveerde cascade van γ-transities kan dan worden geïnterpreteerd als een E2 cascade tussen de 8^+, 6^+, 4^+, 2^+ toestanden en de 0^+ grondtoestand van ^{218}Po. Het experimentele niveauschema werd vergeleken met een schillenmodelberekening in Fig. 4.23. Het experimentele spectrum wijkt duidelijk af van wat geobserveerd werd in het magische ^{210}Po isotoop (zie Fig. 4.22) en we leiden hieruit af dat de extra proton- en neutronparen aanleiding geven tot verhoogde collectiviteit in de kern. Deze wordt echter niet gereproduceerd in de theoretische berekening.

β-vertraagde neutronemissie van neutronrijke thalliumisotopen

In deze paragraaf bespreken we twee metingen die tot doel hadden de halfwaardetijd van neutronrijke thalliumisotopen te bepalen. De halfwaardetijden van exotische kernen vormen immers een belangrijke test voor kernmodellen in de astrofysische beschrijving van het r-proces.
Aangezien in deze thalliumisotopen β-vertraagde neutronemissie werd verwacht (zie Tabel 5.1), probeerden we hun halfwaardetijd te bepalen op basis van de geobserveerde neutronen. Geen van beide experimenten was echter succesvol; waarschijnlijk verdwijnt het resonante thalliumsignaal in de veel sterkere achtergrond van geïnduceerde (α,n) reacties op de aluminium wanden van de implantatiekamer. Om dit te vermijden, werd in het tweede experiment een goudlaagje aangebracht binnenin deze kamer, omdat de

(α,n) opbrengst hier veel kleiner zou zijn. Waarom ook dit tweede experiment faalde, is onduidelijk.

In-bron laserspectroscopie van neutronarme loodkernen

Met behulp van de in-bron laserspectroscopiemethode werd de isotoopverschuiving in de neutronarme isotopen $^{188-183}$Pb gemeten. Hieruit werd de gemiddelde kwadratische straal voor deze isotopen bepaald. Dit betekent dat we voor het eerst deze systematische meting konden uitvoeren bij het midden van de neutronschil (N=104), nl. in het gebied waar de indringtoestanden hun minimale excitatieënergie bereiken.
De eerste bedoeling van deze metingen is de invloed van de gedeformeerde indringtoestanden op de sferische grondtoestand na te gaan. Een quasi-sferische vorm van de loodisotopen werd geobserveerd en in tegenstelling tot bijvoorbeeld de kwikisotopen, werd er geen abnormaal oneven-even effect waargenomen (zie Fig. 6.12). De vergelijking met de voorspellingen van het sferische "droplet model" toont echter een beperkte afwijking in het gebied van A=194 tot A=183. Verschillende theoretische modellen werden gebruikt om deze afwijking te begrijpen, en om te onderzoeken of dit effect kan toegeschreven worden aan de menging van gedeformeerde indringtoestanden in de grondtoestand. Berekeningen in het algebraïsche IBM model (Interacting Boson Model) en het GCM model (Generator Coordinate Model) werden uitgevoerd, maar er werd geen sluitende verklaring voor deze afwijking gevonden.

In de isotopen met oneven massagetal, kan uit de hyperfijnsplitsing van de atomaire niveaus ook het magnetisch moment worden bepaald. In deze isotopen zijn telkens twee isomere toestanden gekend, met tentatieve spin- en pariteitstoekenning I=$13/2^+$ en I=$3/2^-$. Voor beide isomeren werd het magnetisch moment bepaald, met de hierbovenvermelde spinaanname. De bekomen waarden zijn consistent met deze voor de zwaardere isotopen [Dut91]. Dit wijst erop dat de configuraties een relatief zuiver één-deeltjeskarakter behouden, dat we associëren met een ongepaard neutron in de $i_{13/2}$ en $p_{3/2}$ orbitalen.

Besluit en toekomstperspectieven

In dit werk werd een gedetailleerde studie van het β-verval van een selectie van neutronrijke isotopen in de buurt van dubbelmagisch ^{208}Pb voorgesteld. Resultaten werden

besproken voor het verval van ^{213,215}Pb en ^{218}Bi.
Proton geïnduceerde spallatie van een actinide trefschijfkern werd gebruikt om deze isotopen aan te maken, in een gebied waar nog slechts weinig van de kernstructuur gekend is. Cruciaal in deze studie was de methode van gepulste uitstroom: deze liet toe de sterke contaminatie van zwaardere elementen zoals francium aanzienlijk te reduceren. Bovendien leverde het gebruik van de resonante laserionisatie bundels van één specifiek element, of zelfs isomeer.
Om het onderzoek in dit gebied verder te zetten, naar nog meer neutronrijke kernen, zullen echter nieuwe, sterkere productie-, selectie- en detectiemethodes onmisbaar zijn. Dit geldt in het bijzonder voor de bismuthisotopen, waar de gepulste uitstroommethode niet langer kan worden gebruikt.

In een tweede deel van dit werk werd een laserspectroscopische meting van de neutronarme loodisotopen met A=183-188 besproken. Gemiddelde kwadratische stralen en magnetische momenten werden bepaald.
In de toekomst kunnen ook de neutronarme poloniumisotopen nabij het midden van de neutronschil worden bestudeerd met in-bron laserspectroscopie. In tegenstelling tot de loodisotopen, waar de grondtoestand overwegend sferisch blijft, hebben α-verval studies aangetoond dat vervormde configuraties domineren in de ^{190,188}Po grondtoestand [Van03b]. Bovendien werd via α-verval een verschillende vorm afgeleid voor de positieve- en negatieve pariteitsisomeer in het oneven-A isotoop ^{191}Po, vergelijkbaar met bijvoorbeeld ^{185}Hg [And99c]. De verschillende koppeling van het ongepaard neutron in de toestanden met positieve en negatieve pariteit geeft aanleiding tot een verschillende vorm voor de grondtoestand en de isomere toestand. Het ionisatieschema voor resonante ionisatie van poloniumatomen werd echter nog niet experimenteel getest met de ISOLDE laserionenbron.

De recente ontwikkelingen met naversnelde radioactieve bundels zullen in de toekomst nieuwe experimenten mogelijk maken, d.m.v. nieuwe trefschijf- en bundelcombinaties. Voor de studie van de indringtoestanden in de neutronarme loodisotopen zouden transferreacties complementaire informatie kunnen opleveren. Deze reacties geven namelijk directe informatie over de onderliggende microscopische structuur van de indringtoestanden, zoals bijvoorbeeld werd aangetoond in de tinisotopen. Experimenten met radioactieve kwikbundels worden momenteel overwogen aan de REX-ISOLDE faciliteit.

Bibliography

[Ako92] Akovali Y.A., Nucl. Data Sheets **66** (1992), 237.

[Alk92] Alkhazov G.D. *et al.*, Nucl. Instr. Meth. B **69** (1992), 517.

[All98] Allatt R.G. *et al.*, Phys. Lett. B **437** (1998), 29.

[And99a] Andreyev A.N. *et al.*, Eur. Phys. J. A **6** (1999), 381.

[And99b] Andreyev A.N. *et al*, J. Phys. G: Nucl. Part. Phys. **25** (1999), 835.

[And99c] Andreyev A.N. *et al.*, Phys. Rev. Lett. **82** (1999), 1819.

[And00] Andreyev A.N. *et al.*, Nature **405** (2000), 430.

[And02a] Andreyev A.N. *et al.*, Eur. Phys. J. A **14** (2002), 63.

[And02b] Andreyev A.N. *et al.*, Phys. Rev. C **66** (2002), 014313.

[And04] Andreyev A.N. *et al.*, Phys. Rev. C **69** (2004), 054308.

[Ans86] Anselment M. *et al.*, Nucl. Phys. A **451** (1986), 471.

[Ant78] Anton K.-R. *et al.*, Phys. Rev. Lett. **40** (1978), 642.

[Bar57] Bardeen J., Cooper L.N. and Schrieffer J.R., Phys. Rev. **108** (1957), 1175.

[Bau73] Bauer R. *et al.*, Nucl. Phys. A **209** (1973), 535.

[Ben04] Bender M. *et al.*, Phys. Rev. C **69** (2004), 064303.

[Ber00] Bergmann U.C. Ph.D. thesis, University of Aarhus, unpublished, 2000.

[Bha79] Bhatia T.S. *et al.*, Nucl. Phys. A **314** (1979), 101.

[Bij96] Bijnens N. *et al.*, Zeit. Phys. A **356** (1996), 3.

[Bij98] Bijnens N. *et al.*, Phys. Rev. C **58** (1998), 754.

[Bil95] Billowes J. and Campbell P., J. Phys. G: Nucl. Part. Phys. **21** (1995), 707.

[Bon71] Bonn J. *et al.*, Phys. Lett. B **36** (1971), 41.

[Bon72] Bonn J. *et al.*, Phys. Lett. B **38** (1972), 308.

[Bon76] Bonn J. *et al.*, Zeit. Phys. A **276** (1976), 203.

[Bor03] Borzov I.N., Phys. Rev. C **67** (2003), 025802.

[Cam95] Campbell P. *et al.*, Phys. Lett. B **346** (1995), 21.

[Cap85] Capurro O.A. *et al.*, J.Radioanal.Nucl.Chem. **89** (1985), 519.

[Cau99] Caurier E. *et al.*, Phys. Rev. C **59** (1999), 2033.

[Cau03] Caurier E. *et al.*, Phys. Rev. C **67** (2003), 054310.

[Cau04] Caurier E. *et al.*, arXiv:nucl-th **0402046 v1** (2004).

[Chu97] Chumin V.G. *et al.*, Zeit. Phys. A **358** (1997), 33.

[Coc98] Cocks J.F.C *et al*, Eur. Phys. J. A **3** (1998), 17.

[Coe85] Coenen E. *et al.*, Phys. Rev. Lett. **54** (1985), 1783.

[Coe86] Coenen E. *et al.*, Zeit. Phys. A **324** (1986), 485.

[Cov99] Covello A. *et al.*, Acta Phys. Pol. B **30** (1999), 715.

[Dab79] Dabkiewicz P. *et al.*, Phys. Lett. B **82** (1979), 199.

[De 00] De Coster C. *et al.*, Phys. Rev. C **61** (2000), 067306.

[Den89] Dendooven P. *et al.*, Phys. Lett. B **226** (1989), 27.

[Den92] Dendooven P. Ph.D. thesis, University of Leuven, unpublished, 1992.

[Dew03] Dewald A. *et al.*, Phys. Rev. C **68** (2003), 034134.

[Din90] Dinger U. *et al.*, Hyperfine interactions **59** (1990), 77.

[Dra98] Dracoulis G.D. *et al.*, Phys. Lett. B **432** (1998), 37.

[Dra03] Dracoulis G.D. *et al.*, Phys. Rev. C **67** (2003), 051301R.

[Dug03] Duguet T. *et al.*, Phys. Lett. B **559** (2003), 201.

[Duo89] Duong H.T. *et al.*, Phys. Lett. B **217** (1989), 401.

[Dut91] Dutta S.B. *et al*, Zeit. Phys. A **341** (1991), 39.

[Duv81] Duval P.D. and Barrett B.R., Phys. Lett. B **100** (1981), 223.

[Enq96] Enqvist T. *et al.*, Zeit. Phys. A **354** (1996), 1.

[Ewa80] Ewan G.T. *et al.*, Zeit. Phys. A **296** (1980), 223.

[Fed03] Fedosseev V.N. *et al.*, Nucl. Instr. Methods B **204** (2003), 353.

[Fir96] Firestone R.B., *Table of Isotopes*, John Wiley & Sons Inc., 1996.

[For98] Fornal B. *et al.*, Eur. Phys. J. A **1** (1998), 355.

[Fos03] Fossion R. *et al.*, Phys. Rev. C **67** (2003), 024306.

[Fos04] Fossion R., *private communication* (2004).

[Fra01] Franchoo S. *et al.*, Phys. Rev. C **64** (2001), 054308.

[Fra04] Frank A. *et al.*, Phys. Rev. C **69** (2004), 034323.

[gea] `http://wwwinfo.cern.ch/asd/geant/`.

[Gra04] Grawe H., *The Euroschool lectures on Physics with exotic beams , Vol. I*, Lecture notes in physics, Springer Verlag, Berlin Heidelberg, 2004. Eds. Al-Khalili J. and Roeckl E.

[Hag69] Hager R.S and Seltzer E.C., Nucl. Data A **6** (1969), 1.

[Har97] Harder M.K. *et al.*, Phys. Lett. B **405** (1997), 25.

[Hax49] Haxel O., Jensen J.H.D. and Suess H.E., Phys. Rev. **75** (1949), 1766.

[Hee93] Heese J. *et al.*, Phys. Lett. B **302** (1993), 390.

[Hee04] Heenen P.-H., *private communication* (2004).

[Hey83] Heyde K. *et al.*, Phys. Reports **102** (1983), 291.

[Hey87] Heyde K. *et al.*, Nucl. Phys. A **466** (1987), 189.

[Hey88] Heyde K. *et al.*, Nucl. Phys. A **484** (1988), 275.

[Hey89] Heyde K. *et al.*, Phys. Lett. B **218** (1989), 287.

[Hey94a] Heyde K., *Basic ideas and concepts in nuclear physics*, Institute of Physics Publishing, Bristol, 1994.

[Hey94b] Heyde K., *The nuclear shell model*, Springer Verlag, Berlin Heidelberg, 1994.

[Hil92] Hilberath Th. *et al.*, Z. Phys. A **342** (1992), 1.

[Huy92] Huyse M. *et al.*, Phys. Rev. C **46** (1992), 1209.

[iso] `http://isolde.cern.ch/`.

[Jac79] Jacquinot P. and Klapisch R., Rep. Prog. Phys. **42** (1979), 773.

[Jen00] Jenkins D.G. *et al*, Phys. Rev. C **62** (2000), 021302R.

[Jen02] Jenkins D.G. *et al*, Phys. Rev. C **66** (2002), 011301R.

[Jul01a] Julin R. *et al.*, Eur. Phys. J. A **15** (2001), 189.

[Jul01b] Julin R. *et al.*, J. Phys. G: Nucl. Part. Phys. **27** (2001), R109.

[Kin85] King W.H. and Wilson M., J. Phys. G: Nucl. Part. Phys. **11** (1985), L43.

[Klu03] Kluge H.-J. and Nörtershäuser W., Spectrochimica Acta B **58** (2003), 1031.

[Koe02] Koester U., Nucl. Phys. A **701** (2002), 441c.

[Koe03] Koester U. *et al.*, Nucl. Instr. Methods B **204** (2003), 347.

[Kow91] Kowalewska D. *et al.*, Phys. Rev. A **44** (1991), R1442.

[Kro88] Kroenert U. *et al.*, Z. Phys. A **331** (1988), 52.

[Kue77] Kuehl T. *et al.*, Phys. Rev. Lett. **39** (1977), 180.

[Kug00] Kugler E., Hyperfine Interactions **129** (2000), 23.

[Kuo71] Kuo T.T.S. and Herling G.H., US Naval Research Laboratory Report **2258** (1971), unpublished.

[Kur00] Kurpeta J. *et al.*, Eur. Phys. J. A **7** (2000), 49.

[Kur03a] Kurpeta J. *et al.*, Eur. Phys. J. A **18** (2003), 5.

[Kur03b] Kurpeta J. *et al.*, Eur. Phys. J. A **18** (2003), 31.

[Lan01] Lane G.J. *et al.*, Nucl. Phys. A **682** (2001), 71c.

[Lan03] Langanke K.-H. and Martínez-Pinedo G., Rev. Mod. Phys. **75** (2003), 819.

[Le 99a] Le Blanc F. *et al.*, Phys. Rev. C **60** (1999), 054310.

[Le 99b] Le Coz Y. *et al.*, EPJdirect A **3** (1999), 1.

[Let97] Lettry J. *et al.*, Nucl. Instr. Methods B **126** (1997), 130.

[Lia97] Liang C.F., Paris P. and Sheline R.K., Phys. Rev. C **56** (1997), 2324.

[Lia99] Liang C.F., Paris P. and Sheline R.K., Phys. Rev. C **59** (1999), 648.

[Lun03] Lunney D., Pearson J.M. and Thibault C., Reviews of Modern Physics **75** (2003), 1021.

[Mad56] Madansky L. and Rasetti F., Phys. Rev. C **102** (1956), 464.

[Mai89] Maier K.H. *et al.*, Zeit. Phys. A **332** (1989), 263.

[Map77] Maples C., Nucl. Data Sheets **22** (1977), 207.

[May49] Mayer M.G., Phys. Rev. **75** (1949), 1969.

[May77] May F.R., Frauendorf S. and Pashkevich V.V., Phys. Lett. B **68** (1977), 113.

[mbs] `http://daq.gsi.de/`.

[Mis93] Mishin V.I. *et al.*, Nucl. Instr. Meth. B **73** (1993), 550.

[Moe95] Moeller P. *et al.*, At. Data Nucl. Data Tables **59** (1995), 185.

[Moe97] Moeller P., Nix J.R. and Kratz K.L., At. Data Nucl. Data Tables **66** (1997), 131.

[Moe02] Moeller P., Pfeiffer B. and Kratz K.-L., Report LANL-UR (2002), 02–2919.

[Mor95] Morita K. *et al.*, Z. Phys. A **352** (1995), 7.

[Mye66] Myers W. D. and Swiatecki W.J., Nucl. Phys. **81** (1966), 1.

[Mye83] Myers W.D. and Schmidt K.-H., Nucl. Phys. A **410** (1983), 61.

[Nav03] Navrátil P. and Ormand W.E., Phys. Rev. C **68** (2003), 034305.

[Ney03] Neyens G., Rep. Prog. Phys. **66** (2003), 633.

[Nil95] Nilsson S.G. and Ragnarsson I., *Shapes and shells in nuclear structure*, Cambridge University Press, 1995.

[nnd] `http://www.nndc.bnl.gov`.

[Ots01a] Otsuka T., Nucl. Phys. A **693** (2001), 383.

[Ots01b] Otsuka T. *et al.*, Phys. Rev. Lett. **87** (2001), 082502.

[Ott89] Otten E.W., *Treatise on heavy-ion science*, volume 8, Plenum Press, New York, 1989. Ed. Bromley D.A.

[Paa79] Paar V., Nucl. Phys. A **331** (1979), 16.

[paw] `http://wwwinfo.cern.ch/asd/paw/`.

[Pea00] Pearson M.R. *et al.*, J. Phys. G: Nucl. Part. Phys. **26** (2000), 1829.

[Pen87] Penninga J. *et al.*, Nucl. Phys. A **471** (1987), 535.

[Pfu98] Pfuetzner M. *et al.*, Phys. Lett. B **444** (1998), 32.

[Pie02] Pieper S.C., Varga K. and Wiringa R.B., Phys. Rev. C **66** (2002), 044310.

[Pov01] Poves A. and Nowacki F., *An advanced course in modern nuclear physics*, Lecture notes in physics, Springer Verlag, Berlin Heidelberg, 2001. Eds. Arias J.M. and Lozano M.

[Pu 97] Pu Y.H. *et al.*, Zeit. Phys. A **357** (1997), 1.

[Ram89] Raman S. *et al.*, At. Data and Nucl. Data Tables **42** (1989), 1.

[Ras59] Rasmussen J.O., Phys. Rev. **113** (1959), 1593.

[Rej97] Rejmund M.*et al.*, Zeit. Phys. A **359** (1997), 243.

[Rej98] Rejmund M. *et al.*, Eur. Phys. J. A **1** (1998), 261.

[Rej00] Rejmund M. *et al.*, Eur. Phys. J. A **8** (2000), 161.

[Rin96] Ring P., Prog. Part. Nucl. Phys. **37** (1996), 193.

[Rod04] Rodríguez-Guzmán, Egido J.L. and Robledo L.M., Phys. Rev. C **69** (2004), 054319.

[Rou03] Roussière B., *private communication* (2003).

[Ruc90] Ruchowska E. *et al.*, J. Phys. G **16** (1990), 255.

[Sch99] Schmidt K.H., *private communication* (1999).

[Seb98] Sebastian V. *et al.*, AIP Conf. Proc. (ENAM '98) **455** (1998), 126.

[Seg82] Segré E. , *Nuclei and particles*, Benjamin and Cummings, 1982.

[Sel69] Seltzer E.C., Phys. Rev. **188** (1969), 1916.

[Sel03] Seliverstov M., *private communication* (2003).

[She02] Shergur J. *et al.*, Phys. Rev. C **65** (2002), 034313.

[Smi99] Smith M.B. *et al.*, Eur. Phys. J. A **5** (1999), 43.

[Smi00] Smith M.B. *et al.*, J. Phys. G: Nucl. Part. Phys. **26** (2000), 787.

[Smi04] Smirnova N.A. *et al.*, Phys. Rev. C **69** (2004), 044306.

[sri] `http://www.srim.org/`.

[Sta90] Staudt A. *et al.*, At. Data and Nucl. Data Tables **44** (1990), 79.

[Ste64] Stelson P.H. and McGowan F.K., Phys. Rev. **133** (1964), B911.

[Sto] Stone N. *Table of nuclear moments*, `http://www.nndc.bnl.gov/`.

[Str67] Strutinsky V.M., Nucl. Phys. A **95** (1967), 420.

[Tac90] Tachibana T. *et al.*, Prog. Theor. Phys. **84** (1990), 641.

[Tal84] Talmi I., Nucl. Phys. A **423** (1984), 189.

[Tho83] Thompson R.C. *et al.*, J. Phys. G: Nucl. Phys. Part. Phys **9** (1983), 443.

[Tre67] Treytl W. and Valli K., Nucl. Phys. A **97** (1967), 405.

[Uus03] Uusitalo J. *et al.*, to be published (2003).

[Van84] Van Duppen P. *et al.*, Phys. Rev. Lett. **52** (1984), 1974.

[Van91] Van Duppen P. *et al.*, Nucl. Phys. A **529** (1991), 268.

[Van98] Van Duppen P. *et al.*, Nucl. Instr. Meth. B **134** (1998), 267.

[Van00] Van Duppen P. and Huyse M., Hyperfine Interactions **129** (2000), 149.

[Van02] Van Roosbroeck J. Ph.D. thesis, University of Leuven, unpublished, 2002.

[Van03a] Van de Vel K. Ph.D. thesis, University of Leuven, unpublished, 2003.

[Van03b] Van de Vel K. *et al.*, Eur. Phys. J. A **17** (2003), 167.

[Van03c] Van de Vel K. *et al*, Phys. Rev. C **68** (2003), 054311.

[Ver00] Verney D. *et al.*, Hyperfine interactions **127** (2000), 79.

[Wal87] Wallmeroth K. *et al.*, Phys. Rev. Lett. **58** (1987), 1516.

[War91] Warburton E.K. and Brown B.A., Phys. Rev. C **43** (1991), 602.

[Wau91] Wauters J. *et al.*, Nucl. Instr. Methods B **61** (1991), 178.

[Wau94] Wauters J. *et al.*, Phys. Rev. C **50** (1994), 2768.

[Wei35] Weizsäcker C.F., Zeit. Phys. **96** (1935), 431.

[Wei99] Weissman L. *et al.*, Nucl. Instr. Methods A **423** (1999), 328.

[Woo92] Wood J.L. *et al.*, Phys. Reports **215** (1992), 101.

[Woo99] Wood J.L. *et al.*, Nucl. Phys. A **651** (1999), 323.